



HAL
open science

Beamforming and time-reversal techniques for aeroacoustic source identification in a wind-tunnel using three-dimensional microphone arrays

Yinshi Zhou

► **To cite this version:**

Yinshi Zhou. Beamforming and time-reversal techniques for aeroacoustic source identification in a wind-tunnel using three-dimensional microphone arrays. Acoustics [physics.class-ph]. Université de Poitiers, 2021. English. NNT : 2021POIT2278 . tel-03592852

HAL Id: tel-03592852

<https://theses.hal.science/tel-03592852v1>

Submitted on 1 Mar 2022

HAL is a multi-disciplinary open access archive for the deposit and dissemination of scientific research documents, whether they are published or not. The documents may come from teaching and research institutions in France or abroad, or from public or private research centers.

L'archive ouverte pluridisciplinaire **HAL**, est destinée au dépôt et à la diffusion de documents scientifiques de niveau recherche, publiés ou non, émanant des établissements d'enseignement et de recherche français ou étrangers, des laboratoires publics ou privés.

THESE

Pour l'obtention du Grade de

DOCTEUR DE L'UNIVERSITE DE POITIERS

(Faculté des Sciences Fondamentales et Appliquées)
(Diplôme National - Arrêté du 25 mai 2016)

Ecole Doctorale : Sciences et Ingénierie des Matériaux, Mécanique, Énergétique - SIMME

Secteur de Recherche : Acoustique et Aéroacoustique

Présentée par

Yinshi ZHOU

Techniques de formation de voies et de retournement temporel pour
l'identification de sources aéroacoustiques en soufflerie par antenne
microphonique tri-dimensionnelle

*Beamforming and time-reversal techniques for aeroacoustic source
identification in a wind-tunnel using a three-dimensional microphone
array*

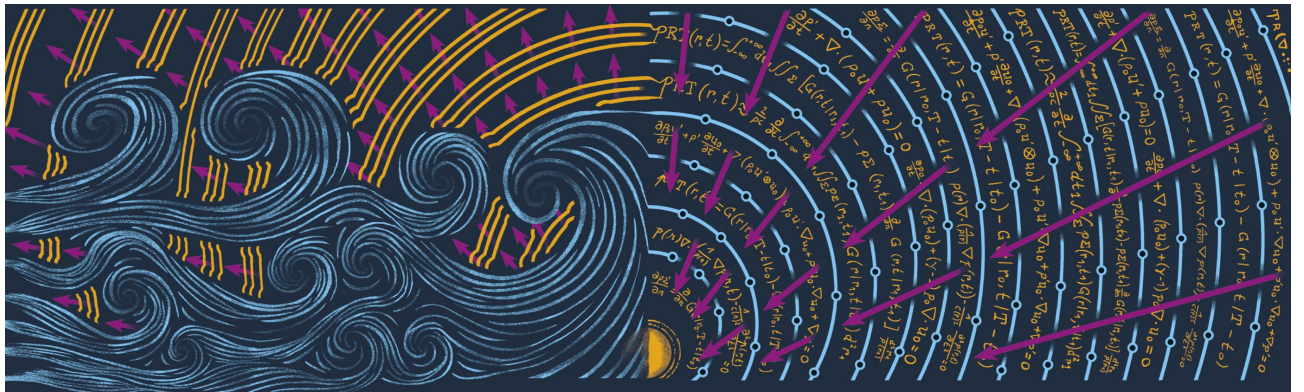
Directeur de Thèse : Vincent VALEAU

Co-direction : Régis MARCHIANO, David MARX, Christian PRAX

Soutenue le 08 juillet 2021
devant la Commission d'Examen

JURY

Xavier GLOERFELT	Professeur, ENSAM Paris	Président
Éric BAVU	Maître de conférences HDR, CNAM Paris	Rapporteur
Quentin LECLERE	Maître de conférences HDR, INSA Lyon	Rapporteur
Con DOOLAN	Professeur, University of New South Wales	Examineur
Régis MARCHIANO	Professeur, Sorbonne Université	Examineur
David MARX	Chargé de recherche, CNRS	Examineur
Christian PRAX	Maître de conférences HDR, Université de Poitiers	Examineur
Vincent VALEAU	Professeur, Université de Poitiers	Examineur
Sandrine FAUQUEUX	Ingénieur de recherche, ONERA	Invitée



Time-reversed sound waves in flows - from Kronos, Morgane PARISI (2020)
 Work produced as part of a residency at the University of Poitiers

Acknowledgements

For the jury of the thesis, I'm deeply grateful to Éric Bavu and Quentin Leclere for having accepted to review this manuscript. Your invaluable feedback for the current work, and advice for the future work are really appreciated. I'm also grateful to Xavier Gloerfelt as the head of jury, and to Con Doolan as a member of jury. Thanks to Sandrine Fauqueux for accepting the invitation to participate to the PhD defense.

I would like to express my sincere gratitude to my thesis director Vincent Valeau, who has provided a great deal of invaluable support, advice and guidance throughout my PhD studies. Your expertise, encouragement and confidence are also helpful for me.

I would like to offer my special thanks to my thesis supervisors, Régis Marchiano, David Marx and Christian Prax, who have given invaluable advice and assistance, especially for the part of numerical simulations. I benefited from your research experience and expertise. I'm especially grateful for good work conditions in Institut d'Alembert provided by Régis Marchiano for my short visits in Paris. The discussions with François Ollivier, who has followed my thesis but not in the official supervision, are also appreciated.

I'm deeply grateful for the administrative support from Bouba El Harchi and Marlène Martin, and the assistance related to computers, information and software from Jean-Christophe Verge.

I would like to extend my sincere thanks to Pascal Biais, Laurent Phillipon, Janick Laumonier and Philippe Szeger for their help to prepare and conduct the experiments presented in this thesis.

Thanks to François Ollivier, Pascal Challande, Jacques Marchal, Hugo Dutilleul, Hélène Moingeon and Christian Ollivon (Institut d'Alembert) for their invaluable technical support of the MegaMicro system.

I also wish to thank Manuel A. Diaz, who have provided a lot of support and assistance for the use of the acoustic solver ParadigmS. Thanks to Éric Foucault, who gave me a tutorial on OpenFOAM and introduced it to me.

Thanks to the members Institut Pprime who organized lectures and after-work activities. I'm also thankful to all the members of the building B17 for offering a great ambiance, especially during the time of sharing snacks, drinks and ideas. I can not forget the happy time together with my colleagues Manuel A. Diaz, Wagner Pinto, Robin Sebastian, Christian Zumi Doli, Yoann Beausse, Woodlens Chery, Mohamed Elhawary, Robin Prinja, Louise Chiocchetti, Erwin Geraud, Ahmed Nilikkar etc.

My thanks also go to my friends Esghi Jamalov, Robin Prinja, etc., with whom I spent a lot of after-work time and had a lot of fun.

Finally, I would like to acknowledge my sponsors, the China Scholarship Council (CSC), the Civil Aviation University of China (CAUC) and the Agence Nationale de la Recherche (ANR) who financially supported me throughout my PhD studies.

Contents

Introduction	1
1 Literature review	5
1.1 Experimental aeroacoustics	6
1.2 The time-reversal technique	11
1.3 Aeroacoustic noise sources produced by airfoils	17
1.4 Aeroacoustic noise sources produced by high-lift devices	27
1.5 Summary of the chapter	30
2 Experimental apparatus	31
2.1 The wind-tunnel BETI	32
2.2 Flow measurements by hot-wire anemometry	33
2.3 Acoustic measurement system	33
2.4 Microphone arrays	36
2.5 Synthetic noise source in a 3/4 open test section	37
2.6 Experiments with a streamlined acoustic source	38
2.7 Wall-mounted airfoil	40
2.8 Experimental device of a high-lift model	41
2.9 Summary of the chapter	43
3 CFD and acoustic solvers	45
3.1 CFD solver	46
3.2 Acoustic solver	47
3.3 Validation of the acoustic solver	53
3.4 Summary of the chapter	58
I Noise source identification in a wind tunnel based on the beamforming technique	59
4 Beamforming technique	61
4.1 Time-domain beamforming	62
4.2 Frequency-domain beamforming	63
4.3 Flow-effect correction	65
4.4 Summary of the chapter	70
5 Experimental results of 3D beamforming	71
5.1 3D beamforming using a single orientation of dipole	71
5.2 3D beamforming using two orientations of dipole	92

5.3	Summary of the chapter	94
6	Noise source identification of a high-lift device model using beamforming technique	97
6.1	Far-field spectrum results	98
6.2	2D beamforming results of the high-lift device model	99
6.3	3D beamforming results of the high-lift device model	106
6.4	Summary of the chapter	109
II	Noise source identification based on the time-reversal technique	111
7	2D numerical time-reversal	113
7.1	2D numerical TR without flow	114
7.2	Identification of a dipole scattered by an airfoil in a flow	126
7.3	Summary of the chapter	131
8	3D numerical time-reversal	133
8.1	Flow simulation by RANS	134
8.2	3D numerical TR with flow	138
8.3	Summary of the chapter	150
9	Experimental results using 3D time-reversal	153
9.1	Geometry and acoustic mesh	154
9.2	Comparison of the results between beamforming and TR	155
9.3	Summary of the chapter	160
	Conclusions and perspectives	161
A	Time-reversed pressure field	I
B	Plans of a streamlined acoustic source and of a high-lift device model	III
B.1	Plan of the streamlined object	III
B.2	Plans of the high-lift device model	V
C	Numerical methods for the acoustic solver ParadimgS	XI
C.1	Numerical Discretization	XI
C.2	Time integration and stability criterion	XIV
D	Beamforming results of a high-lift device model	XV
D.1	2D beamforming results	XV
D.2	3D beamforming results	XX
E	Some generic applications of the 3D TR technique	XXIII
E.1	Identification of an acoustic pulse	XXIII
E.2	Identification of a monopole using different microphone arrays	XXIV
E.3	Identification of a monopole in a cavity	XXV
E.4	Identification of a dipole	XXVIII

F	Flow simulation by RANS	XXXIII
E1	CFD Mesh	XXXIII
E2	Numerical results	XXXV
E3	Flow structures	XXXVI
	Bibliography	XXXVII

List of Figures

1	Noise measurements for a commercial aircraft ¹	1
2	Aircraft noise source, taken from [34].	2
1.1	Comparison of wind-tunnels with closed or open test section, taken from [68]. 'cs' stands for close section and 'os' stands for open section.	6
1.2	Scattering of a noise source by a shear layer (a) $f_0 = c_0/\delta$ (b), taken from [35].	7
1.3	Noise source distribution shown by a colour television for calibrations of the array (top left and bottom left) and the engine at low power setting (top right) and high power setting (bottom right), taken from [15].	8
1.4	(a) Aeroacoustic measurements for a model of Airbus using a planar micro- phone array located out of flow, taken from [92]; (b) Sound map at frequency of 1 kHz using the beamforming technique, taken from [92].	10
1.5	Schematic depiction of the time-reversal process: (a) direct numerical simula- tion and signal recording; (b) convergent wave; (c) interference between con- vergent and divergent wave; (d) divergent wave, taken from Bavu <i>et al.</i> [14].	12
1.6	The first step of the TR process with a cavity, taken from [30]. A point-like source generates the pressure field. The cavity surrounds the noise source. The boundary of the cavity contains an infinite set of transducers to measure the acoustic pressure field and its normal derivative across the surface.	12
1.7	The second step of the TR process with a cavity, taken from [30]. The initial source is removed. The time-reversed pressure field and its normal derivative measured during the first step are re-emitted. A time-reversed pressure field is generated in the cavity with reconstructed wavefronts propagating back to the emission point.	13
1.8	Leading edge noise spectra of a two-dimensional airfoil noise in grid-generated flow field [96, 26].	17
1.9	Typical directivity patterns of leading edge noise according to an analytical model. The Mach number is 0.05. The flow direction is from the left to the right, taken from [105].	18
1.10	Self-noise mechanisms in subsonic conditions, taken from [25].	19
1.11	The dependence of airfoil trailing edge noise as chord-based Reynolds number, angle of attack and trailing edge bluntness with h the thickness of trailing edge, y_f the wake thickness, U the velocity of incoming flow, and δ the displacement thickness of boundary layer, taken from [18].	19
1.12	Acoustic spectra of the trailing edge noise of a NACA 0012 airfoil with differ- ent degrees of trailing edge bluntness at different incoming speeds. Degree of bluntness: solid lines for a airfoil with sharp trailing edges, dashed lines for airfoils with blunt trailing edge, taken from [22].	20

1.13	Sound maps of a wall-mounted airfoil with an aspect ratio of 3 (a) at flow speed of 40 m/s and angle of attack of 6° at beamforming frequency of 1000 Hz (tonal noise); (b) at flow speed of 60 m/s and angle of attack of 4° at beamforming frequency of 2500 Hz (broadband noise), taken from [86].	21
1.14	(a) Compactness of trailing edge noise source depending on velocity [17, 91], (b) Directivity patterns of trailing edge noise at several frequencies. From left to right and top to bottom: $kC = \pi/2, \pi, 4\pi$ and 8π . Mach number is 0.05. Solid lines stand for analytical solutions and symbols for numerical solutions. The flow direction is from the left to the right, taken from [88].	22
1.15	(a) Airfoil noise spectrum showing hump with equidistant tone frequencies, taken from [7], (b) Tonal noise generation mechanism, taken from [39].	23
1.16	Narrowband SPL of primary tone against Reynolds number for geometric angles of attack of 2° , adapted from [101]. "s.s." stand for suction side and "p.s." stands for pressure side.	24
1.17	(a) Sound map of a wall-mounted airfoil with an aspect ratio of 3 at flow speed of 60 m/s and angle of attack of 0° at beamforming frequency of 3350 Hz; (b) Integrated 1/12th octave band wing tip noise for a wall-mounted NACA 0012 airfoil at flow speed of 30-60 m/s and angle of attack of 0° - 12° , taken from [85]. For clarity, the spectra have been offset by 20 dB with each increase in flow speed.	25
1.18	Oil visualization for the junction of a wall-mounted airfoil in a wind-tunnel flow, taken from [20].	26
1.19	(a) Sound map of a wall-mounted airfoil with an aspect ratio of 3 at flow speed of 60 m/s and angle of attack of 4° at beamforming frequency of 1500 Hz; (b) Sound map of the wall-mounted airfoil with an aspect ratio of at flow speed of 60 m/s and angle of attack of 4° , taken from [86].	26
1.20	Far-field spectrum of a slat, taken from [19]. UT CTS stands for closed test section and UT OTS for open test section of wind-tunnel of University of Twente.	28
1.21	(a) Slat noise model as a dipole (based on Dobrzynski and Pott-Pollenske [45]); (b) contours of instantaneous pressure perturbations, taken from [32].	28
1.22	Slat flow, adapted from [31].	29
2.1	Photograph of the wind-tunnel BETI.	32
2.2	Sketch of the wind-tunnel BETI in the 3/4 open configuration.	32
2.3	Measurements by the hot-wire anemometry (a) in the wake of a wall-mounted airfoil; (b) in the wake of two cylinders with square cross sections placed at the outlet of the nozzle of the wind-tunnel.	33
2.4	(a) Left photograph: a MEMS microphone inserted in a PCB; right photograph: a PCB mounted in a metallic bar; (b) photograph of the measurement microphone (G.R.A.S Type 40AF) and the preamplifier (01dB-Stell Type PRE21S/PRE21A).	34
2.5	Frequency response of a group of 32 MEMS microphones obtained by the same procedure depicted by Vanwynsberghe <i>et al.</i> [120] (a) relative amplitude; (b) relative phase, taken from Zhou <i>et al.</i> [127]. Red line-average; blue shaped area: variation over the group.	34
2.6	Sketch of the acoustic data acquisition system with photographs of a buffer board, interface for data acquisition and cables, adapted from Vanwynsberghe <i>et al.</i> [120]. The group of colored cables are RJ45 linking the buffer cards to acquisition system.	35

2.7	(a) 3D model of the array structure; (b) the 3D microphone array containing 768 microphones of sides ‘left’, ‘top’ and ‘right’ installed in the open test section of the wind-tunnel.	36
2.8	Arrangement of microphones (a) for a 3D array with 256 microphones; (b) for a 3D array with 768 microphones. The black points stand for the positions of the microphones.	37
2.9	Photograph of a synthetic monopole noise source at a height of (a) 0m; (b) 0.35 m. The red circles indicate the position of the free extremity of the pipe in the two cases.	37
2.10	Far-field acoustic power spectral density for the broadband streamlined acoustic source. The frequency band between the dashed lines indicates the third-octave band [2245 Hz; 2828 Hz] studied in Chapter 10.	38
2.11	The streamlined acoustic source besides a NACA 0012 airfoil with a finite span in the open test section of the wind-tunnel.	39
2.12	The streamlined acoustic source in the open test section of the wind-tunnel with two square cylinders being placed at the outlet of the nozzle.	39
2.13	Velocity profiles along the y -direction at different distances from the nozzle of the wind-tunnel at an incoming speed of 40 m/s. The red dashed lines stand for the positions of the two cylinders in the y -direction.	40
2.14	Wall-mounted airfoil with a perpendicular cylinder with circular cross section installed on its top.	41
2.15	Cross section of a high-lift model (L1T2 configuration).	41
2.16	Photograph of (a) the experimental device containing the high-lift model installed in the open test section of the wind-tunnel; (b) the angle control device for the high lift device. The blue arrow indicates the direction of the flow.	43
3.1	Sketch for a simulation domain with interior qualities inside the domain and requested physical qualities outside a domain. \mathbf{n} is a outward normal vector.	50
3.2	A 3D mesh with two partitions for a cubic domain: (a) volume mesh; (b) surface mesh.	51
3.3	Unstructured mesh around a cylinder with 80 partitions shown by different colors.	54
3.4	Snapshot of the sound pressure field for the scattering of an acoustic pulse off a cylinder.	55
3.5	Comparison between the analytical and numerical results. Red lines stand for numerical simulations. Black points stand for analytical solutions.	55
3.6	Unstructured mesh around a cylinder with 200 partitions shown by different colors. The arc indicates the position of the 91 recording points.	56
3.7	Snapshot of the sound pressure field for the scattering of a monopole off a cylinder. The arc indicates the position of the 91 recording points.	57
3.8	Comparison between the analytical and numerical results for the scattering of a monopole off a cylinder.	57
4.1	Sketch showing the principle of <i>delay & sum</i> beamforming, adapted from Johnson and Dudgeon [64].	62

4.2	Variation of the distance Δx_{3D} (normalized by the acoustic wavelength λ at 3 kHz) as a function of the Mach number of the wind-tunnel flow for two monopole noise sources at positions (0.68 m, 0 m, 0.35 m) (symbol 'x') and (0.68 m, 0 m, 0 m) (symbol 'Δ'). The linear regression laws are respectively depicted by the dashed and the dotted lines.	66
4.3	Sketch of the application of two ray-tracing methods for the flow-effect correction.	67
4.4	Sound maps for the synthetic noise source emitted by the streamlined body, at a third-octave band of nominal midband frequency 2.5 kHz. The noise source in a quiescent flow at position (a) (436 mm, 0 mm, 350 mm), (b) (436 mm, -120 mm, 350 mm). The noise source in a non-uniform flow with incoming speed $U_\infty = 40$ m/s at position (c) (436 mm, 0 mm, 350 mm), (d) (436 mm, -120 mm, 350 mm). The red symbols 'x' denote the position of synthetic monopole noise source. The grey patches stand for the cylinders. The shadows and the black symbols 'x' correspond respectively to the projection of the 3D sound source imaging and the noise source position in the y - direction direction. The 3D isosurface in each sound map is plotted at 6 dB below the maximum.	69
5.1	Far-field acoustic power spectral density for the wall-mounted finite airfoil with and without a cylinder at incoming velocity $U_\infty = 40$ m/s and angle of attack $\alpha = 0^\circ$	92
5.2	Sound maps for the wall-mounted finite airfoil with a perpendicular cylinder at incoming velocity $U_\infty = 40$ m/s and angle of attack $\alpha = 0^\circ$, at two third-octave bands of nominal midband frequency 2.5 kHz (top figures) and 4 kHz (bottom figures). (a) and (c): 3D dipolar beamforming with respectively a maximum value of 44.2 dB and 37.0 dB on the sound map; (b) and (d): CLEAN-SC technique with respectively a maximum value of 43.7 dB and 36.2 dB on the sound map. The 3D isosurface in each sound map is plotted at 10 dB below the maximum value of the sound map.	94
6.1	Far-field acoustic power spectral density for the high-lift device model at incoming velocity $U_\infty = 20, 30, 40$ and 50 m/s. PSD (dB/Hz ref. 2.10^{-5} Pa) as a function of frequency for angle of attack (a) $\alpha = 0^\circ$, (b) $\alpha = 6^\circ$	98
6.2	Far-field acoustic power spectral density for the high lift device model at incoming velocity $U_\infty = 10 - 30$ m/s for angle of attack $\alpha = 10^\circ$. (a) PSD (dB/Hz ref. 2.10^{-5} Pa) as a function of frequency, (b) PSD (dB/Hz ref. M^6) as a function of frequency.	99
6.3	Sound maps for the high-lift device model at incoming velocity $U_\infty = 40$ m/s and angle of attack $\alpha = 0^\circ$, at two third-octave bands of nominal midband frequency 2.5 kHz (top figures) and 4 kHz (bottom figures). (a) and (c): 2D beamforming using monopole steering vector; (b) and (d): CLEAN-SC technique using monopole steering vector.	101
6.4	Sound maps for the high-lift device model without flap at incoming velocity $U_\infty = 40$ m/s and angle of attack $\alpha = 0^\circ$, at two third-octave bands of nominal midband frequency 2.5 kHz (top figures) and 4 kHz (bottom figures). (a) and (c): 2D beamforming using monopole steering vector; (b) and (d): CLEAN-SC technique using monopole steering vector.	102

6.5	Sound maps for the high-lift device model at incoming velocity $U_\infty = 40$ m/s and angle of attack $\alpha = 6^\circ$, at two third-octave bands of nominal midband frequency 2.5 kHz (top figures) and 4 kHz (bottom figures). (a) and (c): 2D beamforming using monopole steering vector; (b) and (d): CLEAN-SC technique using monopole steering vector.	103
6.6	Sound maps for the high-lift device model without flap at incoming velocity $U_\infty = 40$ m/s and angle of attack $\alpha = 6^\circ$, at two third-octave bands of nominal midband frequency 2.5 kHz (top figures) and 4 kHz (bottom figures). (a) and (c): 2D beamforming using monopole steering vector; (b) and (d): CLEAN-SC technique using monopole steering vector.	104
6.7	Sound maps for the high-lift device model at incoming velocity $U_\infty = 30$ m/s and angle of attack $\alpha = 10^\circ$, at two third-octave bands of nominal midband frequency 2.5 kHz (top figures) and 4 kHz (bottom figures). (a) and (c): 2D beamforming using monopole steering vector; (b) and (d): CLEAN-SC technique using monopole steering vector.	105
6.8	Schematic depicting the scanning domain for the high-lift device model (a) at angle of attack $\alpha = 0^\circ$ and $\alpha = 10^\circ$; (b) at angle of attack $\alpha = 6^\circ$. (c) Cross section of the high-lift device model with two orientations for a dipolar radiation model. The black points indicate the positions of the 256 microphones. The cubes enclosing the high-lift device model stand for the scanning domain. The blue patches stands for the nozzle of the wind-tunnel.	106
6.9	Sound maps for the high-lift device model at incoming velocity $U_\infty = 40$ m/s and angle of attack $\alpha = 0^\circ$, at two third-octave bands of nominal midband frequency 2.5 kHz (top figures) and 4 kHz (bottom figures). (a) and (c): 3D dipolar beamforming with respectively a maximum value of 41.3 dB and 37.0 dB on the sound map; (b) and (d): CLEAN-SC technique with respectively a maximum value of 38.9 dB and 36.2 dB on the sound map. The 3D isosurface in each sound map is plotted at 9 dB below the maximum value of the sound map. The shadows correspond to the projection of the 3D sound source imaging in different directions.	107
6.10	Sound maps using CLEAN-SC technique for the high-lift device model at incoming velocity $U_\infty = 40$ m/s and angle of attack $\alpha = 6^\circ$, at two third-octave bands of nominal midband frequency 2.5 kHz (a) and 4 kHz (b) with respectively a maximum value of 38.9 dB and 37.8 dB. The 3D isosurface in each sound map is plotted at 9 dB below the maximum value of the sound map. The shadows correspond to the projection of the 3D sound source imaging in different directions.	108
6.11	Sound maps using CLEAN-SC technique for the high-lift device model at incoming velocity $U_\infty = 30$ m/s and angle of attack $\alpha = 10^\circ$, at two third-octave bands of nominal midband frequency 2.5 kHz (a) and 4 kHz (b) with respectively a maximum value of 48.0 dB and 43.8 dB. The 3D isosurface in each sound map is plotted at 9 dB below the maximum value of the sound map. The shadows and correspond respectively to the projection of the 3D sound source imaging in different directions.	109
7.1	Unstructured mesh around a cylinder with 190 partitions shown by different colors.	115

7.2	Results of 2D TR for an acoustic pulse scattered by a cylinder (a) at the instant $t = 12$ s, (b) at the final instant. The white cross stands for the position of the source.	115
7.3	Comparison between the analytical and numerical results for the 2D TR. Red lines stand for numerical simulations. Black points stand for analytical solutions.	116
7.4	Results of 2D direct numerical simulation for an acoustic pulse inside a semi-open cavity (a) at initial instant, (c) at $t_1 = 7.24 \times 10^{-4}$ s, (e) at the final instant. Results of 2D TR for an acoustic pulse inside a semi-open cavity (b) at the initial instant, (d) at an instant close to $T - t_1$, (f) at the final instant.	118
7.5	Non-uniform sound speed distribution inside the semi-open cavity.	119
7.6	Results of 2D direct numerical simulation for an acoustic pulse inside a semi-open cavity with non-uniform sound speed (a) at the initial instant, (c) at $t_1 = 5.69 \times 10^{-4}$ s. Results of 2D TR for an acoustic pulse inside a semi-open cavity (b) at $T - t_1 = 0.0194426$ s, (d) at the final instant.	120
7.7	(a) 2D mesh for the direct simulation and TR; (b) sketch of the different TR mirrors used for TR.	121
7.8	(a) Snapshot of the pressure field of 2D direct simulation concerning the scattering of an acoustic pulse by an airfoil. Pressure fields of 2D TR at the final instant using the pressure information recorded (b) at a boundary (bottom, TR 1); (c) at two boundaries (top and bottom, TR 2); (d) at two boundaries (left and right, TR 2 right); (e) at three boundaries (left, bottom, and right, TR 3); (f) at four boundaries (the whole cavity, TR 4)	122
7.9	(a) The pressure profiles over a line in the x -direction intersecting the position of the source for the direct simulation and for the 2D TR simulations for the different TR mirrors defined in Figure 7.7(b). (b) error between the direct simulation and the 2D TR simulations.	123
7.10	Sketch for the implementation of the acoustic sink for the 2D TR, adapted from [49].	124
7.11	Snapshots of the pressure field at: (a) $t_1 = 0.0022$ s, (d) $t_2 = 0.0045$ s, and (g) $t_3 = 0.007$ s; results of 2D TR without acoustic sink (b) $t = T - t_3$, (e) $t = T - t_2$, and (h) $t = T - t_1$; results of 2D TR with acoustic sink (c) $t = T - t_3$, (f) $t = T - t_2$, and (i) $t = T - t_1$. Note that $T = 0.0075$ s.	125
7.12	RMS of the pressure field of (a) direct simulation from 0.002 s to 0.0045s; (b) TR without acoustic sink from 0.003 s to 0.0055s; (c) TR with acoustic sink from 0.003 s to 0.0055s.	126
7.13	Mesh for the numerical simulation by (a) OpenFOAM; (b) Acoustic solver.	128
7.14	Mean flow field around the airfoil NACA 0012 on the grid of the mesh of the acoustic solver.	128
7.15	Snapshot of the pressure field of the direct simulation of a synthetic dipole source near the trailing edge of the airfoil. The lines inside the domain are streamlines based on the stationary mean flow.	129
7.16	Snapshot of the pressure field of the TR of a synthetic dipole source near the trailing edge of the airfoil. All the signals recorded at the boundary are used for the TR. The lines inside the domain are streamlines based on the stationary mean flow.	130

7.17	Snapshot of the pressure field of the TR of a synthetic dipole source near the trailing edge of the airfoil. A part of the energy recorded at the boundary (128 isolated "microphones") is used for the TR. The lines inside the domain are streamlines based on the stationary mean flow.	131
8.1	Geometry of a wall-mounted airfoil at an angle of attack of 0° and the cuboid domain surrounding the airfoil for the RANS simulation. The different patches of the simulation domain were shown by different colors.	135
8.2	Velocity field in a planar cross section for the wall-mounted airfoil (a) at a height of 253 mm; (b) at a height 503 mm.	136
8.3	(a) Velocity field around a NACA 0012 airfoil at angle of attack of 0° at an incoming speed of 40 m/s; (b) comparison of the velocity profiles above the surface (along the black line plotted in Figure 8.3(a)) of the wall-mounted airfoil between numerical and experimental results (PIV measurements); (c) comparison of the velocity profiles in the wake of the wall-mounted airfoil between numerical and experimental results (hot wire measurements) at a measurement plane of $Z = 503$ mm (near the wing tip).	137
8.4	Generation of the 3D mesh for the wall-mounted airfoil using GMSH. (a) The domain of the 3D acoustic mesh concerning a wall-mounted airfoil with the positions of the 768 microphones indicated by the black points on the three patches 'Left', 'Top' and 'Right' of the domain; (b) the unstructured 3D acoustic mesh for the wall-mounted airfoil with 80 partitions shown by different colors.	138
8.5	Visualisation of the 3D mesh and the mean flow information in a horizontal section. (a) The mesh in a planar cross section XY at $z = 0.4$ m; (b) the velocity field in the same plane.	139
8.6	Generation of the 3D mesh and the mean flow information in a vertical section. (a) The mesh of in a planar cross section YZ at $x = 0.35$ m; (b) the velocity field in the same plane.	140
8.7	Results of the 3D direct simulation for a synthetic monopole noise source of 2 kHz beside the wall-mounted airfoil with an incoming flow speed of 39.2 m/s (left to right) shown in a horizontal section. (a) Snapshot of the pressure field in a planar cross section XY at $z = 0.3$ m; (b) RMS of the pressure field integrated from 0.05 s to 0.07 s in the same plane.	141
8.8	Results of the 3D TR for a synthetic monopole noise source of 2 kHz beside the wall-mounted airfoil with an incoming flow speed of 39.2 m/s (left to right) shown in a horizontal section. (a) Snapshot of the pressure field in a planar cross section XY at $z = 0.3$ m; (b) RMS of the pressure field integrated from 0.05 s to 0.07 s in the same plane.	142
8.9	Results of the 3D TR for a synthetic monopole noise source of 2 kHz without considering the solid boundaries of the wall-mounted airfoil with an incoming flow speed of 39.2 m/s (left to right) shown in a horizontal section. (a) Snapshot of the pressure field in a planar cross section XY at $z = 0.3$ m; (b) RMS of the pressure field integrated from 0.05 s to 0.07 s in the same plane.	143
8.10	Snapshot of the pressure field in a planar cross section XY at $z = 0.3$ m for the 3D direct simulation for a synthetic dipole noise source of frequency 2 kHz near the trailing edge of the wall-mounted airfoil: (a) with an incoming speed of 39.2 m/s; (b) with an incoming speed of 100 m/s.	144

- 8.11 RMS of the pressure field integrated from 0.05 s to 0.07 s in a planar cross section XY at $z = 0.3$ m for the 3D direct simulation for a synthetic dipole noise source of frequency 2 kHz near the trailing edge of the wall-mounted airfoil: (a) with an incoming speed of 39.2 m/s; (b) with an incoming speed of 100 m/s. 144
- 8.12 Results of the 3D TR for a synthetic dipole noise source of frequency 2 kHz near the trailing edge of the wall-mounted airfoil shown in a horizontal section. Snapshot of the pressure field in a planar cross section XY at $z = 0.3$ m: (a) with an incoming speed of 39.2 m/s; (b) with an incoming speed of 100 m/s. 145
- 8.13 Results of the 3D TR for a synthetic dipole noise source of frequency 2 kHz near the trailing edge of the wall-mounted airfoil shown in a horizontal section. RMS of the pressure field integrated from 0.05 s to 0.07 s in a planar cross section XY at $z = 0.3$ m: (a) with an incoming speed of 39.2 m/s; (b) with an incoming speed of 100 m/s. 146
- 8.14 Results of the 3D TR for a synthetic dipole noise source of frequency 2 kHz near the trailing edge of the wall-mounted airfoil with an incoming speed of 100 m/s shown in a horizontal section. Only the subarray on the 'Left' patch was used for the 3D TR (located at the top of the figure). Snapshot of the pressure field in a planar cross section XY at $z = 0.3$ m (a) at time $t = 2.45 \times 10^{-3}$ s; (b) at time $t = 4.95 \times 10^{-3}$ s. 147
- 8.15 Results of the 3D TR for a synthetic dipole noise source of frequency 2 kHz near the trailing edge of the wall-mounted airfoil with an incoming speed of 100 m/s. Two cylinders using "free" boundary conditions near the trailing edge acting as acoustic sinks were placed in the simulation domain. (a) Snapshot of the pressure field in a planar cross section XY at $z = 0.3$ m; (b) RMS of the pressure field integrated from 0.05 s to 0.07 s in the same plane. 148
- 8.16 Results of the 3D TR for a synthetic dipole noise source of frequency 2 kHz near the trailing edge of the wall-mounted airfoil with an incoming speed of 100 m/s. Five subarrays on the five patches 'Left', 'Top', 'Right', 'Front' and 'Back' were used for the 3D TR process. (a) The domain of the 3D acoustic mesh concerning a wall-mounted airfoil with the positions of the 1133 microphones indicated by the black points on the five patches 'Left', 'Top', 'Right', 'Front' and 'Back'; (b) Snapshot of the pressure field in a planar cross section XY at $z = 0.3$ m; (c) RMS of the pressure field integrated from 0.05 s to 0.07 s in the same plane. 149
- 8.17 Results of the 3D TR for a synthetic dipole noise source of frequency 2 kHz near the trailing edge of the wall-mounted airfoil with an incoming speed of 100 m/s. Five subarrays on the five patches 'Left', 'Top', 'Right', 'Front' and 'Back' were used for the 3D TR process. Two cylinders using "free" boundary conditions near the trailing edge acting as acoustic sinks were placed in the domain of simulation. (a) Snapshot of the pressure field in a planar cross section XY at $z = 0.3$ m; (b) RMS of the pressure field integrated from 0.05 s to 0.07 s in the same plane. 150

9.1	Generation of the 3D acoustic mesh of a NACA 0012 airfoil at an angle of attack $\alpha = 0^\circ$ and of the streamlined acoustic source, using GMSH. (a) The domain of the 3D acoustic mesh with the positions of the 256 microphones indicated by the black points on the three patches ‘Left’, ‘Top’ and ‘Right’ of the domain; (b) the triangular mesh elements on the patches of ‘Airfoil’ and ‘Streamlined-Source’; (c) the triangular mesh elements on the patches of ‘Left’, ‘Top’ and ‘Right’; (d) the triangular mesh elements on the patches of ‘Front’, ‘Back’, ‘Left1’, ‘Left2’, ‘Left3’, ‘Right1’, ‘Right2’, ‘Right3’ and ‘Bottom’. The mesh elements with different colors in (b), (c) and (d) correspond to different partitions.	155
9.2	(a) Original signal of the channel 545 and the interpolated signal; (b) a zoom of (a).	156
9.3	Results of the 3D TR concerning the synthetic noise source emitted by the streamlined body shown in different cross sections in the third-octave band [2245; 2828] Hz. 256 channels of acoustic data are used. (a) Snapshot of the pressure field in a planar cross section XY at $z = 0.35$ m; (b) RMS of the pressure field integrated from 0.005 s to 0.015 s in the same plane; (c) snapshot of the pressure field in a planar cross section XZ at $y = -0.075$ m; (d) RMS of the pressure field integrated from 0.005 s to 0.015 s in the same plane; (e) snapshot of the pressure field in a planar cross section YZ at $x = 0.402$ m; (f) RMS of the pressure field integrated from 0.005 s to 0.015 s in the same plane.	157
9.4	Results of the 3D TR concerning the synthetic noise source emitted by the streamlined body shown in different cross sections in the third-octave band [2245; 2828] Hz. 768 channels of acoustic data are used. (a) Snapshot of the pressure field in a planar cross section XY at $z = 0.35$ m; (b) RMS of the pressure field from 0.005 s to 0.015 s in the same plane; (c) snapshot of the pressure field in a planar cross section XZ at $y = -0.075$ m; (d) RMS of the pressure field from 0.005 s to 0.015 s in the same plane; (e) snapshot of the pressure field in a planar cross section YZ at $x = 0.402$ m; (f) RMS of the pressure field from 0.005 s to 0.015 s in the same plane.	158
9.5	Sound maps for the synthetic noise source diffracted by a NACA 0012 airfoil with finite span length at an angle of attack $\alpha = 0^\circ$, at a third-octave bands of nominal midband frequency 2.5 kHz. The shadows and the red symbols ‘x’ correspond respectively to the projection of the 3D sound source imaging and the noise source position. (a): 3D beamforming with a maximum value of 56.2 dB on the sound map; (b): CLEAN-SC technique with a maximum value of 56.1 dB on the sound map. The 3D isosurface in each sound map is plotted at 9 dB below the maximum value of the sound map.	159
C.1	Node distribution inside a tetrahedral element for $N = 6$, taken from from [58].	XII
D.1	Sound maps for the high-lift device model at incoming velocity $U_\infty = 40$ m/s and angle of attack $\alpha = 0^\circ$, at two third-octave bands of nominal midband frequency 2.5 kHz (top figures) and 4 kHz (bottom figures). (a) and (c): 2D beamforming using monopole steering vector; (b) and (d): CLEAN-SC technique using monopole steering vector.	XVI

- D.2 Sound maps for the high-lift device model without flap at incoming velocity $U_\infty = 40$ m/s and angle of attack $\alpha = 0^\circ$, at two third-octave bands of nominal midband frequency 2.5 kHz (top figures) and 4 kHz (bottom figures). (a) and (c): 2D beamforming using monopole steering vector; (b) and (d): CLEAN-SC technique using monopole steering vector. XVII
- D.3 Sound maps for the high-lift device model at incoming velocity $U_\infty = 40$ m/s and angle of attack $\alpha = 6^\circ$, at two third-octave bands of nominal midband frequency 2.5 kHz (top figures) and 4 kHz (bottom figures). (a) and (c): 2D beamforming using monopole steering vector; (b) and (d): CLEAN-SC technique using monopole steering vector. XVIII
- D.4 Sound maps for the high-lift device model without flap at incoming velocity $U_\infty = 40$ m/s and angle of attack $\alpha = 6^\circ$, at two third-octave bands of nominal midband frequency 2.5 kHz (top figures) and 4 kHz (bottom figures). (a) and (c): 2D beamforming using monopole steering vector; (b) and (d): CLEAN-SC technique using monopole steering vector. XIX
- D.5 Sound maps for the high-lift device model at incoming velocity $U_\infty = 30$ m/s and angle of attack $\alpha = 10^\circ$, at two third-octave bands of nominal midband frequency 2.5 kHz (top figures) and 4 kHz (bottom figures). (a) and (c): 2D beamforming using monopole steering vector; (b) and (d): CLEAN-SC technique using monopole steering vector. XX
- D.6 Sound maps without deconvolution for the high-lift device model at incoming velocity $U_\infty = 40$ m/s and angle of attack $\alpha = 6^\circ$, at two third-octave bands of nominal midband frequency 2.5 kHz (a) and 4 kHz (b) with respectively a maximum value of 41.4 dB and 38.1 dB. XXI
- D.7 Sound maps without deconvolution for the high-lift device model at incoming velocity $U_\infty = 30$ m/s and angle of attack $\alpha = 10^\circ$, at two third-octave bands of nominal midband frequency 2.5 kHz (a) and 4 kHz (b) with respectively a maximum value of 48.0 dB and 43.8 dB. The 3D isosurface in each sound map is plotted at 9 dB below the maximum value of the sound map. XXI
- E.1 Results of 3D TR concerning an acoustic pulse at different instants with the pressure field shown by (a) two isosurfaces of 0.025 (yellow isosurface) and 0.08 (blue isosurface) at an early instant; (b) three isosurfaces of 0.025 (yellow isosurface), 0.08 (blue isosurface) and 0.2828 (red isosurface) at the final instant of 3D TR simulation. The grey area represents the nodes of the 3D acoustic mesh with the mesh element size being 10 cm ($N=3$). The black points on the ‘Left’, ‘Top’ and ‘Right’ patches indicate the positions of the 256 virtual microphones. The white cross in (b) stands for the real position of the acoustic pulse. XXIV
- E.2 Maximum pressure fields of 3D TR concerning a monopole noise source of 3 kHz in two simulation domains using (a) 256 virtual microphones; (b) 672 virtual microphones. They are respectively shown by an isosurface of a value of $(1/\sqrt{2})$ times the corresponding peak level at the final instant. The grey area in the two domains represent the nodes of the 3D acoustic mesh with the mesh element size being 10 cm ($N=3$). The black points on the ‘Left’, ‘Top’ and ‘Right’ patches of the two domains indicate the positions of the 256 microphones. The white cross in the two domains stands for the real position of the acoustic pulse. XXV

- E.3 Generation of the 3D acoustic mesh for a cavity with rectangular splits using GMSH: (a) the positions of the 768 virtual microphones indicated by the black points on the three patches ‘Left’, ‘Top’ and ‘Right’ of the domain; (b) the triangular mesh elements on the patches ‘Left’, ‘Top’, ‘Right’ and ‘Bottom’. The triangular mesh elements with different colors correspond to different mesh partitions. XXVI
- E.4 Results of the 3D TR concerning a synthetic monopole noise source of 3.9 kHz inside a cavity with splits in cross sections of the simulation domain. The white cross indicates the real position of the noise source. (a) Snapshot of the pressure field in a horizontal planar cross section XY at $z = 0.6$ m (X is horizontal, Y is vertical in the figure); (b) RMS of the pressure field integrated from 0.002 s to 0.004 s in the same plane; (c) snapshot of the pressure field in a vertical planar cross section YZ at $x = 0.5$ m (Y is horizontal, Z is vertical in the figure); (d) RMS of the pressure field integrated from 0.002 s to 0.004 s in the same plane. XXVIII
- E.5 Results of the 3D direct simulation concerning a dipole noise source of 3 kHz in a horizontal section. The white cross indicates the real position of the noise source. (a) Snapshot of the pressure field in a planar cross section XY at $z = 0.5$ m; (b) RMS of the pressure field integrated from 0.002 s to 0.004 s in the same plane. XXIX
- E.6 Results of the 3D TR concerning a dipole noise source of 3 kHz in a horizontal section. The white cross indicates the real position of the noise source. (a) Snapshot of the pressure field in a planar cross section XY at $z = 0.5$ m; (b) RMS of the pressure field integrated from 0.002 s to 0.004 s in the same plane. XXX
- E.7 3D TR result concerning a dipole noise source of 3 kHz: (a) maximum pressure field; (b) maximum amplitude of the fluctuating velocity field. They are respectively shown by an isosurface of a value of 3dB below the corresponding peak level. The big black points indicate the positions of the 672 microphones. The blue point in the two domains stands for the real position of the dipole noise source. XXXI
- F.1 The hybrid mesh for the RANS simulation concerning a wall-mounted airfoil. (a) 3D mesh for numerical simulation of the wall-mounted airfoil; (b) mesh refinement around the surface of the wall-mounted airfoil; (c) mesh refinement near the trailing edge of the wall-mounted airfoil. XXXIV
- F.2 Residuals of the numerical simulation during the iterations. XXXV
- F.3 Iso-surface of Q criterion for the mean flow around the wall-mounted airfoil. XXXVI

List of Tables

- 7.1 Comparison of the lift coefficients of the NACA 0012 airfoil at an angle of attack of 10° and a chord-based Reynolds number of 5×10^5 127
- E.1 Statistics of the values of y_+ for the patches of 'airfoil' and 'bottom'. XXXV

Introduction

Flow-induced noise is an important issue in engineering applications such as flight vehicles, ground transports, submarines and wind turbines. However, it is not a positive effect, which can lead to health problem for humans and cause acoustic fatigue for structures of vehicles. Studies concerning noise generation mechanisms, sound wave propagation, noise source identification, noise reduction strategies, etc., have been promoted by the increasing activities in these engineering domains. In particular, aeroacoustics, referring to the studies of aerodynamically generated noise, has been developed since the 1950s and the pioneering work of Lighthill [71]. Apart from theoretical modelling, experimental testing and numerical simulations have become two important approaches for aeroacoustic studies thanks to the continuous improvement of measurement and computation capabilities.

Aeroacoustics has been attracting a lot of attention in aeronautics for the reason that more and more strict regulations on aircraft noise have been proposed by the International Civil Aviation Organization for commercial aircrafts, in order to protect the public in the vicinity of airports from noise pollution. Every type of new commercial aircraft needs to be certificated in terms of noise emission before being available for markets. According to Chapter 4 of Annex 16 to the Convention on International Civil Aviation, Volume I [2], noise emissions are evaluated based on noise measurements at three reference points *i.e.*, lateral full-power reference point, flyover reference point and approach reference point as shown in Figure 1¹. The maximum noise level for noise emission for each reference point is determined by the maximum take-off mass of the aircraft and/or number of engines. For example, the maximum permitted noise level at the approach reference point is 105 EPNdB for an aircraft with a maximum certificated take-off mass of 280 000 kg or over.

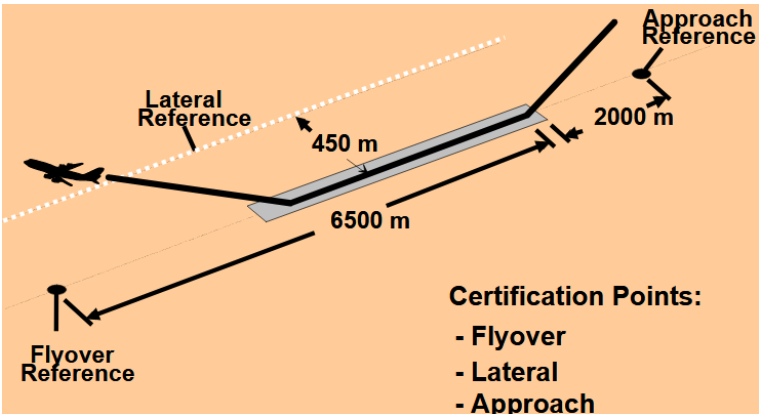


Figure 1: Noise measurements for a commercial aircraft¹.

¹https://www.icao.int/Meetings/EnvironmentalWorkshops/Documents/Noise-Certification-Workshop-2006/Depitre_4.pdf

The noise emission of aircrafts originates from different components. Figure 2 shows some principal noise sources of a commercial aircraft: they are classified as airframe noise, jet noise, fan noise, core noise, etc. Airframe noise is principally generated by landing gears and deployed high-lift devices. During the approach of an aircraft, on the one hand, the deployed high-lift devices and the landing gear increase the overall airframe noise level by about 10 dB with respect to the take-off phase [112]; on the other hand, the engines work at low power level. Therefore, airframe noise becomes as important as the engines during the approach [1]. Moreover, the engine installation effect on fan, jet and core noise is also important when evaluating noise emission because it appears to affect the aircraft flight noise levels [34]. For example, the noise generated by an engine installed under a wing can be reflected and diffracted by the components of the high-lift devices. An engine mounted on a wing is always likely to generate more noise in comparison to the isolated one [112].

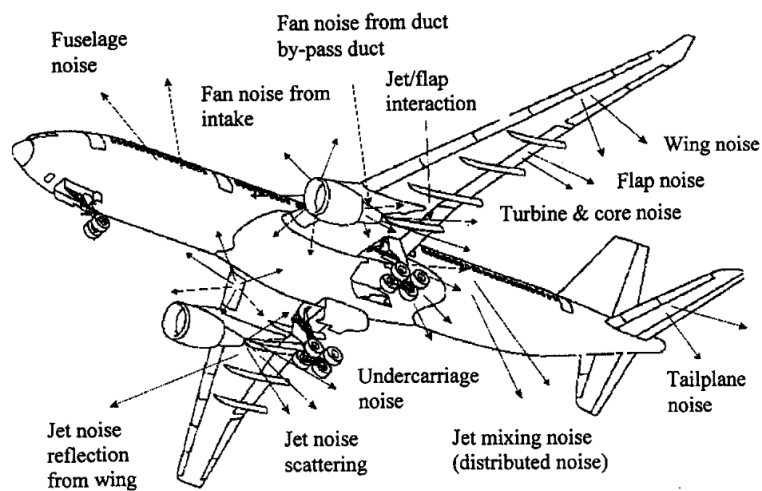


Figure 2: Aircraft noise source, taken from [34].

Noise source identification is important in engineering domains because it is the first step for reducing noise emissions. Although some *in situ* tests were reported for aircrafts and trains [100, 111, 124], this process is usually carried out in anechoic wind-tunnels for studying academic configurations or scale-models because it is less expensive. In the context of wind-tunnel testing, identifying such aeroacoustic sources in terms of spectrum, directivity, spatial distribution and generation mechanism is still a challenging task for the reason that such complex measurements rely highly on wind-tunnel facilities, microphone arrays (a set of microphones with known spatial positions), flow measurement techniques and advanced data processing methods [4, 94]. The standard array processing technique for identifying noise source distributions is the beamforming technique. This technique is known to be very robust, but until recent years, it is still limited to two-dimensional (2D) arrays, providing 2D sound maps. With the increasing capacities of multi-channel measurements systems, and the emergence of new technologies such as Micro-Electro-Mechanical Systems (MEMS), the use of three-dimensional (3D) arrays, enclosing the flow but requiring a large number of microphones, is possible nowadays. Such facilities make possible the identification of sound sources in 3D domains, provided that the beamforming technique should be adapted, in particular by taking into account the dipolar nature of the noise sources generated by flow-obstacle interaction [99]. However, the beamforming technique requires an

analytical expression of the propagation operator (the Green's function), which is generally not achievable in the case of severe non-uniform flows, or when complex geometries in the flow generate potential installation effects.

An alternative technique based on the time-reversal (TR) principle has been developed since the 1990s, initially for ultrasound applications to medical imaging. Its principle relies first on a microphone array measurement, and then on the back-propagation (numerical or experimental) of the measured acoustic waves, from the same positions as the recording microphones, in order to reconstruct in the time domain the history of the pressure field, from which the noise source can be interpreted. A few years ago, this technique has been applied to two-dimensional noise source identification in wind-tunnels [94]. This technique should now be extended to 3D domains, and to applications where the presence of objects in the flow can potentially generate installation effects.

This thesis aims at developing new methodologies for aeroacoustic source identification in an anechoic wind-tunnel using the beamforming technique and the TR technique, allowing 3D estimations of the sound source distribution in the flow. Acoustic measurements are conducted using a prototypal 3D microphone array using MEMS microphones, with a tunnel-shaped enclosing the wind-tunnel test section. The 3D beamforming technique is extended to 3D applications for the investigation of wall-mounted airfoils and a model of high-lift device. The TR process is conducted numerically by solving the 3D linearized Euler Equations (LEE). The background mean flow around objects and solid boundaries are considered for noise source identification and its performances are evaluated in such situations. The methodologies developed in this thesis could bring progress towards the improvement of experimental aeroacoustic methods for engineering applications involving obstacle geometries with a strong 3D character.

The organization of the thesis is as follows.

Chapter 1 is dedicated to a literature review of (i) signal processing methods (the beamforming and TR techniques) for noise source identification; (ii) aeroacoustic sources produced by airfoils and by high-lift devices. Attention is paid to the applications of the beamforming and the TR techniques for aeroacoustic studies in wind-tunnels. Chapter 2 presents the experimental apparatus for the thesis including the wind-tunnel facility, the 3D microphone arrays, data acquisition system, and the different test models under study. As the TR process needs to simulate acoustic wave propagation with/without the presence of a background mean flow, Chapter 3 gives a presentation of the numerical tools. For simulations of mean flow around objects, the Reynolds-averaged Navier–Stokes equations, a turbulence model and an open source CFD software named OpenFOAM are firstly presented. For sound wave propagation simulations, the governing equations, source terms, initial and boundary conditions of an in-house acoustic solver are addressed.

The first part (Chapter 4 to 6) deals with noise source identification in the wind-tunnel based on the beamforming technique. Chapter 4 introduces the beamforming technique and a deconvolution technique to improve the interpretability of sound maps. The flow-effects of wind-tunnel flows on the localization error in 3D sound maps are assessed together with the models for correcting them. In Chapter 5, the performances of the 3D beamforming technique are evaluated for wall-mounted airfoils. In Chapter 6, a preliminary study of the aeroacoustic source distributions for a high-lift device model is carried out using the 2D beamforming. Then 3D beamforming results are compared with the 2D results in order to evaluate the performances of the 3D beamforming technique for more complex cases.

The second part (Chapter 7 to 9) concerns noise source identification based on the TR

technique and some comparisons with the beamforming technique. In Chapter 7, the 2D TR technique is used for the identification of synthetic noise sources (simulated data instead of experimental data) in different situations where the BF technique may fail: (i) with a heterogeneous medium; (ii) with the presence of solid boundaries of objects in the flow. A preliminary study to improve the interpretability of the TR results is also conducted. The interest of Chapter 8 is to evaluate the performances of the TR technique in two situations (widely encountered in real applications): (i) with an installation effect for noise radiation; (ii) with trailing edge noise produced by an airfoil. To this end, synthetic noise sources near a wall-mounted airfoil in a flow are identified using the 3D TR technique, for which the background mean flow around the wall-mounted airfoil is simulated and validated by experimental measurements. Chapter 9 concerns an application of the TR technique to process experimental data obtained from the 3D array measurements in the wind-tunnel, *i.e.*, the identification of a noise source diffracted by a NACA airfoil in a quiescent medium. 3D TR results (with consideration of solid boundaries) are compared with 3D beamforming results (without consideration of solid boundaries) in order to show the trade-off between localization error and computation time.

In the end of the thesis, the conclusions and perspectives are given.

Chapter 1

Literature review

Contents

- 1.1 Experimental aeroacoustics 6**
 - 1.1.1 Wind-tunnel with open test section 6
 - 1.1.2 The beamforming technique 7
- 1.2 The time-reversal technique 11**
 - 1.2.1 Basic principle 12
 - 1.2.2 Applications for aeroacoustic source identification 14
 - 1.2.3 Post-processing methods 16
 - 1.2.4 The acoustic sink 16
- 1.3 Aeroacoustic noise sources produced by airfoils 17**
 - 1.3.1 Leading edge noise 17
 - 1.3.2 Airfoil self-noise 18
 - 1.3.3 Junction noise for a wall-mounted airfoil 25
- 1.4 Aeroacoustic noise sources produced by high-lift devices 27**
 - 1.4.1 Slat noise characteristics 27
 - 1.4.2 Slat noise generation mechanism 29
 - 1.4.3 Scaling laws 30
- 1.5 Summary of the chapter 30**

The first part of this chapter is dedicated to the literature review of signal processing methods (beamforming and time-reversal) for noise source identification. Importance is attached to their applications for the investigation of aeroacoustic noise sources in wind-tunnel with open test section. The second part summarizes aeroacoustic noise sources of airfoils (2D and wall-mounted airfoils). The final part introduces aeroacoustic noise sources of high-lift devices.

1.1 Experimental aeroacoustics

Despite the important advances in computational aeroacoustics, experimental aeroacoustics is still an important approach for the aeroacoustic studies. Jacob [63] highlighted three motivations for experimental aeroacoustics, *i.e.*, (i) characterising basic mechanisms of sound generation by unsteady flows for fundamental studies in aeroacoustics; (ii) validation for CAA codes and mixed CFD/CAA methods; (iii) characterising the sound generated by highly complex systems of real applications based on special wind-tunnel experiments. Wind-tunnel experiments have been widely conducted for experimental aeroacoustics using acoustic and aerodynamic measurements. Basically, two types of wind-tunnels exist, one is with open test section, the other is with closed test section. The acoustic measurement can be carried out using a single microphone to characterize the far-field radiation or using a microphone array to identify noise sources based on signal processing techniques like beam-forming or time-reversal. The aerodynamic measurements can be performed by hot wire anemometry and/or Particle Image Velocimetry (PIV).

1.1.1 Wind-tunnel with open test section

In this thesis, some experiments are conducted in a wind-tunnel with open test section for acoustic measurements. In such a facility, several issues can occur, such as shear layer refraction and turbulence scattering in the shear layer. Indeed the microphones are located outside the flow while the acoustic sources are in the flow, so that the acoustic waves propagate through the shear layer, undergoing refraction effects and scattering by turbulence. Kröber [68] found that wind-tunnels with open test section allow better performances than with closed test section in terms of low frequency acoustic measurements, because wind-tunnels with closed section are more influenced by background noise as the microphones are flush-mounted on the walls. However, sound scattering by the turbulent structures of shear layers of wind-tunnel with open test section increases significantly for high frequency measurements as shown in Figure 1.1.

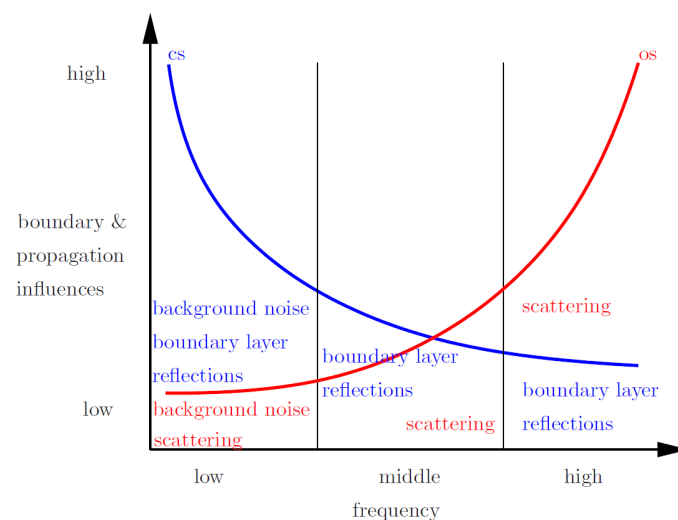


Figure 1.1: Comparison of wind-tunnels with closed or open test section, taken from [68]. ‘cs’ stands for close section and ‘os’ stands for open section.

1.1.1.1 Refraction of sound by shear layers

The refraction of sound by an infinitely thin shear layer was investigated by Amiet [5]. When sound waves reach the shear layer, they are refracted due to the flow velocity gradient. This leads to a change of angle and amplitude in the far field. Amiet proposed a robust analytical model (usually called “Amiet’s method” in the literature), based on ray-tracing, in order to evaluate the angle and amplitude change of the ray when crossing the shear layer. This model is widely used in the beamforming technique (presented further in Section 1.1.2) to make so-called “shear layer corrections” of the Green function in a quiescent fluid. In addition, the reflected waves can usually be ignored, allowing the correction to be independent of the source type and frequency. For the application of the correction for a single plane zero-thickness shear layer, the shear layer needs not to be in the far-field of the source.

1.1.1.2 Turbulence scattering of shear layers

For tonal noise, Clair and Gabard [35] conducted numerical simulations to investigate the scattering of a harmonic monopole by a turbulent layer with constant width. This study discards the refraction effects encountered in jet shear layer. The scattering leads to spectral broadening, *i.e.*, reduction of peak amplitude with sidebands at the source frequency. The authors found that the scattering effect increases with source frequency and mean flow velocity. Figure 1.2 shows a snapshot of the field of scattered pressure fluctuations and contours of turbulent velocity for a low frequency case, showing how the wavefronts are altered upside the turbulent layer. For broadband noise, Brooks and Humphreys [23] reported that broadband one-third-octave levels measured outside the wind-tunnel flow are reduced due to shear layer turbulence scattering.

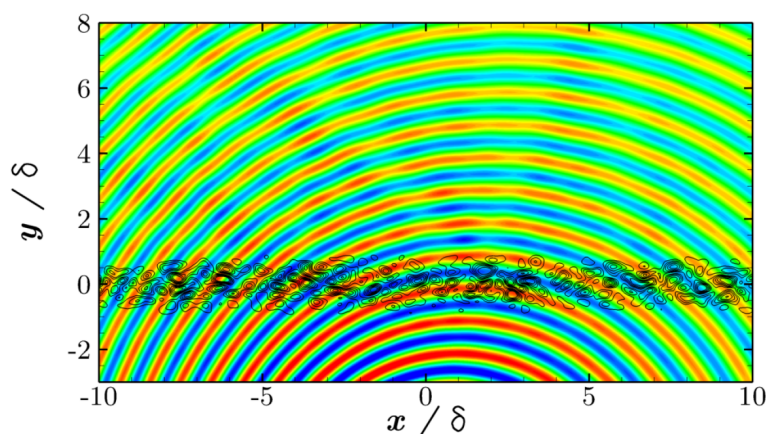


Figure 1.2: Scattering of a noise source by a shear layer (a) $f_0 = c_0/\delta$ (b), taken from [35].

1.1.2 The beamforming technique

The beamforming technique is a standard technique for noise source identification. The signal processing of beamforming requires channels of acoustic data recorded by a microphone array, which is usually called phased microphone array. A microphone array is a group of microphones with a specific optimized arrangement in space allowing a synchronous acoustic measurement. This technique applies a spatial filter by selecting a propagation model and a so-called scanning domain in which the noise sources are identified. Sound maps can be

obtained using such technique in the frequency domain [87] and the time domain [52], from which the distribution and strength of noise sources can be interpreted. Additionally, based on the sound maps, the acoustic spectrum radiated by a certain part of the scanning domain can be computed using an integration method [79].

1.1.2.1 A little history

The first acoustic array could be the device for the detection of aircrafts during World War I [64]. The array consisted of two groups of 6 sensors arranged hexagonally. However, no electrical components were used. The first application with microphone measurement and signal processing may be the work of Billingsley and Kinns in 1976 [15]. A system called "Acoustic Telescope" consisting of an array of 14 microphones connected to a mini-computer for noise source localization of a full-size jet engines was developed. Additive processing of signals was conducted to present the noise source intensity as a function of position and frequency. The noise source distribution could be displayed in real-time using a colour television. The array was calibrated by using a loudspeaker with known positions. The noise source position of the engine at low and high power settings is shown in Figure 1.3.

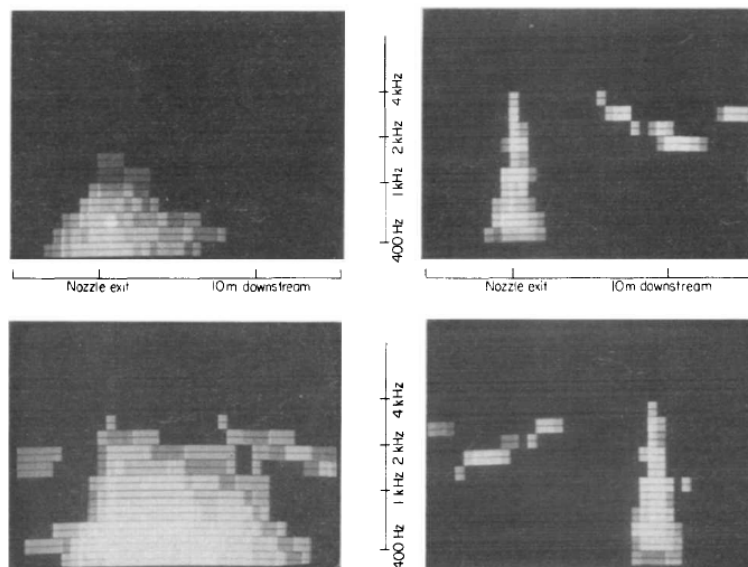


Figure 1.3: Noise source distribution shown by a colour television for calibrations of the array (top left and bottom left) and the engine at low power setting (top right) and high power setting (bottom right), taken from [15].

King and Bechert [65] used a linear array of 14 microphones for noise source identification of railway noise. Importance was attached to mechanical noise sources generated by wheel/rail interaction. The microphone array had two versions: one with a uniform microphone separation of 0.2 m and the other with a separation of 0.1 m. Conventional beamforming in the time domain was used for signal processing. It was found that the array with a microphone separation of 0.1 m allowed higher aliasing frequency.

1.1.2.2 Applications in wind-tunnels

The identification of aeroacoustic sources for engineering domains such as aeronautics and ground transport are generally conducted in wind-tunnels using scale models. Some works of the subject are presented in the following.

Meadows *et al.* [76] conducted aeroacoustic measurements for the sound generation of high-lift wing configurations using two arrays of different sizes (a large one for sound maps and a small one for spectra/directivity plots). The beamforming technique was used for signal processing. The phase corrections for the effect of the shear layer were conducted. However, the shear layer was highly curved and additional pitot probe measurements was conducted to determine the shear layer position. The high-lift wing consisted of a main element and a flap with Reynolds number being about 1.7 million. The dominant noise sources on the flap-side edge were identified.

Brooks and Humphreys [21] performed acoustic measurements for a calibrator source and a flap edge model setup using two planar microphone arrays of different sizes in order to examine the effect of array size on source maps and total noise source levels. The array with large aperture consisted of 35 microphones spaced logarithmically in spiral patterns. The array with small aperture, which was used for the measurements of directivity and spectra of a certain portion of the wing-flap model, was composed of 33 microphones (one microphone at the center and 4 irregular circles of 8 microphones each). It provided approximately the same model noise directivity for all the microphones. It was found that the large array could reveal much more details in source regions than the small array. In addition, it was subjected to substantial reduction of measured source levels due to better resolution. The increases in source size and frequency, and scattering by shear layer turbulence could also cause such reduction.

Blacodon [16] analyzed the airframe noise of a scaled 1:11th A320/A321 Airbus model in a wind-tunnel with open test section. Acoustic measurements were conducted using a planar microphone array composed of two sub cross-shaped arrays with 40 microphones positioned out of the flow. The author highlighted that conventional beamforming had poor spatial resolution and that it provided an overestimation of the expected power levels in many applications. The beamforming results of the aircraft model were used to validate the spectral estimation method. The actual locations and levels of noise sources were obtained by conducting shear layer correction.

Oerlemans *et al.* [92] assessed the reliability of absolute and relative array levels for wind-tunnel with open test section. Acoustic measurements were carried out for a 1:10.6 scaled Airbus A340 model in a wind-tunnel using a 4-m diameter out-of-flow planar microphone array consisting of 128 microphones (see Figure 1.4(a)). Figure 1.4(b) shows the noise source distribution of the aircraft model at 1 kHz. It was found that the absolute integrated array level (power integration method on source maps) could be too low by more than 10 dB because of coherence loss. However, the relative sound levels determined with the array, which were the differences between configurations of the model (angle of attack and flap angle), were accurate within 0.5 dB. It was also found that the amount of coherence loss depended on the wind-tunnel flow speed.

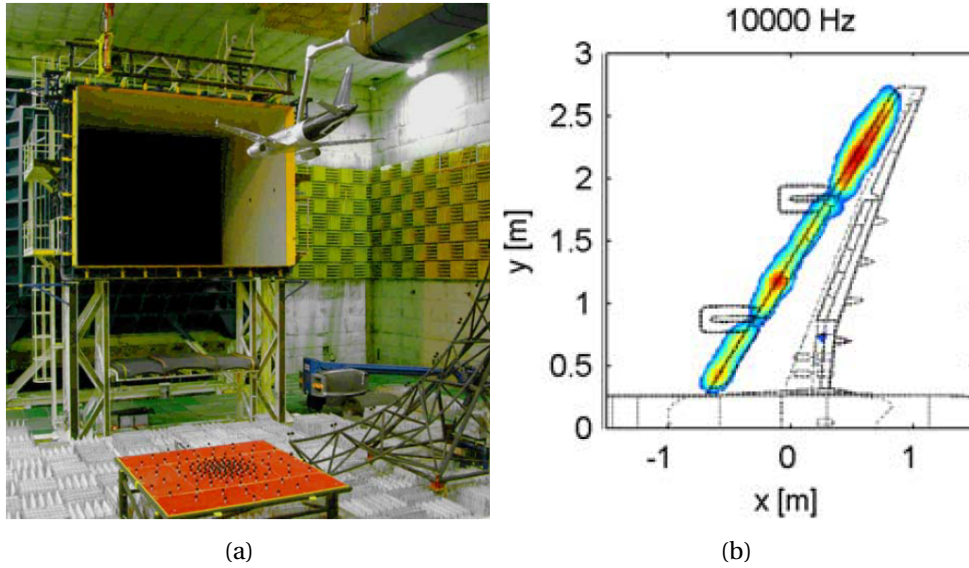


Figure 1.4: (a) Aeroacoustic measurements for a model of Airbus using a planar microphone array located out of flow, taken from [92]; (b) Sound map at frequency of 1 kHz using the beamforming technique, taken from [92].

Lauterbach *et al.* [69] conducted microphone array measurements on a model of high-speed train (a complex 3D geometry) installed on a splitter plate in a wind-tunnel with open test section. The array consisted of 143 microphones mounted on an aluminium lattice. They were arranged in a 3D array layout after an optimization for a frequency range between 10 kHz and 35 kHz in order to have a satisfactory spatial resolution and mainlobe-to-sidelobe ratio. The phase calibration was conducted to obtain an accurate position of all microphones, which allowed to increase the signal-to-noise ratio. Shear layer corrections were carried out using the Amiet's method. The noise sources from the bogie section were identified. Also, some strong acoustical reflections (mirror sources due to installation effects) were observed.

Ahlefeldt and Quest [3] conducted experimental measurements for the aeroacoustic radiation of an Airbus K3DY half-model of scale 1:13.6 using a microphone array consisting of 96 microphones in a wind-tunnel. Such wind-tunnel could provide real-flight Reynolds numbers. The microphone array was mounted into the side wall of the test section under combined cryogenic and pressurized conditions for wind-tunnel testing. The beamforming method associated with the deconvolution method CLEAN-SC was used for signal processing. The influence of temperatures and pressures was corrected. The significant dependency of Reynolds number for various sources was highlighted by sound maps. It was found that several dominant sources were identified on the flap at real-flight Reynolds numbers.

Fischer and Doolan [51] conducted an investigation of the effect of specular reflection on beamforming results in the closed test section of a wind-tunnel. Two approaches were considered to account for reflections in beamforming maps by using a more adapted steering vector in the beamforming algorithms. One of them is based on experimental Green's function through array measurements in the test section. Results showed that it allows a better resolution for sound maps when using the CLEAN-SC method associated to the experimental Green's function.

Most of the applications of beamforming technique were based on 2D scanning planes. 3D beamforming associated with 3D microphone array can also be found in the literature

(see the introduction of the paper in Chapter 5 and the works of Battista *et al.* [11] and Battista *et al.* [12]) but more rarely. It is promising for the noise source identification for flow-induced noise by complex geometries [128].

1.1.2.3 Deconvolution

Noise source distributions can not be truly interpreted from sound maps of traditional array results because they are convolved with array response functions [23]. Therefore, a deconvolution method is required in order to obtain a better spatial resolution.

Brooks and Humphreys [23] developed a complete Deconvolution Approach for the mapping of Acoustic Sources (the DAMAS technique) to accurately qualify the results of conventional beamforming in terms of position and strength of noise sources. This was achieved by solving a linear system of N equations with N unknowns, where N is the number of grid points in a scanning area. It was validated through the identification of synthetic point and line noise sources, and airframe noise sources generated by flap edge/cove, trailing edge, leading edge and slat.

Sijtsma [110] proposed a deconvolution method called CLEAN-SC. This method is based on the fact that the main lobes and side lobes of the results of conventional beamforming are coherent. CLEAN-SC was tested for aeroacoustic measurements of an Airbus A340 1:10.6 scale in a wind-tunnel with closed test section. The advantage of the method was demonstrated. It was very effective to remove dominant noise sources from sound maps in order to unmask secondary sources. It could also provide some good spatial resolution like other deconvolution methods. Its processing time was found to be relatively short: about two times of that of conventional beamforming.

1.2 The time-reversal technique

The beamforming technique is mostly based on a source propagation model using an analytical Green's function. Despite its robustness, this technique based on beamforming fails to account for the influence of acoustic scattering while dealing with complex geometries in a flow (with solid boundaries and complex flow profiles) because in real applications, the required analytical Green's functions are extremely difficult to derive, defeating potentially the beamforming process. Over the last years, some alternative approaches for identifying aeroacoustic sources have been developed in France and Australia, based on an array processing technique called the time-reversal technique (TR). This technique was originally proposed by Fink *et al.* [48, 50] for solving inverse problems. The TR technique is based on two assumptions: the first one is the invariance of the propagation by time inversion (which is true in a non-dissipative quiescent medium), and the second one is the reciprocity property in the propagation medium. The main idea of the TR technique is to back-propagate the recorded acoustic data in time to reconstruct acoustic pressure fields. The focalization spots of the time-reversed pressure field can be considered as noise sources. This is an approach different to the BF technique, which provides directly the distribution of the noise sources.

The TR process contains two steps. The first step is usually carried out in a cavity, enclosing the noise source area, with microphones at the boundary of the cavity (corresponding to (a) in Figure 1.5). The microphones measure the radiated acoustic field for a finite time duration. During the second step (focusing step), the recorded signals of each microphone are reversed and re-emitted from their recording points in an experimental or numerical way.

Reversed wavefront can be established in the cavity (see (b) in Figure 1.5). In this thesis, the focusing step is performed by using a numerical simulation.

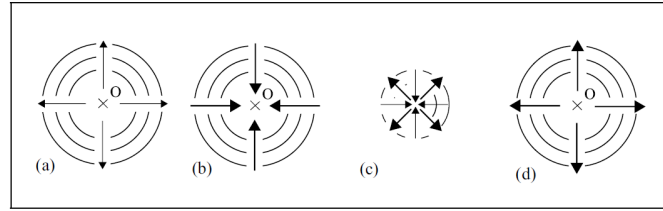


Figure 1.5: Schematic depiction of the time-reversal process: (a) direct numerical simulation and signal recording; (b) convergent wave; (c) interference between convergent and divergent wave; (d) divergent wave, taken from Bavu *et al.* [14].

For applications of the TR technique with the presence of a background flow, the flow direction should be reversed in the TR process in order to maintain the invariance of the propagation equation [107]. The property of reciprocity in flows was also investigated by Rakotoarisoa [102], and it was shown that this property is maintained for uniform flows, but that this property is broken in shear flows (even though the TR technique still gives good results in such cases). In several research studies for aeroacoustic noise source identification, the flow direction was reversed in a numerical way for the TR process [38, 46, 104], because it is impossible to be conducted experimentally.

1.2.1 Basic principle

Cassereau and Fink [30] described the basic theory of the closed TR cavity for time-reversal of acoustic fields. During the first step, the pressure field of an object source is generated in free unbounded space. The pressure field and its normal derivative across the surface of the cavity are measured without perturbation for the pressure field (Figure 1.6).

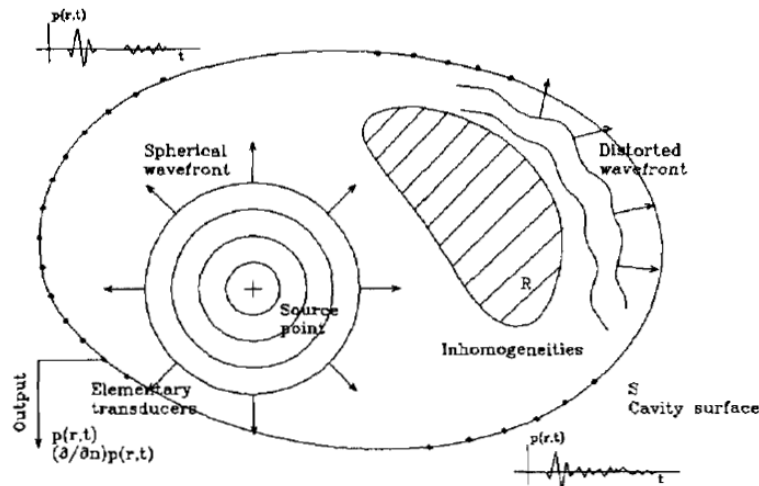


Figure 1.6: The first step of the TR process with a cavity, taken from [30]. A point-like source generates the pressure field. The cavity surrounds the noise source. The boundary of the cavity contains an infinite set of transducers to measure the acoustic pressure field and its normal derivative across the surface.

During the second step, the secondary sources on the surface of the cavity (monopole and dipole sources), corresponding to the time-reversed pressure field and its normal derivative measured during the first step, are created without the initial source in the cavity (Figure 1.7). Once the convergent wave reaches (or collapses) at the position of real source, it continues to propagate as a divergent wave (see (c) in Figure 1.5). This is not good for noise source identification because it interferes with the convergent wave. Then, for a homogeneous medium, the time-reversed pressure field corresponds to two impulse spherical waves that respectively converge to and diverge from the initial source position. The maximum available resolution for the TR process with a closed cavity in the frequency domain is half-wavelength. The theoretical focusing limitations is due to the superimposition of the two spherical waves at the end of the TR process. When no convergent wave collapses to the source position, only the divergent wave propagates in the cavity (see (d) in Figure 1.5).

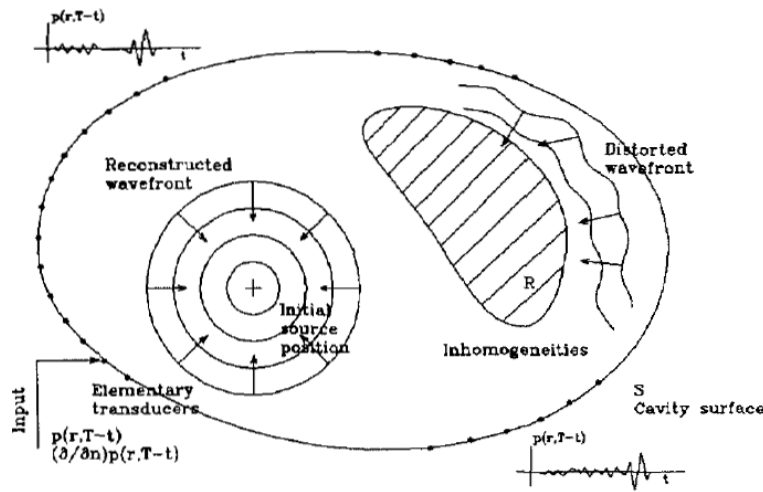


Figure 1.7: The second step of the TR process with a cavity, taken from [30]. The initial source is removed. The time-reversed pressure field and its normal derivative measured during the first step are re-emitted. A time-reversed pressure field is generated in the cavity with reconstructed wavefronts propagating back to the emission point.

The equations corresponding to the basic principal of the TR method are given below. The wave equation with a source term being a point-like monopole is given by

$$\left(\frac{1}{c_0} \frac{\partial^2}{\partial t^2} - \Delta \right) p(\mathbf{x}, t) = \phi(t) \cdot \delta(\mathbf{x} - \mathbf{x}_s), \quad (1.1)$$

with c_0 the sound speed, $p(\mathbf{x}, t)$ the pressure, $\delta(\mathbf{x})$ the Dirac distribution in the three-dimensional (3D) space, and \mathbf{x}_s the position of the source. The source emits a signal $\phi(t)$ during a finite time T ($\phi(t) = 0$ for $t < 0$ and $t > T$).

The pressure in the free unbounded medium at a position \mathbf{x} and instant t can be obtained by solving Equation (1.1)

$$p(\mathbf{x}, t) = G_d(\mathbf{x}, \mathbf{x}_s; t) * \phi(t) = \frac{1}{4\pi|\mathbf{x} - \mathbf{x}_s|} \cdot \phi\left(t - \frac{|\mathbf{x} - \mathbf{x}_s|}{c_0}\right), \quad (1.2)$$

with $G_d(\mathbf{x}, \mathbf{x}_s; t) = \frac{1}{4\pi|\mathbf{x} - \mathbf{x}_s|} \cdot \delta\left(t - \frac{|\mathbf{x} - \mathbf{x}_s|}{c_0}\right)$ being the Green function corresponding to an impulse diverging spherical wave and $*$ the convolution operator in the time domain.

The pressure field $p_M(\mathbf{x}_0, t)$ and its normal derivative $\frac{\partial p_M(\mathbf{x}_0, t)}{\partial \mathbf{n}_0}$ are measured at the boundary of cavity during the direct simulation. For the time-reversal process, they are expressed as $p_M(\mathbf{x}_0, T - t)$ and $\frac{\partial p_M(\mathbf{x}_0, T - t)}{\partial \mathbf{n}_0}$ at the surface of the cavity. Additionally due to the invariance of the propagation equation by time inversion, the time-reversed pressure field satisfies the wave equation without source term:

$$\left(\frac{1}{c_0} \frac{\partial^2}{\partial t^2} - \Delta \right) p(\mathbf{x}, t) = 0. \quad (1.3)$$

According to Cassereau and Fink [30], the expression of the time-reversed pressure field is

$$p_{TR}(\mathbf{x}, t) = \iint_S \left(\frac{\partial p_M(\mathbf{x}_0, T - t)}{\partial \mathbf{n}_0} * G_d(\mathbf{x}, \mathbf{x}_0; t) - p_M(\mathbf{x}_0, T - t) * \frac{\partial G_d(\mathbf{x}, \mathbf{x}_0; t)}{\partial \mathbf{n}_0} \right) dS, \quad (1.4)$$

with \mathbf{n}_0 the normal vector to the cavity surface with orientation away from the cavity, S the boundary surface of the cavity, $\frac{\partial}{\partial \mathbf{n}_0}$ the directional derivative with respect to the normal vector \mathbf{n}_0 , and \mathbf{x}_0 a point at the surface. Equation (1.4) is the so-called Kirchhoff–Helmholtz integral equation resulting from Kirchhoff’s formula (Howe *et al.* [59]) by removing the volume integral over the volume in the cavity. It means that the pressure field in a cavity with no source is determined if the pressure and velocity at the cavity surface are known. Equation (1.4) is used by Lobréau *et al.* [72] to determine the pressure field in a half-sphere volume based on the acoustic measurements by a hemispherical double-layer array. Another interest of using double-layer array is to conduct time-reversal in reverberant environments.

Following Equation 1.4, it was demonstrated by Cassereau and Fink [30] that the time-reversed pressure field is also given by (see details in Appendix A)

$$\begin{aligned} p_{TR}(\mathbf{x}, t) &= \frac{1}{4\pi|\mathbf{x} - \mathbf{x}_s|} \cdot \phi \left(T - t - \frac{|\mathbf{x} - \mathbf{x}_s|}{c_0} \right) - \frac{1}{4\pi|\mathbf{x} - \mathbf{x}_s|} \cdot \phi \left(T - t + \frac{|\mathbf{x} - \mathbf{x}_s|}{c_0} \right) \\ &= G_d(\mathbf{x}, \mathbf{x}_s; -t) * \phi(T - t) - G_d(\mathbf{x}, \mathbf{x}_s; t) * \phi(T - t), \end{aligned} \quad (1.5)$$

where the convergent wave is described by the term $G_d(\mathbf{x}, \mathbf{x}_s; -t) * \phi(T - t)$ and the divergent wave is described by the term $-G_d(\mathbf{x}, \mathbf{x}_s; t) * \phi(T - t)$. Note that the singularity at the source position \mathbf{x}_s doesn’t lead to an infinite value of pressure (Cassereau and Fink [30]).

1.2.2 Applications for aeroacoustic source identification

Deneuve *et al.* [38] applied the TR method to three numerical test cases for which the noise sources were generated by injection of mass, vibrating surfaces and a plane mixing layer. During the simulations, variables are stored at the computational boundaries. A sensitivity analysis of the time-reversed flow field based on the complex differentiation method was conducted to detect the regions with sound generation. The results showed that the coupling between the TR method applied to the Euler equation and the complex differentiation method allowed to detect successfully the noise generation zones in terms of shape and location. Later, Druault *et al.* [46] extended the application of this coupling process for aeroacoustic sources localization to the dissipative medium. The test cases of mass injection and a plane mixing layer were simulated. It was found that the time TR technique allowed to retrieve the aeroacoustic sources with a reduced amplitude of the sources due to the viscous

energy loss and detect noise sources in turbulent flow in spite of the loss of reversibility of the governing fluid equations. Rakotoarisoa *et al.* [104, 102] conducted a numerical investigation on the localization of a noise source in a heated flow using the TR technique and the beamforming technique with ray tracing [28]. Two configurations were considered for the heated flow, *i.e.*, a shear layer flow typical of wind-tunnels and a jet flow. In addition to the refraction due to velocity gradients, the refraction due to temperature gradients is also taken into account for the two techniques. Results showed that for shear flows with high Mach number and severe thermal gradients, the thermal stratification should be accounted for in order to improve the precision of the localization for the two methods.

In addition to these works based on a numerical approach, some experimental studies in aeroacoustics using microphones partially enclosing a noise source (a configuration called a Time-Reversal Mirror (TRM) [50]) were reported. Padois *et al.* [94] demonstrated, for the first time, the possibility of using TR technique to locate a noise source in a wind tunnel flow at low Mach number. A linear array, located above the wind tunnel test section and outside the flow region, was used for acoustic measurements. A monopolar noise source generated by a loudspeaker and a dipolar noise source generated by two out-of-phase loudspeakers were placed parallel to the mean flow. The time-reversed acoustic pressure field of the experimental data was obtained by solving numerically the Linearized Euler Equations (LEE) [10]. The mean flow velocity profile information used in the numerical calculation was obtained by anemometric measurements. The monopolar noise sources positions were well estimated with an error inferior to the wavelength and the dipolar noise sources were also well characterized in terms of position and radiation pattern. In the same wind tunnel, Rakotoarisoa *et al.* [103] conducted the experiments on the detection of intermittent aeroacoustic sources of a three-dimensional bluff body using the TR technique applied to LEE and a planar microphone array located outside of the flow was used for acoustic measurements. A focusing plane parallel to the microphone array and below the bluff body was chosen, so that the effect of the complex geometry was not accounted for. The authors concluded that although the TR technique is much more computationally expensive compared with BF technique, it is a promising technique for complex configurations where the Green function can not be derived.

Recently, Mimani *et al.* [83] carried out some experiments for a benchmark test-case of a full-span circular cylinder with the TR applied to LEE and the Point-Time-Reversal-Sponge-Layer (PTRSL) techniques. PTRSL [81] can remove the spurious local maxima regions throughout the computational domain and enhance the focal-resolution of the TR technique. Far-field acoustic measurements were conducted by two linear arrays located above and below the cylinder outside the flow. The dipolar nature of the Aeolian tone was revealed by the sound maps with a small error of $3/20$ Aeolian tone wavelength. The authors also modeled the acoustic reflection effect of the experimental set-up (contraction-outlet). The improvement of the resolution through the reduction of side-lobes was obtained. Some improvements were reported by the work of Mimani *et al.* [82], which implemented different methods based on the TR and conventional beamforming technique for the identification of aeroacoustic sources for a rod-airfoil system located in the same plane in a wind-tunnel. Two linear arrays, consisting of 64 microphones, were located below and above the test model. The 2D TR process was conducted without and with the modeling of the solid boundaries of the airfoil and the experimental facilities. Results showed that the TR and beamforming technique are equal in terms of source localization. It was also found that the modeling of such solid boundaries helps the noise source identification and improves significantly the

resolution of the TR results, demonstrating the interest of accounting for the scattering effect introduced by the solid boundaries for the TR process. However, the thickness of the airfoil was not taken into account for the modeling by supposing that the airfoil was acoustically compact.

Despite the previous research studies in the methodology of TR technique, it has not been applied to the aeroacoustic sources identification accounting for the effects of the boundary conditions of complex geometries (without simplification for the modeling) in wind tunnel testing and no 3D application of the TR technique in aeroacoustics has been reported before. This is a challenging task, which involves both experiments and numerical simulation.

1.2.3 Post-processing methods

To achieve better spatial resolution, several methods were reported in the literature: the acoustic sink (Rosny *et al.* [37]; Bavu *et al.* [14]; Bavu *et al.* [13]), deconvolution (Ulrich *et al.* [118]; Anderson *et al.* [6]), the point-time-reversal-sponge-layer (PTRS damping method (Mimani *et al.* [83]) and some post-treatment based on statistic method named Kurtosis (Mahenc [73]; Mahenc *et al.* [74]). The PTRSL method has been used for the noise source identification of aeolian tone of cylinder in a wind-tunnel. The Kurtosis has been applied for noise source identification of jets.

1.2.4 The acoustic sink

In this section, the acoustic sink in a homogeneous and quiescent medium is introduced. In this purpose, the idea is to remove the divergent wave in order to improve the resolution, a term of acoustic sink presented by the term $p_{AS}(\mathbf{x}, t) = G_d(\mathbf{x}, \mathbf{x}_s; t) * \phi(T - t)$ should be added to equation (1.5). As demonstrated by Bavu *et al.* [14], the time-reversal field with acoustic sink is given by

$$p_{TRAS}(\mathbf{x}, t) = p_{TR}(\mathbf{x}, t) + p_{AS}(\mathbf{x}, t) = G_d(\mathbf{x}, \mathbf{x}_s; -t) * \phi(T - t) = p(\mathbf{x}, T - t) \quad (1.6)$$

It means that the reversed pressure field only with convergent wave can be obtained during the time-reversal process if we add an antinnoise source emitting a signal $\phi(T - t)$ at the real source position.

According to Cassereau and Fink [30], and Lobréau *et al.* [72], the time-reversed pressure satisfying Equation (1.3) at the real source position \mathbf{x}_s is given by

$$p_{TR}(\mathbf{x}_s, t) = -\frac{1}{2\pi c_0} \phi'(T - t) \quad (1.7)$$

with $\phi'(t)$ the temporal derivation of $\phi(t)$. Using this relation, the antinnoise source signal $\phi(T - t)$ at the source position is reconstructed through the integral of the signal $\phi'(T - t)$ by Lobréau *et al.* [72]. In this way, the acoustic sink process can be conducted. However, the source position is, *a priori*, not known. To find its position, spatiotemporal search of the maximum level of the sound source imaging or other methods can be used. The acoustic sink method is also suitable for sound source imaging of multiple monopole sources using time-reversal through an iteration process (Lobréau *et al.* [72]).

1.3 Aeroacoustic noise sources produced by airfoils

Airfoils have numerous applications in engineering domains such as propellers, blades of wind turbines, wings of airplanes, rotors and stators of turbomachines, and diving planes of submarines. They are under a wide range of flow conditions in these applications. Flow-induced noise of airfoils is an important issue, which has been greatly studied since the 1970s. In this thesis, some experiments are carried out using airfoils in the wind-tunnel flow. For this reason, a literature review of noise sources of airfoils (2D and wall-mounted airfoils) in terms of their characteristics and generation mechanisms is presented.

1.3.1 Leading edge noise

An airfoil radiates noise from its leading edge (leading edge noise) when the impingement and breakdown of turbulence structures of the incoming flow occurs at the leading edge. More exactly, the pressure fluctuations, primarily generated by the impact of the turbulence upon the surface of airfoil, radiate a portion of their energy to the far field and produce what we hear as sound (Devenport *et al.* [41]). Leading edge noise source has a dipolar nature (Gershfeld [55]). Note that the interaction between the turbulent boundary layers and the trailing edge of the airfoil can also produce noise. Geyer *et al.* [56] indicated that leading edge dominates the noise generation if the flow has a higher turbulence intensity than that of the turbulence in the boundary layer.

Paterson and Amiet [96] performed acoustic measurements for an airfoil NACA 0012 (chord length of 23 cm and span length of 0.53 m) in a grid-generated turbulence field with a turbulence intensity of order 4% to 5% in an open-jet anechoic wind tunnel. Acoustic measurements were conducted in the mid-span plan. It was found that leading edge dominated the airfoil noise generation. As shown in Figure 1.8, leading edge noise is of broadband nature with higher sound pressure level at low frequencies.

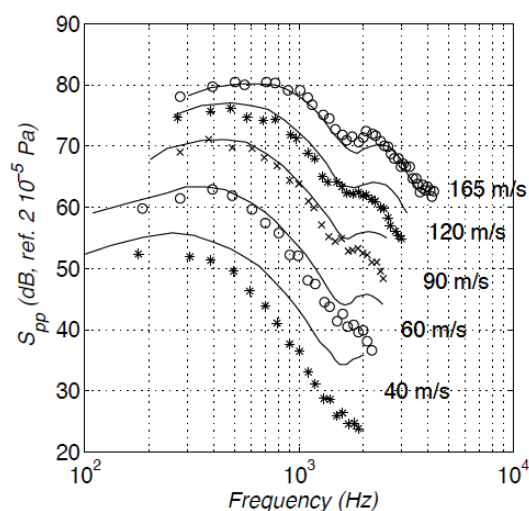


Figure 1.8: Leading edge noise spectra of a two-dimensional airfoil noise in grid-generated flow field [96, 26].

Results of Roger *et al.* [105] showed that the leading edge noise sources radiate preferentially downstream with more lobes when the product kC (with k the wavenumber and C

the airfoil chord) increases (Figure 1.9), *i.e.*, when the emission frequency increases. It was found that the number of lobes in the directivity pattern was determined primarily by kC and less importantly by the Mach number.

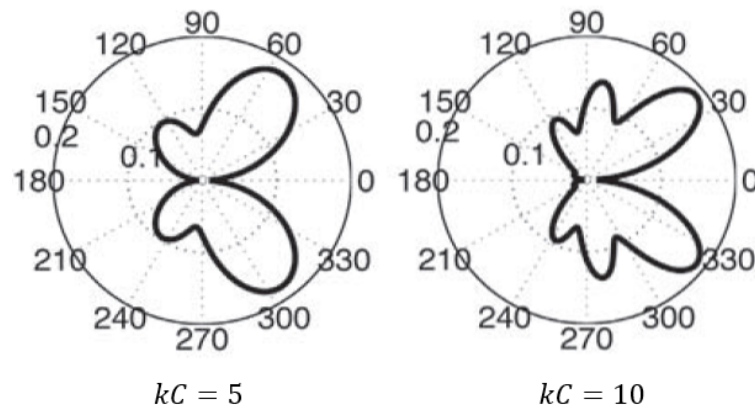


Figure 1.9: Typical directivity patterns of leading edge noise according to an analytical model. The Mach number is 0.05. The flow direction is from the left to the right, taken from [105].

Migliore and Oerlemans [80] conducted acoustic measurements for six airfoils of different thickness for wind turbine applications in an open jet anechoic wind-tunnel with a turbulence grid installed in the tunnel. It was found that leading edge dominates noise generation for all the airfoils. Results showed that boundary layer tripping devices has no influence on the leading edge noise generation, and that the directivity of leading edge noise is symmetrical around the chord of airfoil. The leading edge noise intensity increased as the airfoil thickness decreased. Additionally, a six-power scaling law of velocity was obtained for leading edge noise.

1.3.2 Airfoil self-noise

Airfoil self-noise is generated by the interaction between an airfoil blade and the turbulence emanating from its own boundary layer on the surface and near wake, for which a smooth incoming flow without turbulence is required [25]. Base on a data set from a series of aerodynamic and acoustic tests of seven NACA 0012 airfoil blade sections of different sizes (chord-based Reynolds number up to 3×10^6 ; angles of attack from 0° to 25.2°), Brooks *et al.* [25] identified five self-noise mechanisms and developed corresponding prediction models. As shown in Figure 1.10, the five mechanisms presented in subsonic flow conditions are: (a) broadband noise due to the turbulent boundary layer scattering at the trailing edge at high Reynolds number; (b) noise generated by wing tip vortex containing highly turbulent flow; (c) tonal noise with multiple tones due to laminar boundary layer instabilities at low Reynolds number; (d) noise generated by vortex shedding from blunt trailing edge; (e) low-frequency noise from large-scale separation at very high angle of attack.

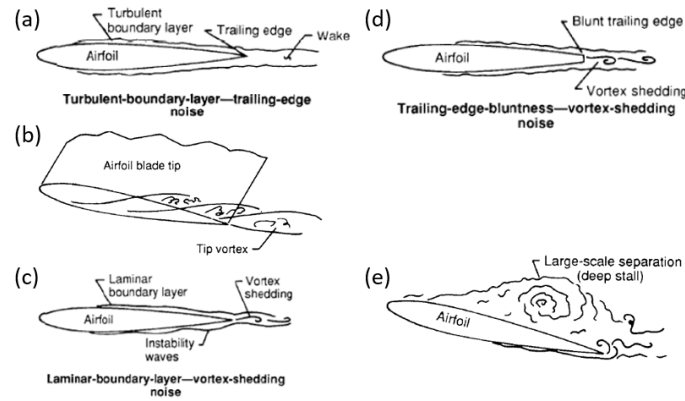


Figure 1.10: Self-noise mechanisms in subsonic conditions, taken from [25].

1.3.2.1 Trailing edge noise

When a turbulent flow passing a surface which is terminated by a half plane, flow-induced noise radiates as dipoles. The noise generated by the interaction between the boundary layers and trailing edge of the airfoil is called trailing edge noise.

The nature of trailing edge noise According to Blake *et al.* [18], the nature of trailing edge noise of an airfoil (tonal or broadband) depends on several parameters: boundary layer state (laminar or turbulent), trailing edge form (sharp or blunt), and angle of attack. Figure 1.11 shows the nature of trailing edge noise under different flow conditions. Blake *et al.* [18] indicated that tonal noise generated by airfoils with blunt trailing edge, similar to the aeolian tone of cylinder in a cross-flow, was due to the periodic wake vorticity results from Helmholtz instability in the airfoil wake. Tonal noise generated by airfoils with a sharp trailing edge will be addressed in the following sections. For broadband noise, it is generally generated in two cases: (i) airfoils at large angles of attack, (ii) airfoils with sharp trailing edge at high Reynolds numbers.

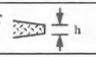


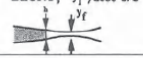
REYNOLDS NUMBER	ANGLE OF ATTACK	TRAILING EDGE FORM	SPECTRAL CHARACTER
LAMINAR FLOW $Re_c < 2 \times 10^5$	SMALL $\alpha < O[10^\circ]$	BLUNT 	TONAL, $f \sim U$ $f_b/U = \text{CONST}$
		SHARP 	TONAL, $f \propto U = \text{CONST}$ $f \sim U^{3/2}, \delta \sim U^{-1/2}$
	LARGE $\alpha > O[10^\circ]$	BLUNT OR SHARP	CONTINUOUS SPECTRUM
TURBULENT FLOW $Re_c > 2 \times 10^5$	SMALL $\alpha < O[10^\circ]$	SHARP 	CONTINUOUS SPECTRUM
		BLUNT, $y_f > 9000 \nu/U$ 	$f y_f / U = \text{CONST}$ $f \sim U$ $y_f = 0.8h$
	LARGE $\alpha > O[10^\circ]$	BLUNT OR SHARP	CONTINUOUS SPECTRUM

Figure 1.11: The dependence of airfoil trailing edge noise as chord-based Reynolds number, angle of attack and trailing edge bluntness with h the thickness of trailing edge, y_f the wake thickness, U the velocity of incoming flow, and δ the displacement thickness of boundary layer, taken from [18].

Brooks and Hodgson [22] carried out a comprehensive experimental investigation of trailing edge noise of a 2D airfoil with different trailing edge bluntness. The Reynolds number for all the tests are high and the boundary layer was fully turbulent. Figure 1.12 shows the acoustic spectra of trailing edge noise. For the sharp trailing edge case, trailing edge noise was broadband with the high sound pressure levels at low frequencies. For the blunt trailing edge cases, spectra were significantly influenced with the presence of spectral hump even though the degree of bluntness was only a fraction of the displacement thickness of boundary layer. In addition, it was found that the change of the angle of attack from 0° to 5° for the airfoil with sharp trailing edge at two incoming velocities (38.6 m/s and 69.5 m/s) tended to shift the peak levels of one-third octave spectra to lower frequencies but did not lead to significant influence on the overall sound pressure level.

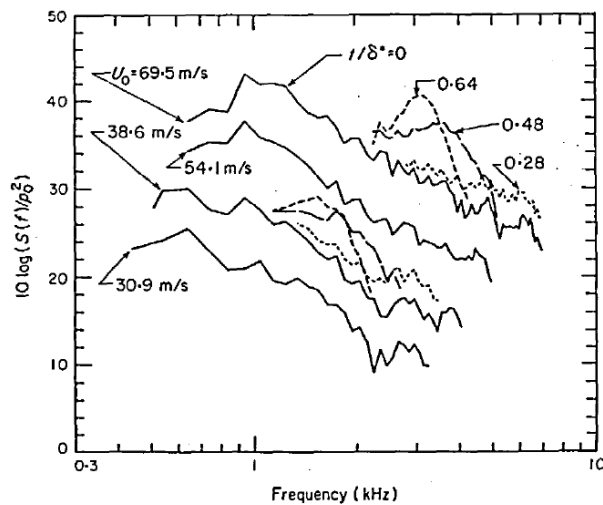


Figure 1.12: Acoustic spectra of the trailing edge noise of a NACA 0012 airfoil with different degrees of trailing edge bluntness at different incoming speeds. Degree of bluntness: solid lines for a airfoil with sharp trailing edges, dashed lines for airfoils with blunt trailing edge, taken from [22].

Moreau and Doolan [86] conducted acoustic measurements for a wall-mounted airfoil with sharp trailing edge and smooth surface. Different noise sources including tonal and broadband noise sources were identified under different flow conditions using conventional beamforming technique without deconvolution. Tonal trailing edge noise source was found to be concentrated at the trailing edge of airfoil (Figure 1.13(a)). Conversely, broadband trailing edge noise distributed more evenly along the span of the airfoil (Figure 1.13(b)).

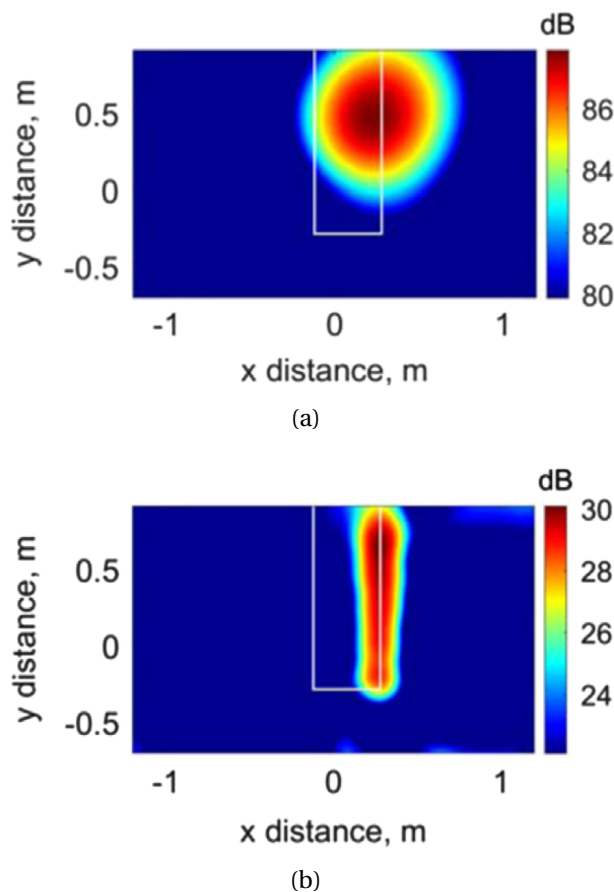


Figure 1.13: Sound maps of a wall-mounted airfoil with an aspect ratio of 3 (a) at flow speed of 40 m/s and angle of attack of 6° at beamforming frequency of 1000 Hz (tonal noise); (b) at flow speed of 60 m/s and angle of attack of 4° at beamforming frequency of 2500 Hz (broadband noise), taken from [86].

Directivity of trailing edge noise Moreau and Roger [88] assessed an analytical model of trailing edge noise through comparisons with several analytical and numerical computations in the literature. It was demonstrated that the acoustic compactness of the trailing edge noise source depended on the product kC (Figure 1.14). At low frequencies ($kC \ll 1$), the chord is much smaller than the wavelength, the trailing edge noise presents the directivity of a compact dipole, and its acoustic intensity follows a six-power scaling law of velocity. For higher frequencies ($kC > 2\pi$), the airfoil is not acoustically compact and scatters the trailing edge noise, so that its directivity exhibits more and more additional lobes, and its acoustic intensity follows a five-power scaling law of velocity (Figure 1.14(a)). It was also shown that trailing edge noise sources radiated preferentially upstream at high frequencies. The parameters like camber and thickness of the airfoil were not accounted for by the analytical model, but the errors remain tiny in terms of decibels.

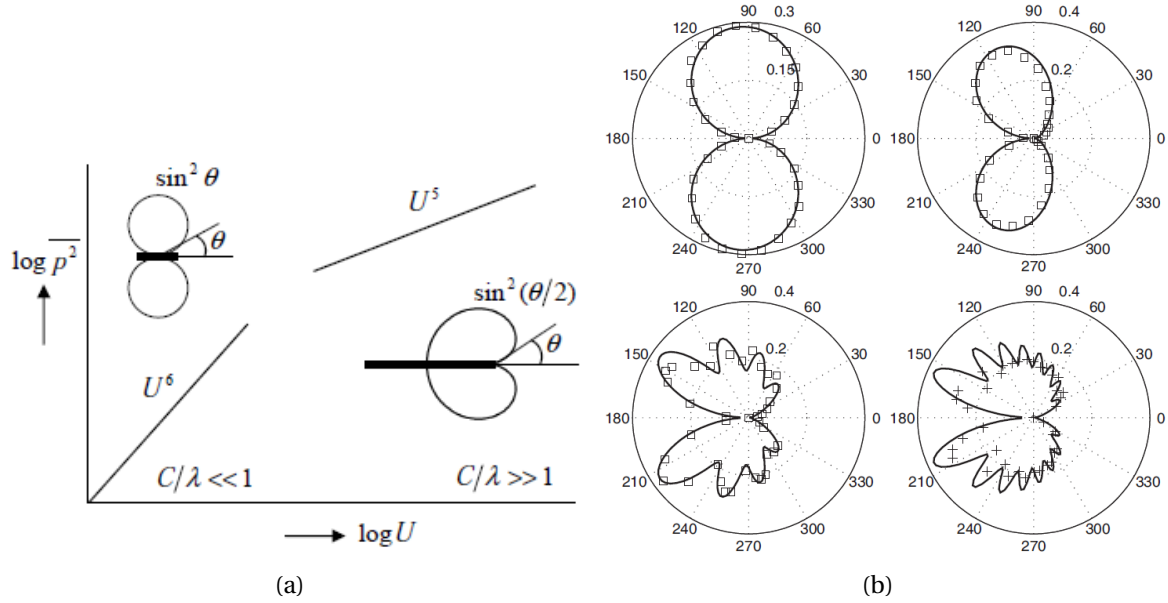


Figure 1.14: (a) Compactness of trailing edge noise source depending on velocity [17, 91], (b) Directivity patterns of trailing edge noise at several frequencies. From left to right and top to bottom: $kC = \pi/2, \pi, 4\pi$ and 8π . Mach number is 0.05. Solid lines stand for analytical solutions and symbols for numerical solutions. The flow direction is from the left to the right, taken from [88].

Tonal noise characteristics and generation mechanism The pioneering work for tonal noise generated by airfoils at low Reynolds numbers may be that of Paterson *et al.* [97] in 1973 for the investigation of tonal noise generated by 2D models of NACA 0012 and NACA 0018 in subsonic flows. It was observed that multiple tones of some test cases followed a 0.8 power velocity scaling law was observed. Several discrete jumps in frequency between rungs, showing a “ladder structure”, was demonstrated. Arbey and Bataille [7] performed experiments for NACA 0012 airfoils at zero angle of attack and chord-based Reynolds numbers from 2.0×10^5 to 6×10^5 . Two different contributions in acoustic spectra were highlighted, *i.e.*, a broadband hump centered on a primary tone $f_{n, max}$ and some secondary tones f_n (Figure 1.15(a)).

The tonal noise generation mechanism of airfoils with sharp trailing edge has been studied since the 1970s. Firstly, Paterson *et al.* [97] believed that the discrete tones were due to the periodic vortex shedding from the airfoils. In 2007, Desquesnes *et al.* [39] proposed a feedback mechanism to explain the tonal noise generation generated by an airfoil in a flow. On the pressure, Tollmien-Schlichting waves (TS waves) developed in a wide range of frequencies and were amplified. A separation bubble near the trailing edge acted as an amplifier and the main tone frequency (closed to the most amplified frequency of the TS waves) was selected by the boundary layer before it. The hydrodynamic fluctuations interacted with the trailing edge, which acted as the dipolar acoustic source near the trailing edge. The acoustic waves propagated upstream along the airfoil and excited instabilities on the pressure side, which yielded a feedback loop (Figure 1.15(b)). In addition, the secondary discrete components f_n (Figure 1.15(a)) were due to a periodic amplitude modulation of the main tonal frequency f_s .

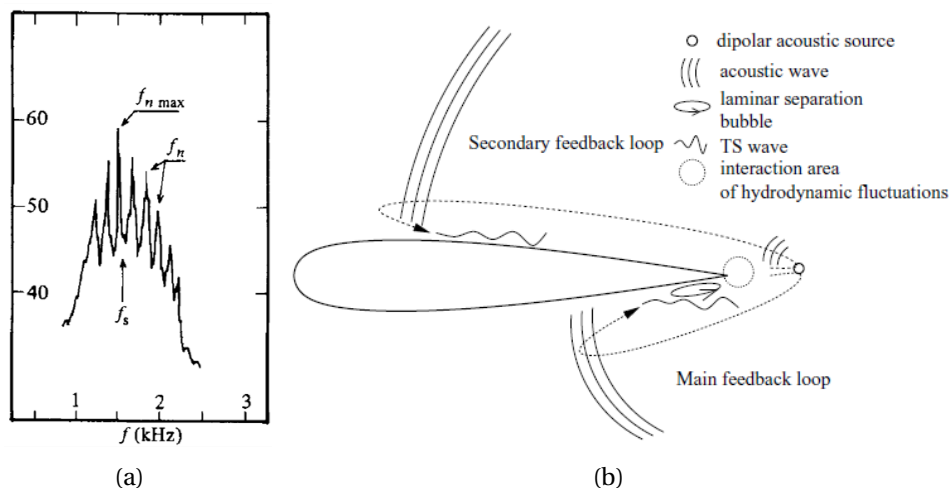


Figure 1.15: (a) Airfoil noise spectrum showing hump with equidistant tone frequencies, taken from [7], (b) Tonal noise generation mechanism, taken from [39].

Effects of tripping on noise generation As shown before, tonal noise generation is related to low Reynolds numbers. It could be generated by scale models for wind-tunnel testing, blades of wind-turbines etc. Boundary layer tripping devices such a band of sandpaper, generating forced transition to turbulent boundary layer, can be added on their surfaces in order to remove such tones.

Migliore and Oerlemans [80] carried out aeroacoustic tests of seven airfoils (six airfoils for candidates for use on small wind turbines and a NACA 0012 for comparison to benchmark data) in an open jet anechoic wind-tunnel using a microphone array consisting of 48 microphones. Based on beamforming results, 1/3-octave-band spectra for the mid-span of the model can be obtained using integration method, which allowed to suppress noise source at junctions of the model and endplates. The models were tested with and without boundary layer tripping device on the suction and pressure sides of the airfoils. It was found that proper tripping of boundary layer eliminated pure tones and lead to broadband noise instead. In addition, even airfoils generating broadband noise had a reduction of sound power level up to 3 dB when they were tripped.

Probsting *et al.* [101] surveyed the regimes of tonal noise generation over an extended range of flow conditions (chord-based Reynolds number between 0.3×10^5 and 2.3×10^5 and geometric angles of attack between 0° and 8°) for a NACA 0012 airfoil. Tests were conducted with a boundary layer tripping device on the pressure side or on the suction side of the airfoil, which were compared with that with smooth surface. They plotted the narrowband sound pressure level (SPL) of primary tones at different flow conditions (Figure 1.16), from which good agreement was observed for the SPL of smooth and pressure-side tripped airfoil at low Reynolds number. It indicated that events on the suction side dominate the tonal noise generation at low Reynolds number. After a transition between suction- and pressure-side-dominated regimes, the smooth and suction-side tripped cases demonstrated better agreement at high Reynolds numbers. Moreover, the same the investigation was conducted for some secondary tones (at least 30 dB above the background noise level and at most 15 dB below the the intensity of the primary tone). Similarly, their generation were found to be dominated by the suction side at low Reynolds numbers and the pressure side at high Reynolds numbers.

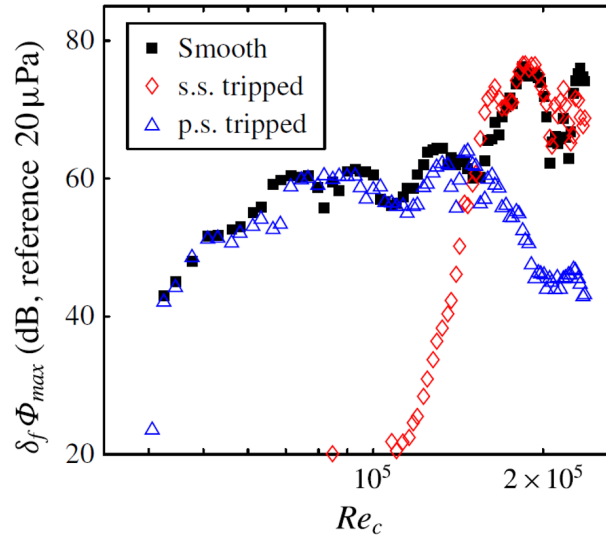


Figure 1.16: Narrowband SPL of primary tone against Reynolds number for geometric angles of attack of 2° , adapted from [101]. “s.s.” stand for suction side and “p.s.” stands for pressure side.

1.3.2.2 Wing tip noise

Brooks *et al.* [25] indicated that the noise generation mechanism of wind tip noise, caused by the turbulence propagation over the trailing edge of the wing tip, was similar to that of trailing edge noise. Imamura *et al.* [62] analysed the flow field around the tip of a wall-mounted NACA 0012 airfoil with flat ended tip at angle of attack 12° and Mach number 0.175 (the chord-based Reynolds number about 1.6×10^6), and revealed the existence of two different noise sources around the wing tip area with one located close to the suction side near the trailing edge. The authors also indicated that this noise source corresponds to the instability of the tip vortex as observed in the case of flap (Streett *et al.* [113]), for which the tip vortex of an airfoil was reported to be merged from two or three smaller vortex around the wing tip area depending on its geometry (Uzun *et al.* [119]; Imamura *et al.* [62]; Bailey *et al.* [9]).

Brooks and Marcolini [24] investigated the wing tip noise produced by 3D NACA 0012 models mounted to one sideplate with rounded wing tip and sharp trailing edge. Acoustic measurements were conducted using a microphone array. The differences, resulting from subtracting one-third octave spectra of 2D and 3D models, allowed to obtain wing tip noise contribution of 3D models. However, the resulting spectra were not smooth due to an error amplification problem. Only the midrange of such spectrum exhibited greatest confidence. For a 3D model with boundary-layer tripping on both sides of airfoil at flow speed of 71.3 m/s and angle of attack of 10.8° , it was found that the wing tip noise contribution for the overall broadband noise was low with respect to that of turbulent trailing edge noise. The authors suggested that the wing tip noise could contribute much more significantly for a model with flat ended tip.

Moreau and Doolan [85] conducted acoustic measurements for a wall-mounted NACA 0012 airfoil with flat ended tip (chord-based Reynolds number up to 1.6×10^6 ; angles of attack from 0° to 12°). By integrating sound maps of beamforming results over the wing tip region, 1/12th octave band wing tip noise spectra were obtained. It was found that wing tip noise was a dominant source at high frequency, for instance higher than 2.8 kHz at flow speed of 60 m/s. Figure 1.17(a) shows the noise source distribution of the wind tip noise at

a frequency of 3350 Hz. According to the 1/12th octave band wing tip noise spectra shown in Figure 1.17(b), the dominant wing tip noise contributes as a broad peak. Its peak level increases with the angle of attack. Additionally, the contribution frequency of the wing tip noise decreases when the flow speed is reduced (Figure 1.17(b)). Moreover, results showed that the dominant peak of wing tip noise scales with $M^{7.5}$ (M is the free-stream Mach number) at each angle of attack, which suggests a different noise generation mechanism at these frequencies than that of trailing edge noise.

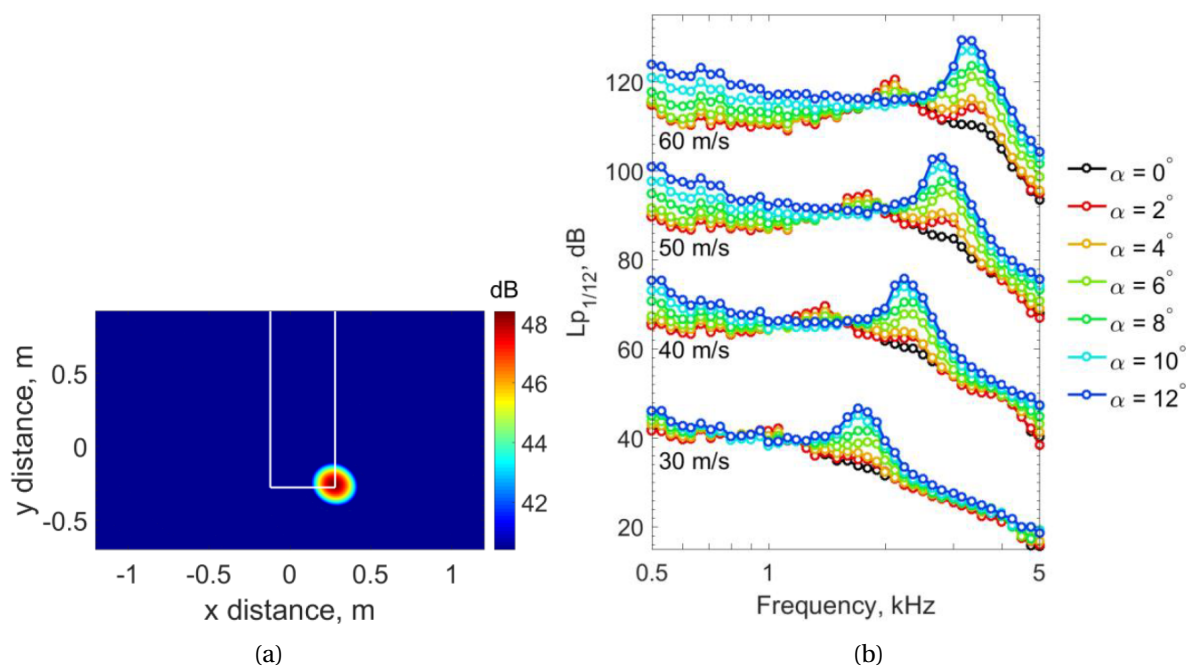


Figure 1.17: (a) Sound map of a wall-mounted airfoil with an aspect ratio of 3 at flow speed of 60 m/s and angle of attack of 0° at beamforming frequency of 3350 Hz; (b) Integrated 1/12th octave band wing tip noise for a wall-mounted NACA 0012 airfoil at flow speed of 30-60 m/s and angle of attack of 0° - 12° , taken from [85]. For clarity, the spectra have been offset by 20 dB with each increase in flow speed.

1.3.3 Junction noise for a wall-mounted airfoil

Figure 1.18 shows the typical junction flow structures, which may contain at the same time a large horseshoe vortex, a small corner vortex near the object, and a corner separation [20]. The horseshoe vortex is generated through the interaction between the incoming wall-bounded flow and the object, where the former is subjected to the skewing, sketching and rolling up [53]. Devenport *et al.* [40] indicated that the primary horseshoe vortex could yield a large-scale low-frequency bistable unsteadiness, seemed to be generated in the nose region, which may lead to undesired noise generation.

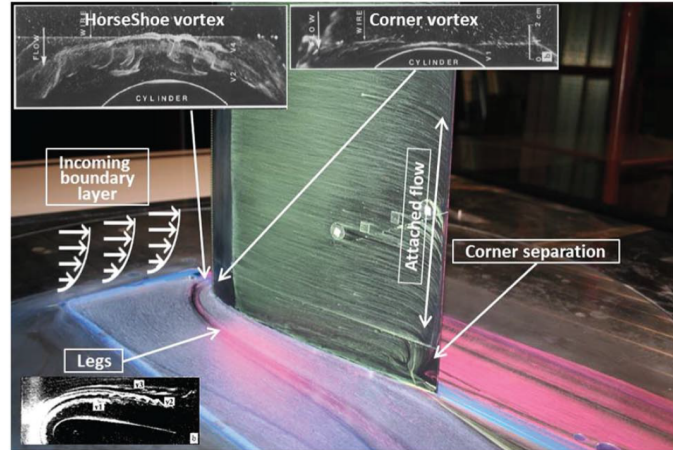


Figure 1.18: Oil visualization for the junction of a wall-mounted airfoil in a wind-tunnel flow, taken from [20].

Moreau and Doolan [86] performed far-field acoustic measurements using a microphone array for a wall-mounted NACA 0012 airfoils with flat ended tip (aspect ratios $L/C = 1 - 3$) at a range of chord-based Reynolds numbers $Re = 7.9 \times 10^5 - 1.6 \times 10^6$ and angle of attack ($\alpha = 0 - 6^\circ$). The surface of the airfoils is smooth without boundary layer tripping device. 1/12th octave band acoustic spectra were obtained by integrating the sound map over several regions. Based on the spectra, it was found that the junction noise dominates at low frequency at all flow speeds and angles of attack for the airfoil with an aspect ratio of 3 (Figure 1.19(b) as an example). Sound maps of beamforming results without deconvolution showed that the position of the junction noise source is primarily at the trailing edge as shown in Figure 1.19(a). The authors related it to the horseshoe vortex structures in the junction area when they pass over the trailing edge.

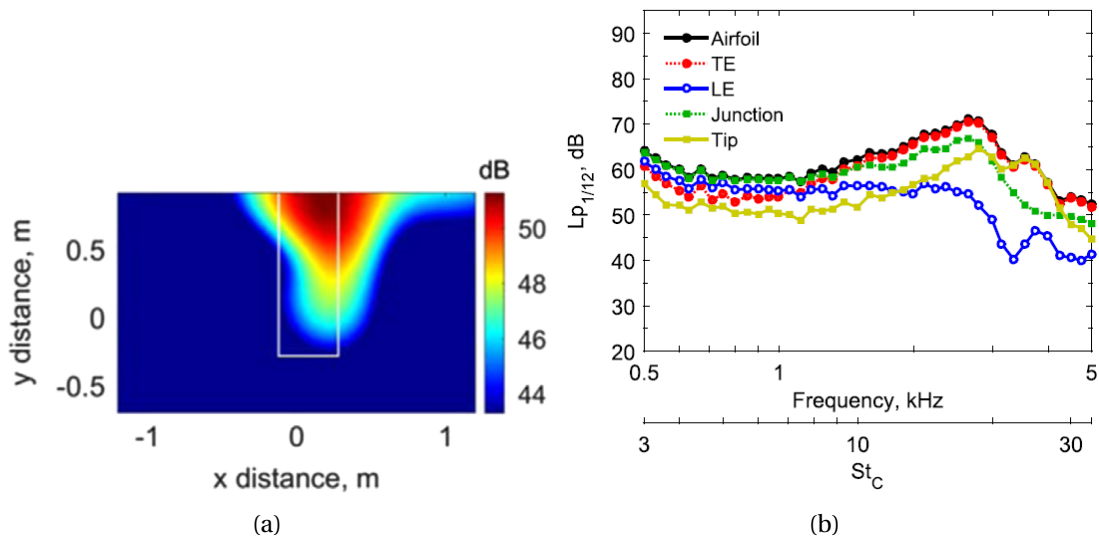


Figure 1.19: (a) Sound map of a wall-mounted airfoil with an aspect ratio of 3 at flow speed of 60 m/s and angle of attack of 4° at beamforming frequency of 1500 Hz; (b) Sound map of the wall-mounted airfoil with an aspect ratio of 3 at flow speed of 60 m/s and angle of attack of 4° , taken from [86].

1.4 Aeroacoustic noise sources produced by high-lift devices

In this thesis, some experiments are carried out using a high-lift device model in the wind-tunnel flow. For this reason, a literature review of noise sources of high-lift devices in terms of their characteristics and generation mechanisms is presented. High-lift devices of airplanes are deployed during their landing phases in order to generate additional lift, but they can generate additional noise. A high-lift device consists basically of a slat, a main element, a flap, slat tracks and flap tracks.

Slat noise was reported to dominate the noise generation of high-lift devices for scale model tests (Mendoza *et al.* [77]; Dobrzynski *et al.* [44]) and flyover tests (Chow *et al.* [33]). To our knowledge, the wind-tunnel test using full scale model is still unavailable. Therefore, high-lift devices of aircrafts are normally simplified to 2D unswept scale models for wind-tunnel tests. Although flap side-edge noise is the second important noise source for high-lift devices (Dobrzynski [42]), most published studies are focused on slat noise. Few works were reported for flap noise in literature. For example, Blacodon [16] identified noise sources for an A320/A321 aircraft model in wind-tunnel. When the flaps were deployed alone, it was found that noise was of broadband nature and dominated at low frequencies from inboard up to midboard leading edge of the flaps (angle of attack of 6° and velocity 60m/s).

1.4.1 Slat noise characteristics

According to Dobrzynski [42], slat noise is of broadband nature. But for scale models of slat, tonal components exist also. These tone artifacts due to model effects were identified in 2D scale model experiments. These tones can be generated by three events: (i) vortex shedding off a blunt trailing edge of slat; (ii) coherent laminar flow separation at the slat hook (low frequency between 1 and 4 kHz for a 1/10 scaled high-lift model); (iii) Tollmien-Schlichting boundary-layer instabilities on the slat suction side (high frequency between 10 and 20 kHz for the same model). Figure 1.20 shows the far-field spectrum of a slat at Reynolds number of 1×10^6 (Mach number of 0.15) for an effective angle of attack of 4.5° . The strouhal number is based on the slat chord length. As expected, some tonal components exist for the experimental results with respect to that of theoretical modeling. Moreover, Bolivar *et al.* [19] indicated that the hump in high frequency is associated with vortex shedding in the slat cove, which can be reduced by a boundary layer tripping on upper side of the slat.

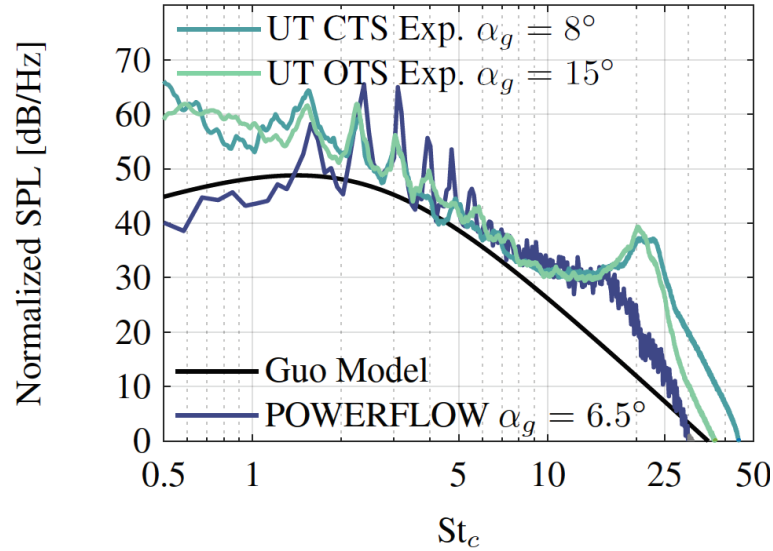


Figure 1.20: Far-field spectrum of a slat, taken from [19]. UT CTS stands for closed test section and UT OTS for open test section of wind-tunnel of University of Twente.

Dobrzynski and Pott-Pollenske [45] modeled the directivity of broadband slat noise sources as that of a dipole near the trailing edge of the slat, with the dipole's orientation being perpendicular to the slat surface (Figure 1.21(a)). This is supported by the results of a numerical simulation conducted by Choudhari and Khorrami [32], *i.e.*, the orientation of the near-field propagating pressure waves shown in Figure 1.21(b) is similar to the model. However, the authors indicated that far-field predictions were required for the comparisons with the model for the validation, because it is a simplified model.

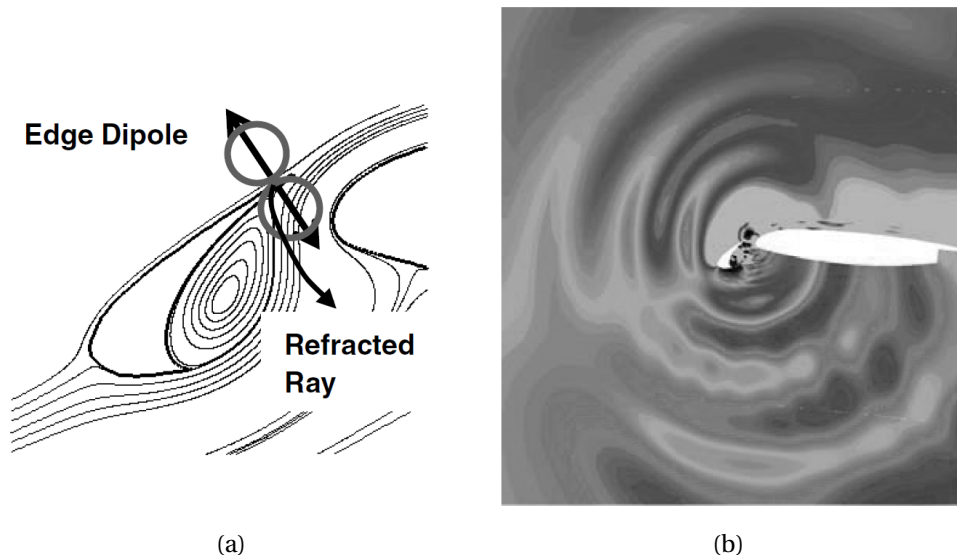


Figure 1.21: (a) Slat noise model as a dipole (based on Dobrzynski and Pott-Pollenske [45]); (b) contours of instantaneous pressure perturbations, taken from [32].

Yser and Bailly [123] conducted large-eddy simulations for the flow around a high-lift device at angle of attack $\alpha = 6.15^\circ$ and Reynolds number of 1.2×10^6 (based on the stowed

chord), from which the directivity of the radiated sound field was computed. It was found that the noise generation was dominated by the shear-layer impingement inside the slat cavity. In addition, two more different noise components existed in the slat area, which were generated by vortex shedding at the slat trailing edge and the interaction of the slat wake with the main body. A dipolar pattern was observed from the directivity of the radiated sound field.

1.4.2 Slat noise generation mechanism

Figure 1.22 shows the sketch of flow structures in the slat area, which leads to a complex mechanism of the generation of slat noise. Konig *et al.* [66] performed a large-eddy simulation for the flow around a high-lift device at an angle of attack $\alpha = 13^\circ$ and a Reynolds number of 1.4×10^6 (based on the chord length of the retracted configuration), and determined the acoustic field by solving the acoustic perturbation equations. The cusp of the slat (lower trailing edge of slat) was blunt and the trailing edge of the slat was sharp. The flow fields of numerical results were validated by Particle image velocimetry (PIV) measurements. It was found that a recirculation zone of very low Mach number (structures rotating in a counter-clockwise direction) existed in the slat cove, which was separated from the flow passing the slat gap by a shear layer emanating at the slat cusp. The shear layer processed the so-called rollers (2D spanwise oriented vortex structure) immediately downstream the cusp. The vortical structures from the recirculation zone mixed and interacted with the shear layer structures, which seemed to enhance the development of streamwise oriented vortical structures between two rollers (ribs). Then the rollers and ribs entered a reattachment area of the slat cove shear layer. In this area, the vortical structures were strongly stretched by the accelerated slat gap flow and aligned with the streamwise direction. Then the vortical structures generated in the slat cove area and the turbulent boundary layer developing on the suction side of the slat merged as the wake downstream of the slat trailing edge. It was found that the strongest noise sources occurred in the shear layer, the reattachment area, and the slat wake corresponding to the highest vortical activity and the highest turbulent kinetic energy.

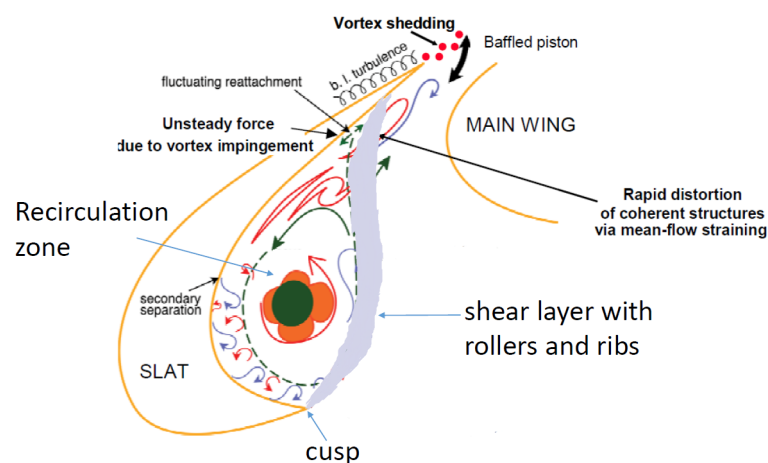


Figure 1.22: Slat flow, adapted from [31].

1.4.3 Scaling laws

Although a test-set up for the outer 30% span of a full-scale A320 aircraft wing immersed in the open test section of a wind-tunnel was reported by Dobrzynski *et al.* [43], full-scale model totally installed in the test section of wind-tunnels is still not possible because of extreme costs. Therefore scaling laws of the slat noise radiation have been investigated by several studies, for which the sound pressure level as a function of M^x (x being a parameter) could be determined. The sound pressure level of slat noise was found to scale with $M^{4.5}$ by Dobrzynski and Pott-Pollenske [45] and M^4 by Pagani, Jr. *et al.* [95] with M being the Mach number. Guo and Joshi [57] found that the sound pressure level of slat noise scales with M^5 in the range of low to mid frequencies.

There are few studies concerning the scaling law of flap noise. The broadband noise generated by flap was found to be governed by power scaling law $M^{5.5}$ power by Blacodon [16] and $M^{5.8}$ by Sen *et al.* [108].

1.5 Summary of the chapter

The first part of the chapter introduces experimental aeroacoustics in terms of its objectives, experimental facilities and signal processing methods. The advantages of using wind-tunnels with open test section for studies of experimental aeroacoustics are first highlighted. The refraction of sound by shear layers and turbulence scattering of shear layers are two important issues for acoustic measurements in wind-tunnels with open test section. The BF technique, a standard signal processing method for noise source identification, is then introduced in terms of its history, applications in such wind-tunnels and deconvolution methods. Additionally, the extend of the beamforming technique to noise source identification in 3D areas using 2D microphone arrays have been conducted over the last ten years. However, the use of the 3D beamforming technique associated to a 3D microphone array with a very large number of microphones for noise source identification in wind-tunnels was not reported before.

The second part presents the TR technique, which is promising to overcome the limits of the BF technique dealing with cases where the effect of solid boundaries on propagation can be significant or complex flow profiles. Some of its applications were reported for the identification of aeroacoustic sources in wind-tunnels and only in two-dimensions for aeroacoustic applications. Moreover, the consideration of solid boundaries has not been reported before.

The third and final parts are dedicated to the literature review of aeroacoustic noise sources of airfoils (2D and wall-mounted airfoils) and high-lift devices. The noise sources of airfoils consists of leading edge noise, self-noise (trailing edge noise and wing tip noise), and junction noise. Slat noise is the first important source for noise generation of high-lift devices. The characteristics of such aeroacoustic sources and their generation mechanisms have been presented.

Chapter 2

Experimental apparatus

Contents

2.1	The wind-tunnel BETI	32
2.2	Flow measurements by hot-wire anemometry	33
2.3	Acoustic measurement system	33
2.4	Microphone arrays	36
2.5	Synthetic noise source in a 3/4 open test section	37
2.6	Experiments with a streamlined acoustic source	38
2.6.1	Source description	38
2.6.2	Experiment for studying source diffraction	38
2.6.3	Experiment for studying non-uniform flow effects	39
2.7	Wall-mounted airfoil	40
2.8	Experimental device of a high-lift model	41
2.9	Summary of the chapter	43

This chapter presents the experimental apparatus including the wind-tunnel facility, the hot-wire anemometry, the acoustic data acquisition system, the microphone arrays, synthetic noise sources, and test models. In particular, two types of 3D microphone array are used for the acoustic measurements (one with 256 microphones, the other with 768 microphones). The synthetic noise sources are generated by a compression chamber and a streamlined acoustic source under different testing conditions. The test models concern wall-mounted airfoils and a high-lift device.

2.1 The wind-tunnel BETI

The anechoic wind-tunnel BETI of the PPRIME Institute is an Eiffel-type wind-tunnel for aerodynamic and aeroacoustic studies. The wind-tunnel flow is drawn by fan assemblies downstream the test section with suction. Figure 2.1 shows the photograph of the wind-tunnel. The open test section is located in an anechoic chamber of 90 m^3 allowing a cutoff frequency of 200 Hz. According to the experimental configurations, the test section can be fully open or 3/4 open, the flow being bounded by a plank of wood on its lower side (like in Figure 2.1). The maximum free-stream velocity of the wind-tunnel flow is 60 m/s (216 km/h).



Figure 2.1: Photograph of the wind-tunnel BETI.

The length of the test section in the flow direction is 1.44 m . The wind-tunnel flow is firstly accelerated in a tunnel with decreasing section area (with a contraction ratio of 10), and enters the test section through a rectangular nozzle of $(0.7 \times 0.7) \text{ m}^2$. At the nozzle exit, the boundary layer thickness is of the order of 10 mm , and the turbulence intensity of the free-stream flow is about 1.5% . The flow is then sucked through a collector of dimensions (width \times height) $(1.00 \times 0.87) \text{ m}^2$. The right-handed coordinate system (O, x, y, z) used for the experiments in this thesis is presented in Figure 2.2. The origin of the coordinate system is located at the center of line AB (Figure 2.2). Axis x follows the wind-tunnel flow direction, and axis z follows the vertical direction.

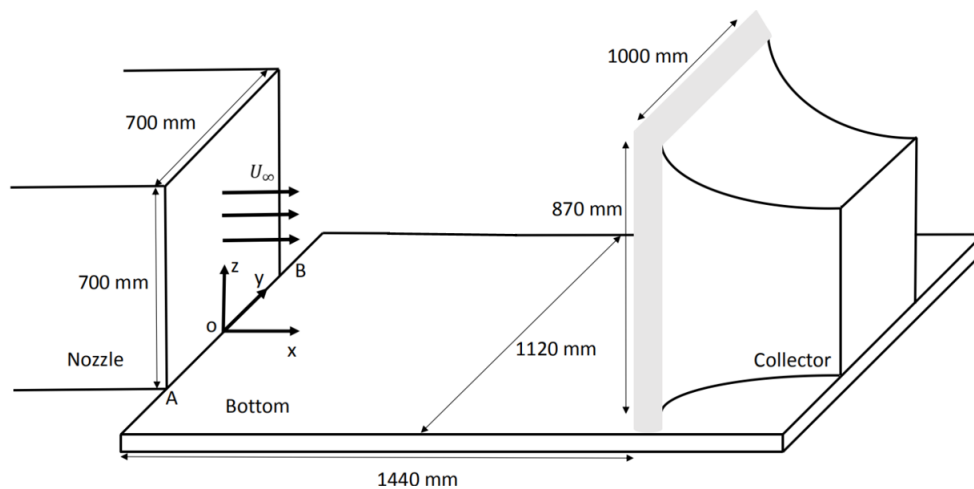


Figure 2.2: Sketch of the wind-tunnel BETI in the 3/4 open configuration.

2.2 Flow measurements by hot-wire anemometry

The hot-wire anemometry is mounted on a 3 axis-robot controlled by a computer. This system allows an accurate measurement of the mean flow profile. Calibrations were conducted for the hot-wire anemometry before measurements. Figure 2.3(a) shows the hot-wire anemometry, supported by a horizontal bar with a streamlined section, in the wake of a wall-mounted airfoil. Several measurements along lines in the direction perpendicular to the surface of the airfoil were conducted. Figure 2.3(b) shows the hot-wire anemometry, supported by a vertical bar, in the wake of two cylinders with square cross sections in front of the nozzle of the wind-tunnel. Measurements were conducted along lines in the x - and y -directions.

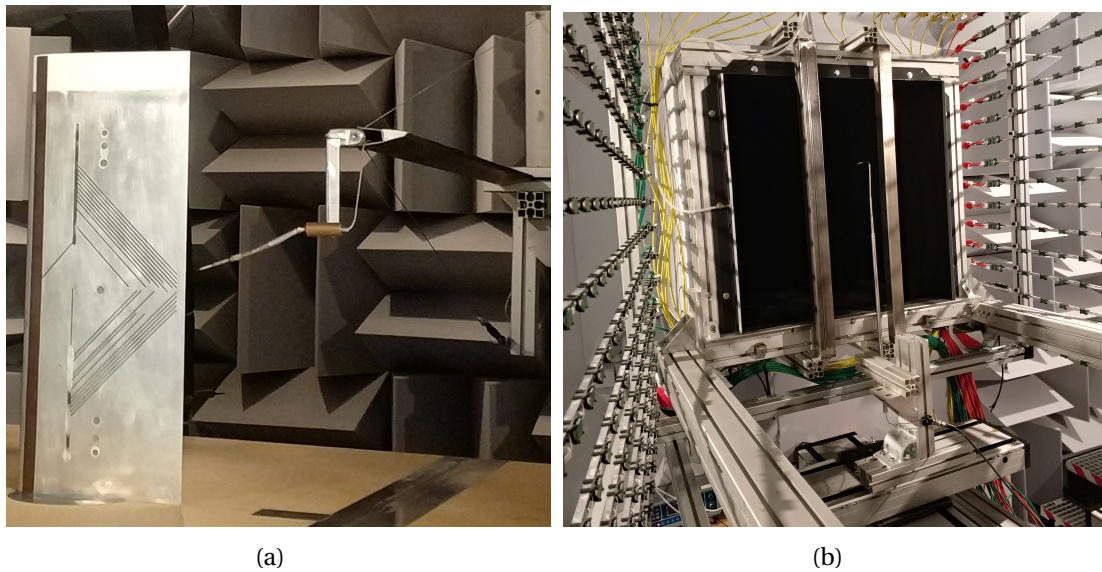


Figure 2.3: Measurements by the hot-wire anemometry (a) in the wake of a wall-mounted airfoil; (b) in the wake of two cylinders with square cross sections placed at the outlet of the nozzle of the wind-tunnel.

2.3 Acoustic measurement system

As presented in [127], the acoustic data acquisition system consists principally of microphones, an interface for data acquisition, cables, and a power supply system. Two types of microphones are used for the acoustic data acquisition system, *i.e.*, digital Micro ElectroMechanical Systems (MEMS) microphones and measurement microphones. The MEMS microphones are of type ICS-43434, developed by InvenSense. Each microphone is inserted in a small PCB (printed circuit board) card as shown in Figure 2.4(a). The PCB is mounted on a metallic bar. The white cables connect the MEMS microphone to the neighbouring ones. The acoustic measurement with the MEMS microphone is conducted through a small hole through the PCB. The channels of the MEMS microphone deliver digital signals because the whole instrumentation chain is directly included on the PCB (a transducer, an amplifier and a 24 bits AD converter). The measurement microphone is a G.R.A.S Type 40AF model, and the preamplifier is 01dB-Stell Type PRE21S/PRE21A (Figure 2.4(b)). The sampling frequency of the microphones can be set by the user up to 50 kHz.

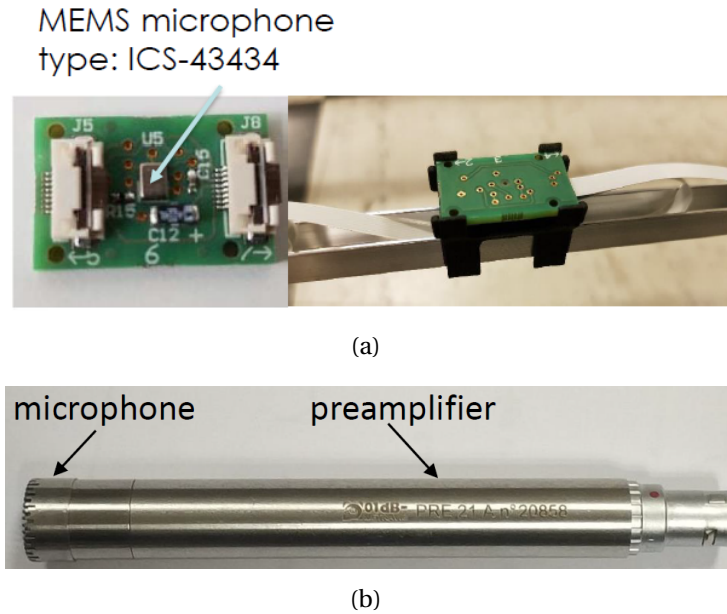


Figure 2.4: (a) Left photograph: a MEMS microphone inserted in a PCB; right photograph: a PCB mounted in a metallic bar; (b) photograph of the measurement microphone (G.R.A.S Type 40AF) and the preamplifier (01dB-Stell Type PRE21S/PRE21A).

The response of the MEMS microphones are provided by Institut Jean le Rond d'Alembert. It was obtained by testing a sample of 32 MEMS microphones of type ICS-43434. MEMS microphones are not measurement microphones, so the frequency response is not flat. Results show that the amplitude response has a variability within 3 dB over the band between 80 Hz and 10 kHz in comparison to a measurement microphone (Figure 2.5(a)). Therefore, it requires some frequency equalization for amplitude response by using the mean response. The variability of the phase response is very good up to 6 kHz. It increases for the frequencies higher than 6 kHz (Figure 2.5(b)). Nevertheless, one study based on simulations demonstrated that the phase dispersion of the MEMS microphones has no significant influence on the response of the array by beamforming by taking consideration of the large number of microphones [125].

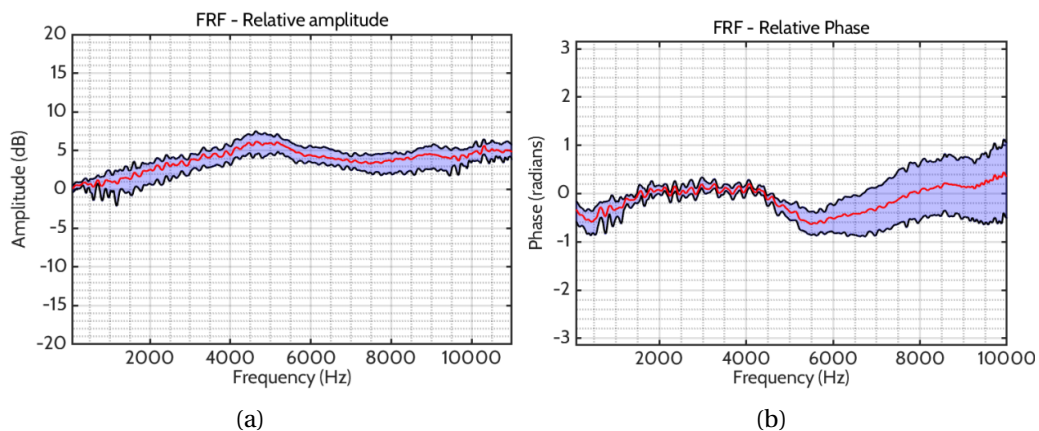


Figure 2.5: Frequency response of a group of 32 MEMS microphones obtained by the same procedure depicted by Vanwynsberghe *et al.* [120] (a) relative amplitude; (b) relative phase, taken from Zhou *et al.* [127]. Red line-average; blue shaped area: variation over the group.

The MegaMicros system was developed at Institut Jean le Rond d'Alembert. The acoustic data acquisition system allows the multiplexing of 1024 digital channels from MEMS microphones and 16 analog channels. The 1024 channels MegaMicros system was installed in the wind-tunnel BETI in the context of a collaboration between PPRIME Institute and d'Alembert Institute. The interface for data acquisition collects all the signals acquired by each channel (digital and analog ones) through two types of connectors (RJ45 connector and analogical channel connector) as shown in Figure 2.6. To adapt to the test section of the wind-tunnel BETI, the 1024 MEMS microphones are divided into 128 groups of microphones. Each group contains 8 microphones, which are controlled by a buffer board linked to the data acquisition system with a RJ45 cable (Figure 2.6). From the MEMS microphones to the interface for data acquisition, signals are handled with the I2S serial protocol. Inside the interface for data acquisition, the analog signals from the measurement microphones are also converted to digital signals. Then, the 24-bit integer samples are converted to 32-bit floats before multiplexing and transfer via the USB 3.0 serial bus or a optical fiber to the host PC.

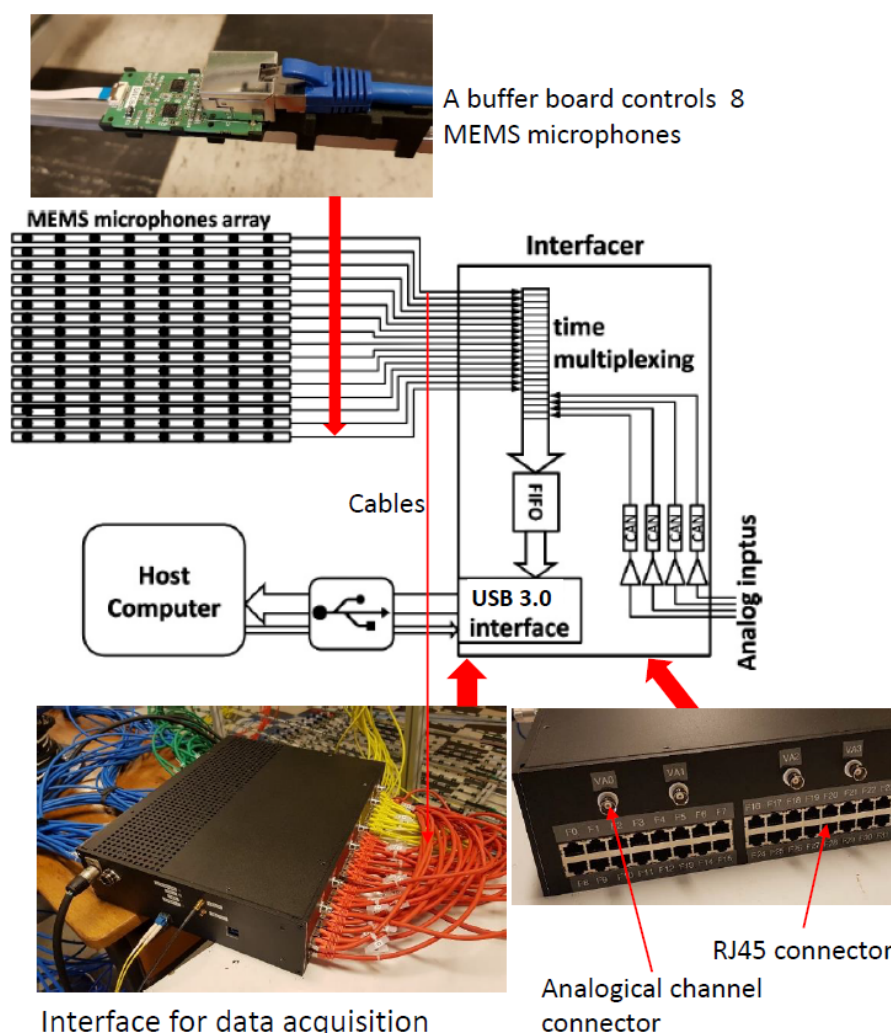


Figure 2.6: Sketch of the acoustic data acquisition system with photographs of a buffer board, interface for data acquisition and cables, adapted from Vanwynsberghe *et al.* [120]. The group of colored cables are RJ45 linking the buffer cards to acquisition system.

2.4 Microphone arrays

Figure 2.7(a) shows the 3D model of the array structure [127]. As presented in [127], the reason for the design of the array structure enlarging from the nozzle to the collector of the wind-tunnel is to account for the development of the shear layers from the nozzle under test conditions, the need to avoid the turbulent regions around the collector, and manufacturing constraints. More exactly, it is a cone with square bases surrounding the wind-tunnel flow. The lengths of the edges of square base 1 (vertices 1, 2, 3 and 4) and square base 2 (vertices 5, 6, 7 and 8) are respectively 1200 mm and 1535 mm. The distance between the two square bases is 1157 mm. The array structure consists of four sides ('left', 'top', 'right' and 'bottom') with 16 bars being placed on each of them (spaced by a distance of 75 mm on square base 1 and 96 mm on square base 2). This allows to mount MEMS microphones on them. Each bar has a U-shaped section with a length of 1.8 m. On each bar, there are two groups of 8 microphones (so 16 microphones on each bar), which are arranged uniformly with a gap of 72 mm between two neighbouring microphones. The experiments in this thesis are conducted using only 3 sides ('left', 'top' and 'right') enclosing the 3/4 open test section of the wind tunnel with 768 microphones for the reason that the supports of the test models cross the side 'bottom' of the array structure. Although some other arrangements of microphones exists, this is the best way to place the microphones under the constraints in our case. The chosen arrangement of microphones was optimized among several options, given the mechanical and mounting constraints, in terms of frequency resolution and relative levels between main and side lobes given by the beamforming technique (presented further in Chapter 4) [127]. Figure 2.7(b) shows the microphone array installed in the open test section of the wind-tunnel.

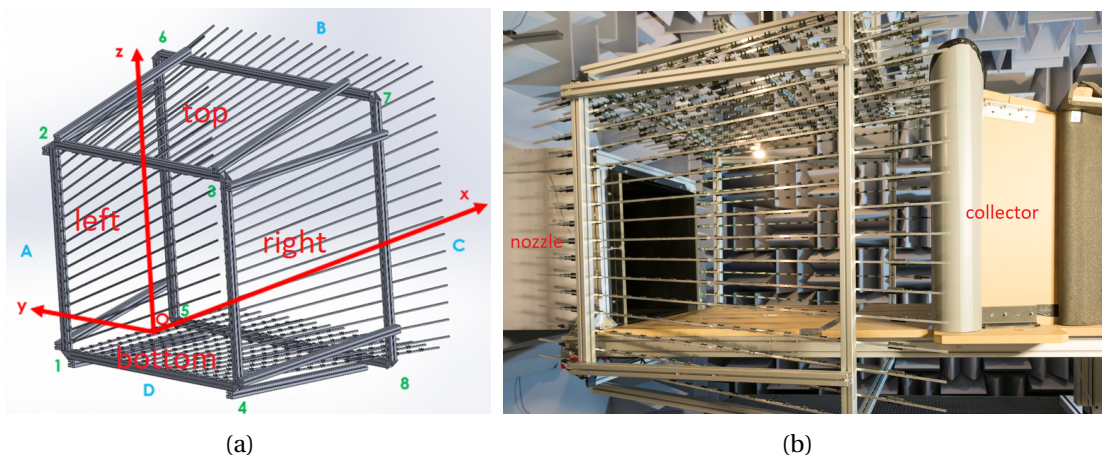


Figure 2.7: (a) 3D model of the array structure; (b) the 3D microphone array containing 768 microphones of sides 'left', 'top' and 'right' installed in the open test section of the wind-tunnel.

Figure 2.8(a) shows the arrangement of the 768 microphones of the 3D microphone array. A similar array structure with 256 microphones is also used this thesis. A detailed description of the 3D array can be found in the paper Zhou *et al.* [128] in Chapter 5. Figure 2.8(b) shows the arrangement of the 256 microphones.

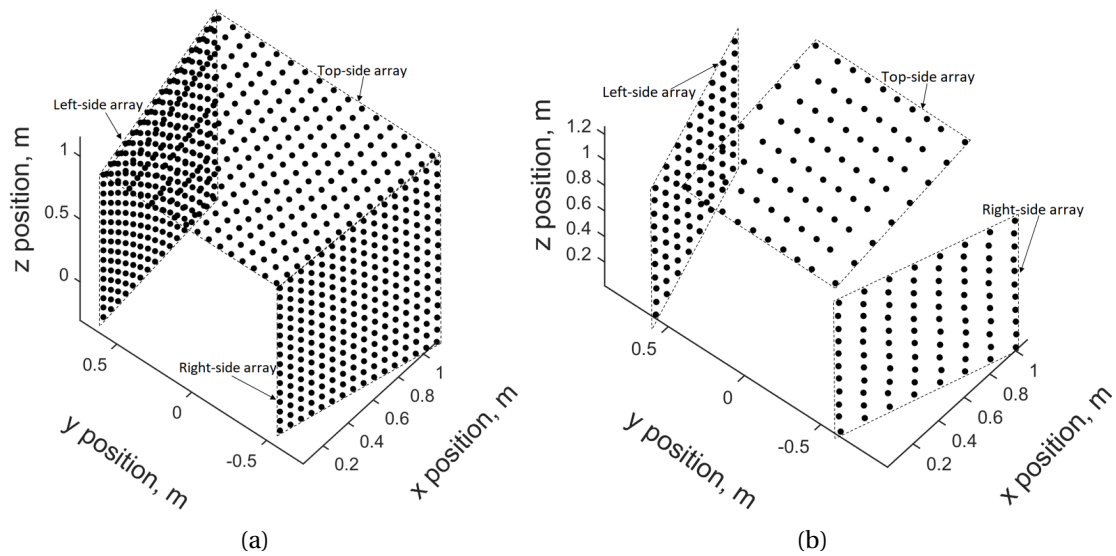


Figure 2.8: Arrangement of microphones (a) for a 3D array with 256 microphones; (b) for a 3D array with 768 microphones. The black points stand for the positions of the microphones.

2.5 Synthetic noise source in a 3/4 open test section

A synthetic noise source with a known position is used for the validation of the algorithms of beamforming. A metal pipe of diameter 30 mm is mounted on the bottom of the test section of the wind-tunnel. It allows a compression chamber to emit into the pipe with two different lengths. The free extremity of the pipe radiates a monopole source of broadband nature up to a frequency of 3.3 kHz. As shown in Figure 2.9, two positions of different heights are considered in the 3/4 open test section: (0.68 m, 0 m, 0.35 m) and (0.68 m, 0 m, 0 m). Experiments were conducted with and without flow. The 3D microphone array with 256 microphones is used for this test model.

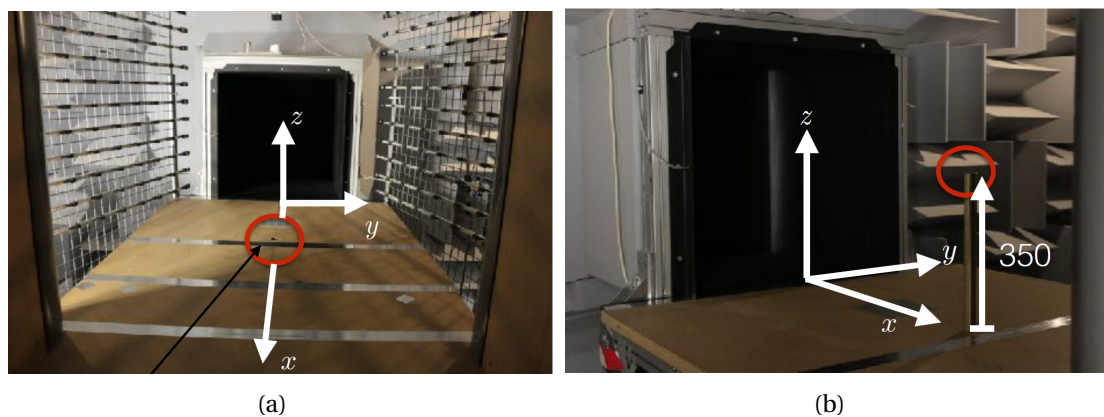


Figure 2.9: Photograph of a synthetic monopole noise source at a height of (a) 0m; (b) 0.35 m. The red circles indicate the position of the free extremity of the pipe in the two cases.

2.6 Experiments with a streamlined acoustic source

2.6.1 Source description

A synthetic noise source is emitted from a streamlined body designed to minimizing the flow perturbation and potential aeroacoustic noise emissions. The structure and the dimensions of a streamlined acoustic source is presented in the Appendix B.1. The front and aft parts of the streamlined body were made by plastic through 3D printing technique. A compression chamber was embedded inside the body. The propagation of the sound is guided by a conical tube inside the body, and the sound is radiated through a hole of diameter 5 mm in the downstream part of the object. The streamlined acoustic source is supported by a metallic cylinder with a diameter of 20 mm. The translation of the streamlined acoustic source in the x -direction and y -direction is conducted by a robotic system. Figure 2.10 shows the acoustic spectrum measured in the far field of the streamlined source. Due to the characteristics of the compression chamber, the emission level is sufficient for measurements for frequencies higher than 2 kHz. The frequency peaks in the spectrum are due to resonances of the tube connecting the compression chamber to the hole radiating the acoustic field.

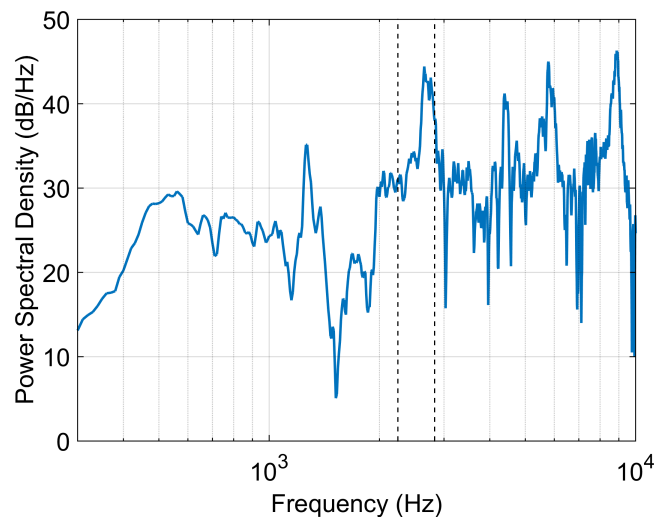


Figure 2.10: Far-field acoustic power spectral density for the broadband streamlined acoustic source. The frequency band between the dashed lines indicates the third-octave band [2245 Hz; 2828 Hz] studied in Chapter 10.

2.6.2 Experiment for studying source diffraction

The diffraction of the synthetic noise source by the solid boundaries of a NACA 0012 airfoil is performed for the identification of the source using the 3D TR technique and the 3D beam-forming technique. The source is placed beside a NACA 0012 airfoil with a span of 890 mm with its chord being 200 mm (Figure 2.11). The airfoil completely crosses the wind-tunnel test section. Its surface is smooth and without boundary layer tripping device. It is supported on a beam. The top of the airfoil is fixed by another beam extended from the nozzle. The leading edge of the airfoil is located at a distance of 310 mm from the outlet of the nozzle of the wind-tunnel. Experiments were conducted with and without flow, and the test-section

is fully open. The 3D microphone array with 768 microphones is used for this test model.

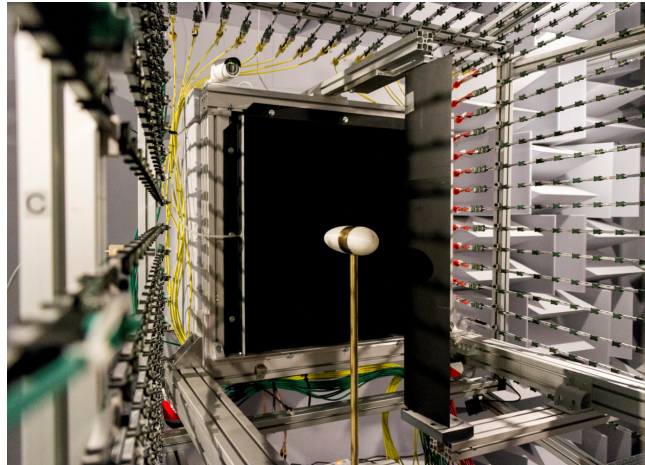


Figure 2.11: The streamlined acoustic source besides a NACA 0012 airfoil with a finite span in the open test section of the wind-tunnel.

2.6.3 Experiment for studying non-uniform flow effects

Acoustic measurements of the same synthetic noise source in a non-uniform flow are performed. The data is used to assess the robustness of the beamforming technique associated to ray-tracing methods for identifying sound sources in non-uniform flows. As shown in Figure 2.12, the non-uniform flow is generated by placing two vertical metallic beams with square cross sections in front of the nozzle of the wind-tunnel under test conditions. The cross section of the beam close to the left sub-array has a dimension of $40\text{ mm} \times 40\text{ mm}$ with its center position being $(20\text{ mm}, 120\text{ mm})$ in the XY plane. The cross section of the beam close to the right sub-array has a dimension of $50\text{ mm} \times 50\text{ mm}$ with its center position being $(25\text{ mm}, -120\text{ mm})$ in the XY plane. The position change of the streamlined acoustic source is achieved by the same robotic system as previously. The 3D microphone array with 768 microphones is used for this test model.

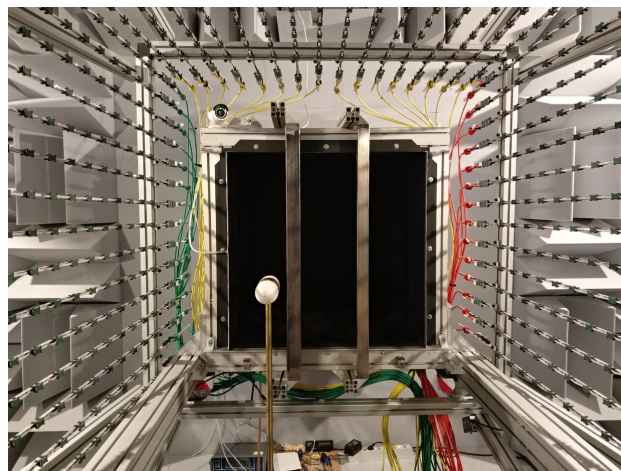


Figure 2.12: The streamlined acoustic source in the open test section of the wind-tunnel with two square cylinders being placed at the outlet of the nozzle.

Flow measurements for the non-uniform flow are performed using the hot wire technique. Figure 2.13 shows the velocity profiles in a horizontal plane in the open test section of the wind-tunnel with an incoming speed of 40 m/s. Each velocity profile corresponds to the measurements along a line in the y -direction. More exactly, 7 measurement lines in the y -direction with different distances (60, 100, 200, 300, 400, 550 and 750 mm) from the outlet of the nozzle are conducted. The wakes of the two cylinders are revealed by the decrease in the zones $[-150 \text{ mm}, -100 \text{ mm}]$ and $[80 \text{ mm}, 160 \text{ mm}]$ shown by the velocity profiles.

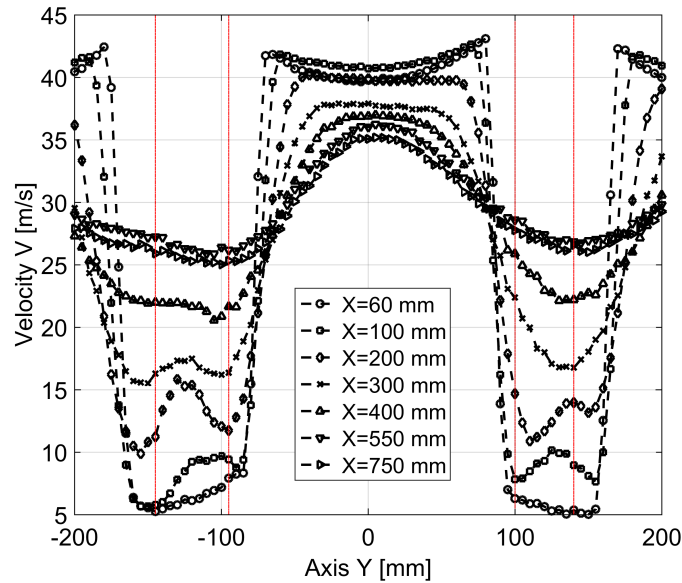


Figure 2.13: Velocity profiles along the y -direction at different distances from the nozzle of the wind-tunnel at an incoming speed of 40 m/s. The red dashed lines stand for the positions of the two cylinders in the y -direction.

2.7 Wall-mounted airfoil

Acoustic measurements of a wall-mounted NACA 0012 airfoil in the flow using the 3D microphone array with 256 microphones are conducted in this thesis. Two test configurations are considered, one is the airfoil alone, and the other is the airfoil associated to a perpendicular cylinder attached to the wing tip. The airfoil with a finite span of 505 mm is mounted on the bottom plate of the test section of the wind-tunnel. The chord length of the airfoil is 200 mm. The distance between the leading edge of the airfoil at angle of attack of 0° and the outlet of the nozzle is 350 mm. A boundary layer tripping device is added on the side of the airfoil closed to the right sub-array. It is a rough band (sandpaper) with a width of 15 mm placed at a distance of 15 mm from the leading edge along the span, which allows a forced transition of boundary layer on this side. The interest is to generate broadband and tonal noise using this configuration under different test conditions. In this thesis only broadband noise is considered. The airfoil is supported by a base, which allows to change its angle of attack. The rotation axis is located at a distance of one third of the chord from the leading edge. More details can be found in the paper Zhou *et al.* [128] in Chapter 5. For the other configuration, a cylinder with a circular cross section, perpendicular to the surface of the airfoil, is installed on the top of the wall-mounted airfoil (see Figure 2.14). The middle of the cylinder is fixed by

a screw on a position at a distance of 90 mm from the leading edge of the airfoil. The length of the cylinder is 400 mm. The diameter of the cylinder is 10 mm.

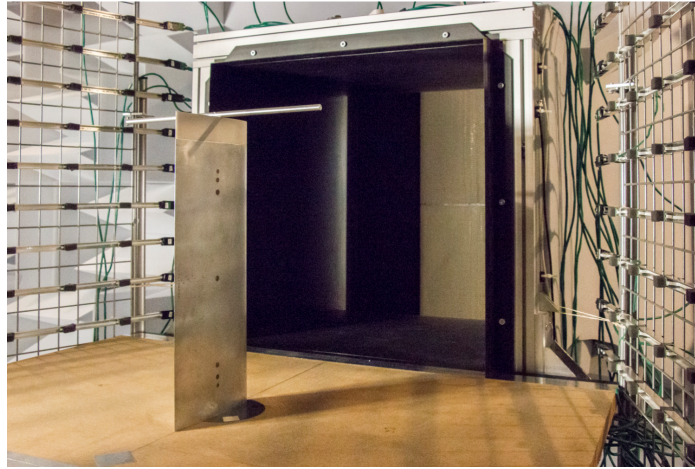


Figure 2.14: Wall-mounted airfoil with a perpendicular cylinder with circular cross section installed on its top.

2.8 Experimental device of a high-lift model

A high-lift model is investigated in terms of its aeroacoustic radiation in the wind-tunnel flow using the 3D array with 768 microphones. The cross section of the the model is the L1T2 configuration (Moir [84]), which is presented in Figure 2.15. It consists of three elements: a slat, a main element, and a flap. The slat is placed upstream of the main element with a deflection angle of $\delta_s = 25^\circ$. The flap is placed downstream of the main element with a deflection angle of $\delta_f = 20^\circ$ (see Figure 2.15). The chord length of the retracted configuration is 400 mm (see Appendix B.2). The Reynolds number for the high-lift model is based on this chord length. Additionally, the chord length of the deployed configuration shown in Figure 2.15 is $c_d = 520$ mm with the chord length of the main element being 345 mm. The angle of attack α of the high-lift model is defined as positive for the incoming flow shown in Figure 2.15.

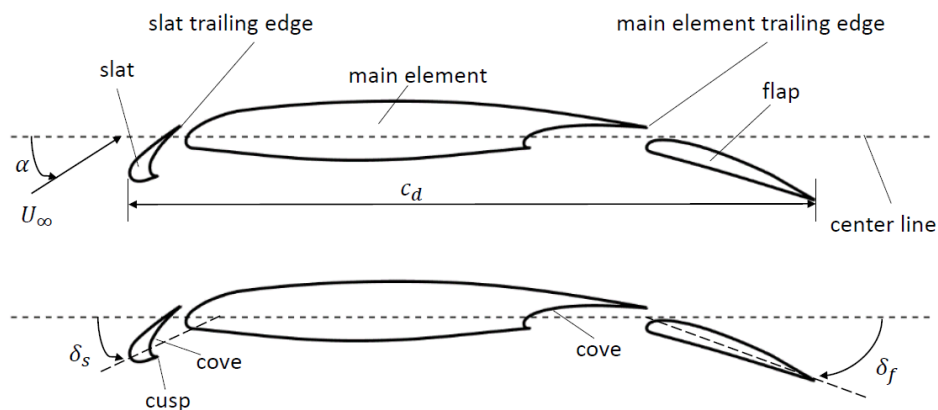
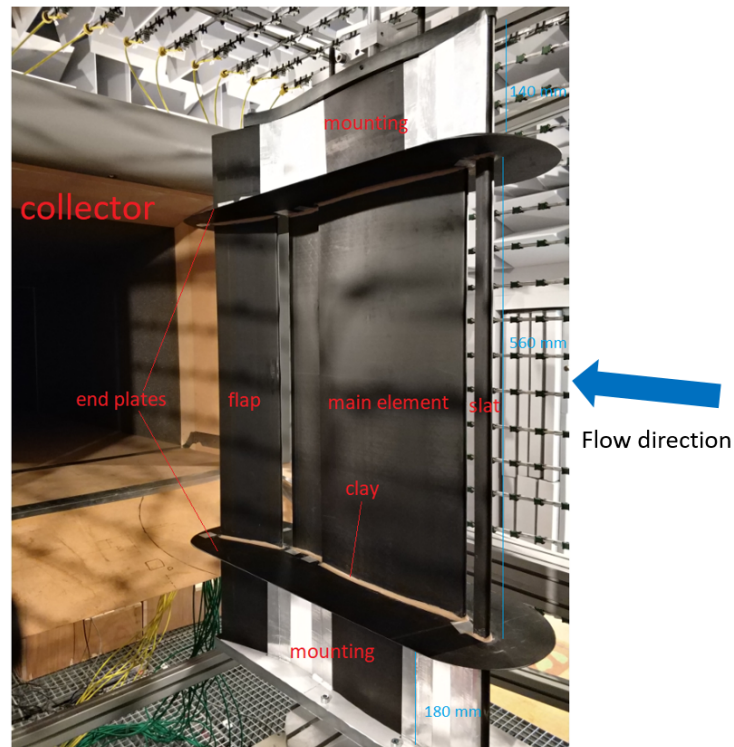
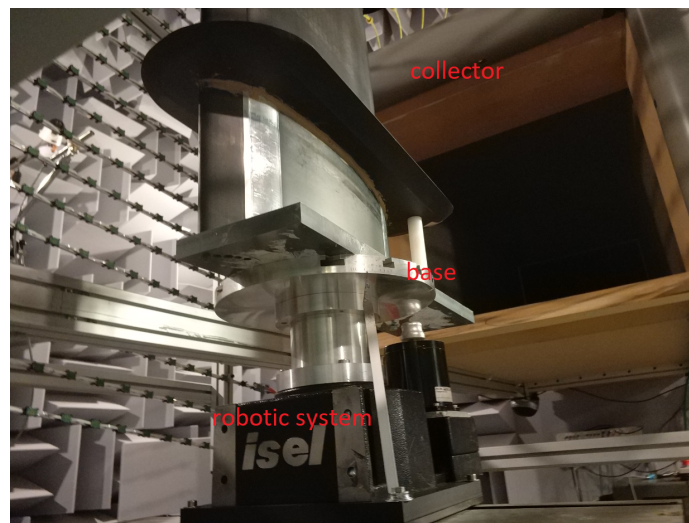


Figure 2.15: Cross section of a high-lift model (L1T2 configuration).

Similar to what was reported by Kröber [68], the high-lift model is isolated between two end plates, which allows to provide a quasi-2D configuration. The experimental device in the open test section of the wind-tunnel consists principally of three components: the high-lift model, the two end plates and the two mountings, which are shown in Figure 2.16(a). According to the velocity measurements of the shear layers of the wind-tunnel (Tran [117]), one can estimate that the high-lift model is located inside the jet core of the wind-tunnel flow, and that the two mountings are immersed partially in the shear layers developing from the nozzle of the wind-tunnel. Therefore, the end plates allow to isolate a quasi-2D flow condition for the high-lift model without the influence of the shear layers. The span length of the experimental device is 900 mm. The high-lift model has a span length of 560 mm. The span length of the two mountings are respectively 180 mm and 140 mm. The two end plates have a thickness of 10 mm. The forward and aft parts of the end plates are rounded. The spaces between the high-lift model and the end plates, which could generate spurious noise sources, are filled by a material similar to clay in order to avoid the leak of air flow. The model is mounted vertically on a base, which can be rotated by a robotic system (see Figure 2.16(b)). The distance between the leading edge of the main element of the high-lift model at angle of attack of $\alpha = 0^\circ$ and the outlet of the nozzle of the wind-tunnel is 350 mm. The rotation axis is located at a distance of 150 mm from the leading edge of the main element (see Appendix B.2). The surface of the high-lift model is smooth, without boundary layer tripping device. The maximum angle of attack of the high-lift model under investigation is $\alpha = 10^\circ$. The flow speed of the wind-tunnel testing is 30, 40 and 50 m/s with the corresponding Reynolds number based on the chord of the retracted configuration being respectively about 8×10^5 , 1.07×10^6 and 1.33×10^6 , for configurations with angle of attack of $\alpha = 0^\circ$ and $\alpha = 6^\circ$.



(a)



(b)

Figure 2.16: Photograph of (a) the experimental device containing the high-lift model installed in the open test section of the wind-tunnel; (b) the angle control device for the high lift device. The blue arrow indicates the direction of the flow.

2.9 Summary of the chapter

In this chapter, the experimental apparatus including the wind-tunnel facility, the hot-wire anemometry, the acoustic data acquisition system, the microphone arrays, synthetic noise sources, and some test models are presented. The test section of the wind-tunnel is fully open or 3/4 open. Two 3D microphone arrays have a tunnel shape, which allow to enclose

the test section. MEMS microphones are used for array measurements. The acoustic data acquisition system allows the acoustic measurements of 1024 digital channels and 16 analog channels. Two types of synthetic noise sources are used in this thesis. They are broadband noise emitting respectively from the end of a metal pipe and a streamlined acoustic source. They are placed in the test section of the wind-tunnel under different testing conditions. They are used to validate the algorithms of the signal processing methods (beamforming and TR) and evaluate their performance. Aeroacoustic noise are generated by wall-mounted airfoils and a high-lift model in flows. The hot-wire anemometry is used to measure the velocity profiles in the wake of a wall-mounted airfoil, and to characterize the flow field in the test-section of the wind-tunnel with non-uniform flows.

Chapter 3

CFD and acoustic solvers

Contents

3.1 CFD solver	46
3.1.1 RANS simulation	46
3.1.2 OpenFOAM	47
3.2 Acoustic solver	47
3.2.1 Linearized Euler Equations	48
3.2.2 Source term	49
3.2.3 Initial conditions	49
3.2.4 Boundary conditions	50
3.2.5 Implementation of the source term and boundary conditions	51
3.3 Validation of the acoustic solver	53
3.3.1 Scattering of an acoustic pulse off a cylinder	53
3.3.2 Scattering of a monopole off a cylinder	56
3.4 Summary of the chapter	58

As the TR process in this thesis needs to back-propagate numerically acoustic waves in a medium with/without a background mean flow, this Chapter is dedicated to a presentation of the numerical tools to implement the process. When using the TR technique for noise source localization in a flow, on the one hand, the mean flow information should be obtained; on the other hand, the flow direction should be reversed for the TR process. In this thesis, the flow is simulated. For simulations of mean flow around objects, the Reynolds-averaged Navier–Stokes equations (RANS), a turbulence model and an open source CFD software named OpenFOAM are presented in the first part. For sound wave propagation simulations, the governing equations, source terms, initial and boundary conditions of an in-house acoustic solver are addressed in the second part. Validations of the acoustic solvers based on two benchmark problems will be presented in the third part.

3.1 CFD solver

The TR technique for the identification of noise sources in a flow with the presence of solid boundaries of objects requires the mean flow information around the objects. There are two approaches to obtain such information, *i.e.*, experimental measurements and numerical simulations. In this thesis, the mean flow is simulated based on a RANS simulation using a turbulence model $k-\omega$ SST [78]. This is achieved by using an open source CFD solver named OpenFOAM.

3.1.1 RANS simulation

A complete presentation of turbulence modeling including RANS simulation is given in [121]. Its presentation in this section is based on this book.

The instantaneous velocity $u_i(\mathbf{x}, t)$ of a turbulence flow can be expressed as a mean velocity $U_i(\mathbf{x})$ and a fluctuating velocity $u'_i(\mathbf{x}, t)$, which is given by

$$u_i(\mathbf{x}, t) = U_i(\mathbf{x}) + u'_i(\mathbf{x}, t). \quad (3.1)$$

The mean velocity is defined by

$$U_i(\mathbf{x}) = \overline{u_i(\mathbf{x}, t)} = \lim_{T \rightarrow \infty} \frac{1}{T} \int_t^{t+T} u_i(\mathbf{x}, t) dt, \quad (3.2)$$

where T is a time much longer than the maximum period of the velocity fluctuation.

According to Wilcox [121], for an incompressible flow without the consideration of gravity, the time averaging of the equations for conservation of mass and momentum are given by

$$\frac{\partial U_i}{\partial x_i} = 0, \quad (3.3)$$

$$\frac{\partial U_i}{\partial t} + U_j \frac{\partial U_i}{\partial x_j} = -\frac{1}{\rho} \frac{\partial P}{\partial x_i} + \frac{1}{\rho} \frac{\partial}{\partial x_j} \left(2\mu S_{ji} - \overline{\rho u'_j u'_i} \right), \quad (3.4)$$

where μ is the dynamic viscosity, and the Reynolds-stress tensor τ_{ij} is defined as

$$\tau_{ij} = -\overline{\rho u'_i u'_j}, \quad (3.5)$$

and the strain-rate tensor S_{ij} is given by

$$S_{ij} = \frac{1}{2} \left(\frac{\partial U_i}{\partial x_j} + \frac{\partial U_j}{\partial x_i} \right). \quad (3.6)$$

Equation (3.4) is called the RANS equations. Note that the Reynolds-stress tensor is a symmetric tensor, so six unknown components are introduced by the RANS equations. For numerical simulations of 3D flows, the pressure and the three velocity components are four additional unknown components. There are only four equations for conservation of mass and momentum, so six additional equations are required in order to close the system. Modelling is used to close the system. It exists two-equation models like $k-\omega$ and $k-\epsilon$. A new model based on the two models was proposed by Menter [78]. It combines the $k-\omega$ model in the near wall region and the $k-\epsilon$ in the outer wake region and in free shear layers, and modifies the eddy viscosity in order to take into consideration the principle turbulent

shear stress. The author concluded that the $k - \omega$ SST model allows to accurately predict pressure-induced separation and should be the choice for aerodynamic applications.

3.1.2 OpenFOAM

OpenFOAM is an open source CFD solver. It allows the numerical simulations including RANS simulations, large eddy simulations and direct numerical simulations. It also provides a programming platform which allows users to develop new modules. OpenFOAM has its own mesh generators called blockMesh and snappyHexMesh. Mesh generator from the third part developer like cfMesh can be installed in OpenFOAM. Additionally, mesh generated by commercial software like StarCCM+ can be transformed into the format of OpenFOAM. In this thesis, blockMesh, SnappyHexMesh and cfMesh are used for mesh generation. Parallel computation can be conducted in clusters with OpenFOAM. It provides several types of solver for numerical simulation of flow dynamics at different regimes. The solver used in this thesis is called 'simpleFoam', which allows to simulate steady-state incompressible flows using RANS simulations. The finite volume method is used for RANS simulations. The implementation of the method in OpenFOAM is described in [89]. The visualization of the numerical results is usually conducted using an open software Paraview.

3.1.2.1 OpenFOAM files

To prepare a numerical simulation using OpenFOAM, three folders call '0', 'system', and 'constant' should be prepared. The folder '0' contains the files for the initial conditions for the numerical simulation. The folder 'system' contains at least three subdirectories: 'controlDict' specifying the running parameters such as start/end time, time step and parameters for data output; 'fvSchemes' specifying the numerical schemes; 'fvSolution' specifying the equation solvers, tolerances and other algorithm controls. The folder 'constant' contains three subdirectories: the 'polyMesh' containing all the mesh information, the 'transportProperties' containing the physical properties for the corresponding simulation case, and the 'turbulenceProperties' containing the choice of turbulence model.

3.1.2.2 Boundary conditions

The boundary conditions provided by OpenFOAM and used in this thesis are the ones below:

- `wall`: It fixes the velocity to zero at walls.
- `cyclic`: It implements a cyclic condition between two boundaries
- `symmetry`: It implements a symmetry constraint.
- `fixedValue`: It supplies a fixed value constraint.
- `zeroGradient`: It applies a zero-gradient condition from the patch of internal field onto the patch of boundaries.

3.2 Acoustic solver

The TR technique in this thesis back-propagates the recorded acoustic signals numerically, simulating acoustic wave propagation with the presence of solid boundaries and/or background mean flow in 2D or 3D simulation domains. To this end, an in-house acoustic solver

ParadigmS was developed by two researchers (Régis MARCHIANO and Manuel A. DIAZ) at Institut Jean le Rond d'Alembert. The solver is coded in C++ and allows the parallel computation using MPI in clusters. Based on a technical report of the acoustic solver provided by Manuel A. DIAZ, the governing equations, numerical methods (details in Appendix C), initial conditions, and boundary conditions of the acoustic solver for 3D applications will be presented in this section. The presentation of the acoustic solver for 2D applications can be found in Zhou *et al.* [126]. Some validations were conducted for the acoustic solver based on benchmark problems.

3.2.1 Linearized Euler Equations

The governing equations are obtained by linearizing the Euler equations around a known stationary mean flow. The simulation of acoustic wave propagation with the presence of the stationary mean flow can be conducted using the LEE by implementing some source terms in these equations [10]. The 3D LEE can be written as

$$\frac{\partial \mathbf{q}}{\partial t} + \frac{\partial \mathbf{E}}{\partial x} + \frac{\partial \mathbf{F}}{\partial y} + \frac{\partial \mathbf{G}}{\partial z} + \mathbf{H} = \mathbf{S} \quad \text{for } t \geq 0, \quad (3.7)$$

where $\mathbf{q} = [\rho_a, u_a, v_a, w_a, \varphi_a]^\top$ is the unknown vector with the density ρ_a , the velocity vector (u_a, v_a, w_a), and the pressure φ_a being small perturbations superimposed on the mean flow. \mathbf{E} , \mathbf{F} and \mathbf{G} are 3D flux vectors. The vector \mathbf{H} contains terms corresponding to the gradients of the mean flow. Its components are zero for uniform flows. If the mean flow becomes quiescent, Equation (3.7) can be simplified to conservative hyperbolic formulation of acoustic wave equations. The vector $\mathbf{S} : \mathbf{S}(\mathbf{x}, t)$ is the source term, which allows to introduce some unsteady sources in the mean flow. The flux vectors are given by

$$\mathbf{E} = \begin{bmatrix} \rho_a u_0 + \rho_0 u_a \\ u_0 u_a + \varphi_a \rho_0^{-1} \\ u_0 v_a \\ u_0 w_a \\ u_0 \varphi_a + \gamma \varphi_0 u_a \end{bmatrix}, \quad \mathbf{F} = \begin{bmatrix} \rho_a v_0 + \rho_0 v_a \\ v_0 u_a \\ v_0 v_a + \varphi_a \rho_0^{-1} \\ v_0 w_a \\ v_0 \varphi_a + \gamma \varphi_0 v_a \end{bmatrix}, \quad \mathbf{G} = \begin{bmatrix} \rho_a w_0 + \rho_0 w_a \\ w_0 u_a \\ w_0 v_a \\ w_0 w_a + \varphi_a \rho_0^{-1} \\ w_0 \varphi_a + \gamma \varphi_0 w_a \end{bmatrix}, \quad (3.8)$$

where γ is the ratio of specific heats with its value being 1.4 for air. The terms ρ_0 , (u_0, v_0, w_0) , and φ_0 denote respectively the density, the velocity vector, and the pressure of the mean flow. The vector \mathbf{H} in 2D cases was derived by Bogey *et al.* [10]. The vector \mathbf{H} in 3D cases is given by

$$\mathbf{H} = \begin{bmatrix} 0 \\ -u_a \left(\frac{\partial v_0}{\partial y} + \frac{\partial w_0}{\partial z} \right) + v_a \frac{\partial u_0}{\partial y} + w_a \frac{\partial u_0}{\partial z} + \left(\varphi_a \frac{\partial \rho_0}{\partial x} - \rho_a \frac{\partial \varphi_0}{\partial x} \right) \rho_0^{-2} \\ u_a \frac{\partial v_0}{\partial x} - v_a \left(\frac{\partial u_0}{\partial x} + \frac{\partial w_0}{\partial z} \right) + w_a \frac{\partial v_0}{\partial z} + \left(\varphi_a \frac{\partial \rho_0}{\partial y} - \rho_a \frac{\partial \varphi_0}{\partial y} \right) \rho_0^{-2} \\ u_a \frac{\partial w_0}{\partial x} + v_a \frac{\partial w_0}{\partial y} - w_a \left(\frac{\partial u_0}{\partial x} + \frac{\partial v_0}{\partial y} \right) + \left(\varphi_a \frac{\partial \rho_0}{\partial z} - \rho_a \frac{\partial \varphi_0}{\partial z} \right) \rho_0^{-2} \\ (\gamma - 1) \left(\varphi_a \left(\frac{\partial u_0}{\partial x} + \frac{\partial v_0}{\partial y} + \frac{\partial w_0}{\partial z} \right) - u_a \frac{\partial p_0}{\partial x} - v_a \frac{\partial p_0}{\partial y} - w_a \frac{\partial p_0}{\partial z} \right) \end{bmatrix}. \quad (3.9)$$

The LEE are solved by using the nodal Discontinuous Galerkin (NDG) method, for which the domain of interest is discretized and represented by a mesh composed of tetrahedral elements inside the domain. Moreover, additional nodes, the number of which depends on a polynomial order N , can be generated inside the tetrahedra in order to increase the precision of numerical simulations. More details are given in Appendix C.

3.2.2 Source term

In Equation (3.7), the components of the vector $\mathbf{S} = [m, f_x, f_y, f_z, e]^\top$ represent, respectively, the mass rate, the force in the x -, y -, and z - directions, and the energy rate introduced in the LEE. Following the idea of Bogey *et al.* [10], we use these terms to introduce acoustic perturbations (monopoles and dipoles) into the density, velocity and pressure fields of the mean flow.

For example, a single point-like harmonic monopole can be modeled by setting \mathbf{S} as

$$\mathbf{S}(\mathbf{r}, t)^{monopole} = \begin{bmatrix} m(\mathbf{r}, t) \\ f_x(\mathbf{r}, t) \\ f_y(\mathbf{r}, t) \\ f_z(\mathbf{r}, t) \\ e(\mathbf{r}, t) \end{bmatrix} = \begin{bmatrix} \mathcal{A}_m \sin(2\pi f t) \delta(\mathbf{r} - \mathbf{r}_0) \\ 0 \\ 0 \\ 0 \\ \mathcal{A}_e \sin(2\pi f t) \delta(\mathbf{r} - \mathbf{r}_0) \end{bmatrix}, \quad (3.10)$$

where $\delta(\mathbf{r})$ is the Dirac distribution in the 3D space. $\mathbf{r} = (x, y, z)$ is the coordinates of any point in the domain. $\mathbf{r}_0 = (x_0, y_0, z_0)$ is the location of the source. f is the source frequency. \mathcal{A}_m and \mathcal{A}_e denote respectively the amplitude of the monopoles. The relation between these amplitudes is $\mathcal{A}_e = c_0^2 \mathcal{A}_m$ with c_0 being the sound speed.

In addition, a single point-like harmonic dipole with its orientation in the x -direction can be modeled by setting \mathbf{S} as

$$\mathbf{S}(\mathbf{r}, t)^{dipole} = \begin{bmatrix} m(\mathbf{r}, t) \\ f_x(\mathbf{r}, t) \\ f_y(\mathbf{r}, t) \\ f_z(\mathbf{r}, t) \\ e(\mathbf{r}, t) \end{bmatrix} = \begin{bmatrix} 0 \\ \mathcal{A}_{f_x} \rho_0^{-1} \sin(2\pi f t) \delta(\mathbf{r} - \mathbf{r}_0) \\ 0 \\ 0 \\ 0 \end{bmatrix}, \quad (3.11)$$

where \mathcal{A}_{f_x} denotes the amplitude of the dipole. Similarly, the dipoles in the y - and z -directions can be modeled by using the components of f_y and f_z of \mathbf{S} .

3.2.3 Initial conditions

In this thesis, two types of initial conditions are mostly used for the acoustic solver. The first one is given by

$$\mathbf{q}(\mathbf{r}, t = 0) = \mathbf{0} \quad \text{for } \mathbf{r} \in \Omega, \quad (3.12)$$

where Ω represents the numerical simulation domain.

The second one is used to simulate an acoustic pulse at the position (x_0, y_0, z_0) with a spatial Gaussian distribution. Its expression is given by

$$\mathbf{q}(\mathbf{r}, t = 0) = \begin{bmatrix} \mathcal{A}_\rho \\ 0 \\ 0 \\ 0 \\ \mathcal{A}_\varphi \end{bmatrix} \exp\left(-\frac{(x-x_0)^2 + (y-y_0)^2 + (z-z_0)^2}{\sigma^2}\right) \quad \text{for } \mathbf{r} \in \Omega, \quad (3.13)$$

where \mathcal{A}_ρ and \mathcal{A}_φ are respectively the amplitude of the density and pressure components. The relation between these amplitudes is $\mathcal{A}_\varphi = c_0^2 \mathcal{A}_\rho$. The parameter σ is used to control the spatial size of the Gaussian distribution.

3.2.4 Boundary conditions

In addition to the initial condition, the boundary conditions are also required for solving the LEE. In this thesis, the boundary conditions *reflective-wall frontiers*, *outflow frontiers*, *pressure-driven frontiers* are considered, which allow respectively to simulate a solid boundary, a non-reflective boundary, and a pressure-driven boundary.

By ensuring that the flux operators are independent of the vector \mathbf{H} , one can impose any of the aforementioned boundary conditions at $\partial\Omega$ using an approximate Riemann solver. Figure 3.1 shows the sketch of a simulation domain Ω and its boundary $\partial\Omega$. The boundary can be divided into several partitions using different boundaries conditions. To apply boundaries conditions, some physical qualities are requested.

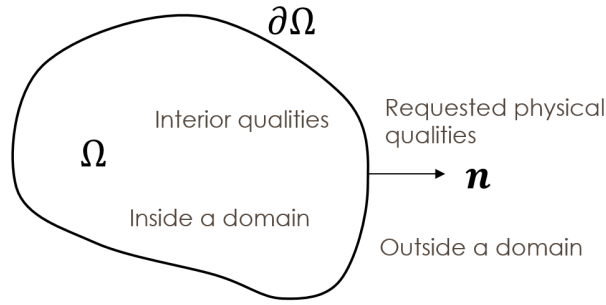


Figure 3.1: Sketch for a simulation domain with interior qualities inside the domain and requested physical qualities outside a domain. \mathbf{n} is a outward normal vector.

More exactly, using the characteristic information that originates from an eigenvalue analysis of flux terms of the LEE and the information concerning the state inside domain (in) and states (R) of a given boundary, a numerical approximation of the flux across the boundary $\partial\Omega$ is given by

$$\mathcal{H}^{\partial\Omega} = \mathcal{H}^{\partial\Omega}(\mathbf{q}^{in}, \mathbf{q}^R), \quad (3.14)$$

where $\mathcal{H}^{\partial\Omega}$ denotes numerical contributions of the fluxes across a boundary $\partial\Omega$ obtained with an approximate Riemann solver. The vectors \mathbf{q}^{in} and \mathbf{q}^R denote respectively the state inside the domain and the state of the boundary conditions we aim to impose. Then, imposing an *outflow frontier*¹ boundary condition is achieved by specifying the state of the boundary as

$$\mathbf{q}_{free}^R(\mathbf{x}, t) = \begin{bmatrix} \varrho_a^R \\ u_a^R \\ v_a^R \\ w_a^R \\ \wp_a^R \end{bmatrix} = \mathbf{0} \quad \text{for } \mathbf{x} \in \partial\Omega^{free}. \quad (3.15)$$

Similarly, a *reflective-wall frontier* boundary condition is given by

$$\mathbf{q}_{wall}^R(\mathbf{x}, t) = \begin{bmatrix} \varrho_a^R \\ u_a^R \\ v_a^R \\ w_a^R \\ \wp_a^R \end{bmatrix} = \begin{bmatrix} \varrho_a^{in} \\ 0 \\ 0 \\ 0 \\ \wp_a^{in} \end{bmatrix} \quad \text{for } \mathbf{x} \in \partial\Omega^{wall}, \quad (3.16)$$

¹Note that this boundary condition is good enough for initial testing. However, it can be improved by using absorbing regions, like *perfect matching layers*.

and a *pressure-driven frontier* boundary condition is given by

$$\mathbf{q}_{pressure}^R(\mathbf{x}, t) = \begin{bmatrix} \varrho_a^R \\ u_a^R \\ v_a^R \\ w_a^R \\ \varphi_a^R \end{bmatrix} = \begin{bmatrix} 0 \\ 0 \\ 0 \\ 0 \\ P_a(\mathbf{x}, t) \end{bmatrix} \quad \text{for } \mathbf{x} \in \partial\Omega^{pressure}, \quad (3.17)$$

where $P_a(\mathbf{x}, t)$ is the pressure signal to be impose at the position \mathbf{x} . Provided that \mathbf{q}^{in} is always known inside the domain, the flux across the boundary is approximated through Equation (3.14). When evaluating the boundary flux, the approximate Riemann solver automatically accounts for the eigenvalues (characteristic lines) of the LEE system and the problem is therefore always well-posed.

3.2.5 Implementation of the source term and boundary conditions

3.2.5.1 Discretization of the domain

To conduct numerical simulations using the acoustic solver, the domain of interest is discretized into a mesh containing volume mesh elements (Figure 3.2(a)) inside the 3D domain and surface mesh elements (Figure 3.2(b)) on the patches of the 3D domain. The mesh can be divided into several partitions (shown by different colors in Figure 3.2) in order to conduct the parallel computation, for which each partition is computed by one processor. The patches generally correspond to different geometry faces of the domain.

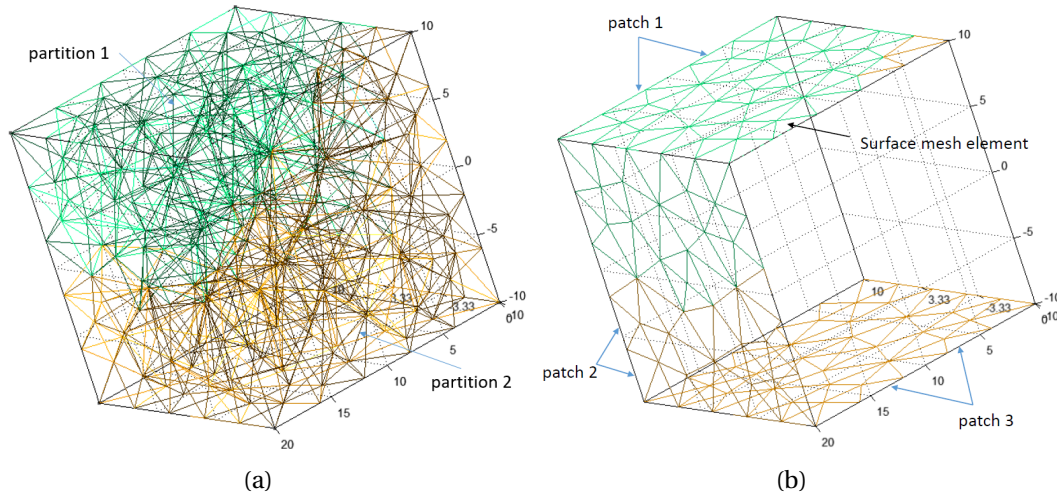


Figure 3.2: A 3D mesh with two partitions for a cubic domain: (a) volume mesh; (b) surface mesh.

3.2.5.2 Implementation of the source term

In section 3.2.2, the source term for the point-like monopoles and dipoles were presented. However it is difficult to deal with such types of sources related to the Dirac distribution for numerical simulation. To overcome this limit, ParadigmS provides two approaches: (i) an approximation of the Dirac distribution by the kernel of a Gaussian distribution; (ii) a *regularized Dirac distribution* based on an integration of the NDG Lagrangian base function of the element where the source is positioned. Both approaches will be briefly presented in the following subsections.

Approximation by a Gaussian distribution: When using the first approach to introduce a source (monopole or dipole) at the position $\mathbf{r}_0 = (x_0, y_0, z_0)$, the Dirac distribution is approximated by the kernel of a Gaussian distribution as

$$\delta(\mathbf{r} - \mathbf{r}_0) \simeq \exp\left(-\frac{(x - x_0)^2 + (y - y_0)^2 + (z - z_0)^2}{\sigma^2}\right), \quad (3.18)$$

where the parameter σ is used to control the spatial size of the Gaussian distribution. Note that this approach is often used in the literature.

Dirac distribution with the Lagrangian base function: When using the second approach to introduce a source (monopole or dipole) at the position $\mathbf{r}_0 = (x_0, y_0, z_0)$, the source term is now only evaluated at the k^{th} element that contains \mathbf{r}_0 . Here, the integration of the Dirac distribution of the source term using the Lagrangian base function of the k^{th} element \mathcal{T}^k is given by

$$\int_{\mathcal{T}^k} \delta(\mathbf{r} - \mathbf{r}_0) l_i^k d\mathbf{r} = J^k \int_{\mathcal{T}^R} \delta(\boldsymbol{\xi} - \boldsymbol{\xi}_0) l_i d\boldsymbol{\xi} = J^k l_i(\boldsymbol{\xi}_0), \quad (3.19)$$

where \mathcal{T}^R is the reference element and J^k is a Jacobian operator. The Lagrangian base function $l_i(\boldsymbol{\xi})$ is evaluated at $\boldsymbol{\xi}_0 = (\xi_0, \eta_0, \zeta_0)$ that corresponds to the position \mathbf{r}_0 of the point source in the reference element coordinates. Therefore, when requesting a regularized point source acting on point $\mathbf{x}_0 = (x_0, y_0, z_0)$, the Dirac distribution in ParadigmS is approximated as

$$\delta(\mathbf{r} - \mathbf{r}_0) \simeq \left(J^k\right)^{-1} l_i(\boldsymbol{\xi}_0). \quad (3.20)$$

Note that the solution at the source position is only a first-order approximation. However, the field generated by the source away from the source position is exact. Indeed, this is similar to the solution of the source term with Dirac distribution, which is preferred for modeling point sources.

3.2.5.3 Implementation of the boundary conditions

The acoustic solver ParadigmS uses the local Lax-Friedrichs method to approximate the flux across elements faces and/or between element faces and boundary faces, so the implementation of the boundary conditions presented in section 3.2.4 in the solver is straightforward. When conducting numerical simulations, ParadigmS reads a mesh file generated by the software GMSH including the information of the *physical-tags* associated to the patches of the discretized domain. If the *physical-tag* is

- “free”: ParadigmS implements a *outflow frontier* boundary condition based on Equation (3.15).
- “free_rec”: ParadigmS implements the same boundary condition as “free”, and records the physical qualities at every time step of the numerical simulation for each node of the patch.
- “wall”: ParadigmS implements a *reflective-wall frontier* boundary condition based on Equation (3.16).

For the *pressure-driven frontier* boundary condition based on Equation (3.17), two special variations are used in this thesis. These two types of boundary condition are used during the time-reversal process, which aims to back-propagate the signals recorded by microphones. If the *physical-tag* is

- “BCfile”: imposes a discrete pressure signal on each node of the patch.
- “BC_gauss_spot”: is used to introduce discrete pressure signals at isolated positions (not mandatory to be at the positions of the nodes). However, a spatial Gaussian distribution is associated to each discrete pressure signal.

Setting a boundary condition “BCfile” When using a “BCfile” boundary condition, the pressure signals $P(\mathbf{x}_i, t)$ should be constructed externally as P_i^n , which is a table containing discrete values, for every node $\mathbf{x}_i \in \partial\Omega^{imposed}$ and for every time step $0 \leq n \leq N_t$ of the numerical simulation. Once that they are read by ParadigmS before starting the numerical simulation, it should be ensured that the correct value is called and assigned at each node of the patch at every time-step. To speed-up this process, the table of signals for all the nodes is divided into smaller tables. Every table is used for one partition of the mesh so that it can be read and loaded in parallel using all MPI ranks available during the numerical simulation.

Setting a boundary condition “BC_gauss_spot” In real applications using experimental data, measured by a channels of microphones, for the TR process, the number of channels of the pressure signals can not be the same as that of the nodes of the patches of the mesh. As a result, it is not straightforward to implement the boundary condition “BC_gauss_spot” in order to back-propagate these signals into the domain Ω . Two approaches may be used: (i) using the nodes closest to the microphones to introduce the channels of signals; (ii) interpolating these signals to the closest nodes to the microphones. However, such strategies turned out to be numerically impractical.

To properly introduce the channels of signals at a set of isolated positions, a Gaussian distribution is used. Therefore, introducing these pressure signals is equivalent to impose

$$P(\mathbf{x}, t) = P(\mathbf{x}, n\Delta t) = P_j^n \exp\left(-\frac{(x-x_j)^2 + (y-y_j)^2 + (z-z_j)^2}{\sigma^2}\right) \quad \text{for } \mathbf{x} \in \partial\Omega^{prescribed}, \quad (3.21)$$

where $n = 1, \dots, N_t$, is the number of the time step of the numerical simulation. $j = 1, \dots, N_{micro}$ denotes the index of every channel of the pressure signals. The parameter P_j^n is the amplitude of the pressure signal at n^{th} time step for the j^{th} channel. The parameter σ is used to control the spatial size of the Gaussian distribution. This is the strategy for the implementation of a boundary condition “BC_gauss_spot”.

3.3 Validation of the acoustic solver

In this section, two benchmark problems will be considered for the validation of the acoustic solver in 2D cases. It concerns the scattering of an acoustic pulse and a harmonic monopole with a spatial Gaussian distribution off a cylinder. The numerical results will be compared to the analytical results.

3.3.1 Scattering of an acoustic pulse off a cylinder

The results in this section are taken from [126]. A benchmark problem concerning an acoustic scattering by a cylinder [116] in a quiescent medium is revisited using the acoustic solver. The analytical solution of the problem was provided by [115]. The interest of this case is

to check if the interaction between the sound wave and the boundaries is well solved by the acoustic solver. The domain of simulation is a square of dimensions $20\text{ m} \times 20\text{ m}$. The sound speed is 1 m/s . The density of the medium is 1 kg/m^3 . An acoustic pulse with a spatial Gaussian distribution is initially placed at the right side of the cylinder with a distance of 4 m from the center of the cylinder. The diameter of the cylinder is 1 m . Figure 3.3 shows the unstructured acoustic mesh for the numerical simulation, which is more refined for the mesh elements closer to the cylinder. The cylinder surface uses the "wall" boundary condition. The boundaries of the domain the "free" boundary condition. The mesh is decomposed into 80 partitions for the parallel computation, which are shown using different colors. A polynomial order of 3 is used for the nodal DG method. Three recording points are placed around the cylinder with a distance of 5 m from its center. Free boundary conditions were imposed at the boundaries of the domain for the simulation.

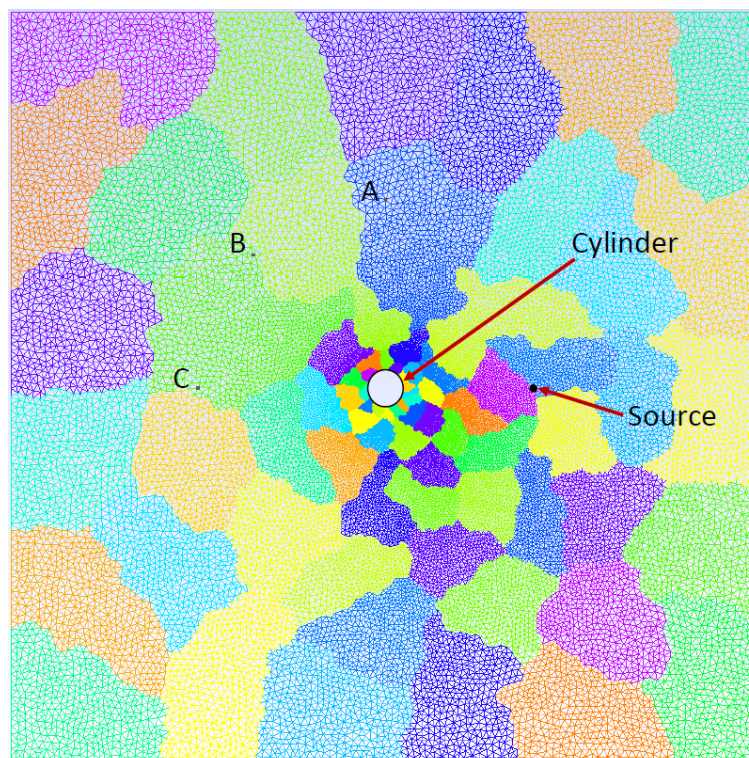


Figure 3.3: Unstructured mesh around a cylinder with 80 partitions shown by different colors.

Figure 3.4 shows a snapshot of the sound pressure field during the propagation of the acoustic pulse. Compared to the previously published numerical result [116] on the same test case, the propagation of the acoustic pulse is well simulated. Several wave fronts were observed. The wavefront shown by the large circle with high intensity in Figure 3.4 corresponds to the direct propagation. A part of the wavefront is reflected by the cylinder, which generates the wavefronts shown by the smaller circles with lower intensity. As the free boundary conditions are imposed, no significant reflection of the sound wave was observed at the right part of the domain.

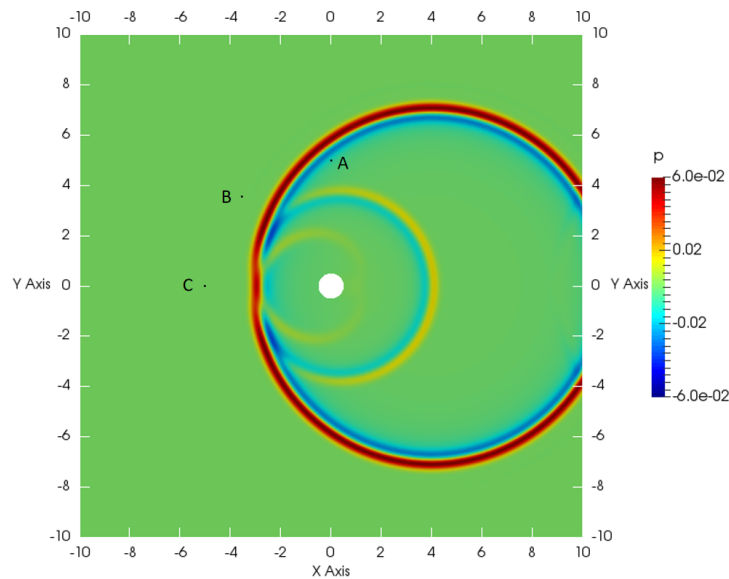


Figure 3.4: Snapshot of the sound pressure field for the scattering of an acoustic pulse off a cylinder.

Figure 3.5 shows the sound pressure signals recorded at the three points A, B and C by red lines. They are compared to analytical results which are indicated by black points. The numerical and analytical results superimpose well for the signals at the three points. Therefore, the acoustic solver is validated for the interaction between a sound wave and solid boundaries in a 2D case using parallel computation.

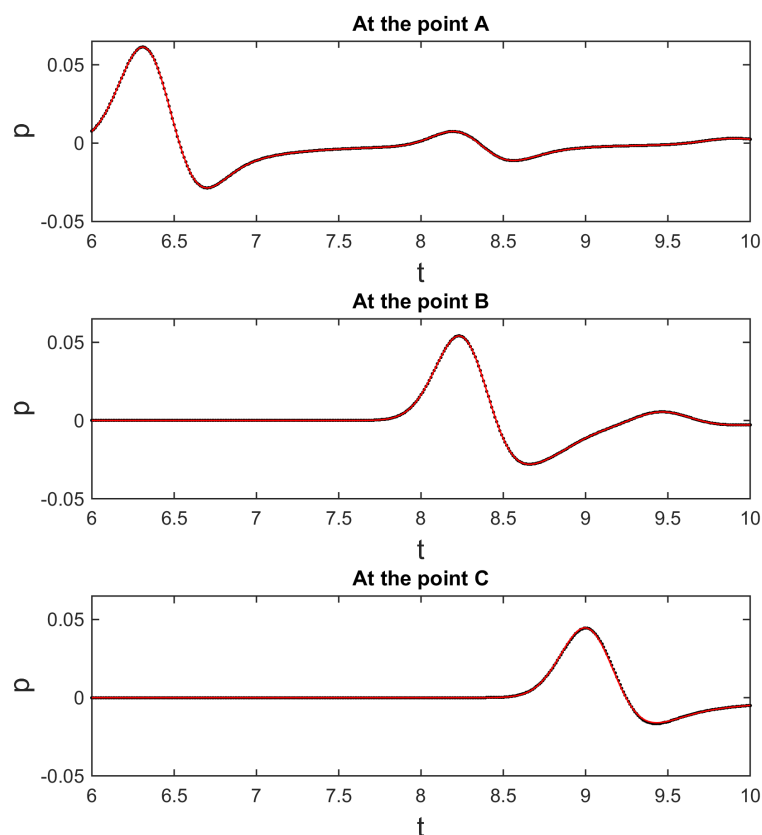


Figure 3.5: Comparison between the analytical and numerical results. Red lines stand for numerical simulations. Black points stand for analytical solutions.

3.3.2 Scattering of a monopole off a cylinder

Another benchmark problem concerning the scattering of a harmonic monopole of frequency 3 Hz source with a spatial Gaussian distribution [116] is revisited in order to validate the acoustic solver in a more general case. The monopolar noise source is located at the position (4, 0). The center of the cylinder with a diameter of 1 is located at the position (0, 0). The analytical solution is given by [116]. 91 evenly distributed recording points are located on an arc with radius 7 from 90° to 180° . The objective is to compute the values of $r\overline{p^2}$ at the recording points with $r = 7$. The sound speed is 1 m/s. The density of the medium is 1 kg/m^3 . Figure 3.6 shows the unstructured mesh for the acoustic solver. A polynomial order of 5 is used for the nodal DG method. The cylinder surface uses the "wall" boundary condition. The boundaries of the domain use the "free" boundary condition. 200 partitions were created for the parallel computation. The inner square domain containing fine mesh elements with a dimension of $60 \text{ m} \times 60 \text{ m}$. The outer square has a dimension of $80 \text{ m} \times 80 \text{ m}$. The physical time of the numerical simulation time is 35 s. The monopolar noise source was introduced smoothly during the numerical simulation by multiplying the source term with a terms $r(t)$ with $t_s = 10 \text{ s}$, which is given by

$$\begin{cases} r(t) = 3\left(\frac{t}{t_s}\right)^2 - 2\left(\frac{t}{t_s}\right)^3, & t < t_s; \\ 1, & t \geq t_s. \end{cases} \quad (3.22)$$

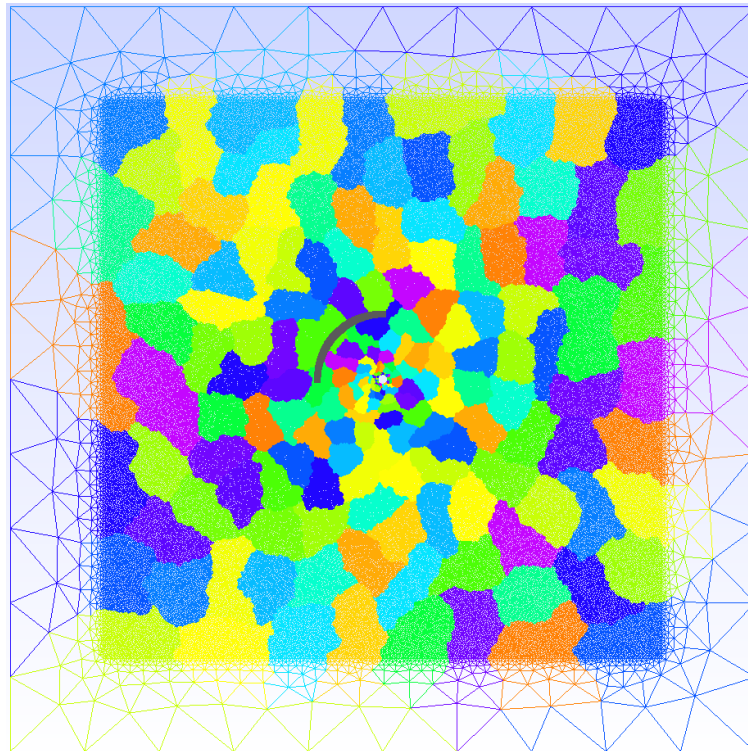


Figure 3.6: Unstructured mesh around a cylinder with 200 partitions shown by different colors. The arc indicates the position of the 91 recording points.

Figure 3.7 shows a snapshot of the pressure field at an instant when the wavefronts inside the simulation domain reaches a permanent regime. It was observed that wavefronts originating from the direct propagation of the monopolar noise source are altered by the

wavefronts reflected by the surface of the cylinder. In addition, the waves on the left side of the cylinder are relatively weak with respect to that of other areas.

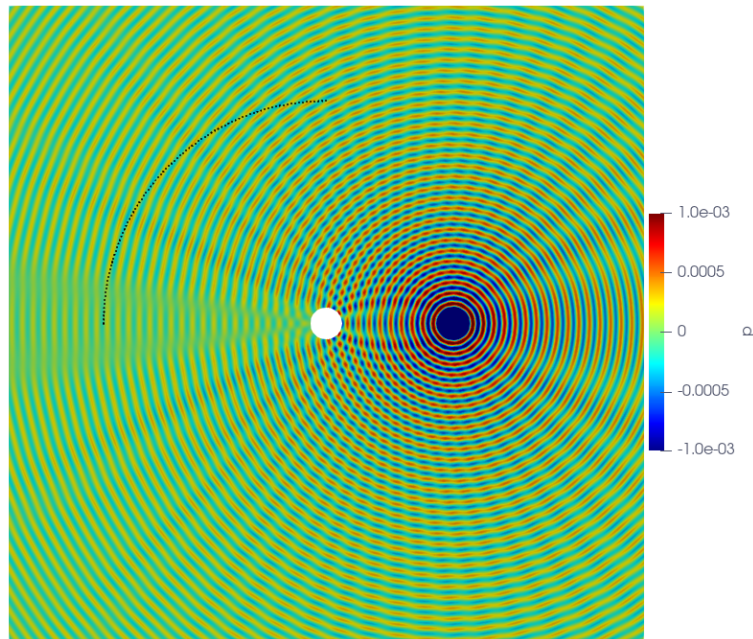


Figure 3.7: Snapshot of the sound pressure field for the scattering of a monopole off a cylinder. The arc indicates the position of the 91 recording points.

Figure 3.8 shows the values of $r \overline{p^2}$ at the 91 recording points. They are compared to analytical results which are indicated by circles. The numerical and analytical results superimpose well for the signals at the 91 points. Therefore, the acoustic solver is validated for the interaction between a sound wave and solid boundaries in a 2D case using parallel computation for a more general case.

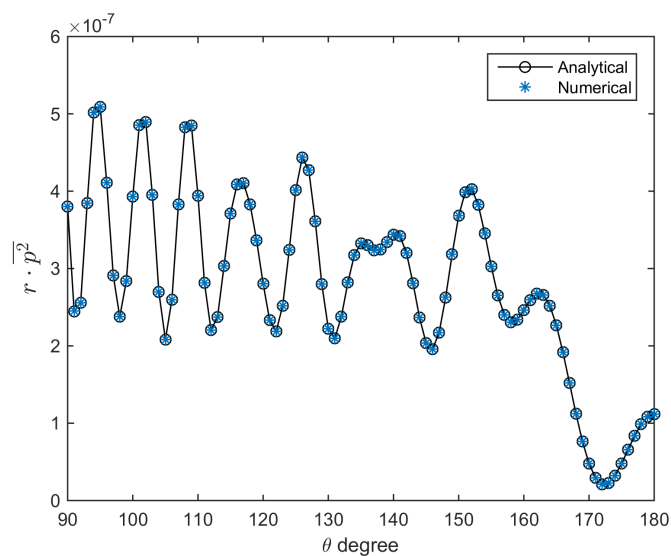


Figure 3.8: Comparison between the analytical and numerical results for the scattering of a monopole off a cylinder.

3.4 Summary of the chapter

This chapter has presented two solvers for numerical simulations in terms of mean flow around objects and acoustic wave propagation with the presence of solid boundaries and/or background mean flow in 2D or 3D simulation domains, for the reason that the TR technique back-propagate the recorded acoustic signals numerically, and the mean flow should be obtained and reversed for the TR process. For the CFD software OpenFOAM, the RANS equations and a turbulence model $k - \omega$ SST are first introduced. The files, solvers and boundary conditions of OpenFOAM used in this thesis are then presented. For the in-house acoustic solver, the governing equations, numerical methods (details in Appendix C), initial conditions, and boundary conditions for 3D applications are first presented. Then, the acoustic solver is validated in terms of the interaction between sound waves and solid boundaries using two benchmark problems.

Part I

Noise source identification in a wind tunnel based on the beamforming technique

Chapter 4

Beamforming technique

Contents

4.1 Time-domain beamforming	62
4.2 Frequency-domain beamforming	63
4.2.1 Processing techniques (conventional beamforming)	63
4.2.2 Deconvolution	64
4.3 Flow-effect correction	65
4.3.1 Assessment of the flow-effects	66
4.3.2 Ray-tracing methods	67
4.3.3 Assessment of Amiet’s method with non-uniform flow	68
4.4 Summary of the chapter	70

This chapter introduces the beamforming technique in both the time and frequency domains. In this thesis, this technique is used for the identification of aeroacoustic sources in the wind-tunnel with open test section. In this context, the flow effects on the noise source identification should be taken into account when using the beamforming technique. The flow-effects of the wind-tunnel on 3D beamforming results are then assessed, followed by the presentation of two ray-tracing methods for the flow-effect correction. Finally, the robustness of the Amiet’s method will be studied.

4.1 Time-domain beamforming

A complete introduction of the beamforming technique can be found, for example, in the references of Sijtsma [109], Koop [67], Oerlemans [91] and Allen *et al.* [4]. It can be applied to noise source identification in different regions. One is the Fraunhofer region where the wavefronts can be considered as planes, the other is the Fresnel region where the wavefront are spherical. In this study, the potential noise sources are close to the microphone array, so the beamforming in the Fresnel region is considered. This section is dedicated to a general presentation of this technique.

As reported by Leclère *et al.* [70], it exists several types of beamforming technique. In this thesis, the beamforming technique in the time domain is based on the process of *delay & sum* (Johnson and Dudgeon [64]; Allen *et al.* [4]), which is called conventional beamforming. Consider a monopole noise source in a quiescent medium, for which the far-field pressure signals are recorded by an array of M microphones. The pressure field radiation of a point monopole located at \mathbf{x}_0 in a homogeneous medium at rest can be computed by solving the following wave equation with a source term:

$$\left(\Delta - \frac{1}{c_0} \frac{\partial^2}{\partial t^2}\right) p(\mathbf{x}, t) = q(t) \delta(\mathbf{x} - \mathbf{x}_0), \quad (4.1)$$

with $q(t)$ being the signal of the monopole noise source, and c_0 being the sound speed. The solution of the equation in a 3D free domain is given by

$$p(\mathbf{x}, t) = \frac{q(t - \tau(\mathbf{x}, \mathbf{x}_0))}{4\pi \|\mathbf{x} - \mathbf{x}_0\|}, \quad (4.2)$$

with the time delay $\tau(\mathbf{x}, \mathbf{x}_0)$ from \mathbf{x}_0 to \mathbf{x} being $\|\mathbf{x} - \mathbf{x}_0\|/c_0$. Therefore, the recorded pressure signals of the m^{th} microphone located at the position \mathbf{x}_m of the array is

$$p(\mathbf{x}_m, t) = \frac{q(t - \tau(\mathbf{x}_m, \mathbf{x}_0))}{4\pi \|\mathbf{x}_m - \mathbf{x}_0\|}, \quad m = 1 \dots M. \quad (4.3)$$

As illustrated in Figure 4.1, the beamforming technique consists in summing the signals recorded by each microphone with a supposed time-delay $\tau_{ds}(\mathbf{x}_m, \mathbf{x}_f) = \|\mathbf{x}_m - \mathbf{x}_f\|/c_0$, which describes the propagation time between the microphone position \mathbf{x}_m and a point \mathbf{x}_f in a domain containing the monopole noise source.

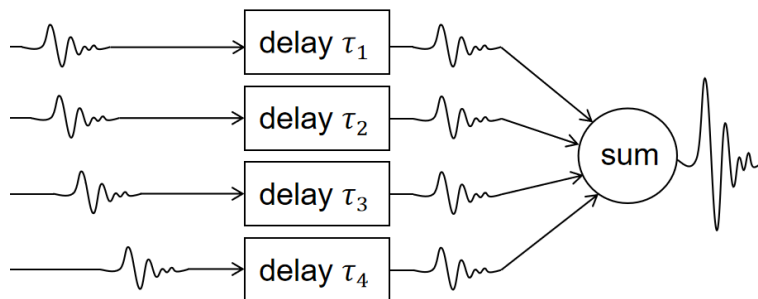


Figure 4.1: Sketch showing the principle of *delay & sum* beamforming, adapted from Johnson and Dudgeon [64].

In real applications, the domain could be a plane for 2D beamforming or a cubic volume for 3D beamforming. The domain is discretized as a scanning grid. Following this principle, the “beamformed signal” at each point \mathbf{x}_f of the grid is given by

$$z(\mathbf{x}_f, t) = (1/M) \sum_{m=1}^M w(\mathbf{x}_m, \mathbf{x}_f) p(\mathbf{x}_m, t + \tau_{ds}(\mathbf{x}_m, \mathbf{x}_f)), \quad (4.4)$$

with w the weighting function $w(\mathbf{x}_m, \mathbf{x}_f)$ compensating the geometrical attenuation of waves. If the measured field originates from a monopole, then Eq. (4.4) becomes

$$z(\mathbf{x}_f, t) = (1/M) \sum_{m=1}^M w(\mathbf{x}_m, \mathbf{x}_f) \frac{q(t - \tau(\mathbf{x}_m, \mathbf{x}_0) + \tau_{ds}(\mathbf{x}_m, \mathbf{x}_f))}{4\pi \|\mathbf{x}_m - \mathbf{x}_0\|}. \quad (4.5)$$

If the sound source is located at the point \mathbf{x}_f , the signals recorded by microphones after time shifting are in phase (no phase difference between them), which leads to a maximum ($z(\mathbf{x}_f, t) = q(t)$ if $\mathbf{x}_f = \mathbf{x}_0$). Otherwise, the sum will be lower than the maximum when out of phase (with phase difference between them). Hence, the idea is to compute $z(\mathbf{x}_f, t)$ for all the points \mathbf{x}_f in the scanning region, and detect the maximum of $|z|^2$. By repeating this process for all the points of the scanning grid, the sound map can be obtained by mapping the squared amplitudes of the sum to the corresponding scanning points.

4.2 Frequency-domain beamforming

4.2.1 Processing techniques (conventional beamforming)

In this thesis, the beamforming technique is conducted in the frequency domain. The Fourier transform of a signal $p(t)$ is defined as

$$P(\omega) = \int_{-\infty}^{\infty} p(t) \cdot e^{-j\omega t} dt. \quad (4.6)$$

Therefore, the Fourier transform of the term $p(\mathbf{x}_m, t + \tau_{ds}(\mathbf{x}_m, \mathbf{x}_f))$ in Eq. (4.5) is given by

$$\int_{-\infty}^{\infty} p(\mathbf{x}_m, t + \tau_{ds}(\mathbf{x}_m, \mathbf{x}_f)) \cdot e^{-j\omega t} dt = P(\mathbf{x}_m, \omega) \exp(j\omega \tau_{ds}(\mathbf{x}_m, \mathbf{x}_f)), \quad (4.7)$$

with $P(\mathbf{x}_m, \omega)$ being the Fourier transform of the $p(\mathbf{x}_m, t)$, and $\omega = 2\pi f$ being the angular frequency. We introduce the vector notation

$$\begin{cases} \mathbf{P} = (P(\mathbf{x}_1, \omega) \dots P(\mathbf{x}_M, \omega))^T, \\ \mathbf{e} = (e(\mathbf{x}_1, \mathbf{x}_f, \omega) \dots e(\mathbf{x}_M, \mathbf{x}_f, \omega))^T, \end{cases} \quad (4.8)$$

with the symbol T indicating the transpose operator. \mathbf{e} is called steering vector with $e(\mathbf{x}_m, \mathbf{x}_f, \omega) = \exp(-j\omega \|\mathbf{x}_m - \mathbf{x}_f\|/c_0)$, which supposes that the source is a radiating monopole. Then the “beamformed signal” in the frequency domain is given by

$$\begin{aligned} Z(\mathbf{x}_f, \omega) &= (1/M) \sum_{m=1}^M w(\mathbf{x}_m, \mathbf{x}_f) P(\mathbf{x}_m, \omega) e^*(\mathbf{x}_m, \mathbf{x}_f, \omega) \\ &= (1/M) (e^*(\mathbf{x}_1, \mathbf{x}_f, \omega) \dots e^*(\mathbf{x}_M, \mathbf{x}_f, \omega)) \mathbf{W} (P(\mathbf{x}_1, \omega) \dots P(\mathbf{x}_M, \omega))^T \\ &= (1/M) \mathbf{e}^H \mathbf{W} \mathbf{P}, \end{aligned} \quad (4.9)$$

with the symbol H being the Hermitian transpose operator, the symbol * being the complex conjugate operator, and the weighting of the microphones in the diagonal of matrix \mathbf{W} being

$$\mathbf{W} = \begin{bmatrix} w(\mathbf{x}_1, \mathbf{x}_f) & 0 & \cdots & 0 \\ \vdots & w(\mathbf{x}_2, \mathbf{x}_f) & & \vdots \\ \vdots & & \ddots & \vdots \\ 0 & \cdots & 0 & w(\mathbf{x}_M, \mathbf{x}_f) \end{bmatrix}. \quad (4.10)$$

Similarly, one can obtain the sound map in the frequency domain by mapping the square of the module of $Z(\mathbf{x}_f, \omega)$ to each scanning point of the domain. $Z(\mathbf{x}_f, \omega)$ is a complex number at the scanning point \mathbf{x}_f , so $Z^*(\mathbf{x}_f, \omega) = Z^H(\mathbf{x}_f, \omega)$. The square of its module $|Z(\mathbf{x}_f, \omega)|^2$ is then given by

$$\begin{aligned} |Z(\mathbf{x}_f, \omega)|^2 &= Z(\mathbf{x}_f, \omega)Z^*(\mathbf{x}_f, \omega) \\ &= Z(\mathbf{x}_f, \omega)Z^H(\mathbf{x}_f, \omega) \\ &= (1/M^2)e^H \mathbf{W} \mathbf{P} (e^H \mathbf{W} \mathbf{P})^H \\ &= \frac{e^H \mathbf{W} \mathbf{P} \mathbf{P}^H \mathbf{W} e}{\|e\|^4}, \end{aligned} \quad (4.11)$$

with the modulus of the steering vector based on a monopolar assumption being $\|e\| = \sqrt{M}$. The visualization of $|Z(\mathbf{x}_f, \omega)|^2$ gives what is usually called a sound map. The steering vector allows the algorithm to steer to a certain scanning point \mathbf{x}_f . For 2D beamforming, \mathbf{x}_f describes a plane to make a 2D sound map, while for 3D beamforming, \mathbf{x}_f describes a volume (in this thesis, a cubical domain). The reason for using the weighting matrix \mathbf{W} is twofold, *i.e.*, (i) accounting for the wave attenuation of the signals recorded by each microphone of the array; (ii) shading out some microphones using ($W_{mm}=0$) for processing beamforming algorithm. The cross spectral matrix (CSM) ($M \times M$) is computed using $\mathbf{C} = E(\mathbf{P}\mathbf{P}^H)$ with $C_{ij}(\omega) = C_{ji}^*(\omega)$, where $E(*)$ denotes an averaging process over time blocks using the Welch's method for the large number of sampling points. The diagonal elements of the CSM can be set to zero (trimmed version of the CSM) in order to improve the quality of the beamforming results (Allen *et al.* [4]).

In this thesis, \mathbf{W} is a identity matrix, which means that all the selected data channels are active for the signal processing of beamforming, and that the sound pressure levels of the sound maps correspond to average values via the *delay & sum* process without considering the geometrical attenuation of waves.

4.2.2 Deconvolution

As explained in Section 1.1.2.3, a deconvolution technique is required to improve the interpretability of sound maps. In this thesis, the CLEAN-SC method developed by Sijtsma [110] is used. The process of the implementation of the CLEAN-SC method contains some iterations. At iteration (i), the dominant noise source on the sound map (the "dirty map") is searched by finding the position $\xi_{max}^{(i)}$ of the peak value $P_{max}^{(i-1)}$ of the sound map of iteration ($i-1$). Then, together with its side lobes, they are removed from the "dirty map". Therefore, the source power $P_j^{(i)}$ at a scanning point ξ_j of the sound map at iteration (i) is given by

$$P_j^{(i)} = P_j^{(i-1)} - e_j^H \overline{\mathbf{G}}^{(i)} e_j, \quad (4.12)$$

where $\mathbf{G}^{(i)}$ is the CSM for computing the dominant noise source and its side lobes at iteration (i) , and \mathbf{e}_j is the steering vector associated to the scanning point ξ_j . $\overline{\mathbf{G}}^{(i)}$ is the trimmed version of $\mathbf{G}^{(i)}$.

According to Sijtsma [110], the matrix $\mathbf{G}^{(i)}$ can be obtained by introducing a vector $\mathbf{l}^{(i)}$:

$$\mathbf{G}^{(i)} = P_{max}^{(i-1)} \mathbf{l}^{(i)} \mathbf{l}^{(i)H}, \quad (4.13)$$

and $\mathbf{l}^{(i)}$ can be obtained by solving the following equation

$$\mathbf{l}^{(i)} = \frac{1}{\sqrt{1 + \mathbf{e}_{max}^{(i)H} \mathbf{L}^{(i)} \mathbf{e}_{max}^{(i)}}} \left(\frac{\overline{\mathbf{D}}^{(i-1)} \mathbf{e}_{max}^{(i)}}{P_{max}^{(i-1)} + \mathbf{L}^{(i)} \mathbf{e}_{max}^{(i)}} \right), \quad (4.14)$$

where $\mathbf{D}^{(i-1)}$ is the trimmed version of the CSM at iteration $(i-1)$, $\mathbf{e}_{max}^{(i)}$ is the steering vector associated to the scanning point at the peak location $\xi_{max}^{(i)}$ at iteration (i) , and $L_{mn}^{(i)}$ is given by

$$L_{mn}^{(i)} = \begin{cases} 0, & \text{if } m = n, \\ \mathbf{l}^{(i)} \mathbf{l}^{(i)H}, & \text{if } m \neq n. \end{cases} \quad (4.15)$$

Once the $\mathbf{l}^{(i)}$ is known, the dominant noise source and its side lobes at iteration i will be replaced by a clean beam $Q_j^{(i)}$, and the CSM of iteration $(i-1)$ i.e., $\mathbf{D}^{(i-1)}$ can be updated to $\mathbf{D}^{(i)}$. Then the trimmed version of $\mathbf{D}^{(i)}$ can be used to compute $P_j^{(i)}$ in order to obtain a new "dirty map". The corresponding equations are given by

$$\begin{cases} Q_j^{(i)} = P_{max}^{(i-1)} \Phi(\xi_j - \xi_{max}^{(i)}), \\ \mathbf{D}^{(i)} = \mathbf{D}^{(i-1)} - \varphi P_{max}^{(i-1)} \mathbf{l}^{(i)} \mathbf{l}^{(i)H}, \\ P_j^{(i)} = \mathbf{e}_j^H \overline{\mathbf{D}}^{(i)} \mathbf{e}_j, \end{cases} \quad (4.16)$$

where φ is called the safety factor. Φ is a normalized clean beam, and its width is defined empirically to optimize the readability of the sound map. It is a Gaussian beam used in this thesis. In a 3D domain, the expression of a Gaussian beam at the position (x_0, y_0, z_0) is given by

$$\Phi(x, y, z) = \exp\left(-\frac{(x-x_0)^2 + (y-y_0)^2 + (z-z_0)^2}{2\sigma^2}\right). \quad (4.17)$$

In this thesis, the safety factor is set to 0.99, and the clean beamwidth σ is set to 0.05 m.

4.3 Flow-effect correction

In this thesis, the acoustic measurements by microphone arrays are conducted in a wind tunnel with open or 3/4 open test section as presented in Chapter 2. Shear layers can develop from the nozzle of the wind-tunnel under testing conditions. The array microphones are placed *outside* the shear layers. Thus the propagation of the sound waves to the microphones is subjected to the convection and refraction effects caused by the wind-tunnel flow. If these effects are not considered for the signal processing of beamforming, it leads to an apparent shift of the noise sources downstream of their real position. The wind-tunnel flow can also affect the sound pressure level of sound maps, but it is not addressed in this thesis.

4.3.1 Assessment of the flow-effects

Such effects have been assessed experimentally by using two synthetic broadband monopole noise sources at different heights ($z = 0$ or 0.35 m) in the test section of the wind-tunnel (see the experimental apparatus in Section 2.5). $z = 0$ means that the monopole radiates from the closed boundary of the test section (Figure 2.9(a)) while for $z = 0.35$ the source is at the center of the test section (Figure 2.9(b)). The testing velocities are 0, 10, 20, 30, 40 and 50 m/s (the Mach number M ranged from 0 to about 0.15). The 3D sound maps are produced by using a monopole steering vector. A 3D scanning grid with a spatial resolution of 5 mm was set for the 3D beamforming. The position with maximum level of the 3D beamforming sound map was considered to be the estimated position of the monopolar source.

To investigate the effect of the Mach number M of the wind-tunnel flow on the apparent downstream shift Δx_{3D} of the 3D sound maps (established without flow corrections), the position errors need to be determined systematically. This was achieved by using 3D beamforming results at 3 kHz for the two positions of the monopolar noise sources, and at all testing velocities. The variations of the distance Δx_{3D} (normalized by the acoustic wavelength at 3 kHz) as a function of the Mach number are shown in Figure 4.2, for which a linear relation of $\Delta x_{3D} = h_{3D} \cdot M + x_0$ fitting the data based on the linear least-squares method can be obtained, with the values of y-intercept x_0 being negligible. As shown by Padois *et. al.* [93], for 2D beamforming applications in open wind tunnels, the apparent shift in the streamwise direction Δx is governed by a simple approximated law $\Delta x \simeq h \cdot M$, h being the flow thickness between the source and the shear layer of the wind-tunnel flow. In 3D beamforming applications, the regression coefficient h_{3D} is *a priori* difficult to determine, because the distance from the source to the shear layer varies according to the direction; however, the linear relationship between Δx_{3D} and M is clearly demonstrated by the results of Fig. 4.2. In addition, the shift Δx_{3D} to be corrected is higher when $z = 0$, which can be explained by the fact that a sound wave radiating from $z=0$ m undergoes more convection effects to reach the top-side array than a sound wave radiated from $z=0.35$ m. Finally, it is found that the flow-effect on the position of noise sources on sound maps is significant (of the order of the wavelength) and that it should be taken into account for noise source identification in the wind-tunnel flow using the 3D beamforming technique.

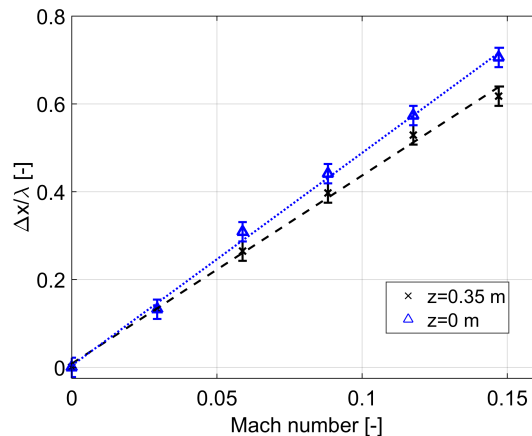


Figure 4.2: Variation of the distance Δx_{3D} (normalized by the acoustic wavelength λ at 3 kHz) as a function of the Mach number of the wind-tunnel flow for two monopole noise sources at positions (0.68 m, 0 m, 0.35 m) (symbol 'x') and (0.68 m, 0 m, 0 m) (symbol 'Δ'). The linear regression laws are respectively depicted by the dashed and the dotted lines.

4.3.2 Ray-tracing methods

Ray-tracing methods allow the modeling of the effects on wave propagation of the shear layers of the wind-tunnel flow. Two-ray tracing methods (Koop [67]; Amiet [5]; Bahr *et al.* [8]) were considered in this paper. These methods assume that the shear layers have zero-thickness, as shown in Figure 4.3. A noise source is supposed to be at position (x_0, y_0, z_0) , and a microphone is placed at position (x_m, y_m, z_m) . The position (x_s, y_s, z_s) is a point on the horizontal shear layer plane with z_s being constant. The flow is supposed uniform in the test section oriented along x -direction.

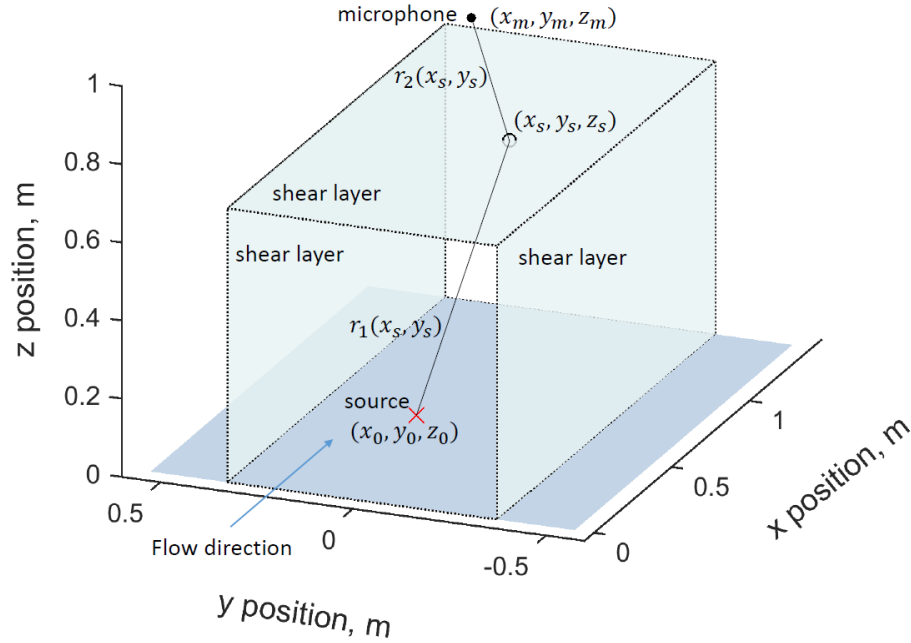


Figure 4.3: Sketch of the application of two ray-tracing methods for the flow-effect correction.

The position $(x_{s_min}, y_{s_min}, z_s)$ is the unknown point where the real ray path intersects the shear layer plane. If we apply the two methods to correct the wind-tunnel flow-effect associated with the horizontal shear layer plane with a constant height, we need to define the distances given by Equations (4.18), (4.19) and (4.20)

$$r(x_s, y_s) = \sqrt{(x_s - x_0)^2 + (1 - M^2)[(y_s - y_0)^2 + (z_s - z_0)^2]}, \quad (4.18)$$

$$r_1(x_s, y_s) = \sqrt{(x_s - x_0)^2 + (y_s - y_0)^2 + (z_s - z_0)^2}, \quad (4.19)$$

$$r_2(x_s, y_s) = \sqrt{(x_m - x_s)^2 + (y_m - y_s)^2 + (z_m - z_s)^2}. \quad (4.20)$$

The first ray-tracing method refers to Koop [67] using the Fermat's principle. By extending it to 3D cases, the total propagation time from the noise source to the microphone is

$$t(x_s, y_s) = \frac{-M(x_s - x_0) + r(x_s, y_s)}{c_0(1 - M^2)} + \frac{r_2(x_s, y_s)}{c_0}. \quad (4.21)$$

The position $(x_{s_min}, y_{s_min}, z_s)$ is obtained by searching the minimum value of t , and the real propagation time is $t(x_{s_min}, y_{s_min})$.

The second ray-tracing method is based on the Amiet's method (Amiet [5]; Bahr *et al.* [8]). By solving the system of Equation (4.22)

$$\begin{cases} \frac{x_s - x_0}{r(x_s, y_s)} - (1 - M^2) \frac{x_m - x_s}{r_2(x_s, y_s)} - M = 0; \\ \frac{y_s - y_0}{r(x_s, y_s)} - \frac{y_m - y_s}{r_2(x_s, y_s)} = 0. \end{cases} \quad (4.22)$$

the position $(x_{s_min}, y_{s_min}, z_s)$ can be found. Then the real propagation time is given by

$$t(x_{s_min}, y_{s_min}) = \frac{r_1(x_{s_min}, y_{s_min})}{c_1(x_{s_min}, y_{s_min})} + \frac{r_2(x_{s_min}, y_{s_min})}{c_0}, \quad (4.23)$$

with

$$c_1(x_s, y_s) = \frac{x_s M c_0}{r_1(x_s, y_s)} + \sqrt{\left(\frac{x_s M c_0}{r_1(x_s, y_s)}\right)^2 + c_0^2 - (M c_0)^2}. \quad (4.24)$$

A test was conducted in a 3D domain containing a set of scanning points surrounded by the shear layers shown in Figure 4.3 using the two ray-tracing methods. These methods are also extended to the two vertical shear layers (Figure 4.3). The 3D microphone array with 256 microphones presented in Chapter 2 is placed outside the shear layer. The propagation time from each scanning point to each microphone is computed using the methods presented above, for which the three shear layers are all considered. It is found that the maximum difference between the propagation times obtained by the two methods can be low to order 10^{-6} s for finding the position $(x_{s_min}, y_{s_min}, z_s)$, so that the two methods give the same result. However, the Koop's method is computationally expensive, so the Amiet's method is used for the flow-effect correction in this thesis.

4.3.3 Assessment of Amiet's method with non-uniform flow

Solid boundaries of objects in flow cannot be accounted for by the Amiet's method because it is based on the assumption of a uniform flow in the test section. However, the assumption of uniform flow is not satisfied for the application to the aeroacoustic radiation study of objects in flows because the wake of these objects generate mean flow gradients within the wind-tunnel flow. To assess the robustness of the Amiet's method for non-uniform flows, the identification of a synthetic noise source in a strongly non-uniform wind-tunnel flow, generated by placing two cylinders with square sections at the nozzle of the wind-tunnel, is carried out (see the apparatus in Section 2.6.3 and the mean flow profile in Figure 2.13). A 3D scanning grid with a spatial resolution of 10 mm is set for the 3D beamforming.

Figure 4.4 shows the 3D beamforming results without deconvolution, based a monopole steering vector, for the synthetic noise source at two positions (436 mm, 0 mm, 350 mm) and (436 mm, -120 mm, 350 mm) at incoming velocities of 0 and 40 m/s. The peak level position of the 3D sound maps is considered to be the identified source position. For the position (436 mm, 0 mm, 350 mm), the streamlined body is located in an area between the wakes of the cylinders. A dominant spot centered on the source position and two side lobes is observed in Figures 4.4(a) and 4.4(c). Taking the result of Figure 4.4(a) as the reference result (quiescent medium), the localization error due to the mean flow is the difference between the peak level position on the sound maps (10 mm). For the position (436 mm, -120 mm, 350 mm), the streamlined body is located in the wake of of the cylinder with larger cross section. The same observation is interpreted from Figures 4.4(b) and 4.4(d), and the difference between the peak level position is 14 mm, which is slightly higher than that of the previous case. As

such non-uniform effect on sound propagation is not modeled by the Amiet's method, these differences can be considered as the errors introduced by this simplification of the method. However, such errors are small with respect to the wavelength (120 mm) even in situations with severe mean flow gradients, indicating the remarkable robustness of the Amiet's in configurations departing significantly from uniform flows.

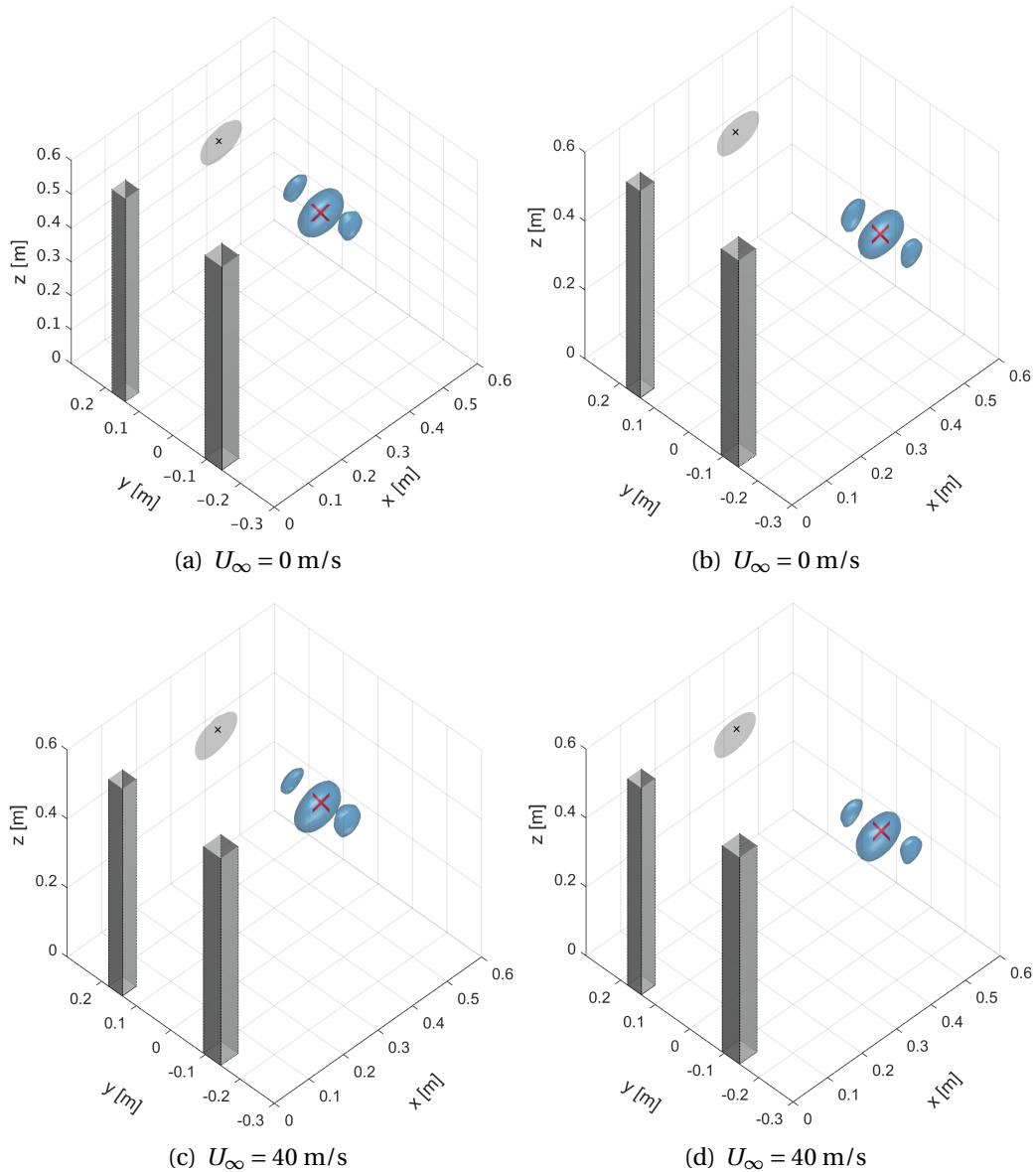


Figure 4.4: Sound maps for the synthetic noise source emitted by the streamlined body, at a third-octave band of nominal midband frequency 2.5 kHz. The noise source in a quiescent flow at position (a) (436 mm, 0 mm, 350 mm), (b) (436 mm, -120 mm, 350 mm). The noise source in a non-uniform flow with incoming speed $U_\infty = 40$ m/s at position (c) (436 mm, 0 mm, 350 mm), (d) (436 mm, -120 mm, 350 mm). The red symbols 'x' denote the position of synthetic monopole noise source. The grey patches stand for the cylinders. The shadows and the black symbols 'x' correspond respectively to the projection of the 3D sound source imaging and the noise source position in the y - direction. The 3D isosurface in each sound map is plotted at 6 dB below the maximum.

4.4 Summary of the chapter

The conventional beamforming technique and the deconvolution method CLEAN-SC is presented in this Chapter. The flow-effects (convection and refraction) of the wind-tunnel on 3D beamforming results are assessed, which shows that such effects can lead to significant localization errors on sound maps (of the order of the wavelength), and that they should be accounted for when using the 3D beamforming technique. To this end, two ray-tracing methods for the flow-effect correction are presented. It was found that the Amiet's method is more computationally efficient. It is found to be robust for testing cases with severe mean flow gradients within the jet core of the wind-tunnel flow, even though such non-uniform effect on sound propagation is not modeled.

Chapter 5

Experimental results of 3D beamforming

Contents

5.1 3D beamforming using a single orientation of dipole	71
5.2 3D beamforming using two orientations of dipole	92
5.2.1 Far-field spectrum results	92
5.2.2 3D beamforming results	93
5.3 Summary of the chapter	94

In this chapter, the 3D beamforming technique is used for the identification of aeroacoustic sources of wall-mounted airfoils. The first part deals with the cases of a wall-mounted airfoil and two parallel wall-mounted airfoils. The 3D beamforming results are based on a dipolar noise radiation model with a single orientation. The results were published in “Journal of Sound and Vibration”. The second part concerns the 3D beamforming results of a wall-mounted airfoil with a cylinder normal to its surface installed on the top of the airfoil. In this case, a dipolar noise radiation model with two orientations is implemented, which is achieved by dividing the scanning domain into two parts with each being applied with a different orientation.

5.1 3D beamforming using a single orientation of dipole

Contents lists available at [ScienceDirect](https://www.sciencedirect.com)

Journal of Sound and Vibration

journal homepage: www.elsevier.com/locate/jsvi

Three-dimensional identification of flow-induced noise sources with a tunnel-shaped array of MEMS microphones



Yinshi Zhou^a, Vincent Valeau^{a,*}, Jacques Marchal^b, François Ollivier^b, Régis Marchiano^b

^a Institut PPRIME UPR 3346, CNRS-Université de Poitiers-ENSMA, B17 - 6, rue Marcel Doré, 86022, Poitiers, Cedex, France

^b Sorbonne Université, CNRS, Institut Jean Le Rond d'Alembert, 4 Place Jussieu, 75005, Paris, France

ARTICLE INFO

Article history:

Received 19 August 2019

Revised 8 May 2020

Accepted 13 May 2020

Available online 20 May 2020

Handling Editor: J Cheer

Keywords:

3D beamforming

Aeroacoustics

MEMS microphone Array

Wind-tunnel

Airfoil

ABSTRACT

This paper deals with the development of a three-dimensional (3D) array for imaging aeroacoustic sources in the open section of an anechoic wind-tunnel, together with the associated signal processing techniques, and presents an application to the case of a wall-mounted airfoil in a flow. The 3D antenna is made of 256 digital Micro ElectroMechanical Systems (MEMS) microphones, arranged into three nearly perpendicular planar arrays enclosing the test section, the lower part of the flow being bounded by a rigid planar surface. The source under consideration is a wall-mounted NACA 0012 airfoil located in the wind-tunnel flow at a chord-based Reynolds number of 5.33×10^5 for angles of attack at 0° , 4° , 10° and 20° , generating several broadband sources of noise. A configuration with two wall-mounted airfoils in a flow using a similar large array system is also studied. The data processing is based on the beamforming technique associated to a deconvolution method (CLEAN-SC) developed in 3D and to a dipolar radiation model. The flow effects on propagation are taken into account in the beamforming technique by using the Amiet's method in terms of angle correction. The application to the airfoil demonstrates that the performances of the 3D source localization method are excellent for the wall-mounted airfoil, due to the high number of microphones and to the "tunnel" geometry allowing to surround the sources in the flow. The different sources of noise that are to be expected are accurately identified in the third-octave bands under investigation, and are in good agreement with experimental results published in the literature. The presented results prove that a tunnel-type array including several hundreds of microphones associated to an appropriate array processing technique performs very well for studying in 3D complex aeroacoustic sources, and that cheap MEMS microphones are good candidates for measuring the sound radiation efficiently.

© 2020 Elsevier Ltd. All rights reserved.

1. Introduction

The aeroacoustic noise resulting from the impingement of a flow on a rigid body is encountered widely in engineering domains, such as aeronautics, ground transport and wind turbines whereas it is not a positive effect and should be reduced. For example, noise nuisance is of main concern for the public facing nowadays the increasing aeronautical activities, and thus more and more stringent civil aircraft noise regulations have been proposed by the International Civil Aviation Organization (ICAO)

* Corresponding author.

E-mail address: vincent.valeau@univ-poitiers.fr (V. Valeau).

in Annex 16 to the Convention on International Civil Aviation [1]. To reduce noise emission, the noise source identification and the aeroacoustic optimization should be carried out during the conception phase of aircrafts, ground vehicles, wind turbines, etc. This is usually carried out in anechoic wind-tunnels by using scale models [2], albeit the vital achievements of computational aeroacoustics [3]. However, the identification of noise sources in terms of position, strength, directivity and generation mechanism still remains a challenging task because this kind of complex measurements rely highly on wind-tunnel facilities, microphone arrays (a set of arranged microphones, typically several tenths, with known spatial positions), flow measurement techniques and data processing strategies.

The standard experimental method widely used by research studies and industries for imaging noise sources is the beamforming technique with phased microphone arrays, which enables the directional scanning on an area consisting of a set of discretized grid points through an acoustic signal processing approach called *delay & sum* [4,5]. The beamforming results are plotted on this scan area, which generates what is usually called a sound map. Some of its applications, most of which were conducted with planar microphone array, planar scanning area and monopole noise source propagation model assumption, can be found in experimental investigations of the aeroacoustic sources of flight and ground vehicles [2,6–8]. Additionally, the beamforming technique can be associated with a deconvolution method such as DAMAS [9] and CLEAN-SC [10] in order to improve the spatial resolution of the sound maps.

Over the last ten years, this approach has been extended to the noise source identification in 3D areas for more efficient sound imaging. Some studies intended to perform 3D sound source imaging by using a monopolar noise source assumption and planar arrays, although the spatial resolution in the direction perpendicular to a planar array is known to be bad. Brooks and Humphreys [11] firstly demonstrated the feasibility of using planar microphone arrays with 3D beamforming and the DAMAS technique, with an application to the case of a flap in flow. It was found that a microphone array with a larger size provided a beam pattern more “focused” and less elongated. However, the computational cost of the DAMAS method in 3D applications is very high. Using the CLEAN-SC method, Sarradj [12] conducted 3D beamforming tests with a planar microphone array of 64 microphones for simulated noise sources with different depth. Although four different steering vectors were examined, none of them could provide both correct positions and strength of the noise sources. Geyer et al. [13] identified the noise sources on an airfoil located in the turbulent flow of an open jet wind-tunnel, using a planar array of 56 microphones. The sound maps calculated on a 3D scanning grid including the potential noise source area of nozzle exit and airfoil were obtained using the CLEAN-SC method. However, no correction of the noise source position due to the shear layer of the wind-tunnel flow was made, and the leading edge noise sources, located near the midspan of the airfoil, spread in the direction perpendicular to the airfoil.

Other studies focusing on 3D beamforming by developing non-planar arrays were also reported. Using four sub-arrays of 192 microphones mounted on the closed test section wall of a wind-tunnel, Padois et al. [14] identified the noise source generated by a cylinder in a flow without considering the dipolar nature of the aeolian tone [15]. It was found that the CLEAN-SC provided a better spatial resolution and less side lobes. Similarly, Dobler et al. [16] used a larger 3D microphone array of 576 microphones consisting of three sub-arrays for the noise source identification of a real car in a wind-tunnel. Although the sub-arrays were used to measure the acoustic data simultaneously, they were not considered as one unique array during the beamforming processing. The 3D sound maps were obtained by merging the beamforming results of each sub-array before using the CLEAN-SC method in a 3D scanning grid. Padois and Berry [17] examined the performance of four deconvolution methods including the DAMAS and CLEAN-SC methods for synthetic monopole noise sources in terms of accuracy of position and sound intensity, and their computational cost. This was accomplished by using a single or two perpendicular planar arrays for the beamforming processing in two-dimensional (2D) and 3D scanning zones. They found that the advantage of using the 3D array with the CLEAN-SC method are twofold, *i.e.*, (i) a significant performance improvement of beamforming processing in 3D scanning area; (ii) a good trade-off between less computation time and good accuracy of noise source identification.

However, the beamforming technique with monopole radiation assumption can not identify correctly sources of dipolar nature if their orientation is not nearly perpendicular to the planar array [18]. It then becomes necessary to implement another noise source model, especially for non-planar arrays, when identifying the flow-induced noise of complex geometries such as cylinders [15] or airfoils [19]. Hence, an approach where the dipolar noise source model was adapted for 3D beamforming algorithms, *i.e.*, conventional beamforming and multiplicative cross-spectral beamforming and the CLEAN-SC method was proposed by Porteous et al. [20], for which the beamforming performances were compared for the aeroacoustic noise sources identification of a cylinder and an airfoil using a non-planar microphone array of 62 microphones. Their simulations suggested that the conventional beamforming associated to the CLEAN-SC method is the most efficient method in spite of its computational cost. However, the two perpendicular sub-arrays only enclosed partially the noise source area. Due to this array geometry and the relatively weak number of microphones, the sound maps for experimental sources remained difficult to interpret, especially concerning a finite airfoil in a wind-tunnel flow.

Despite the advantage of the traditional microphone array systems, the high cost and the complexity of such devices limit evidently the implementation of large arrays of microphone. In recent years, some efforts based on using the cheap MEMS microphones were made. It involves the work of Arnold et al. [21], which demonstrated the cost reduction and the data processing efficiency of a modular directional acoustic array system based on 16 hybrid-packaged MEMS silicon piezoresistive microphones installed on a printed board. The system, comparable to conventional ones, provided a higher signal to noise ratio and a larger measuring frequency range than that of a single microphone. However, extensive calibration of the system in terms of directivity and accuracy was not conducted. Furthermore, Humphreys et al. [22] used a planar array of 128 MEMS microphones with comparable performance to the current generation of array for the aeroacoustic radiation study of a scaled landing gear. With the

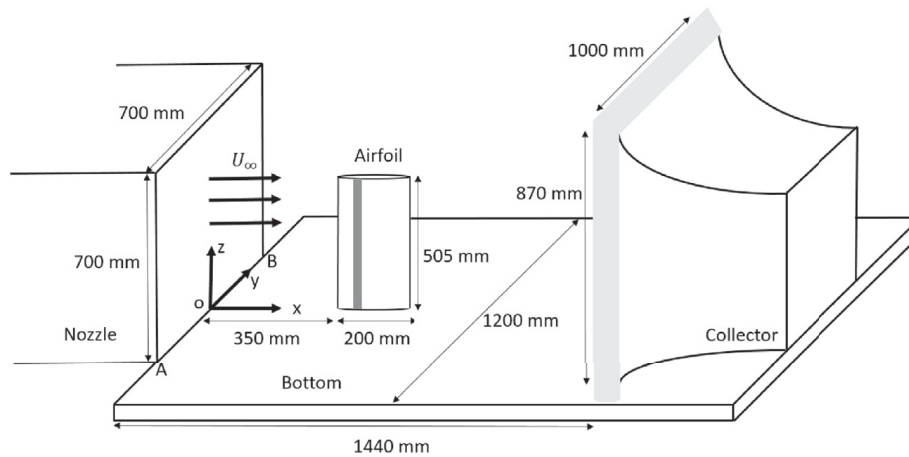


Fig. 1. Diagram of the test section of the anechoic wind-tunnel, with (from left to right): the nozzle, the wall-mounted airfoil, the collector. The dark band on the airfoil stands for the boundary layer tripping device.

design of a unique array mounting architecture to the closed test section of a wind-tunnel, the measurement system presented lower cost and complexity than the traditional directional array system.

To our knowledge, the use of the 3D beamforming technique associated to a microphone array with a very large number of microphones enclosing the wind-tunnel test section was not reported before. Therefore, the main objective of this paper is to demonstrate the effectiveness of such a massive 3D array of MEMS microphones for the identification of aeroacoustic sources in wind-tunnels. This is achieved by the identification of the noise sources of a wall-mounted airfoil yielding complex aeroacoustic noise radiation at different test conditions. The 3D beamforming results are compared with the published ones of experimental and numerical investigations. The organization of the papers is as follows. The experimental apparatus including the anechoic wind-tunnel, the test model and the microphone array are presented in Sec. II. The 3D beamforming method, the deconvolution technique CLEAN-SC and its application to simulated sources, and the modeling of the flow effects are highlighted in Sec. III. Finally, the results in terms of noise sources identification for one, and then two wall-mounted airfoils using the massive 3D array are presented in Sec. IV, followed by some concluding remarks.

2. Experimental set-up

2.1. Anechoic wind-tunnel and sound source configurations

The experiments presented in this paper were carried out in the anechoic wind-tunnel of the PPRIME Institute (Fig. 1). The flow is accelerated through a nozzle with a contraction ratio of 10, enters an anechoic room with a section outlet of (0.7×0.7) m², and is then sucked through a collector of dimensions (width \times height) (1.00×0.87) m². The streamwise length of the test section is 1.44 m, and the anechoic chamber has a volume of 90 m³ and a cutoff frequency of 200 Hz. The flow is bounded on its lower part by a plank of wood, and the dimension of the boundary layer is of the order of 10 mm at the nozzle exit. The maximum flow speed of the wind-tunnel is 60 m/s (216 km/h), and the turbulence intensity of the flow is about 1.5% at the nozzle exit. The coordinate system used for this study is represented in Fig. 1. The origin of the streamwise coordinate x is located at the nozzle exit, while the origin of the vertical coordinate z is located at the lower boundary of the flow.

In order to calibrate the microphone coordinates and to evaluate the flow effects on sound propagation, a well-controlled noise source is used. It is a compression chamber emitting into a metal pipe of diameter 30 mm with two different lengths, mounted on the bottom of the test section of the wind-tunnel. The free extremity of the pipe radiates a monopole source up to a frequency of 3.3 kHz. It allows to generate a monopole noise source of broadband nature at two positions of different heights in the test section: $(0.68 \text{ m}, 0 \text{ m}, 0.35 \text{ m})$ and $(0.68 \text{ m}, 0 \text{ m}, 0 \text{ m})$.

The test model generating the aeroacoustic source under study is a wall-mounted finite length NACA 0012 airfoil with a flat-ended tip and sharp trailing edge. It has a chord length $C = 200$ mm, a span length $L = 505$ mm and an aspect ratio $L/C = 2.525$. The airfoil model is mounted vertically to the bottom of the open test section, and the leading edge is located 350 mm downstream of the nozzle exit at zero-angle of attack. The NACA airfoil can be rotated around an axis located at 66.6 mm (a third of the chord length) from the leading edge; the angle of attack is then controlled by using a motorized rotating table, allowing a precision of 0.05° on the angle of attack. Special care has been taken to ensure a perfectly smooth surface of the airfoil. For all tests, the airfoil was tripped using a rough band (sandpaper) with a width of 15 mm placed at a distance of 15 mm from the leading edge along the span on one side of the airfoil surface, which allowed a forced transition of boundary layer to occur on this side and a natural transition of boundary layer to occur on the other side of the airfoil surface. The sign of the angle of attack of the finite wall-mounted airfoil is defined as positive when the tripping device is on the pressure side of the airfoil. In this paper, results are given for positive angles of attack at 0° , $+4^\circ$, $+10^\circ$ and $+20^\circ$, and a flow speed of 40 m/s, corresponding to

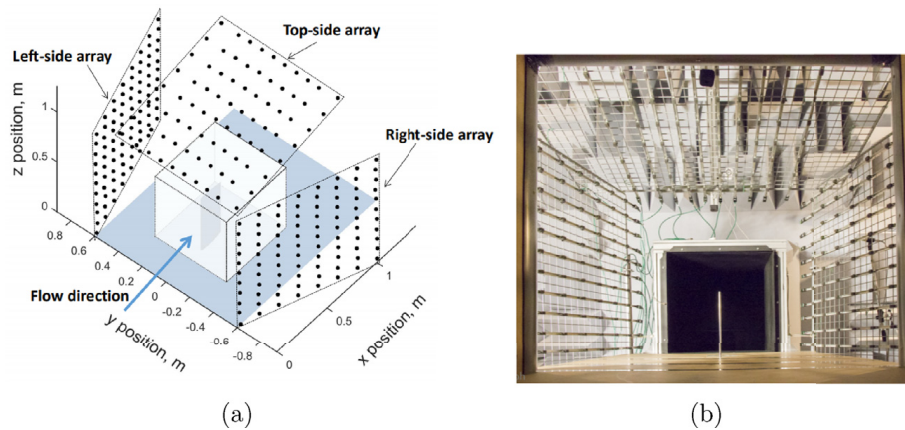


Fig. 2. (a) Schematic depicting the 3D microphone array and the wall-mounted airfoil. The black points indicate the positions of the microphones of the 3D microphone array. The cube with dashed edges enclosed by the 3D microphone array shows the 3D scanning grid for the beamforming calculation in a volume of dimension $0.6 \text{ m} \times 0.6 \text{ m} \times 0.6 \text{ m}$. (b) Picture of the experimental setup, taken from the collector of the wind-tunnel. The NACA airfoil and the collector appear at the center of the picture, and the three sub-arrays are on the top, left and right sides of the picture.

a chord-based Reynolds number of 5.33×10^5 . At these testing conditions, tonal noise generation is eliminated and broadband noise dominates the noise radiation, which is similar to formerly reported experimental results [23–25].

2.2. The MegaMicros system

The acoustic field is recorded by a 3D array of microphones. The development of a 3D antenna requires the use of a high number of microphones for the acoustic field to be correctly sampled and to lower spatial aliasing artifacts. Microphones dedicated to measurement are generally very reliable but they require a non versatile installation: power supply, analog/digital conversion module, many cables and in addition they are expensive. On the contrary, digital MEMS microphones embed their conditioning circuitry and analog to digital conversion stage. They require very low power supply and deliver noise free numerical signals. Consequently they provide great compactness and allow to build very versatile arrays. In addition, these microphones being used in mobile telephony are massively produced which leads to significantly low costs. As a counterpart, these microphones might be believed to provide poorer measurements. Nevertheless, Vanwynsberghe et al. [26] have shown that their characteristics are largely sufficient for acoustic imaging applications by using an antenna of 128 ADMP441 microphones developed by Analog Device. Indeed, these microphones are quasi-omnidirectional (1.7 dB maximum variation between -90° and $+90^\circ$). The standard deviation of their sensitivity is low (0.8 dB). The variations of the phase are acceptable because they remain lower than $\pi/20$ rad between 70 and 3000 Hz, and lower than 0.24 rad between 3000 and 10,000 Hz. Finally the frequency response is not flat but since it does not vary much from one element to the other, it is known and can be corrected *a posteriori*.

The array of microphones used in this study is similar to the system described in Ref. [26], but uses 256 MEMS microphones. It is not a commercial device, and was developed at the d'Alembert Institute. The microphones are grouped by beams of 8 microphones connected to a concentrator which makes it possible to synchronize all the signals and to transfer them to a PC via a USB serial bus (see description in Ref. [26]). The beams are connected to the concentrator by a RJ45 cable. Thus each beam can be deported over large areas. For this configuration, the RJ45 cables had a length of 10 m. The beams of microphones are arranged on rigid rectilinear bars on which they are spaced regularly (every 15 cm). This mechanical constraint involves that the microphones are arranged into parallel lines of 8 regularly spaced microphones, creating a regular array.

The 3D antenna is made of three flat panels: two vertical panels (left and right-side array on Fig. 2(a)) and one quasi-horizontal panel (top-side array on Fig. 2(a)). As shown in the picture of Fig. 2(b), the 3D array totally encloses the 3/4 open test section of the wind-tunnel. These panels are placed in such a way that they form a rectangular base cone of size (width \times height) about $1.2 \text{ m} \times 1.0 \text{ m}$ near the air inlet and $2.0 \text{ m} \times 1.2 \text{ m}$ near the outlet. The 32 beams are positioned horizontally in the direction of the flow, and each of them is fixed on one of the three panels (beams 0 to 10 on left-side array, beams 11 to 20 on the top-side and beams 21 to 31 on the right-side array). The gap between two neighbouring beams is 10 cm (except for beams 11–12 and 19–20 for which the gap is 15 cm). In this way, the acoustic field measured by the three panels is mostly meshed with rectangles of dimension 10 cm (streamwise direction) \times 15 cm (spanwise direction).

The measurement by hand of the 3D positions of 256 microphones is impractical for the array geometry used in this study. For this reason, the microphones coordinates are assessed by two methods. First we used the blind alignment method developed by Ono et al. [27]. Later on the microphone relative positions were verified using the robust method developed by Vanwynsberghe et al. [28]. More exactly, these methods provide the relative positions between the 256 microphones. To obtain the absolute positions of the microphones in the coordinate system associated with the wind-tunnel (Fig. 1), the calibration process should be completed by using a reference noise source with known position. By using the 3D beamforming results associated to a monopolar radiation assumption (the algorithm will be presented in Section 3.1), and applying it to the case of the artificial monopolar noise source at position (0.68 m, 0 m, 0.35 m) with no flow, the estimated position was compared to the actual

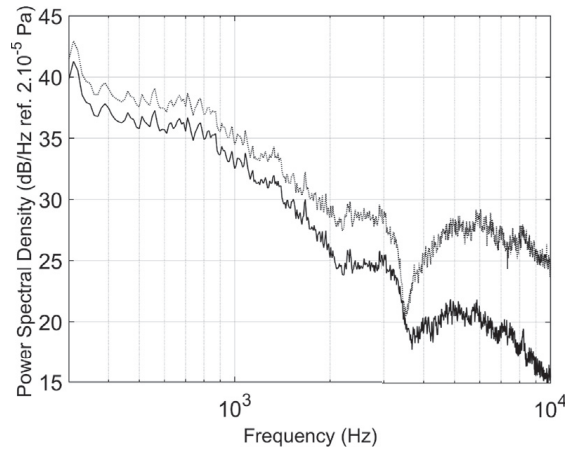


Fig. 3. Comparison of the far-field acoustic power spectral density for the wall-mounted finite airfoil at velocity $U = 40$ m/s for angle of attack $\alpha = 10^\circ$ using a MEMS microphone (dotted line) and a GRAS microphone (plain line).

position of the source. The absolute coordinates of the 256 microphones were then obtained by subtracting to their coordinates the position errors in x , y and z -directions.

Fig. 3 shows the far-field spectra of the wall-mounted airfoil measured by a MEMS microphone and a measurement microphone (type GRAS 40F mounted with a Preamplifier 26AK) with a flat frequency response up to frequency 10 kHz, at the same location. The spectrum of the GRAS microphone is taken as a reference result. The considered case is the noise radiated by the airfoil at angle of attack 10° and flow speed 40 m/s. As expected, the noise radiated by the airfoil is of broadband nature, with no tonal components. The energy content decreases with frequency, with a sudden drop around frequency 3.5 kHz that could be attributed to a wind-tunnel effect. A similar spectral behaviour was observed by Moreau et al. for a wall-mounted NACA 0012 airfoil at 35 m/s [19].

Some differences are observed in terms of spectra between the reference and the MEMS microphone, especially at high frequencies. It indicates a trend of the MEMS microphones to overestimate the noise level, from around 1 dB at 300 Hz, increasing up to around 5 dB at 3 kHz. The overestimation drops down around 3.5 kHz, and increases again up to 8–10 dB for frequencies higher than 5 kHz. Such differences were already reported in Ref. [26], based on a sample of 128 microphones. With a high number of microphones, it is not possible to perform an individual amplitude calibration for each microphone. However, it is possible to perform some frequency equalization with the mean frequency response of the MEMS microphones. In this study, such a frequency equalization was carried out, using the frequency variation of the average sensitivity obtained from the test of a set of microphones (model ADMP441) by Vanwynsberghe et al. [26]. This will allow the levels in dB ref. 2.10^{-5} Pa, that are given in different octave bands, to be compared to each other.

3. Array processing technique

3.1. Three-dimensional beamforming

Processing techniques. The beamforming method used in this study is based on the *delay & sum* process. Consider an array of M microphones (described by their position \mathbf{x}_m , with $1 \leq m \leq M$) located in the pressure far-field generated by noise sources. A scanning domain, that is a plane (generally parallel to a planar array) for 2D beamforming or a volume for 3D beamforming, is chosen to enclose the potential noise sources. During the beamforming process, it is discretized and represented by a scanning grid (described by the position \mathbf{x}_f). For each point \mathbf{x}_f , the “beamformed signal” in the frequency domain is given by the following equation:

$$Z(\mathbf{x}_f, \omega) = 1/M \sum_{m=1}^M P(\mathbf{x}_m, \omega) e^*(\mathbf{x}_m, \mathbf{x}_f, \omega), \quad (1)$$

where $\omega = 2\pi f$ is the angular frequency, $P(\mathbf{x}_m, \omega)$ the Fourier transform of the far-field pressure signals recorded by the m th microphone, the symbol $*$ the complex conjugate operator, and $e(\mathbf{x}_m, \mathbf{x}_f, \omega)$ the steering function. This steering function describes the propagation between \mathbf{x}_m and \mathbf{x}_f , and is dependent on the assumption that is made on the source radiation: most generally, a monopolar radiation is considered.

Using the vector notation $\mathbf{P} = (P(\mathbf{x}_1, \omega) \dots P(\mathbf{x}_M, \omega))^T$ and $\mathbf{e} = (e(\mathbf{x}_1, \mathbf{x}_f, \omega) \dots e(\mathbf{x}_M, \mathbf{x}_f, \omega))^T$ with the symbol T indicating the transpose operator, the frequency-domain beamforming function at each scanning point \mathbf{x}_f is given by:

$$A(\mathbf{x}_f, \omega) = Z(\mathbf{x}_f, \omega) Z(\mathbf{x}_f, \omega)^H = \frac{\mathbf{e}^H \mathbf{C} \mathbf{e}}{\|\mathbf{e}\|^4}, \quad (2)$$

where the Cross Spectral Matrix (CSM) of size $(M \times M)$ is defined as $\mathbf{C} = \mathbf{P}\mathbf{P}^H$, H being the Hermitian transpose operator. The CSM is a Hermitian matrix ($C_{ij}(\omega) = C_{ji}^*(\omega)$).

The steering vector \mathbf{e} enables the microphone array to “steer” to different scanning points \mathbf{x}_f . Most generally, a monopolar assumption is used, and the elements e of the corresponding steering vector can be written:

$$e(\mathbf{x}_m, \mathbf{x}_f, \omega) = \exp(-j\omega r_m/c_0), \quad (3)$$

where $r_m = |\mathbf{x}_m - \mathbf{x}_f|$ and c_0 is the speed of sound. In this case, the term $\|\mathbf{e}\|^4$ is equal to M^2 . In the case of a quiescent medium, the time delay $\tau(\mathbf{x}_m, \mathbf{x}_f)$ can be simply given by r_m/c_0 . When the influence of flow on propagation is significant such as in a wind-tunnel, methods based on ray tracing [29,30] could be used to calculate the steering vector. The way that the flow effect on propagation is taken into account in this study is presented in Section 3.3.

For 3D beamforming, the monopolar noise source assumption is usually not appropriate, because aeroacoustic noise sources induced by the interaction of a solid body tend to have a radiation that can be approximated by a dipolar radiation [31]. The steering function for a point dipole source in the beamforming technique can be written by introducing a correction term to the monopolar steering vector of Eq. (3) according to Ref. [20]:

$$e_d(\mathbf{x}_m, \mathbf{x}_f, \omega) = e(\mathbf{x}_m, \mathbf{x}_f, \omega) \left(\xi \cdot \frac{\mathbf{x}_m - \mathbf{x}_f}{r_m} \right), \quad (4)$$

where ξ is the orientation of the dipole source. The advantage of using such a steering vector is that the frequency-domain beamforming function exhibits a maximum at the source location for a dipolar source, so that the sound maps can be readily interpreted. However, Eq. (4) shows that an assumption on the dipole orientation ξ is required. In the present case, the wall-mounted airfoil has a symmetric section of NACA 0012 profile, for which the orientation of the dipole is known to be perpendicular to the airfoil surface.

The matrix \mathbf{A} calculated for a given frequency is a $(N \times N)$ matrix in 2D domain, or a $(N \times N \times N)$ matrix for the 3D domain. N is the grid point number per dimension. The elements of \mathbf{A} are real and positive by definition. The so-called sound map is produced by plotting the matrix \mathbf{A} for a given frequency with respect to the coordinates of the grid points.

To obtain sound maps with a satisfactory dynamical range, the so-called trimmed version of the CSM is used in this study (the diagonal elements of the CSM being set to zero), in order to remove the contribution of the noise induced by the interaction of the wind with the microphones [5]. Indeed in this study the array is located out of the flow, but close enough to the test section, so that hydrodynamic pressure perturbations could be expected due to flow re-circulation at low velocity.

Deconvolution The sound map obtained by beamforming is the result of the convolution of the sound source distribution with the array response to a point source (monopole or dipole) with the corresponding radiation model. The sound map calculated using beamforming consists of a main lobe centered on the source position and of side lobes. As a result, the sound source imaging of the beamforming technique can only provide approximately the source location and its distribution for the reason that the size of the lobes are frequency-dependent and the side lobes can be identified as sound sources. In order to improve the spatial resolution and to make the sound maps more readily interpretable, the so-called deconvolution methods, which deconvolve the array response from the beamforming maps, can be associated to the beamforming algorithm. The advantage are twofold: (i) the side lobes are removed from sound maps; (ii) a good resolution of source distribution can be achieved in all frequency bands.

The DAMAS method (Brooks et al. [9]) is based on Point Spread Functions (discussed in the next section) for which the noise source at each scanning grid is supposed to be a point monopole source with uniform radiation pattern. This technique is computationally expensive because in 3D applications, the number of equations to solve is of the order of N^3 (N being the number of scanning points per dimension). In contrast, the CLEAN-SC method (Sijtsma [10]) is less demanding as it searches the peaks of the sound map at each iteration, and an adaptation of this technique to 3D applications, using monopolar and dipolar radiation models, is used in this paper. The method is similar to the one developed by Porteous et al. [20].

The CLEAN-SC technique works as follows: by finding the peak level in the sound map of beamforming results (or “dirty map” for the CLEAN-SC method), this method allows to determine the main lobe, its values and its coherent source spots including its side lobes. A portion of their amplitude, determined by a safety factor in this approach, are then removed from the “dirty map”. This process is done iteratively with a stop criterion. All the main lobes identified in the process are replaced by so-called clean beams with a predefined beamwidth. A sound map called “clean map” with better spatial resolution is finally obtained. In this paper, the 3D sound maps obtained by using the CLEAN-SC technique contain only clean beams.

The CLEAN-SC method is not efficient for the identification of noise sources that are spatially close, overlapping and forming a single peak level in sound maps. This problem usually arises at low frequencies. In addition, a source area containing coherent noise sources limits the application of the CLEAN-SC method (Bahr and Cattafesta [32]). However, this method has been demonstrated to provide a good compromise between computation cost and efficiency [17,20].

3.2. Numerical simulations

Some simulations were conducted by using synthetic white noise sources (monopole, dipole and distributed dipole noise sources). The actual 3D array geometry used in the wind-tunnel measurements is used in these simulations. The aim is to carry

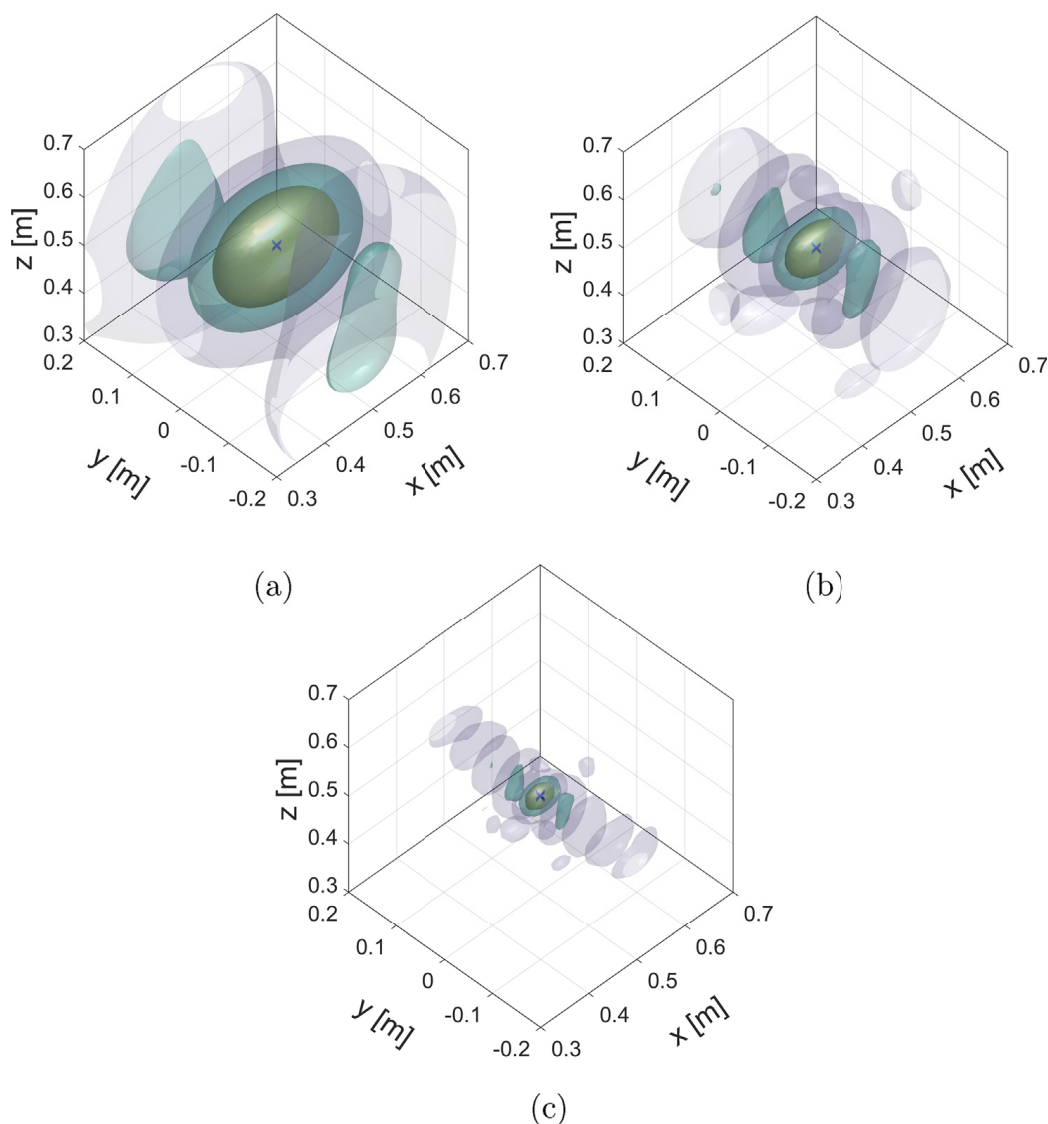


Fig. 4. Sound maps of a synthetic monopole noise source at the position (0.5 m, 0 m, 0.5 m) showing 3D point spread function at frequency (a) 1 kHz, (b) 2 kHz, (c) 4 kHz. The 3D isosurfaces at 3 dB, 6 dB and 12 dB below the peak level are plotted in each sound map from the inside to the outside. The symbols 'x' denote the exact location of simulated monopole noise source.

out a first evaluation of the 3D array performance, and to introduce the corresponding notions of 3D sound maps for dipole noise sources.

Three-dimensional Point Spread Function The sound map showing the beamforming results for a point monopole source is generally called the point spread function (PSF). Fig. 4 yields the simulated 3D PSF at frequencies 1 kHz, 2 kHz and 4 kHz of a broadband point monopole noise source located at position (0.5 m, 0 m, 0.5 m), using the experimental 3D array geometry of Fig. 2(b). Similarly to 2D beamforming results, a main lobe shown by the isosurfaces of ellipsoid shape centered on the noise source position is observed, together with side lobes evidenced by isosurfaces with lower level. At higher frequencies, the side lobes appear periodically in the y -direction, pointing out the need for an efficient deconvolution technique. The presence of such lobes is due to the structure of the array, in particular the two parallel vertical arrays facing each other.

The resolution is generally defined as the beamwidth of the main lobe of the PSF at a value of 3 dB below the peak level for 2D beamforming, and gives an order of magnitude of the minimum distance between two sources for being discriminated. In 3D cases associated with the 3D array geometry in the study, the isosurface below 3 dB of the peak level is an ellipsoid. In order to estimate its size, an average of the three major principle axis of the ellipsoid was computed for each case from the results of Fig. 4. This value for the 3D sound maps of 1 kHz, 2 kHz and 4 kHz is respectively 176 mm, 88 mm and 43 mm (obtained by a 3D scanning grid with spatial resolution of 2 mm), from which an inverse proportionality between the size of the ellipsoid and the beamforming frequency is expected; the results show indeed that the beamwidth at -3 dB is very close to half-a-wavelength. This result was explained by Cassereau et al. [33] in the ultrasound domain. The major principal axis of the ellipsoid is nearly in the x -direction to which no sub-array is perpendicular, which yields a lower spatial resolution in this direction; practically, this direction is the streamwise direction, as no microphone can be located in the flow. Logically, the results show that the size of the main and side lobes decreases at increasing frequency, allowing a better spatial resolution in the medium frequency range ([2 kHz; 4 kHz]).

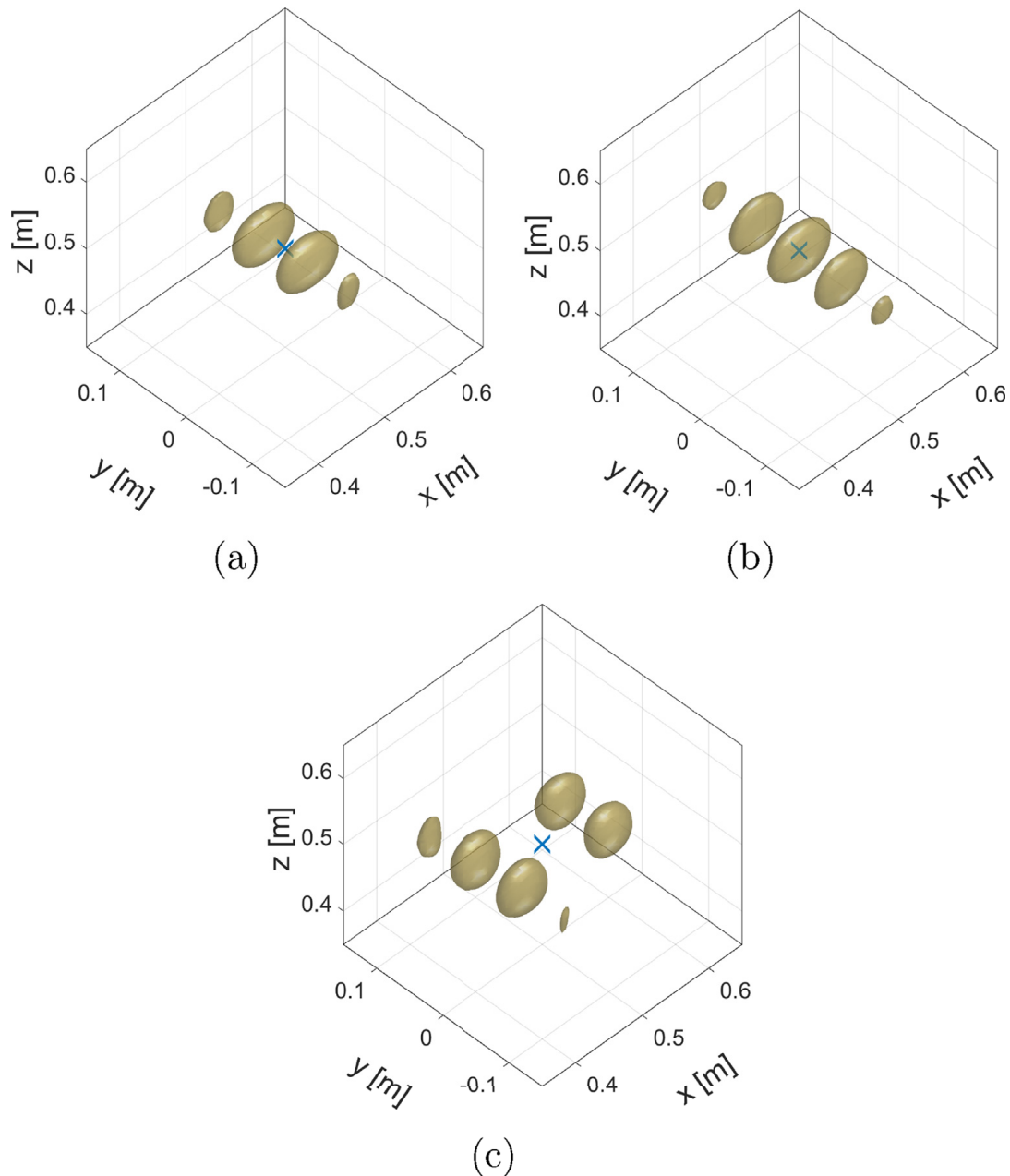


Fig. 5. Sound maps at beamforming frequency $f = 3$ kHz of a synthetic dipole noise source at the position (0.5 m, 0 m, 0.5 m), (a) using a monopole steering vector, (b) using a dipole steering vector with $\xi = (0, 1, 0)$, (c) using a dipole steering vector with wrong orientation of the dipole $\xi = (1, 0, 0)$. The symbols 'x' denote the exact location of simulated dipole noise source. The 3D isosurface in each sound map is plotted at 3 dB below the maximum.

Results for a point dipole source Fig. 5 shows the 3D beamforming results for a simulated broadband dipolar source, located at (0.5 m, 0 m, 0.5 m), and oriented along the y -direction using different steering vectors. Fig. 5(a) shows the sound map obtained using a monopolar steering vector at an analysis frequency of 3 kHz. Two dominant lobes are observed near the real source position. Indeed, it yields the existence of a dipole source (Liu et al. [18]) whereas its exact location is ambiguous: the lobes are in fact two out-of phase monopoles creating the dipolar radiation. Fig. 5(b) shows the sound map obtained using a dipolar steering vector, correctly oriented by setting $\xi = (0, 1, 0)$ (Eq. (4)). In spite of two side lobes near the noise source position, the dipole is clearly identified by the main lobe with a maximum coinciding exactly with the simulated dipole location with comparison to Fig. 5(a). The result of searching for a dipole with incorrect orientation $\xi = (1, 0, 0)$ (perpendicular to the real orientation) is shown in Fig. 5(c). In this case four main lobes appear around the source location. Knowing that incorrect orientation can lead to an incorrect sound map, one disadvantage of beamforming using a dipolar steering vector is that the orientation of dipole should be assessed priorly.

Results for distributed dipole sources Real aeroacoustic sources may have a spatial extent and can be distributed spatially, depending on the geometric characteristics of the object radiating sound. A typical example is the application case of this paper: for the wall-mounted airfoil, the trailing edge noise source can be distributed along the span of the airfoil. In order to evaluate

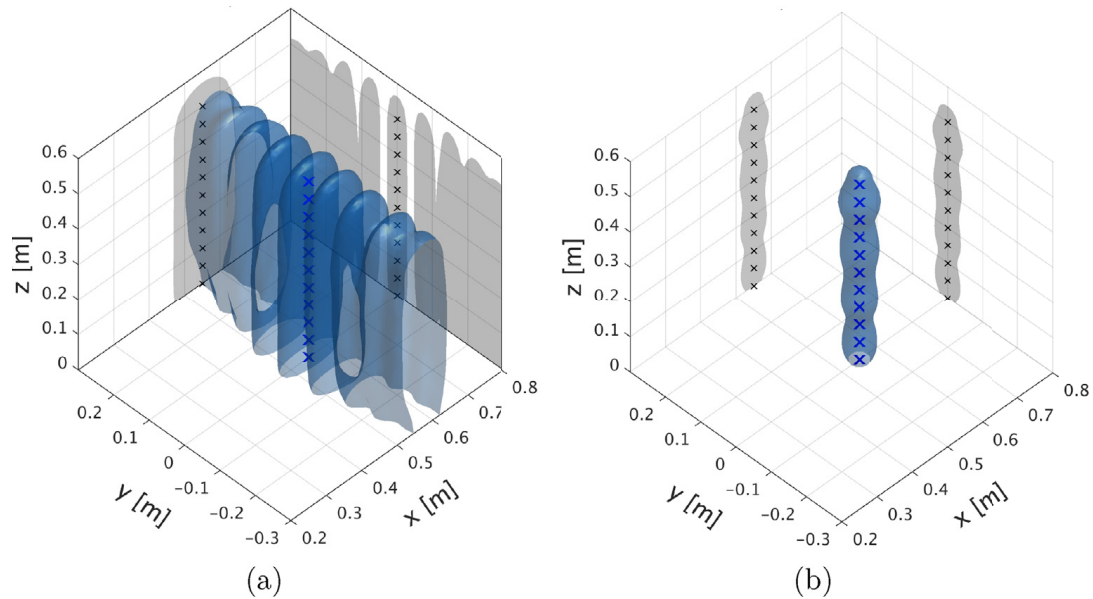


Fig. 6. Sound maps for a distributed noise sources of 11 synthetic dipoles at a third-octave band of nominal midband frequency of 2.5 kHz. (a): 3D dipolar beamforming; (b): CLEAN-SC technique. The symbols 'x' denote the exact location of simulated dipole sources. The shadows and the small black symbols 'x' correspond respectively to the projection of the 3D sound source imaging and the real noise source position in different directions. The 3D isosurface in each sound map is plotted at 9 dB below the maximum.

the CLEAN-SC method for this type of noise source, 11 incoherent dipole noise sources of broadband nature with orientation $\xi = (0, 1, 0)$ and same intensity were simulated on a line in the z -direction; the objective of such a model is to simulate a continuous distribution of broadband dipolar sources, evenly distributed along a vertical line of 0.5 m, approximately equal to the airfoil's span. In this purpose, the distance between two neighbouring sources is 5 cm. The experimental 3D array geometry is used in the simulation, and the sound maps in Fig. 6 are plotted in a third-octave band [2245 Hz; 2828 Hz] of nominal midband frequency of 2.5 kHz. Fig. 6(a) shows that the main and side lobes are distributed evenly in the z -direction because the distance between the neighbouring sources is too small for discriminating the individual dipoles. Indeed the investigation of the PSF indicated a resolution of about half-a-wavelength, and the distance between the sources (5 cm) is here less than the half-a-wavelength. In addition, the position of the main lobe is ambiguous through the observation of the size of the lobes on the sound map. Fig. 6(b) shows the sound map after deconvolution, from which a continuous distribution of noise sources is revealed, exactly located along the linear segment where the sources were generated. The side lobes are perfectly removed after deconvolution. It is concluded that the 3D version of the CLEAN-SC method used in this study is efficient to locate in the 3D space a continuous distribution of dipoles in the mid-frequency range (*i.e.*, frequencies of the order of a few kHz).

3.3. Modeling of the flow effects on sound propagation

The beamforming technique is based on a propagation model from a sound source to a microphone. The most straightforward way of implementing the beamforming technique is to use a model based on the Green function in a quiescent medium. However, in the present application, the sound source is located in a flow while the array is outside the flow, so that the wavefronts undergo convection and refraction effects. If the flow effect is not properly taken into account by using appropriate "flow effect corrections", the beamforming output produces an apparent shift of the source, upstream the actual position of the source [34,35].

In this study, such effects have been assessed experimentally by using the artificial monopolar noise source presented in Section 2.1. The 3D sound maps were produced by using a monopolar steering vector; the clean beamwidth for the CLEAN-SC technique is set to 0.05 m, and the safety factor is set to 0.99. The position with maximum level of the 3D beamforming sound map was considered to be the estimated position of the monopolar source. A 3D scanning grid with a spatial resolution of 5 mm was set for the 3D beamforming concerning the two test cases in this section.

A sample example is given in Fig. 7, which shows the 3D beamforming results without flow effect correction (Green function with a quiescent medium assumption) concerning the monopolar noise source embedded in the floor of the wind-tunnel at flow speed 40 m/s and position (0.68 m, 0 m, 0 m). First, it is observed that the raw beamforming sound map (Fig. 7(a)) is difficult to interpret due to the presence of ambiguous side lobes, while the use of the CLEAN-SC deconvolution technique allows the unambiguous identification of a source located at $z = 0$ m (Fig. 7(d)). However, as expected, the estimated position is significantly shifted downstream the actual position (6.5 cm in this case). This apparent spatial shift in the streamwise direction x is noted down Δx_{3D} in Fig. 7(d). Let us specify here that the number of iterations using the CLEAN-SC method is 16 in the present case, and that only the corresponding clean beam is represented in the sound map of Fig. 7(d). It means that 16 sources

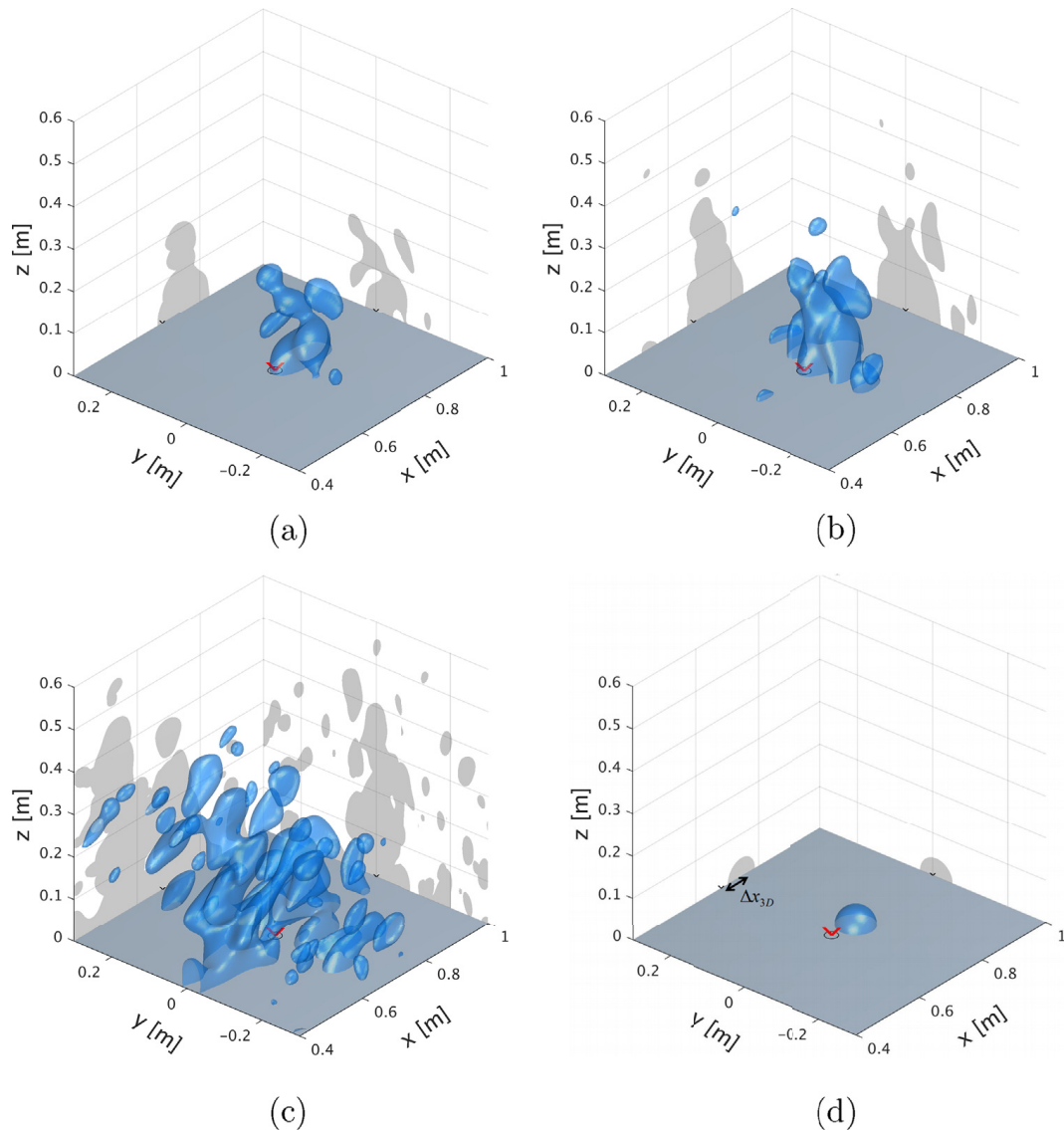


Fig. 7. Sound maps without flow effect correction at frequency 3 kHz of the synthetic noise source at (0.68 m, 0 m, 0 m) generated by a compression chamber at an incoming velocity $U_\infty = 40$ m/s in the wind-tunnel. (a): 3D monopole beamforming with a peak level at 51.3 dB; (b): 3D “dirty map” after the first iteration with a peak level at 31.3 dB; (c): 3D “dirty map” after the second iteration with a peak level at 26.3 dB; (d): CLEAN-SC technique with maximum value of 51.3 dB on the sound map. The red symbols ‘x’ denote the exact location of synthetic monopole noise source. The black circles indicate the metal pipe position. The shadows and the black symbols ‘x’ correspond respectively to the projection of the 3D sound source imaging and the real noise source position in different directions. The 3D isosurface in the sound maps is plotted at 9 dB below the maximum.

were identified before reaching the stop criterion. It can be observed that the peak level of the “dirty map” in Fig. 7(b), obtained after removing the main lobe identified at the first iteration and its coherent side lobes, is 20 dB lower than that of Fig. 7(a). Fig. 7(c) shows that the peak level of the “dirty map” after 2 iterations is 26.3 dB, indicating a much lower background noise level with respect to the synthetic noise source.

The Amiet’s model [29] is a well-known model for taking into account the refraction and convection effects of flow on sound propagation. It is based on a ray-tracing approach and on the assumption that the shear layers are infinitely thin. In this paper, an implementation of the Amiet’s method in three dimensions is used, following the equations derived by Bahr et al. [36]. In the present work, the shear layers are modeled according to three planar and infinitely thin shear layers, as depicted in Fig. 8, and only the angle correction is addressed. To illustrate the interest of the Amiet’s method, a noise source is supposed to be at the position (x_0, y_0, z_0) . Three microphones were considered around the shear layers of the wind-tunnel. The ray paths from the noise source to the three microphones were computed at a wind speed of 40 m/s. Fig. 8 shows that the calculated ray paths (intersecting with the shear layers at point I) are not straight from the noise source to the microphones, which involves a modification of the propagation time from the source to the microphone, compared to a rectilinear path.

An evaluation of the implemented “flow effect correction” technique is now considered, for an experimental case using the artificial noise source at height $z = 0.35$ m and for a flow speed of 40 m/s. Fig. 9 shows the 3D sound beamforming sound maps of this test case. Without flow effect correction, Fig. 9(a) shows that the main lobe of the sound map is not centered at the free

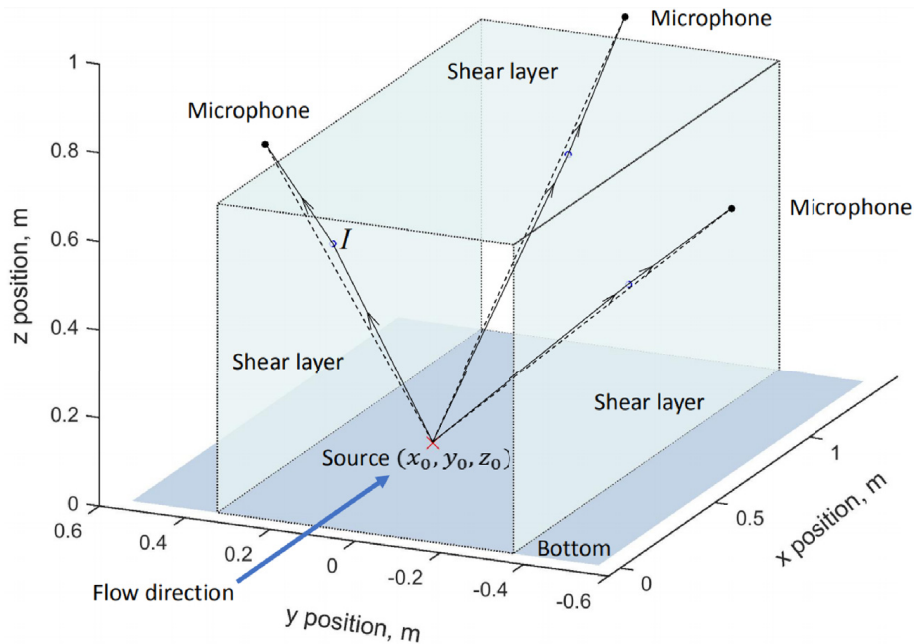


Fig. 8. Sketch of the sound rays in the wind-tunnel flow. The calculated sound rays from the noise source to the microphones are indicated by solid black lines, while the rectilinear paths are depicted by dashed lines.

end of the metal pipe as expected. Similar to Fig. 7(d), the sound map after deconvolution reveals clearly the shift downstream (6 cm in this case) of the noise source with respect to the expected position shown by the red cross (see Fig. 9(b)). Note that the apparent shift Δx_{3D} of the noise source due to the flow effect is not the same at different heights in the test section. According to Fig. 9(c) with flow effect correction, the contribution of the aeroacoustic sources of the cylinder seems to be weak at the beamforming frequency. In addition, the merging of a main lobe and of some side lobes at the top area of the pipe makes it difficult to identify the real noise source. By using the 3D CLEAN-SC code, the noise source is well located at the top of the pipe (Fig. 9(d)). The position error of noise source in 3D sound map is less than 8 mm. It is then concluded that the 3D microphone array provides good performances in terms of noise source position accuracy for isolated noise sources, and that the modeling of the flow effects on propagation is satisfactory, as the source apparent shift (previously observed in Fig. 7(d)) is not present anymore.

4. Results and discussion

4.1. Three-dimensional dipolar beamforming implementation

Acoustic data from the 256 channels were recorded at a sampling frequency of 50 kHz with a sampling time of 5 s for each test case. During the array signal processing, the signal of each channel was filtered by a 256th order numerical high-pass filter with a cutoff frequency of 20 Hz. The CSM was obtained by using the Welch's method, for which each channel data set was divided into 100 blocks containing 2500 sampling points without overlap and a Hanning window. The resulting frequency resolution was 20 Hz, and the computed CSM for 3D beamforming was then a matrix of dimension $(256 \times 256 \times 2500)$, 256 being the number of microphones and 2500 the number of discrete frequency values. A 3D scanning grid containing 226,981 points (61^3) in a cube of dimension $0.6 \text{ m} \times 0.6 \text{ m} \times 0.6 \text{ m}$ enclosing the wall-mounted airfoil, was used for all the sound maps in this section (Fig. 2(a)). The grid was then composed of cubes with an edge length of 10 mm. The safety factor of the CLEAN-SC method was set to 0.99 and the clean beamwidth was chosen as 0.05 m [10]. The dipolar nature of the trailing edge noise [19] and leading edge noise sources [37] was taken into consideration by making the assumption that the dipole orientation is perpendicular to the airfoil symmetry axis.

Beamforming results are given in third-octave bands in the following. This was achieved by calculating the beamforming sound maps for each frequency bin contained in a given third-octave band, and then summing the 3D sound maps. Four third-octave bands are considered in this study, *i.e.*, [707 Hz; 891 Hz], [2245 Hz; 2828 Hz], [3564 Hz; 4490 Hz] and [4490 Hz; 5657 Hz], with respective nominal midband frequencies of 0.8, 2.5, 4 and 5 kHz.

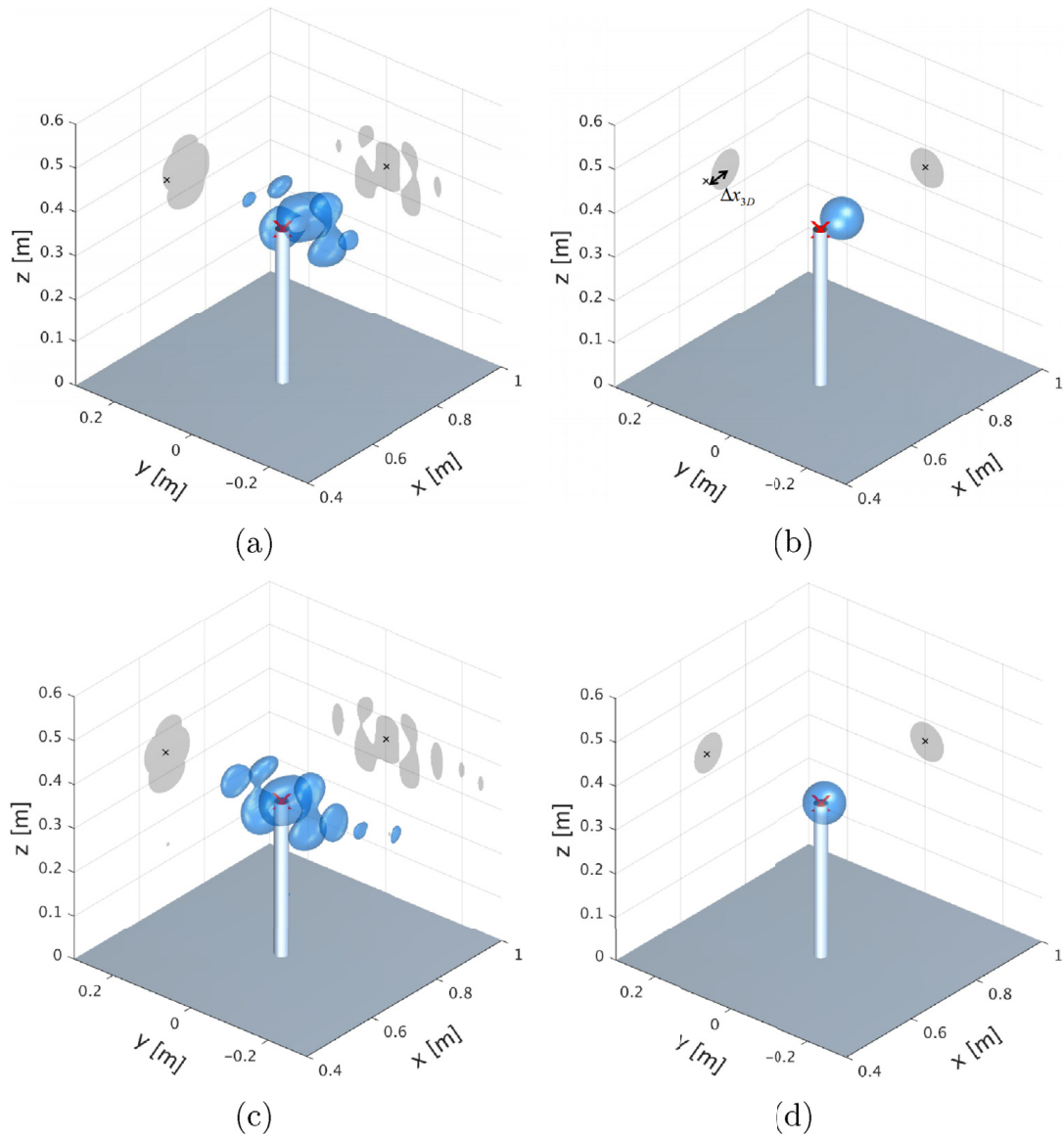


Fig. 9. Sound maps at frequency 3 kHz of the synthetic noise source at (0.68 m, 0 m, 0.35 m) generated by a compression chamber at an incoming velocity $U_\infty = 40$ m/s in the wind-tunnel. (a): 3D dipolar beamforming without flow effect correction with maximum value of 52.2 dB on the sound map; (b): CLEAN-SC technique without flow effect correction with maximum value of 52.2 dB on the sound map; (c): 3D dipolar beamforming with flow effect correction with maximum value of 52.2 dB on the sound map; (d): CLEAN-SC technique with flow effect correction with maximum value of 52.2 dB on the sound map. The red symbols 'x' denote the exact location of synthetic monopole noise source. The white cylinder represents the pipe connected to the compression chamber. The shadows and the black symbols 'x' correspond respectively to the projection of the 3D sound source imaging and the real noise source position in different directions. The 3D isosurface in each sound map is plotted at 9 dB below the maximum value of the sound map.

4.2. Sound source localization results for a wall-mounted airfoil

As mentioned in Section 2.1, this paper focuses on the sources of broadband noise produced by a wall-mounted airfoil in a flow. Several noise sources, including trailing edge noise and wing tip noise (Brooks et al. [38]), leading edge noise (Geyer et al. [13]) and junction noise (Moreau et al. [39]), are expected to be observed in the 3D sound maps. In all the sound maps presented in this section, the 3D isosurface at 9 dB below the maximum is systematically plotted in order to investigate the spatial distribution of the aeroacoustic sources. Figs. 10–12 present the 3D sound maps at incoming flow speed 40 m/s, for midband frequencies of 2.5 and 4 kHz, at increasing angles of attack (4° , 10° and 20°). At the end of the section, the case $\alpha = 0^\circ$ is presented to discuss the results at lower and higher midband frequencies (0.8 and 5 kHz, Fig. 13).

Fig. 10(a) and (c) present the results at angle of attack $\alpha = 4^\circ$ using the 3D beamforming technique, for two third-octave bands with respective midband frequency 2.5 and 4 kHz. At frequency 2.5 kHz, one lobe at the corner of the junction and the leading edge can be observed in Fig. 10(a), which may correspond to dipolar leading edge noise generated by the impingement of the wall turbulent boundary layer on the leading edge [37,39]. At both frequencies, some larger vertical lobes parallel to the airfoil appear, located regularly between the two vertical sub-arrays (Fig. 10(a) and (c)). The lobe with maximum intensity is centered on the trailing edge and may be interpreted as the main lobe of the dipolar source of trailing edge noise. The other

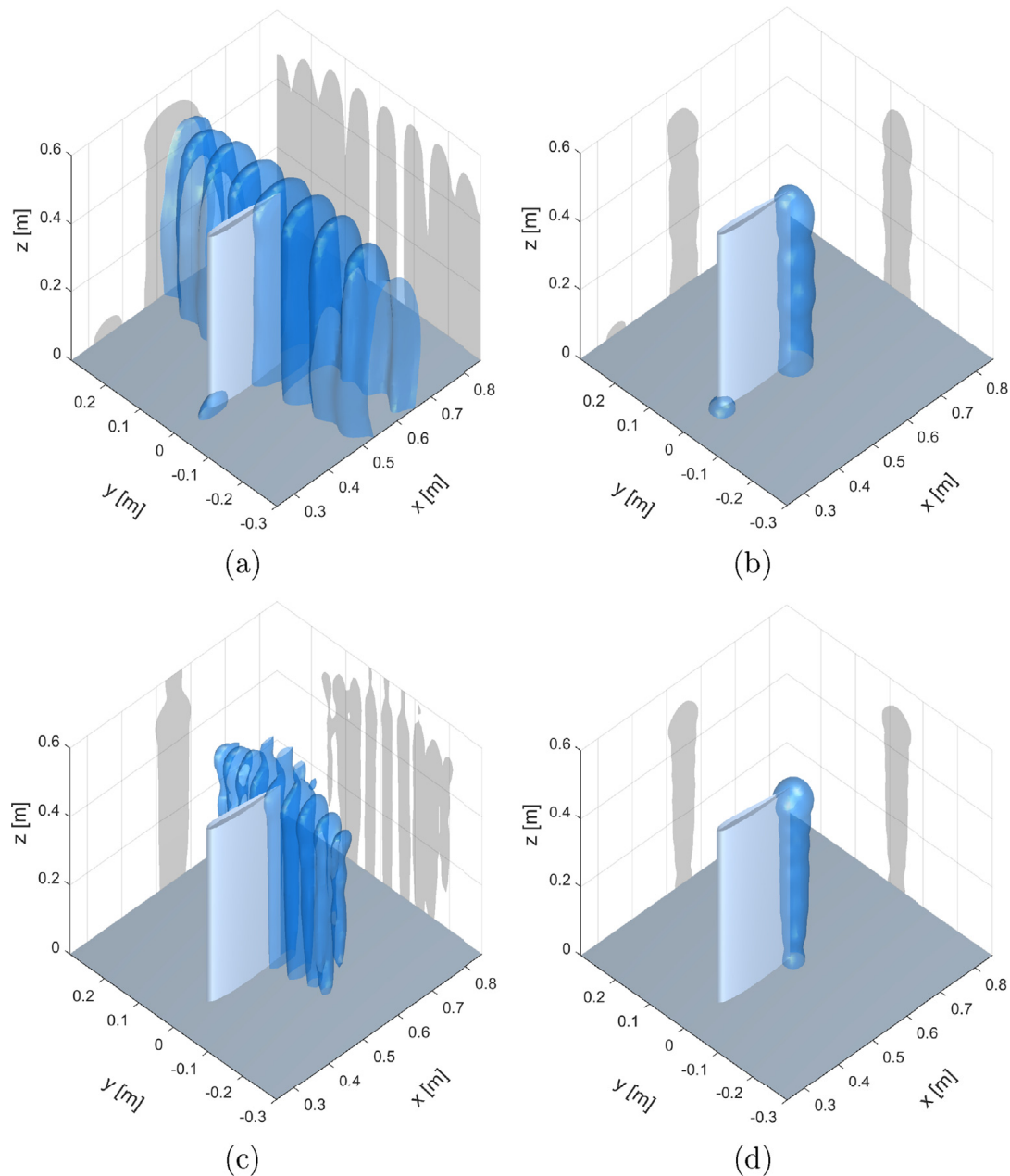


Fig. 10. Sound maps for the wall-mounted finite airfoil at incoming velocity $U_\infty = 40$ m/s and angle of attack $\alpha = 4^\circ$, at two third-octave bands of nominal midband frequency 2.5 kHz (top figures) and 4 kHz (bottom figures). (a) and (c): 3D dipolar beamforming with respectively a maximum value of 35.7 dB and 29.8 dB on the sound map; (b) and (d): CLEAN-SC technique with respectively a maximum value of 33.1 dB and 29.8 dB on the sound map. The 3D isosurface in each sound map is plotted at 9 dB below the maximum value of the sound map.

lobes, parallel to the main lobe, do not coincide with a solid boundary located in the flow, and should be interpreted as side lobes. The observed network of parallel vertical lobes is similar to the map in Fig. 6(a) reporting the simulation of a vertical linear distribution of dipolar sources. The comparison between Fig. 10(a) (2.5 kHz) and 10(c) (4 kHz) also indicates that at increasing frequency, the spatial extent of the main and side lobes diminishes, providing a better resolution, which is similar to 2D beamforming.

Using the deconvolution method CLEAN-SC, an easily interpretable sound map is obtained thanks to the side lobes removal, as shown in Fig. 10(b) and (d). It is found that the noise source is distributed rather evenly along the trailing edge for both frequency bands. These results are, again, similar to the simulation results of Fig. 6(b). Therefore, it is concluded that the CLEAN-SC model, based on a superimposition of incoherent sources, is valid for describing the broadband trailing edge noise source. These results are in agreement with the literature. A similar noise source distribution of a tripped wall-mounted NACA 0012 airfoil identified by two-dimensional beamforming method was reported before in the same frequency range (Moreau et al. [39]; Geyer et al. [40]), with an elongated source evenly distributed along the trailing edge. In addition, at higher frequency (4 kHz), the apparent diameter of the line source along the trailing edge slightly increases close to the tip (Fig. 10(d)), which

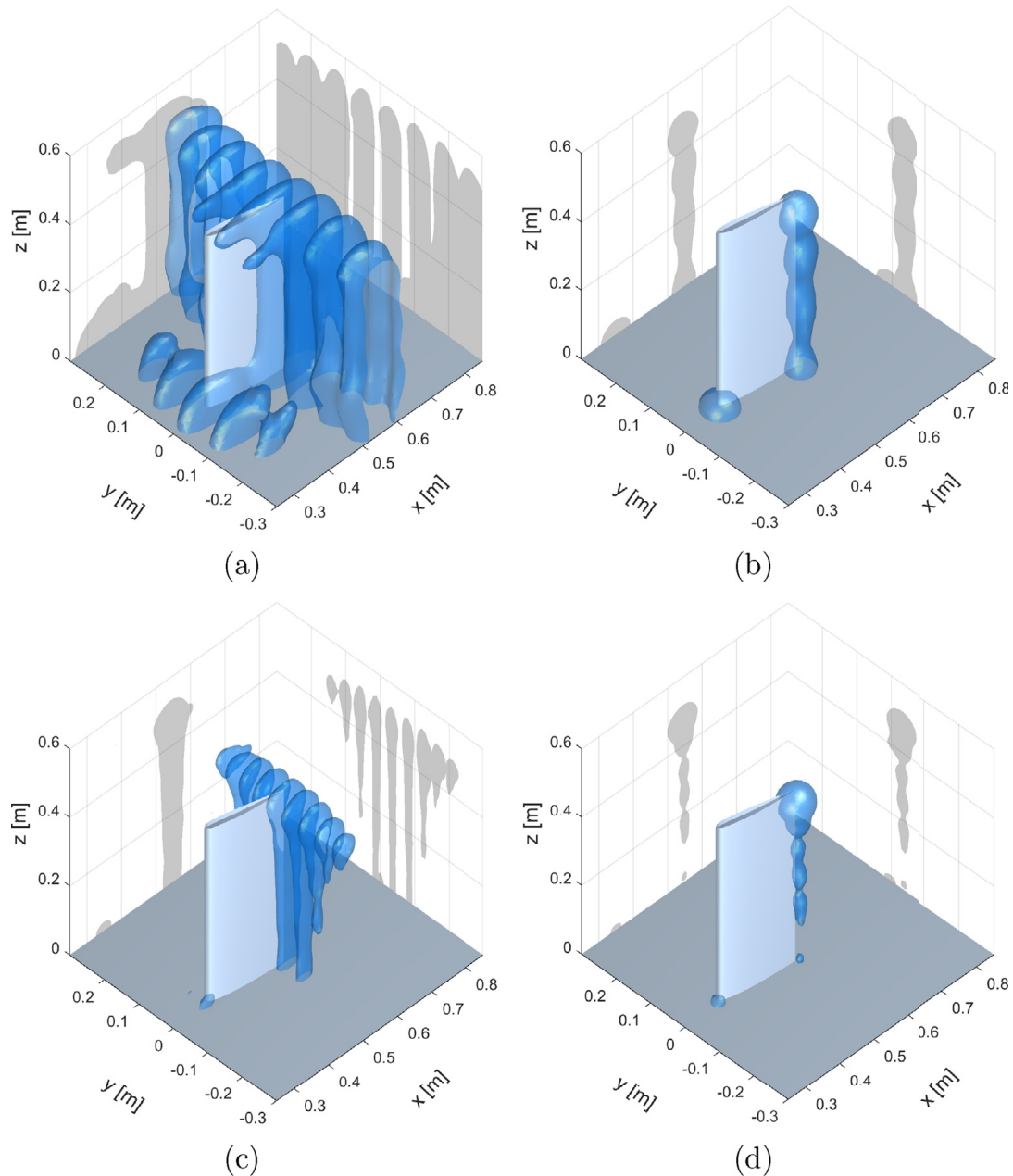


Fig. 11. Sound maps for the wall-mounted finite airfoil at incoming velocity $U_\infty = 40$ m/s and angle of attack $\alpha = 10^\circ$, at two third-octave bands of nominal midband frequency 2.5 kHz (top figures) and 4 kHz (bottom figures). (a) and (c): 3D dipolar beamforming with respectively a maximum value of 35.2 dB and 30.2 dB on the sound map; (b) and (d): CLEAN-SC technique with respectively a maximum value of 34.4 dB and 30.2 dB on the sound map. The 3D isosurface in each sound map is plotted at 9 dB below the maximum value of the sound map.

means that the intensity of the source is higher at the tip. Moreau et al. [39], similarly, reported on a similar tripped NACA 0012 airfoil at angle of attack 4° (with a similar length/chord ratio $L/C = 3$, but at a higher flow speed of 60 m/s) the apparition of tip noise around 4 kHz, but also that trailing edge noise almost disappears at this frequency.

Fig. 11 presents the sound maps of the wall-mounted airfoil at angle of attack $\alpha = 10^\circ$ and flow speed 40 m/s. As shown in Fig. 11(a) and (c), the beamforming results without deconvolution make difficult the interpretation of the noise sources, due to the presence of strong side lobes. Again, the use of the 3D CLEAN-SC method reveals the sound source distribution (Fig. 11(b) and (d)). The sound map at frequency 2.5 kHz (Fig. 11(b)) is quite similar to the one at angle of attack $\alpha = 4^\circ$ at the same frequency (Fig. 10(b)), except that the noise sources are less evenly distributed along the trailing edge. Indeed, it consists of three different parts in the spanwise direction, *i.e.*, a concentrated noise source located at the corner of the trailing edge and the wing tip (tip noise), a distributed noise source in the middle span of the airfoil (trailing edge noise), and a concentrated noise source identified at the corner of the trailing edge and the junction. Tip noise and junction noise originate from complex flow regimes in those corresponding zones, as reported by several research studies focused on the investigation of the wing tip flow

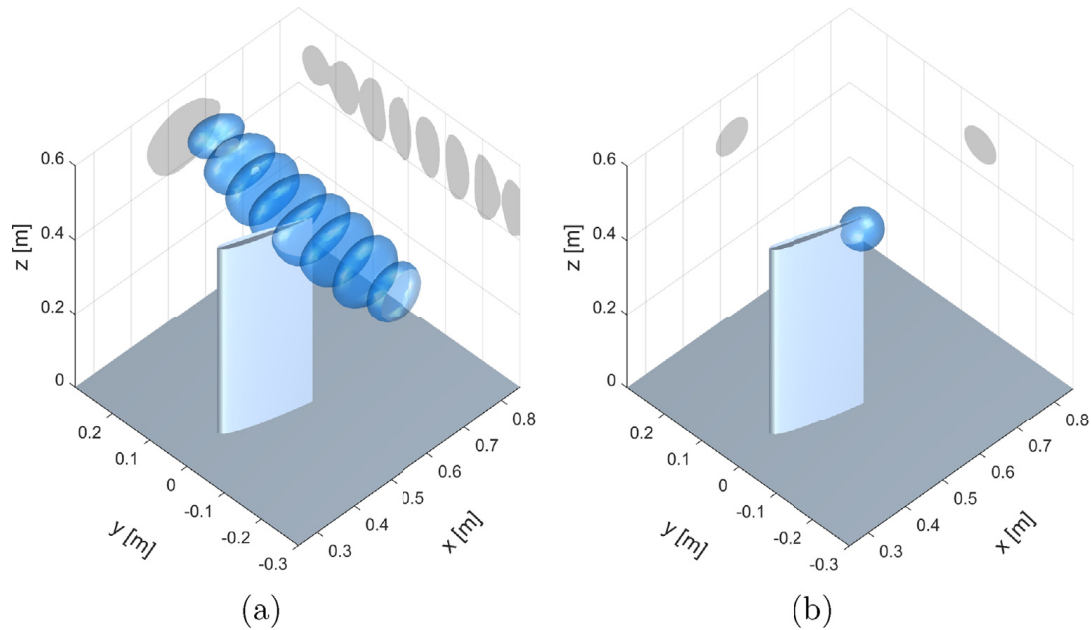


Fig. 12. Sound maps for the wall-mounted finite airfoil at incoming velocity $U_\infty = 40$ m/s and angle of attack $\alpha = 20^\circ$, at a third-octave band of nominal midband frequency 2.5 kHz. (a): 3D dipolar beamforming with maximum value of 52.3 dB on the sound map; (b): CLEAN-SC technique with maximum value of 52.2 dB on the sound map. The 3D isosurface in each sound map is plotted at 9 dB below the maximum value of the sound map.

(Uzun et al. [41], Imamura et al. [42], Bailey et al. [43]) and the wing-body junction flow of wall-mounted airfoils (Fleming et al. [44], Gand et al. [45]).

In the third-octave band of midband frequency 4 kHz (Fig. 11(d)), the tip noise source, located at the corner of the wing tip and the trailing edge dominates the radiation, but weaker trailing edge noise contributions are detected through several isolated noise sources. Similar isolated trailing edge noise sources of a wall-mounted NACA 0012 airfoil on sound maps in 1/12th octave band using three-dimensional dipolar beamforming were reported by Porteous et al. [20]. The fact that a clear sound source is well located at the wing tip supports the assumption of a dipolar radiation of wing tip noise source, orientated similarly to trailing edge noise (*i.e.*, perpendicularly to the airfoil symmetry axis). Furthermore, the results in Figs. 10 and 11 clearly reveal, interestingly, the tendency of the dominant noise sources turning from leading edge noise and trailing edge noise to wing tip noise at increasing frequency. This is in agreement with the previous experimental results showing the dominant contribution of wing tip noise at high-frequencies (Moreau et al. [39], Brooks and Marcolini [46], Geyer et al. [40]).

Fig. 12 plots the sound maps of the wall-mounted finite airfoil at angle of attack $\alpha = 20^\circ$. In this case, the beamforming result in Fig. 12(a) still shows a main lobe with several side lobes presenting almost the same size. The wing tip noise source is unambiguously identified by using the 3D CLEAN-SC technique (Fig. 12(b)). Similarly, it was reported that wing tip noise dominates the radiation for a wall-mounted NACA 0012 airfoils at angle of attack of 20° (Geyer et al. [40]). From the observation of Figs. 10(b), 11(b) and 12(b), it can be concluded that wing tip noise becomes increasingly dominant with increasing angle of attack. The same observation was reported by Moreau and Doolan [47].

The case of the airfoil at angle of attack $\alpha = 0^\circ$ is now considered, in order to investigate more specifically the lowest and higher frequency bands (midband frequency 0.8 and 5 kHz). Fig. 13(a) presents the beamforming result at low frequency, 0.8 kHz. This range of frequency generates some main and side lobes that have very significant extents, so that the airfoil is totally enclosed in the main lobe, making impossible the identification of the source of noise. Fig. 13(b) shows the sound map after applying the deconvolution by using the CLEAN-SC technique, from which a dominant source concentrated in the middle of the junction and a source concentrated at the trailing edge were identified. Similarly, the dominance of junction noise for a wall-mounted airfoil at low frequencies was reported before (Moreau and Doolan [48]).

Considering the higher frequency band (5 kHz), Fig. 13(c) displays periodic side lobes centered around the leading edge, similarly to Figs. 10 and 11. A difference is however noticeable, with the apparition of lobes at $x = 0.2$ m; these lobes are due to spatial aliasing occurring at high frequencies. Interestingly, the deconvolution process removes the aliasing effect and reveals the existence of the source of trailing edge noise in this frequency band.

4.3. Sound source localization results for two wall-mounted airfoils

To demonstrate the potentiality of 3D array of microphones, a last configuration with two airfoils is investigated. Two wall-mounted airfoils of chord length 0.2 m but with different span lengths (458 mm and 400 mm) and angles of attack of 0° are located in an incoming flow with velocity $U_\infty = 40$ m/s. The leading edge of the shorter airfoil is located 10 cm closer to the wind-tunnel nozzle than the leading edge of the longer airfoil (see Fig. 14). Each airfoil has the same characteristics (apart from

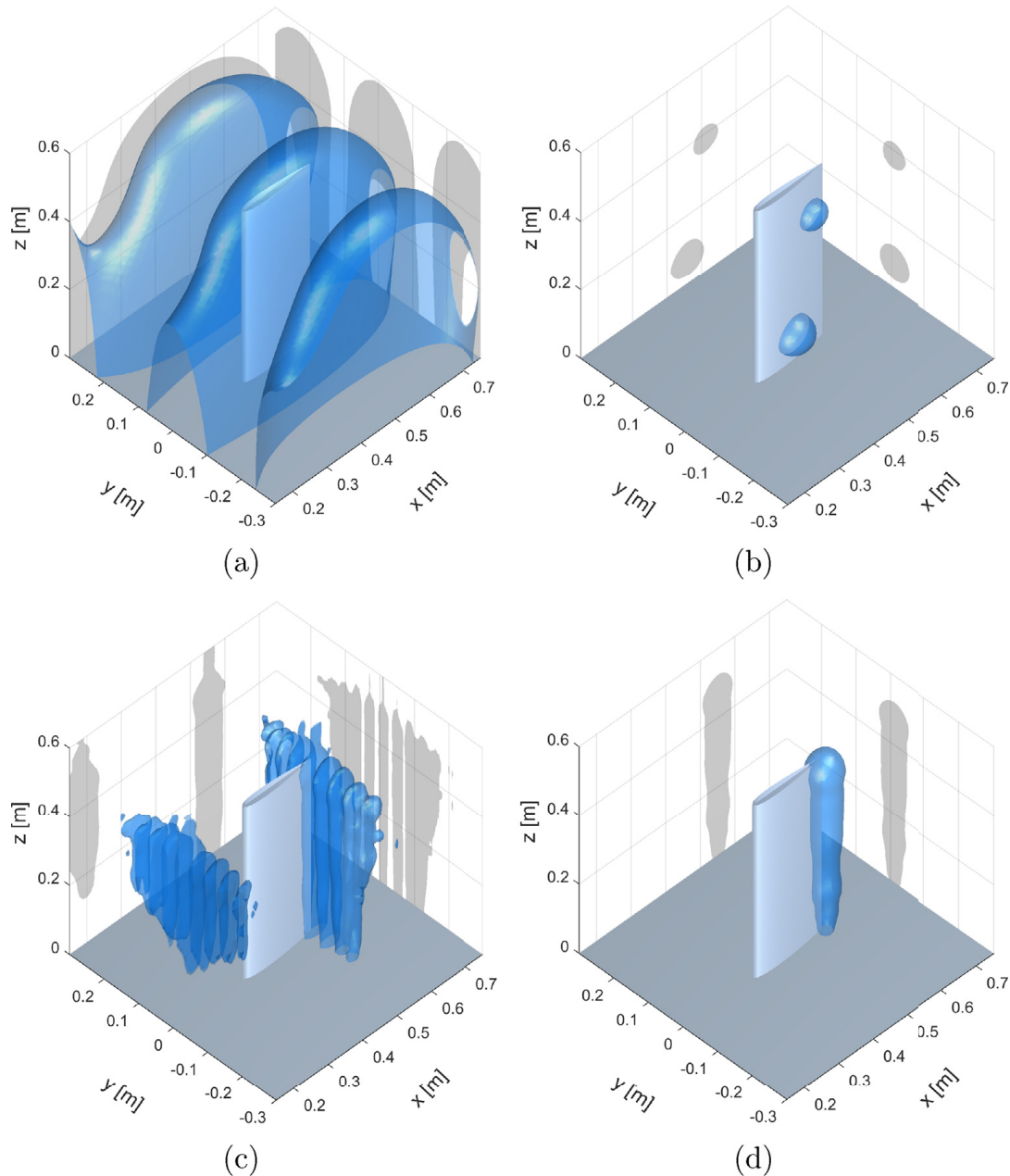


Fig. 13. Sound maps for the wall-mounted finite airfoil at incoming velocity $U_\infty = 40$ m/s and angle of attack $\alpha = 0^\circ$, at two third-octave bands of nominal midband frequency 0.8 kHz (top figures) and 5 kHz (bottom figures). (a) and (c): 3D dipolar beamforming with respectively a maximum value of 41.9 dB and 35.0 dB on the sound map; (b) and (d): CLEAN-SC technique with respectively a maximum value of 40.8 dB and 35.3 dB on the sound map. The 3D isosurface in each sound map is plotted at 9 dB below the maximum value of the sound map.

the span length) as the airfoil described in Sec. 2.1, with a similar boundary layer tripping device. Hence, the generation of broadband noise is expected in the case. This geometry is a real 3D configuration and cannot be treated by a conventional 2D approach. To investigate the sound produced by this configuration, we used a second array of microphones based on the same technology but with more channels [49]. However, to be consistent with the first experiments, we used only 256 channels among the 1024 available. Fig. 14 shows the array geometry with 16 bars of 16 microphones distributed uniformly (every 72 mm) on each side of the antenna.

Fig. 15 yields the sound maps of the two wall-mounted finite airfoils at angles of attack $\alpha = 0^\circ$ and flow speed 40 m/s, in two third-octave bands of midband frequencies 2.5 and 4 kHz. It is found that the overlap of the main lobes and side lobes from the two airfoils makes the beamforming results without deconvolution impossible to interpret (see Fig. 15(a) and (c)). Fig. 15(b) and (d) show clearly the trailing edge noise sources of the two airfoils using the CLEAN-SC method. The dominant noise source of the short airfoil is more concentrated in the part of the trailing edge close to the tip than that of the long airfoil. In Fig. 15(d), a part of the noise sources was not identified exactly at the trailing edge of the long airfoil, which may be caused by the contamination of the side lobes from the short airfoil. The methods to avoid it could be the optimization of the array geometry to minimize the

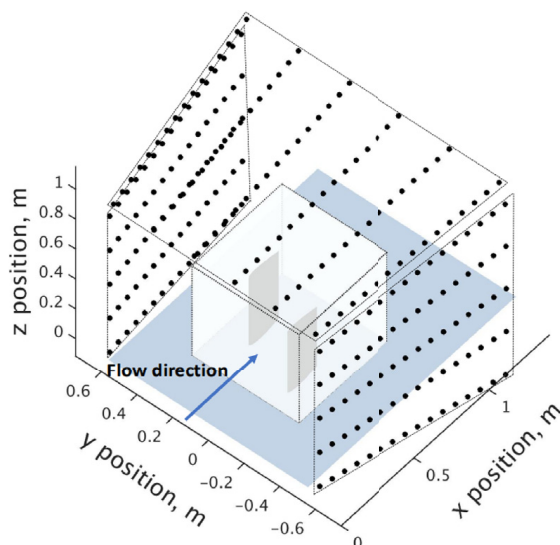


Fig. 14. Schematic depicting the 3D microphone array and the two wall-mounted airfoils under study. The black points indicate the positions of the microphones of the 3D microphone array. The cube with dashed edges enclosed by the 3D microphone array shows the 3D scanning grid for the beamforming calculation in a volume of dimension $0.6 \text{ m} \times 0.6 \text{ m} \times 0.6 \text{ m}$.

side lobes. Note that the distribution of the trailing edge noise sources of the airfoils is not as uniform as that shown in Fig. 10. This may be due mainly to three reasons: (i) the existence of the objects, and in particular their possible mutual diffraction, was not considered in the array signal processing technique; (ii) the two airfoils are shorter than that in Fig. 10; (iii) strong side lobes may cause CLEAN-SC to attribute noise to the wrong airfoil and subtract coherent noise (*i.e.*, actual sources) from the other one. Nevertheless, the large array system can be associated to more advanced signal processing methods to account for the solid boundaries of objects for sound imaging.

The results in this study show that the use of a massive 3D array of MEMS microphones, associated to a 3D array processing adapted to dipolar radiation could locate the noise sources of the wall-mounted airfoil in a 3D domain. This 3D beamforming method can reveal accurately the distribution of the noise sources, and is promising for the investigation of the flow-induced noise of objects in flows with a strong 3D configuration. When the existence of the solid boundaries of objects presents some significant influence on the sound propagation in the flow, the calculation of the corresponding Green function could be associated to the beamforming process in future works [50].

5. Conclusion

This paper has presented the development of a tunnel-shaped array for imaging aeroacoustic sources in the open section of an anechoic wind-tunnel, together with the associated signal processing techniques, and an application to the case of a wall-mounted airfoil. The antenna is made of three perpendicular planar arrays enclosing the test section, the lower part of the flow being bounded by a rigid planar surface. The 256 digital MEMS microphones of the 3D array are mounted on 32 bars surrounding the test section of the wind-tunnel, uniformly distributed on each bar. The source under consideration is a wall-mounted NACA 0012 airfoil located in the wind-tunnel flow, for several angles of incidence ranging from 0° to 20° . Such a configuration results in a complex superimposition of several broadband sources of noise, the main source being the trailing edge noise, but also the tip noise, the leading edge noise and the junction noise. A test case concerning two wall-mounted airfoils with different span lengths in a flow using a similar large array system was also addressed.

The data processing is based on a 3D implementation of the beamforming technique associated to a deconvolution method (CLEAN-SC) developed in 3D in order to remove the numerous side lobes that make the interpretation of the sound maps ambiguous. The wall-mounted airfoil being known to generate dipolar sources, the beamforming technique is implemented by using a dipolar radiation model perpendicular to the airfoil. The simulations indicate that the data processing technique allows to identify a linear distribution of non coherent dipoles, similar to the radiation that should be expected from the trailing edge. The flow effect on propagation is taken into account in the beamforming technique by using the Amiet's method in terms of angle correction.

In spite of the relatively low metrological qualities of the MEMS microphones used in this experimental study (compared to measurement microphones), in particular in terms of variability of the amplitude and phase response, the performances of the 3D source localization method are excellent, due to the high number of microphones and to the tunnel-type geometry allowing to surround the sources in the flow. For the wall-mounted airfoil, the different sources of noise that are to be expected are accurately identified in the third-octave bands under investigation, and are in good agreement with experimental results published in the literature. To our knowledge, no 3D beamforming identification of aeroacoustic sources with such level of accuracy have been published formerly in the literature. The presented results prove that a tunnel-type array including several

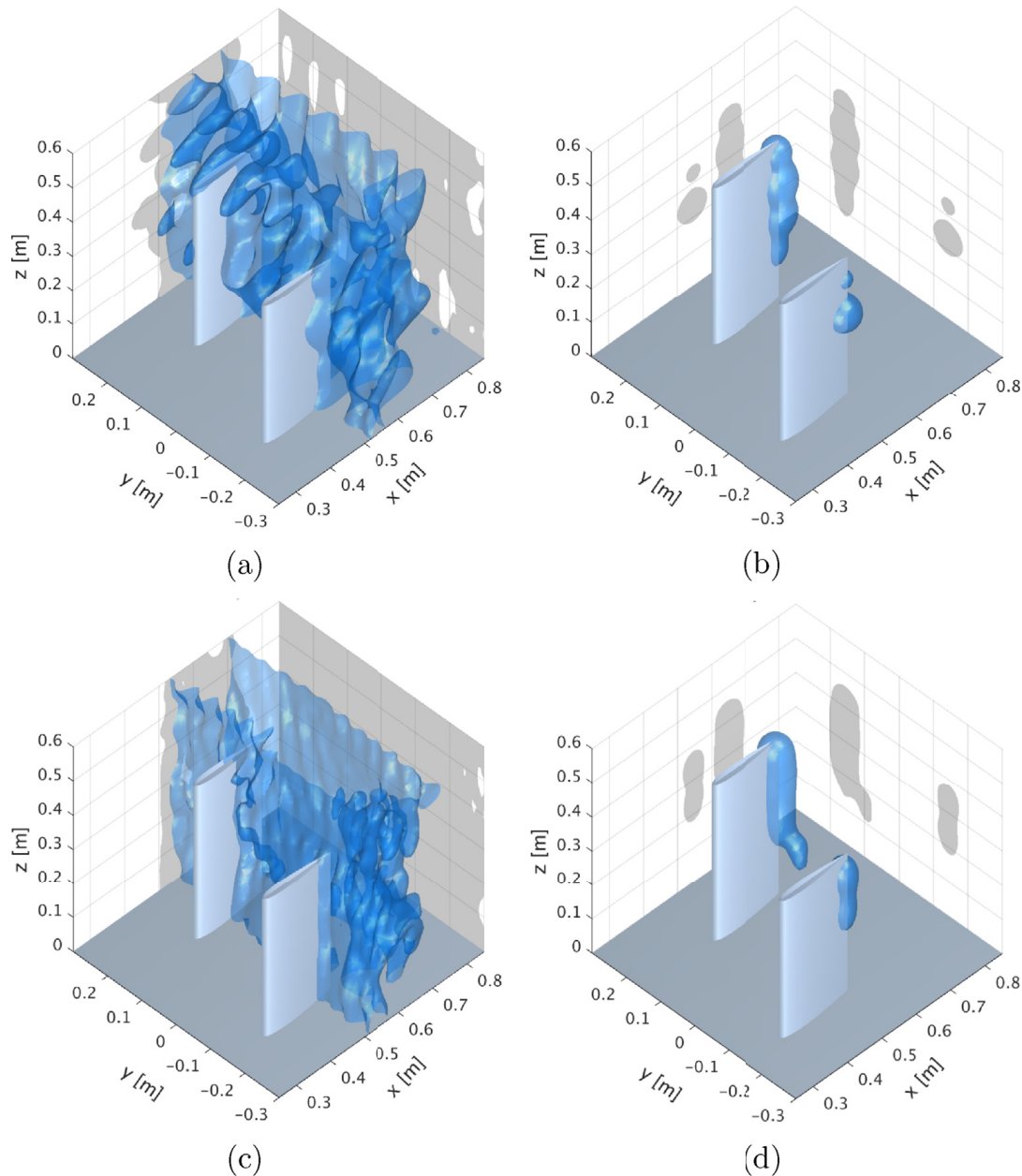


Fig. 15. Sound maps for the two wall-mounted finite airfoils at incoming velocity $U_\infty = 40$ m/s and angles of attack $\alpha = 0^\circ$, at two third-octave bands of nominal midband frequency 2.5 kHz (top figures) and 4 kHz (bottom figures). (a) and (c): 3D dipolar beamforming with respectively a maximum value of 41.9 dB and 36.2 dB on the sound map; (b) and (d): CLEAN-SC technique with respectively a maximum value of 40.5 dB and 35.5 dB on the sound map. The 3D isosurface in each sound map is plotted at 9 dB below the maximum value of the sound map.

hundreds of microphones associated to appropriate 3D array processing techniques performs very well, and that cheap MEMS microphones are good candidates for measuring the sound radiation efficiently. In the future, the 3D signal processing should be further developed in order to take into account sources with non-constant orientation of the dipole, installation effects such as reflection or diffraction, and non-stationary acoustic events such as in Ref. [51]. Additionally, the large array system can be associated to more advanced array signal processing methods like the time-reversal technique for experimental aeroacoustic investigations.

CRediT authorship contribution statement

Yinshi Zhou: Methodology, Software, Visualization, Validation, Writing - original draft. **Vincent Valeau:** Conceptualization, Methodology, Software, Writing - review & editing. **Jacques Marchal:** Methodology, Software. **François Ollivier:** Methodology, Software, Writing - review & editing. **Régis Marchiano:** Conceptualization, Methodology, Software, Writing - review & editing.

Acknowledgements

This work is supported by Agence Nationale de la Recherche (grant ANR-18-CE22-0005-01), the CPER FEDER program "Transport", the Civil Aviation University of China and the China Scholarship Council. The authors wish to thank Pascal Biais, Dominique Busquet, P. Challande, Janick Laumonier, H. Moingeon, Christian Ollivon, Laurent Philippon, Philippe Szeger and Jean-Christophe Vergez for their technical support to this work.

References

- [1] Environmental protection - Annex 16 to the Convention on International Civil Aviation, Volume I - Aircraft noise, in: International Standards and Recommended Practices, International Civil Aviation Organization, 2017.
- [2] S. Oerlemans, L. Broersma, P. Sijtsma, Quantification of airframe noise using microphone arrays in open and closed wind tunnels, *Int. J. Aeroacoustics* 6 (4) (2007) 309–333.
- [3] M. Wang, J.B. Freund, S.K. Lele, Computational prediction of flow-generated sound, *Annu. Rev. Fluid Mech.* 38 (2006) 483–512.
- [4] D.H. Johnson, D.E. Dudgeon, *Array Signal Processing: Concepts and Techniques*, PTR Prentice Hall Englewood Cliffs, 1993.
- [5] C.S. Allen, W.K. Blake, R.P. Dougherty, D. Lynch, P.T. Soderman, J.R. Underbrink, T.J. Mueller, *Aeroacoustic Measurements*, Springer Science & Business Media, 2002.
- [6] H. Siller, M. Drescher, G. Saueressig, R. Lange, Fly-over source localisation on a Boeing 747-400, in: Berlin Beamforming Conference, BeBeC-2010-13, 2010.
- [7] V. Fleury, J. Bult, Extension of deconvolution algorithms for the mapping of moving acoustic sources, *J. Acoust. Soc. Am.* 129 (3) (2011) 1417–1428.
- [8] J. Zhang, X. Xiao, D. Wang, Y. Yang, J. Fan, Source contribution analysis for exterior noise of a high-speed train: experiments and simulations, *Shock Vib.* (2018).
- [9] T.F. Brooks, W.M. Humphreys, A deconvolution approach for the mapping of acoustic sources (DAMAS) determined from phased microphone arrays, *J. Sound Vib.* 294 (4) (2006) 856–879.
- [10] P. Sijtsma, CLEAN based on spatial source coherence, *Int. J. Aeroacoustics* 6 (4) (2007) 357–374.
- [11] T. Brooks, W. Humphreys, Three-dimensional applications of DAMAS methodology for aeroacoustic noise source definition, in: 11th AIAA/CEAS Aeroacoustics Conference, AIAA, 2005, p. 2960.
- [12] E. Sarradj, Three-dimensional acoustic source mapping with different beamforming steering vector formulations, *Adv. Acoust. Vibr.* (2012), <https://doi.org/10.1155/2012/292695> article ID: 292695.
- [13] T. Geyer, E. Sarradj, J. Giesler, Application of a beamforming technique to the measurement of airfoil leading edge noise, *Adv. Acoust. Vibr.* (2012), <https://doi.org/10.1155/2012/905461> article ID: 905461.
- [14] T. Padois, O. Robin, A. Berry, 3D source localization in a closed wind-tunnel using microphone arrays, in: 19th AIAA/CEAS Aeroacoustics Conference, AIAA, 2013, p. 2213.
- [15] A. Mimani, Z. Prime, D. Moreau, C. Doolan, An experimental application of aeroacoustic time-reversal to the aeolian tone, *J. Acoust. Soc. Am.* 139 (2) (2016) 740–763.
- [16] D. Döbler, J. Ocker, C. Puhle, On 3D-beamforming in the wind tunnel, in: Berlin Beamforming Conference, BeBeC-2016-S10, 2016.
- [17] T. Padois, A. Berry, Two and three-dimensional sound source localization with beamforming and several deconvolution techniques, *Acta Acustica United with Acustica* 103 (3) (2017) 392–400.
- [18] Y. Liu, A.R. Quayle, A.P. Dowling, P. Sijtsma, Beamforming correction for dipole measurement using two-dimensional microphone arrays, *J. Acoust. Soc. Am.* 124 (1) (2008) 182–191.
- [19] D.J. Moreau, Z. Prime, R. Porteous, C.J. Doolan, V. Valeau, Flow-induced noise of a wall-mounted finite airfoil at low-to-moderate Reynolds number, *J. Sound Vib.* 333 (25) (2014) 6924–6941.
- [20] R. Porteous, Z. Prime, C.J. Doolan, D.J. Moreau, V. Valeau, Three-dimensional beamforming of dipolar aeroacoustic sources, *J. Sound Vib.* 355 (2015) 117–134.
- [21] D.P. Arnold, T. Nishida, L.N. Cattafesta, M. Sheplak, A directional acoustic array using silicon micromachined piezoresistive microphones, *J. Acoust. Soc. Am.* 113 (1) (2003) 289–298.
- [22] W. Humphreys, Q. Shams, S. Graves, B. Sealey, S. Bartram, T. Comeaux, Application of MEMS microphone array technology to airframe noise measurements, in: 11th AIAA/CEAS Aeroacoustics Conference, AIAA, 2005, p. 3004.
- [23] S. Prbsting, F. Scarano, S. Morris, Regimes of tonal noise on an airfoil at moderate Reynolds number, *J. Fluid Mech.* 780 (2015) 407–438.
- [24] R.W. Paterson, P.G. Vogt, M.R. Fink, C.L. Munch, Vortex noise of isolated airfoils, *J. Aircraft* 10 (5) (1973) 296–302.
- [25] P. Migliore, S. Oerlemans, Wind tunnel aeroacoustic tests of six airfoils for use on small wind turbines, *J. Sol. Energy Eng.* 126 (4) (2004) 974–985.
- [26] C. Vanwynsberghe, R. Marchiano, F. Ollivier, P. Challande, H. Moingeon, J. Marchal, Design and implementation of a multi-octave-band audio camera for realtime diagnosis, *Appl. Acoust.* 89 (2015) 281–287.
- [27] N. Ono, H. Kohno, N. Ito, S. Sagayama, Blind alignment of asynchronously recorded signals for distributed microphone array, in: 2009 IEEE Workshop on Applications of Signal Processing to Audio and Acoustics, IEEE, 2009, pp. 161–164.
- [28] C. Vanwynsberghe, P. Challande, F. Ollivier, J. Marchal, R. Marchiano, Geometric calibration of very large microphone arrays in mismatched free field, *J. Acoust. Soc. Am.* 145 (1) (2019) 215–227.
- [29] R. Amiet, Refraction of sound by a shear layer, *J. Sound Vib.* 58 (4) (1978) 467–482.
- [30] L. Koop, K. Ehrenfried, S. Kroeber, Investigation of the systematic phase mismatch in microphone-array analysis, in: 11th AIAA/CEAS Aeroacoustics Conference, AIAA, 2005, p. 2962.
- [31] M. Howe, The influence of solid boundaries upon aerodynamic sound, *Proc. Roy. Soc. Lond. Math. Phys. Sci.* 231 (1955) 505–514.
- [32] C.J. Bahr, L.N. Cattafesta, Wavenumber-frequency deconvolution of aeroacoustic microphone phased array data of arbitrary coherence, *J. Sound Vib.* 382 (2016) 13–42.
- [33] D. Cassereau, M. Fink, Time-reversal of ultrasonic fields. III. Theory of the closed time-reversal cavity, *IEEE Trans. Ultrason., Ferroelec., Freq. Cont.* 39 (5) (1992) 579–592.
- [34] C. Bahr, N.S. Zawodny, T. Yardibi, F. Liu, D. Wetzel, B. Bertolucci, L. Cattafesta, Shear layer time-delay correction using a non-intrusive acoustic point source, *Int. J. Aeroacoustics* 20 (2011) 497–530.
- [35] T. Padois, C. Prax, V. Valeau, Numerical validation of shear flow corrections for beamforming acoustic source localisation in open wind-tunnels, *Appl. Acoust.* 74 (4) (2013) 591–601.
- [36] C. Bahr, N.S. Zawodny, T. Yardibi, F. Liu, D. Wetzel, B. Bertolucci, L. Cattafesta, Shear layer time-delay correction using a non-intrusive acoustic point source, *Int. J. Aeroacoustics* 10 (56) (2011) 497–530.
- [37] J. Gershfeld, Leading edge noise from thick foils in turbulent flows, *J. Acoust. Soc. Am.* 116 (3) (2004) 1416–1426.
- [38] T.F. Brooks, D.S. Pope, M.A. Marcolini, Airfoil self-noise and prediction, in: Tech. Rep., 1218, NASA Reference Publication, 1989.
- [39] D.J. Moreau, C.J. Doolan, W.N. Alexander, T.W. Meyers, W.J. Devenport, Wall-mounted finite airfoil-noise production and prediction, *AIAA J.* (2016) 1637–1651.
- [40] T.F. Geyer, D. Moreau, J. Giesler, P. Hall, E. Sarradj, C.J. Doolan, Measurement of the noise generated by wall-mounted airfoils of different thickness, in: 2018 AIAA/CEAS Aeroacoustics Conference, AIAA, 2018, p. 3796.
- [41] A. Uzun, M.Y. Hussaini, Simulations of vortex formation around a blunt wing tip, *AIAA J.* 48 (6) (2010) 1221–1234.

- [42] T. Imamura, S. Enomoto, H. Kato, Y. Yokokawa, K. Yamamoto, Numerical simulation of NACA0012 wingtip flow leading to noise generation, in: 11th AIAA/CEAS Aeroacoustics Conference, AIAA, 2005, p. 2864.
- [43] S.C. Bailey, S. Tavoularis, B.H. Lee, Effects of free-stream turbulence on wing-tip vortex formation and near field, *J. Aircraft* 43 (5) (2006) 1282–1291.
- [44] J. Fleming, R. Simpson, J. Cowling, W. Devenport, An experimental study of a turbulent wing-body junction and wake flow, *Exp. Fluid* 14 (5) (1993) 366–378.
- [45] F. Gand, V. Brunet, S. Deck, Experimental and numerical investigation of a wing-body junction flow, *AIAA J.* 50 (12) (2012) 2711–2719.
- [46] T.F. Brooks, M.A. Marcolini, Airfoil tip vortex formation noise, *AIAA J.* 24 (2) (1986) 246–252.
- [47] D.J. Moreau, C.J. Doolan, An experimental study of airfoil tip vortex formation noise, in: Proceedings of ACOUSTICS 2016, Brisbane, Australia, 2016.
- [48] D.J. Moreau, C.J. Doolan, Tonal noise production from a wall-mounted finite airfoil, *J. Sound Vib.* 363 (2016) 199–224.
- [49] Y. Zhou, F. Ollivier, P. Challande, R. Marchiano, V. Valeau, D. Marx, C. Prax, Design and use of a three-dimensional array of MEMS microphones for aeroacoustic measurements in wind-tunnels, in: Berlin Beamforming Conference, BeBeC-2020-D29, 2020.
- [50] S. Bousabaa, J. Bult, D.-C. Mincu, R. Marchiano, F. Ollivier, Sparse green's functions estimation using orthogonal matching pursuit: application to aeroacoustic beamforming, *AIAA J.* 56 (6) (2018) 2252–2270.
- [51] J. Fischer, V. Valeau, L.-E. Brizzi, Beamforming of aeroacoustic sources in the time domain: an investigation of the intermittency of the noise radiated by a forward-facing step, *J. Sound Vib.* 383 (2016) 464–485.

5.2 3D beamforming using two orientations of dipole

In this section, the 3D beamforming technique is used for the aeroacoustic source identification of a more complex geometry, *i.e.*, a wall-mounted airfoil with a cylinder attached perpendicularly to the wing tip (Section 2.7). The aeroacoustic radiation of a cylinder in a flow is dipolar, with its orientation being normal to its axis and to the flow direction. Therefore, dipolar noise sources with two perpendicular orientations are expected for this geometry (cylinder and trailing edge noise). A new strategy should be considered for the signal processing using the 3D beamforming technique.

5.2.1 Far-field spectrum results

Figure 5.1 shows the far-field spectrum of the wall-mounted airfoil with the cylinder at an angle of attack $\alpha = 0^\circ$ and flow speed 40 m/s. A strong tone component is observed at the frequency of 810 Hz (Strouhal number of 0.203). The cylinder is producing an aeolian tone with the Strouhal number close to 0.2, which is in agreement with the studies of Mimani *et al.* [83] and Norberg [90]. Moreover, the sound pressure level is increased in comparison to that of the single wall-mounted airfoil. The noise sources with frequencies in the third-octave bands [2245 Hz; 2828 Hz] and [3564 Hz; 4490 Hz] will be identified, corresponding to the frequency band A and B in Figure 5.1. In these two frequency bands, the noise generation is expected to be dominated by both the wall-mounted airfoil and the cylinder, which is of interest for the identification of dipolar noise sources with two different orientations. In these frequency bands, which lie outside the frequency domain of the aeolian tone, the cylinder emits broadband noise, probably due to the fine turbulence structure developed around the cylinder, superimposed to the Von Karman instability producing the aeolian tone at lower frequency.

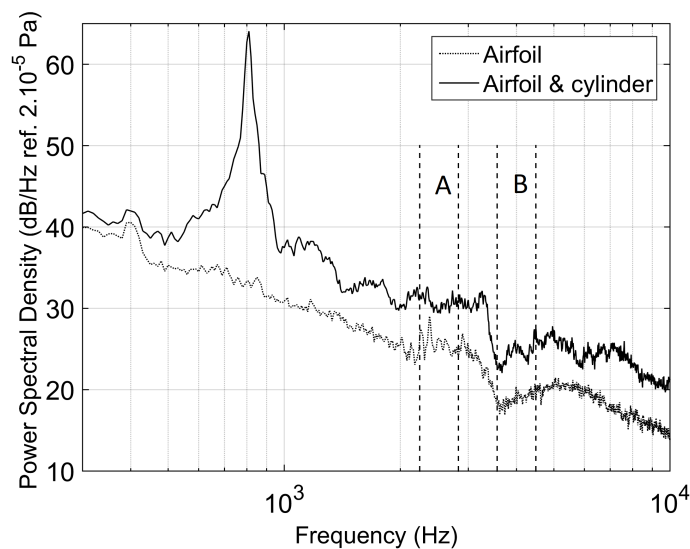


Figure 5.1: Far-field acoustic power spectral density for the wall-mounted finite airfoil with and without a cylinder at incoming velocity $U_\infty = 40$ m/s and angle of attack $\alpha = 0^\circ$.

5.2.2 3D beamforming results

A zonal approach is developed, for which the 3D scanning domain is divided into two parts: one partition contains the cylinder and the junction of the wing and the cylinder in a cuboid ($0.42 \text{ m} \leq x \leq 0.51 \text{ m}$, $-0.3 \text{ m} \leq y \leq 0.3 \text{ m}$, and $0.42 \text{ m} \leq z \leq 0.60 \text{ m}$); the rest of the domain contains the wall-mounted airfoil. For the signal processing using the 3D beamforming technique, a dipolar radiation model with an orientation in the z -direction is implemented for the former area and an orientation in the y -direction for the latter area. Figure 5.2 shows the corresponding sound maps. Figures 5.2(a) and 5.2(c) are difficult to interpret. After deconvolution, a much better spatial resolution is obtained for the sound maps. In Figure 5.2(b), some noise sources are identified on the tip of the airfoil. However, the noise sources may not be well identified because the nature of such sources in the airfoil-cylinder junction area is unknown. In addition, trailing edge noise sources along the span are observed in the area close to the wing tip. At the third-octave band of 4 kHz, in addition to the noise sources located in the areas of the junction and the trailing edge, two isolated noise sources are clearly identified in the tip areas of the cylinder (Figure 5.2(d)). Similarly, such sources are observed for wall-mounted cylinders with a aspect ratio (ratio of the span to the width or diameter) of 18.6 in the same area for the same third-octave band (Porteous [98]). As a conclusion to this preliminary study including two dipolar sources with different orientations, it can be said that a zonal approach for beamforming can be an efficient method producing 3D sound maps, but it requires a physical understanding of the potential sound sources in the flow.

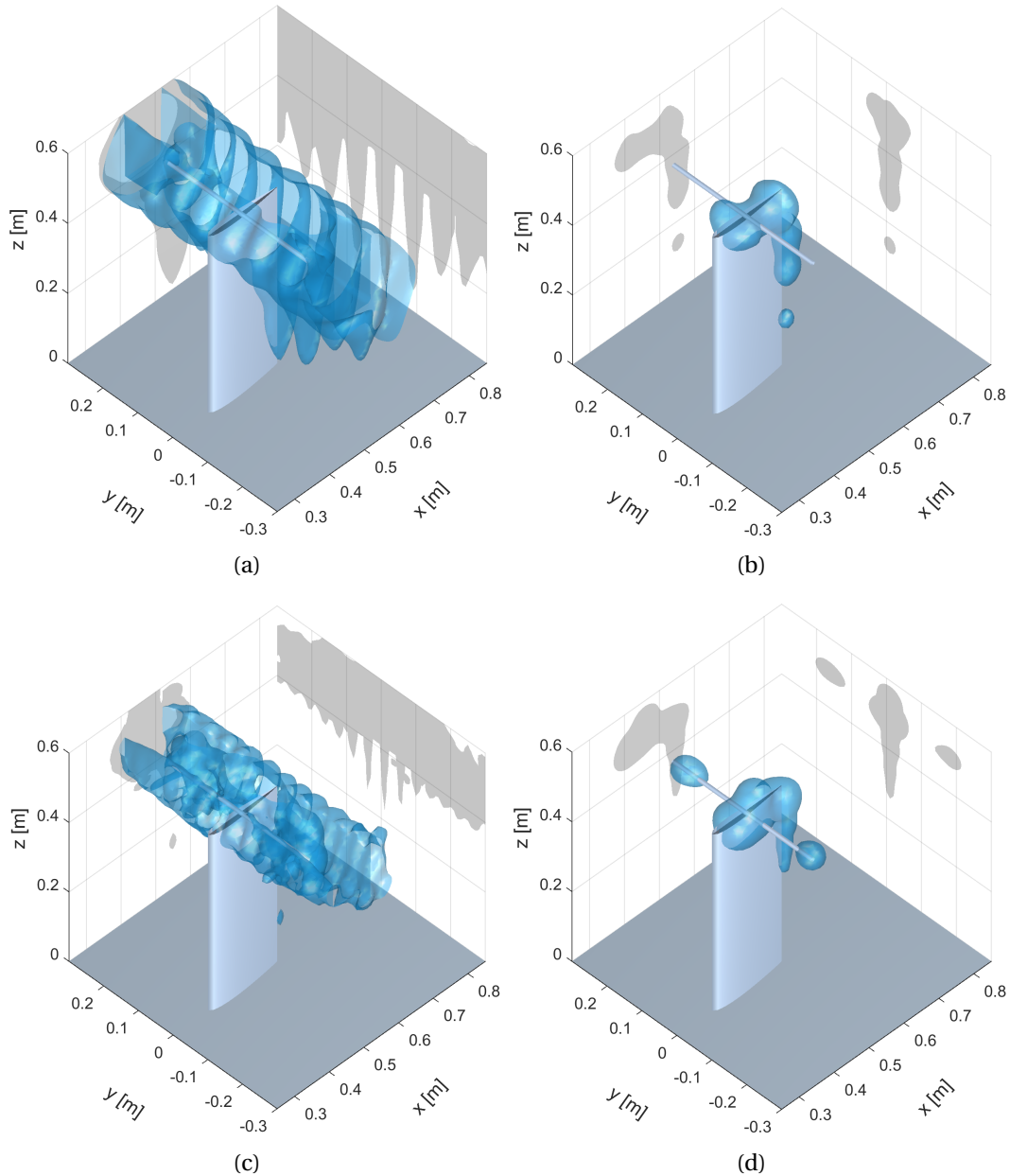


Figure 5.2: Sound maps for the wall-mounted finite airfoil with a perpendicular cylinder at incoming velocity $U_\infty = 40$ m/s and angle of attack $\alpha = 0^\circ$, at two third-octave bands of nominal midband frequency 2.5 kHz (top figures) and 4 kHz (bottom figures). (a) and (c): 3D dipolar beamforming with respectively a maximum value of 44.2 dB and 37.0 dB on the sound map; (b) and (d): CLEAN-SC technique with respectively a maximum value of 43.7 dB and 36.2 dB on the sound map. The 3D isosurface in each sound map is plotted at 10 dB below the maximum value of the sound map.

5.3 Summary of the chapter

In this chapter, the identification of the aeroacoustic sources of wall-mounted airfoils is conducted using the 3D microphone array. The 3D beamforming technique associated with the deconvolution method CLEAN-SC based on a dipolar radiation model is used for signal processing of the acoustic data obtained from the array measurements. The first part of the chapter deals with a wall-mounted airfoil and two parallel wall-mounted airfoils. Results

show that the 3D beamforming technique is promising for the investigation of aeroacoustic sources of complex geometries and MEMS microphones are good candidates for array measurements. The second part brings a first step in using a dipolar radiation model with different orientations in a scanning domain. Noise sources in the areas of the trailing edge of the wall-mounted airfoil and the tips of the cylinder are identified. Some sources are also identified in the airfoil-cylinder junction area, which are difficult to interpret because the nature of such sources is unknown.

This page is intentionally left blank.

Chapter 6

Noise source identification of a high-lift device model using beamforming technique

Contents

6.1 Far-field spectrum results	98
6.2 2D beamforming results of the high-lift device model	99
6.2.1 At angle of attack α 0°	100
6.2.2 At angle of attack α 6°	102
6.2.3 At angle of attack α 10°	105
6.3 3D beamforming results of the high-lift device model	106
6.3.1 At angle of attack α 0°	106
6.3.2 At angle of attack α 6°	108
6.3.3 At angle of attack α 10°	108
6.4 Summary of the chapter	109

In the previous chapter, the 3D beamforming technique was demonstrated to be promising for the noise source identification of objects with complex geometries in flow. In this chapter, a high-lift device model with multiple elements will be tested in the wind-tunnel flow. The far-field acoustic spectra will be first investigated. Then, the 2D beamforming technique will be used for the noise source identification. Finally, noise sources of the high-lift device model in flow will be identified in a 3D domain using the 3D beamforming technique.

6.1 Far-field spectrum results

The character of the aeroacoustic radiation of the high-lift device model and the effect of the flow velocity on the noise generation can be highlighted from the spectra, which will be presented in this section. In the following results, the frequency scale is used, and the sound pressure is normalized by the reference acoustic pressure $2 \cdot 10^{-5}$ Pa to obtain acoustic dB in order to observe the efficiency of the source at different velocities. For the case at angle of attack of $\alpha = 10^\circ$, the square pressure is also normalized by M^6 . The power 6 for the normalization is used following the bibliographical study: (i) the trailing edge noise source scales with U^6 when the chord length of the airfoil is lower than the acoustic wavelength; (ii) a dipolar radiation pattern of the slat noise was reported. The acoustic measurements for the spectra are based on a measurement microphone closed to the left-side sub array placed outside the wind-tunnel flows (Figure 2.8(a)).

Figure 6.1 shows the noise emissions at angle of attack $\alpha = 0^\circ$ and $\alpha = 6^\circ$ for the high-lift device model. In both cases, the noise is broadband at high velocities (40 and 50 m/s). At low velocities (20 and 30 m/s), some tonal components are found at frequencies higher than 5 kHz. However, based on a preliminary study of the noise source distribution, some isolated spurious noise sources were observed. So the spectra are contaminated by such sources. A possible solution is the use of an integration method on the sound maps, to remove the contamination. However, it is beyond the scope of the thesis.

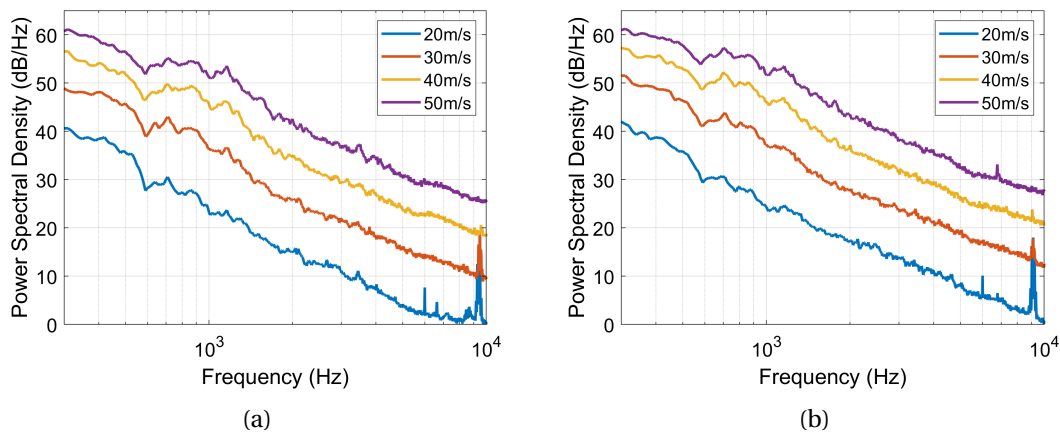


Figure 6.1: Far-field acoustic power spectral density for the high-lift device model at incoming velocity $U_\infty = 20, 30, 40$ and 50 m/s. PSD (dB/Hz ref. $2 \cdot 10^{-5}$ Pa) as a function of frequency for angle of attack (a) $\alpha = 0^\circ$, (b) $\alpha = 6^\circ$.

Figure 6.2(a) shows the noise emissions at an angle of attack $\alpha = 10^\circ$ for the high-lift device model. The increase of the velocities leads to higher sound power levels. For the case with higher velocities (20 and 30 m/s), the noise is of broadband nature. At low velocities of 10 and 15 m/s, tonal noise components are still observed at frequencies higher than 5 kHz. In Figure 6.2(b), the broadband spectra collapses well at frequencies between 1 kHz and 4 kHz for all cases. It means that the radiated sound intensity scales with M^6 . This is the character of compact dipole aeroacoustic source (Blake [17]), such as the noise produced by the trailing edge of an acoustically compact airfoil. Indeed, for the frequency band of [1 kHz; 4 kHz], the wavelength is higher than the chord length of the slat (54 mm). The slat noise can

be considered as acoustically compact. However, this is not in agreement with power scaling laws (M^x with x between 4 and 5) reported in the literature (Section 1.4.3)

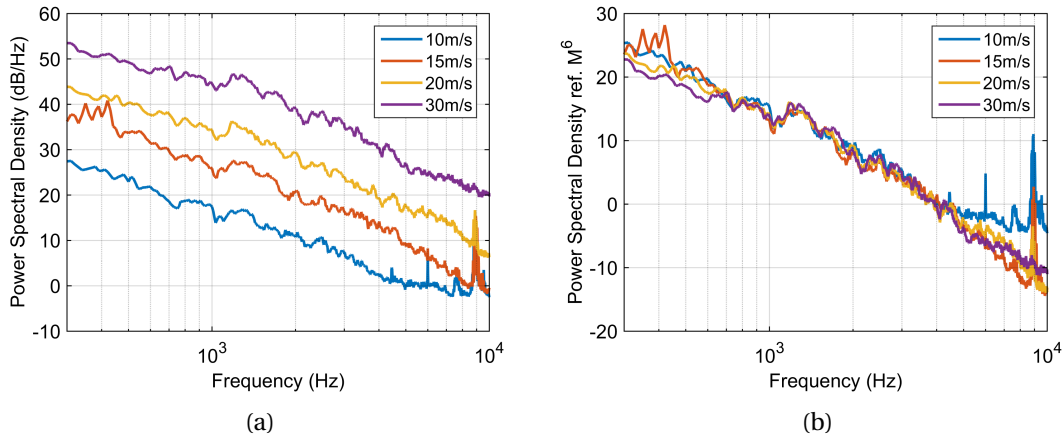


Figure 6.2: Far-field acoustic power spectral density for the high lift device model at incoming velocity $U_\infty = 10\text{--}30$ m/s for angle of attack $\alpha = 10^\circ$. (a) PSD (dB/Hz ref. 2.10^{-5} Pa) as a function of frequency, (b) PSD (dB/Hz ref. M^6) as a function of frequency.

6.2 2D beamforming results of the high-lift device model

The acoustic data from the 256 channels of the left side sub-array (see Chapter 2) are used for the 2D beamforming algorithm. In this case, the sub-array is on the pressure side of the high-lift device model. They were recorded at a sampling frequency of 50 kHz with a sampling time of 15 s for each test case, for which the results of the CSM is reached. The signal of each channel is filtered by a 256th order numerical high-pass filter with a cutoff frequency of 20 Hz to remove the slow variation of pressure occurring in the anechoic chamber. The CSM is computed using the Welch's method: each channel of data set was divided into 300 blocks containing 2500 sampling points without overlap and Hanning window. Thus the resolution frequency is 20 Hz. The CSM for 2D beamforming is a matrix of dimension $(256 \times 256 \times 2500)$ with 256 being the number of channels and 2500 being the number of discrete frequency values. The values of the diagonal elements of the CSM are set to 0. For the high-lift device model at angle of attack of 0° , a 2D scanning grid of dimension $0.8 \text{ m} \times 0.8 \text{ m}$ containing 25291 (161^2) points in a planar section was used for the sound maps. The spatial resolution for the grid is 5 mm. The scanning plane intersects the center line of the cross section of the middle part of the high-lift device model (see chapter 2). The nature of the noise sources is supposed to be monopolar for 2D beamforming. This assumption is normally made for the identification of a dipole noise source with its orientation being nearly normal to the array plane. Kröber [68] demonstrated that the assumption is still good even the angle between the array plane and the orientation of the dipole is up to 45° , only leading to a reduction of the peak level of sound map by 3 dB. The orientations of the dipolar noise sources in our case are not severely deflected with respect to the normal direction of the array plane, so a monopole radiation can be implemented for the 2D beamforming. The Amiet's method is used for the correction of the flow effect. Note that the solid boundaries and the non-uniform flow around objects are not accounted for by the beamforming technique and the Amiet's method. Additionally, a modification of the CSM is conducted in order to remove the

background noise of the test section from sound maps. The equation for the computation of 2D beamforming values in the frequency domain [60] is given by

$$|Z(\mathbf{x}_f, \omega)|^2 = \frac{e^H \mathbf{W} (\mathbf{C} - \mathbf{C}_{BN}) \mathbf{W} e}{M^2}, \quad (6.1)$$

where \mathbf{C} is the CSM based on acoustic signals obtained with the high-lift device model in the test section, and \mathbf{C}_{BN} is the CSM based on acoustic signals of the background noise of the test section without testing models.

2D beamforming results are given in third-octave bands in the following sections, for which the beamforming sound maps for each frequency bin contained in a given third-octave band are computed and summed. Two third-octave bands [2245 Hz; 2828 Hz] and [3564 Hz; 4490 Hz] with respective nominal midband frequencies of 2.5 and 4 kHz are considered for investigations. In the following 2D sound maps, the black points stand for the 256 microphones and the rectangle in the right of the figures stands for the nozzle of the wind-tunnel. The red sketch on top of the figures indicates the position of the elements of the high-lift device model. The zoomed versions of the 2D sound maps presented in this section can be found in the Appendix D.1.

6.2.1 At angle of attack α 0°

Figure 6.3 present the sound maps of the high-lift device model at incoming velocity $U_\infty = 40$ m/s (Reynolds number being 1.07×10^6 as indicated in chapter 2) and angle of attack $\alpha = 0^\circ$. The dashed line intersecting the cross section of the high-lift device model stands for the scanning plane for the beamforming technique. The component between the two black lines represents the part of the high-lift device model under investigation (located between the end plates). Figure 6.3(a) shows the beamforming result for the third-octave band of 2.5 kHz. A dominant lobe evenly distributed along the span in the cove area of the main element is observed. After deconvolution using the CLEAN-SC technique, a better resolution is achieved. It indicates that the dominant noise sources are located upstream of the main element trailing edge together with some secondary noise sources downstream (see Figure 6.3(b)). According to the principle of the CLEAN-SC method, the dominant noise sources are incoherent between each other. Figure 6.3(c) shows the beamforming result for the third-octave band of 4 kHz. The size of the dominant lobe decreases at higher frequencies which allows a better resolution. In Figure 6.3(d), it is highlighted that a line source is centered on the split between the flap and the main element after deconvolution. But it is difficult to know if the generation of the line source is dominated by one of the corresponding objects or both for the reason that the impingement of vortices on the flap leading edge and the scattering of turbulent boundary layer at the main element trailing edge could generate noise. Note that few publications deal with such noise source. Also, the noise sources shown in Figure 6.3(b) are shifted upstream with respect to that in Figure 6.3(d). It is not clear if this is due to the error introduced by the flow effect correction for which the uniform flow hypothesis is questionable. Therefore the advanced method like time-reversal, for which the solid boundaries and the non-uniform flow around objects are considered, could be used to understand this point (which was not achieved in the present thesis).

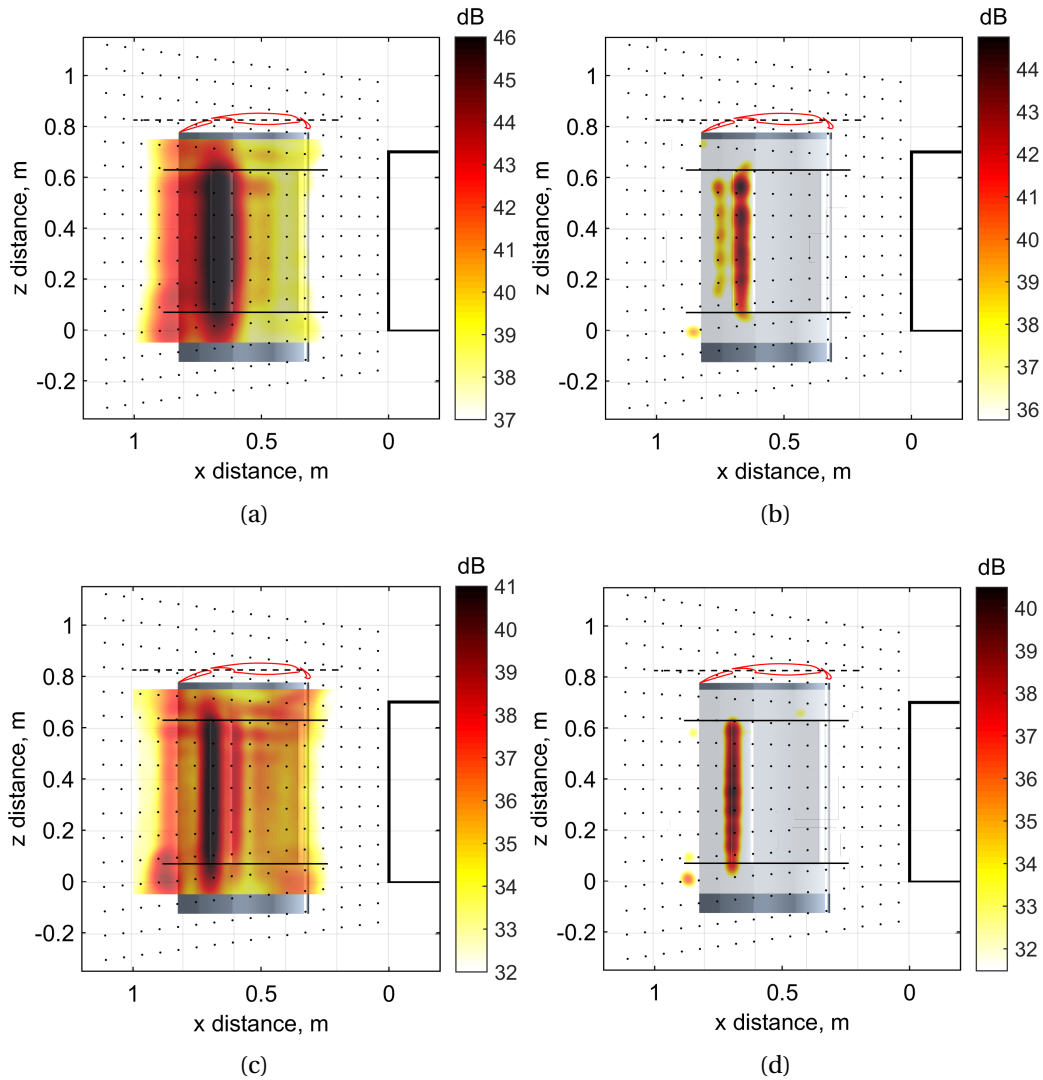


Figure 6.3: Sound maps for the high-lift device model at incoming velocity $U_\infty = 40$ m/s and angle of attack $\alpha = 0^\circ$, at two third-octave bands of nominal midband frequency 2.5 kHz (top figures) and 4 kHz (bottom figures). (a) and (c): 2D beamforming using monopole steering vector; (b) and (d): CLEAN-SC technique using monopole steering vector.

To investigate if the generation of the dominant noise sources shown in Figure 6.3 is dominated by the leading edge of the flap, the flap was removed from the high-lift device model for the wind-tunnel testing under the same conditions. Figures 6.4(a) and 6.4(c) present the beamforming results which are difficult to interpret. Figures 6.4(b) and 6.4(d) show the sound maps after deconvolution. In Figure 6.4(b), several isolated noise sources are identified at the trailing edge of the main element with lower strengths with respect to that in Figure 6.3(b). In Figure 6.4(d), noise sources distributed along the span at the main element trailing edge are detected. The strengths of the line sources is about lower than that in Figure 6.3(d). Additionally, noise sources outside the middle part of the high-lift device model are observed, which are not under investigation: they are due to the interaction of the shear layer with the part of the mock-up located outside the end plates. Therefore, it is suggested that the dominant noise sources in Figure 6.3 originate from a mechanism involving both the trailing edge of the main element and the leading edge of the flap. For the third-octave band of 4 kHz, the generation of the noise sources decreases about 4 dB by removing the flap.

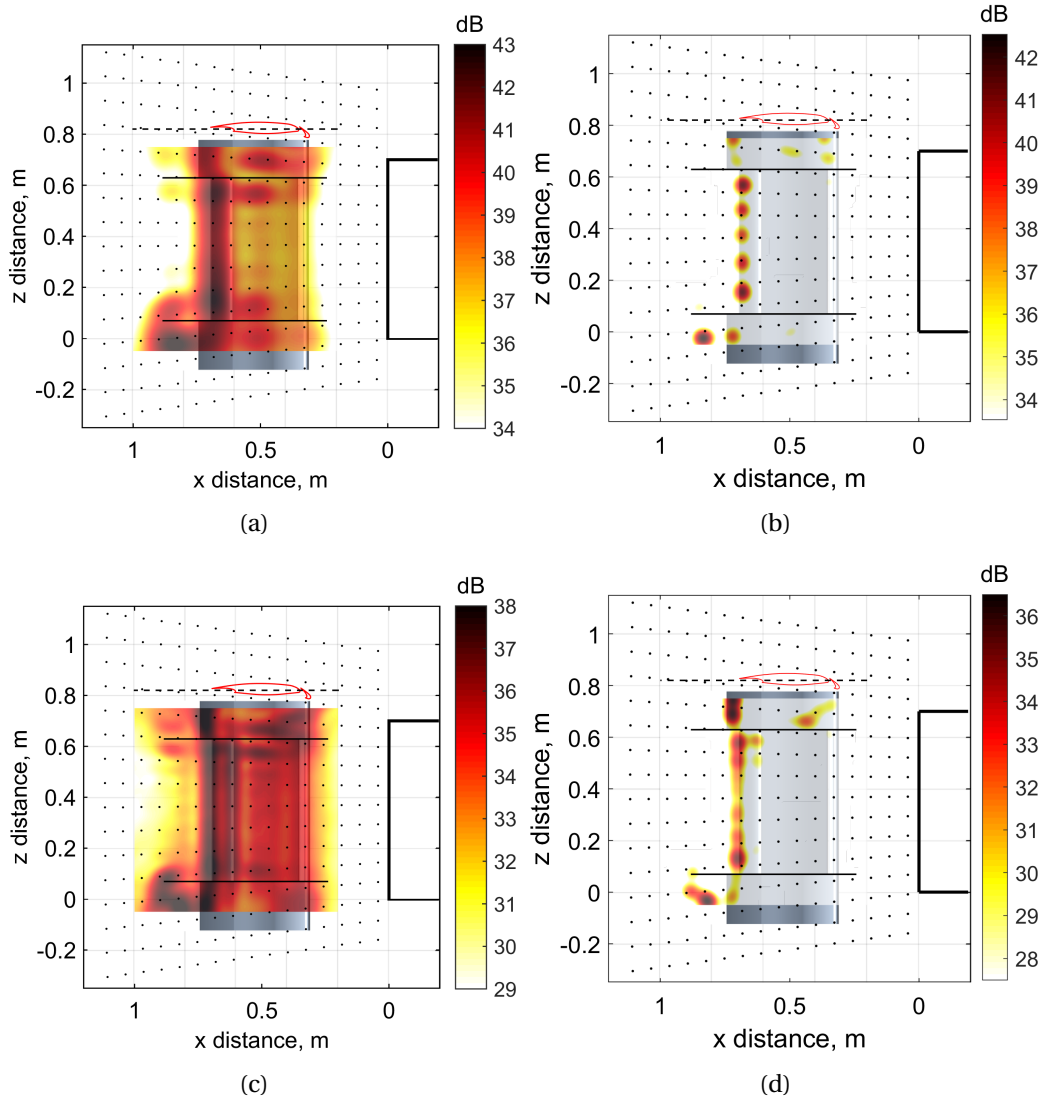


Figure 6.4: Sound maps for the high-lift device model without flap at incoming velocity $U_\infty = 40$ m/s and angle of attack $\alpha = 0^\circ$, at two third-octave bands of nominal midband frequency 2.5 kHz (top figures) and 4 kHz (bottom figures). (a) and (c): 2D beamforming using monopole steering vector; (b) and (d): CLEAN-SC technique using monopole steering vector.

6.2.2 At angle of attack $\alpha = 6^\circ$

The results at incoming velocity $U_\infty = 40$ m/s and angle of attack $\alpha = 6^\circ$ using the 2D beamforming technique are depicted in Figures 6.5(a) and 6.5(c) for two third-octave bands with respective midband frequency 2.5 and 4 kHz. At frequency 2.5 kHz, two dominant spots distributed along the span in the vicinity of the trailing edge of the main element and the slat cove are observed (see Figure 6.5(a)). After deconvolution, five incoherent isolated noise sources are identified at the main element trailing edge. In addition, noise sources take place along the span of the main element leading edge. However, Yser and Bailly [123] indicated that three different noise components exist in the slat area, which are generated by vortex shedding at the slat trailing edge, impingement of shear layer inside the slat cove, and the interaction of the slat wake with the main body at similar angle of attack and Reynolds number. Thus it can be also interpreted as noise sources at the slat trailing edge knowing that

the spatial resolution perpendicular to the scanning plane is bad, *i.e.*, it is difficult to know the real position of the noise sources in this direction. That is the interest for noise source identification in a 3D zone. Similarly, noise sources mainly located along the flap and slat of a high lift device model at angle of attack $\alpha = 6.4^\circ$ and frequency of 2 kHz were reported by Manob and Pott-Pollenske [75]. The difference of the model is that the flap and slat were attached to the main element by brackets. At frequency 4kHz, two dominant line sources along the span can be found in the same place with smaller size thus better resolution (see Figure 6.5(c)). After deconvolution, two line sources with a more even distribution along the span than that at lower frequencies can be seen in Figure 6.5(d). Among them, one is located slightly downstream of the main element trailing edge, the other is located in the slat cove. It is difficult to interpret the source position difference concerning the slat noise in the two third-octave bands. The reason is probably twofold: (i) the noise generation mechanism is different at lower and higher frequencies; (ii) the flow effect correction method introduces some errors in terms of the position.

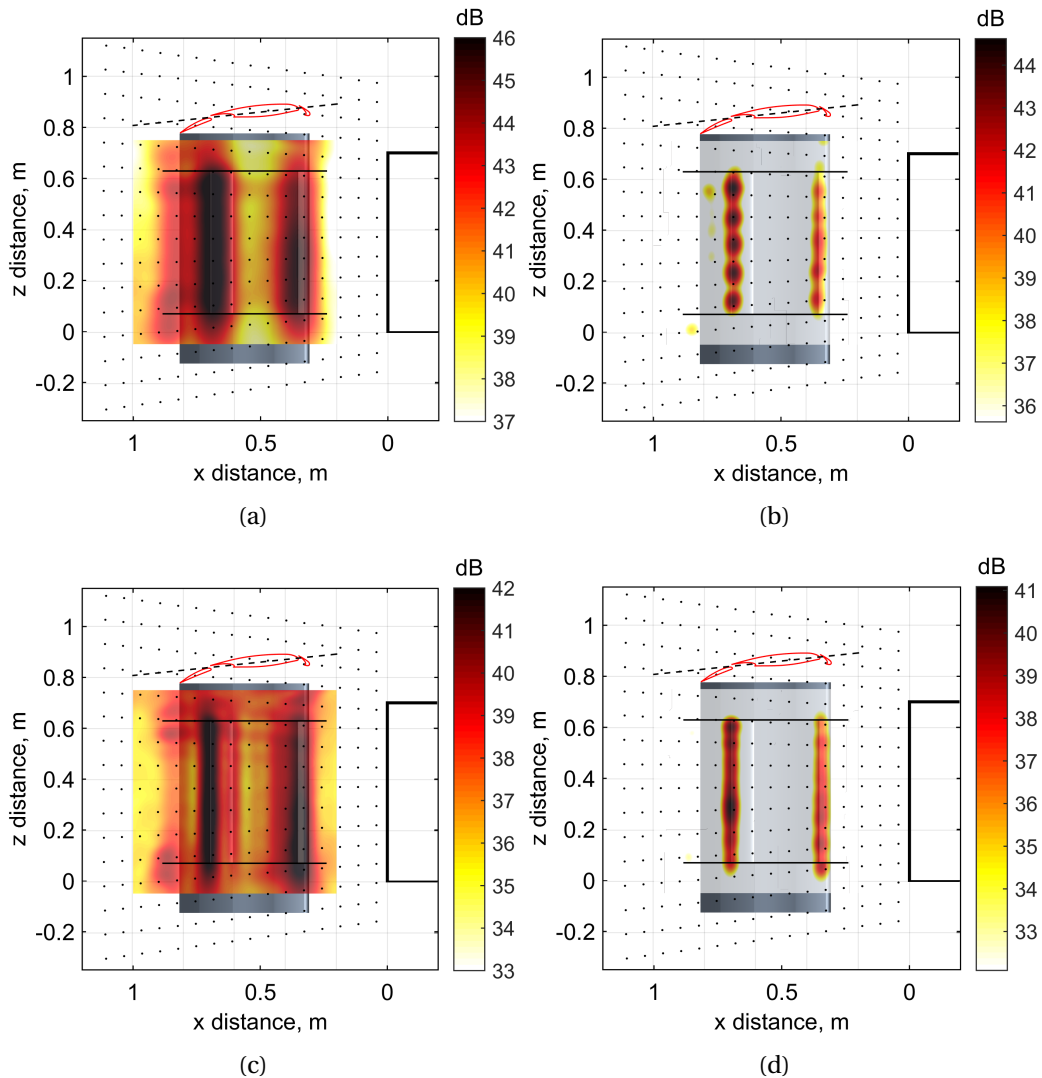


Figure 6.5: Sound maps for the high-lift device model at incoming velocity $U_\infty = 40$ m/s and angle of attack $\alpha = 6^\circ$, at two third-octave bands of nominal midband frequency 2.5 kHz (top figures) and 4 kHz (bottom figures). (a) and (c): 2D beamforming using monopole steering vector; (b) and (d): CLEAN-SC technique using monopole steering vector.

To investigate which part of the high-lift device model dominates the line source in the flap area (see Figure 6.5), the high-lift device model without flap is tested again under the same conditions. Figure 6.6(a) and 6.6(c) shows the beamforming results of third-octave bands at respective frequency 2.5 kHz and 4 kHz, from which the distribution of the noise sources is not clear. After deconvolution, dominant noise sources along the span are found at the trailing edge of the main element with lower intensity than that in Figure 6.5(b). In addition, several isolated noise sources along the span are observed at the leading edge of the main element. In Figure 6.6(d), noise sources evenly distributed along the span are located at the trailing edge of the main element with lower intensity than in Figure 6.5(d). The slat cove also appears as a significant source of noise. It is suggested that the presence of the flap amplifies the noise sources. The distribution of the noise sources in the slat area being slightly different from what is shown in Figure 6.5 may be due to the change of the dynamic range of sound maps and the flow regime around the model.

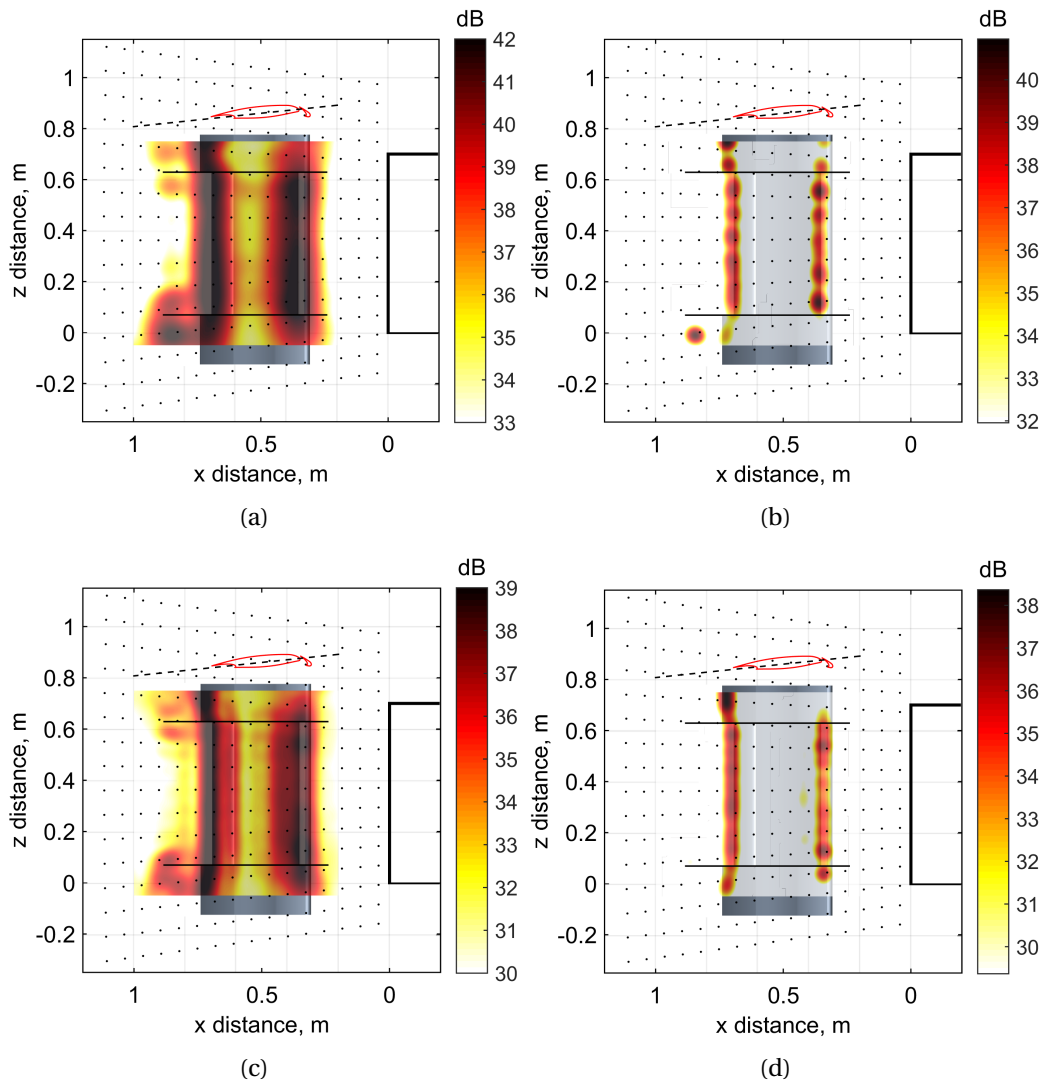


Figure 6.6: Sound maps for the high-lift device model without flap at incoming velocity $U_\infty = 40$ m/s and angle of attack $\alpha = 6^\circ$, at two third-octave bands of nominal midband frequency 2.5 kHz (top figures) and 4 kHz (bottom figures). (a) and (c): 2D beamforming using monopole steering vector; (b) and (d): CLEAN-SC technique using monopole steering vector.

6.2.3 At angle of attack $\alpha = 10^\circ$

The maximum wind-tunnel flow speed for the test case at angle of attack $\alpha = 10^\circ$ is 30 m/s to avoid the potential damage of the microphone array caused by the wind-tunnel flow deflected by the experimental device at high angle of attack. Figure 6.7(a) shows the beamforming results of 2.5 kHz of the high-lift device model, from which a dominant lobe along the span in the slat area can be clearly seen. A line source in the slat cove is well identified, with higher strength in the middle of part of the model. The distribution of the dominant noise source is almost the same at higher frequencies as shown by Figures 6.7(c) and 6.7(d). This is in agreement with the fact that slat noise dominates the noise generation of high-lift device model at high angle of attack (Pascioni and Cattafesta, 2018). The high-lift device of civil aircrafts in landing approach is at high angle of attack. That is the reason why the research of the noise generation of high-lift device in the literature attach importance of the slat noise.

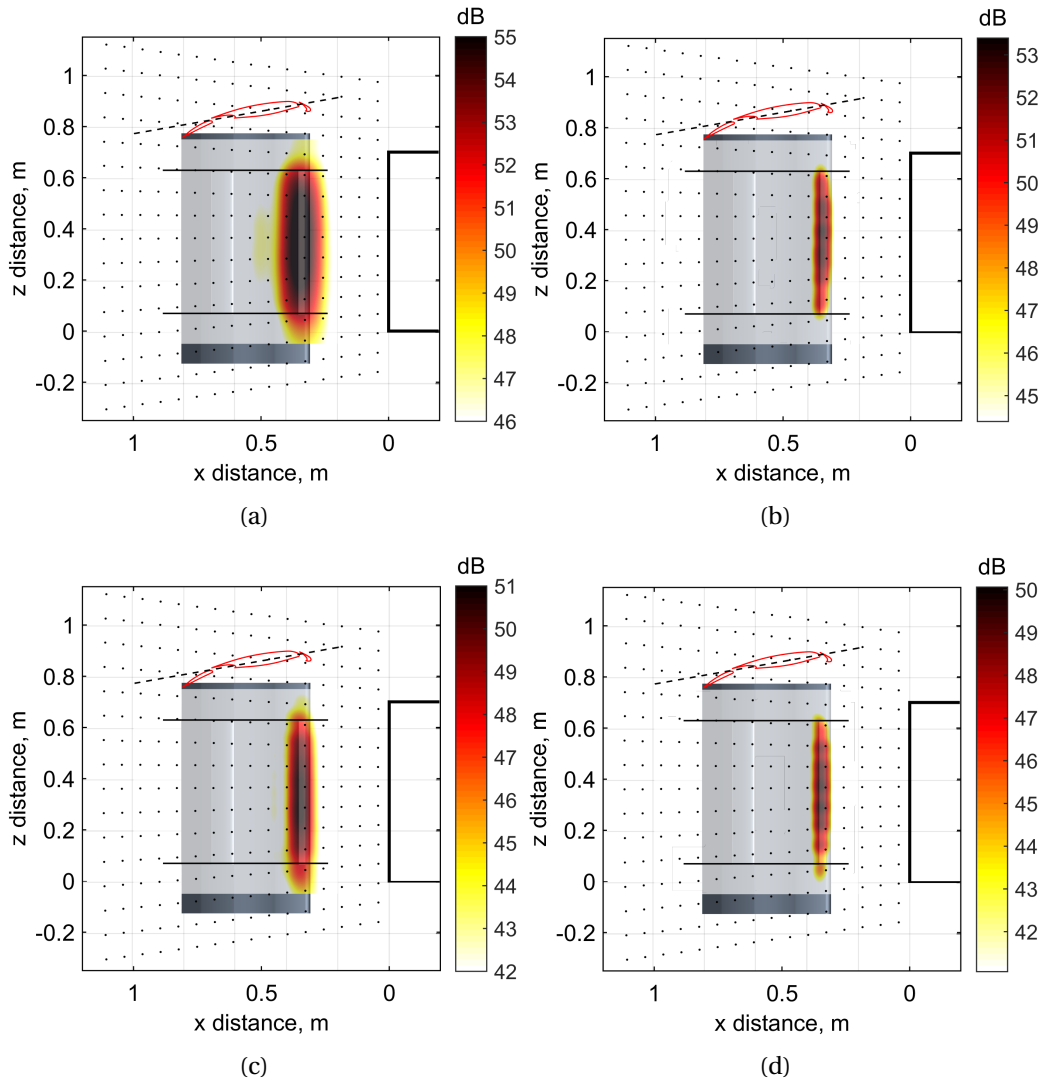


Figure 6.7: Sound maps for the high-lift device model at incoming velocity $U_\infty = 30$ m/s and angle of attack $\alpha = 10^\circ$, at two third-octave bands of nominal midband frequency 2.5 kHz (top figures) and 4 kHz (bottom figures). (a) and (c): 2D beamforming using monopole steering vector; (b) and (d): CLEAN-SC technique using monopole steering vector.

6.3 3D beamforming results of the high-lift device model

256 channels of the acoustic data are selected and used for the 3D beamforming algorithm. They were recorded at a sampling frequency of 50 kHz with a sampling time of 15 s for each test case. The same signal processing method as that of 2D cases is used for the calculation of the CSM. A 3D scanning grid containing 531441 points in a cube of dimensions $0.8 \times 0.8 \times 0.8$ is used for the sound maps (see Figure 6.8). It is composed of cubes with an edge length of 10 mm. The Amiet's method is used for the correction of the flow effect in terms of angle correction. According to the 2D beamforming results, the dominant noise sources are located near the main element trailing edge for the high-lift device model at angle of attack $\alpha = 0^\circ$, and near the slat area at angle of attack $\alpha = 10^\circ$, so a dipolar radiation model with a single orientation is implemented for the whole scanning domain (Figure 6.8(a)). For the high-lift device model at angle of attack $\alpha = 6^\circ$, the dominant noise sources are located near the main element trailing edge and the slat trailing edge. For the signal processing using the 3D beamforming technique, the 3D scanning domain are then divided into two parts (Figure 6.8(b)), each for a dipolar assumption with its orientation being normal to the slat or the flap (Figure 6.8(c)).

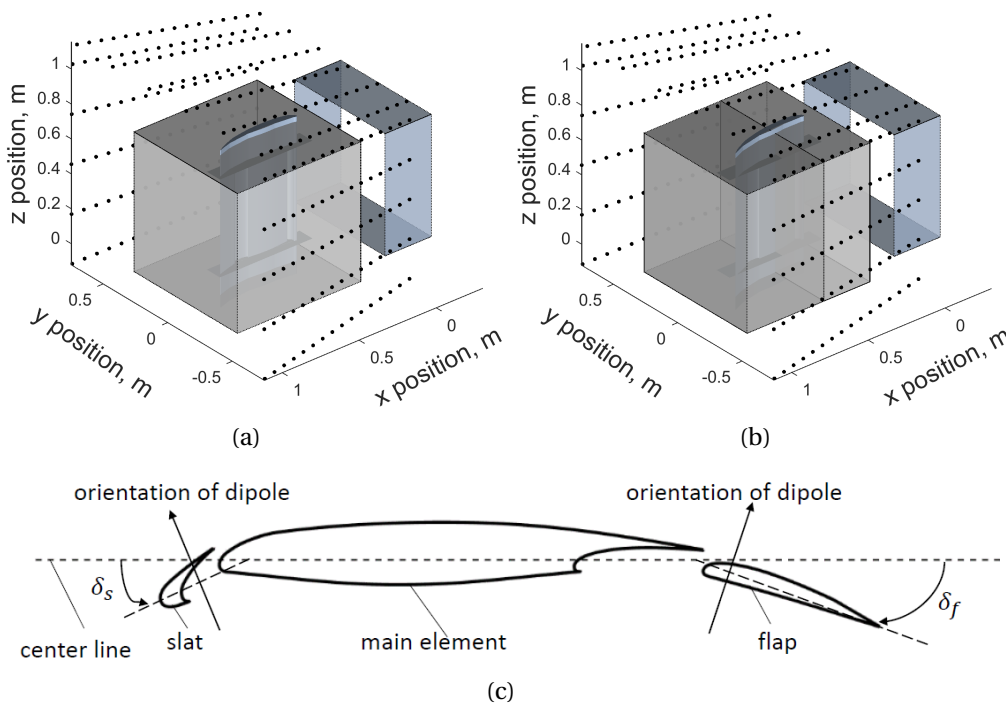


Figure 6.8: Schematic depicting the scanning domain for the high-lift device model (a) at angle of attack $\alpha = 0^\circ$ and $\alpha = 10^\circ$; (b) at angle of attack $\alpha = 6^\circ$. (c) Cross section of the high-lift device model with two orientations for a dipolar radiation model. The black points indicate the positions of the 256 microphones. The cubes enclosing the high-lift device model stand for the scanning domain. The blue patches stands for the nozzle of the wind-tunnel.

6.3.1 At angle of attack $\alpha = 0^\circ$

In this case, a dipolar assumption with its orientation being normal to the flap surface is implemented. Figures 6.9(a) and 6.9(c) present the 3D beamforming results, which are difficult

to interpret. After deconvolution, it is found that noise sources along the span are located along the trailing edge of the main element (see Figures 6.9(b) and 6.9(d)). In Figure 6.9(b), the line source is located upstream of the main element trailing edge, which is consistent with the 2D result (see Figure 6.3(b)). In Figure 6.9(d), noise sources with lower strength take place besides the dominant line source. They may be some artifacts originating from side lobes for the reason that the scanning domain is not large enough.

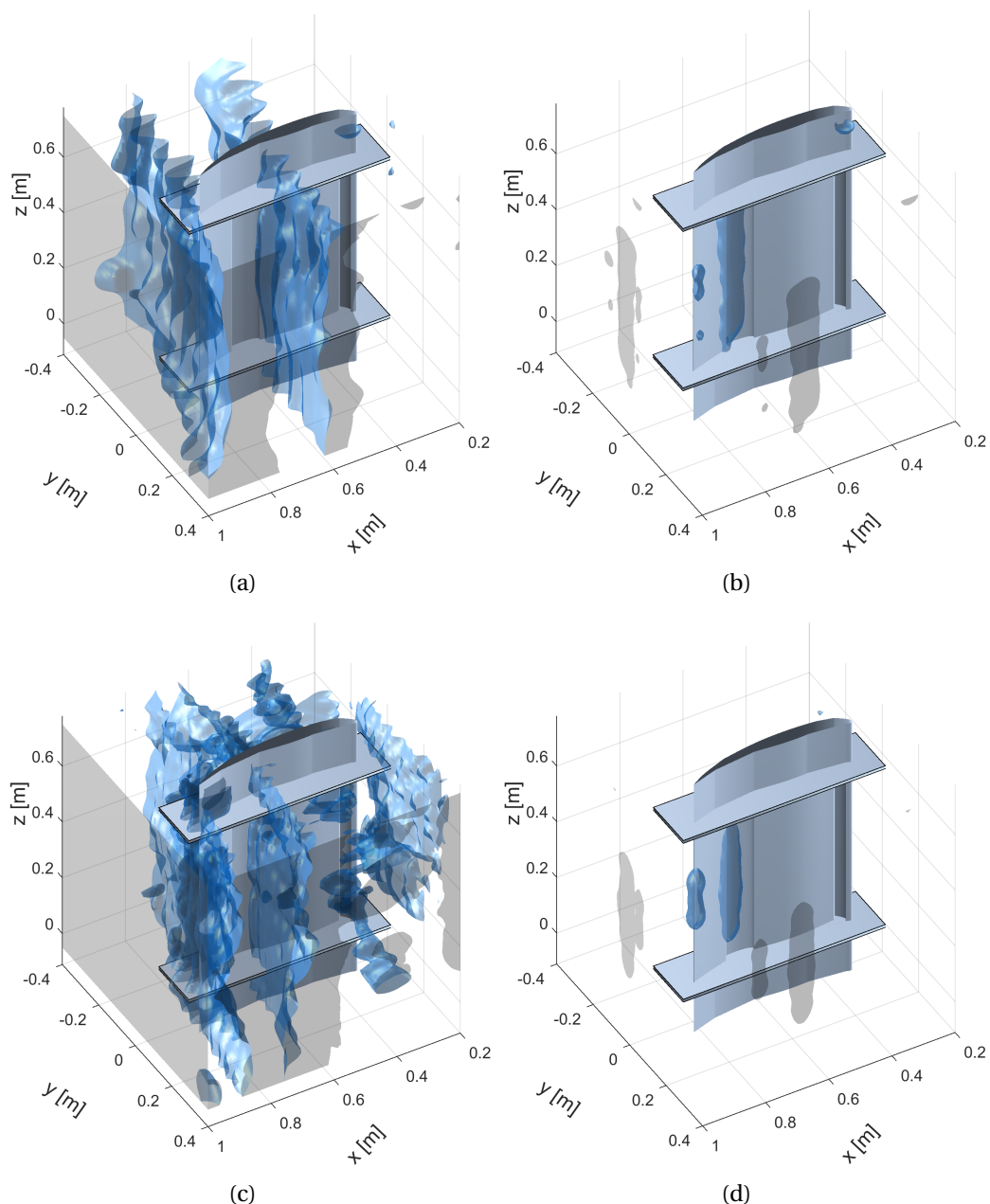


Figure 6.9: Sound maps for the high-lift device model at incoming velocity $U_\infty = 40$ m/s and angle of attack $\alpha = 0^\circ$, at two third-octave bands of nominal midband frequency 2.5 kHz (top figures) and 4 kHz (bottom figures). (a) and (c): 3D dipolar beamforming with respectively a maximum value of 41.3 dB and 37.0 dB on the sound map; (b) and (d): CLEAN-SC technique with respectively a maximum value of 38.9 dB and 36.2 dB on the sound map. The 3D isosurface in each sound map is plotted at 9 dB below the maximum value of the sound map. The shadows correspond to the projection of the 3D sound source imaging in different directions.

6.3.2 At angle of attack α 6°

In this case, a dipolar assumption with its orientation being normal to the slat surface and the flap surface is implemented. For simplicity, the 3D beamforming results without deconvolution are presented in the Appendix D.2. Figures 6.10(a) and 6.10(b) present the 3D beamforming results after deconvolution. At the two third-octave bands, line noise sources are identified near the trailing edge of the main element. Some side lobes beside them are not removed by the CLEAN-SC method, which may be due to the fact that the spatial resolution of the scanning grid is large (10 mm). However, the slat noise are not identified by the 3D beamforming technique (with only one isolated noise source in the slat area). The assumption on the nature of the noise sources in this part may not be correct.

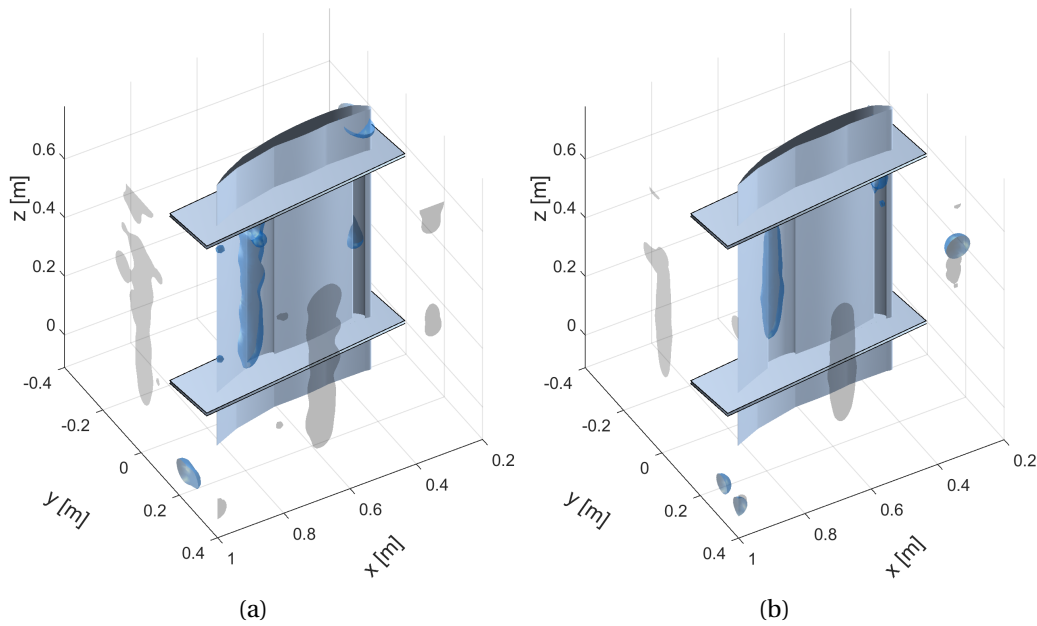


Figure 6.10: Sound maps using CLEAN-SC technique for the high-lift device model at incoming velocity $U_\infty = 40$ m/s and angle of attack $\alpha = 6^\circ$, at two third-octave bands of nominal midband frequency 2.5 kHz (a) and 4 kHz (b) with respectively a maximum value of 38.9 dB and 37.8 dB. The 3D isosurface in each sound map is plotted at 9 dB below the maximum value of the sound map. The shadows correspond to the projection of the 3D sound source imaging in different directions.

6.3.3 At angle of attack α 10°

In this case, a dipolar assumption with its orientation being normal to the slat surface is implemented. For simplicity, the 3D beamforming results without deconvolution are presented in the Appendix D.2. Figures 6.11(a) and 6.11(b) present the 3D beamforming results after deconvolution. At the two third-octave bands, line noise sources are identified near the slat trailing edge or in the cove area, which confirms the 2D results. Some side lobes are found to be located beside the line source at the third-octave band of 2.5 kHz, which may be due to the fact that the spatial resolution of the scanning grid is large (10 mm).

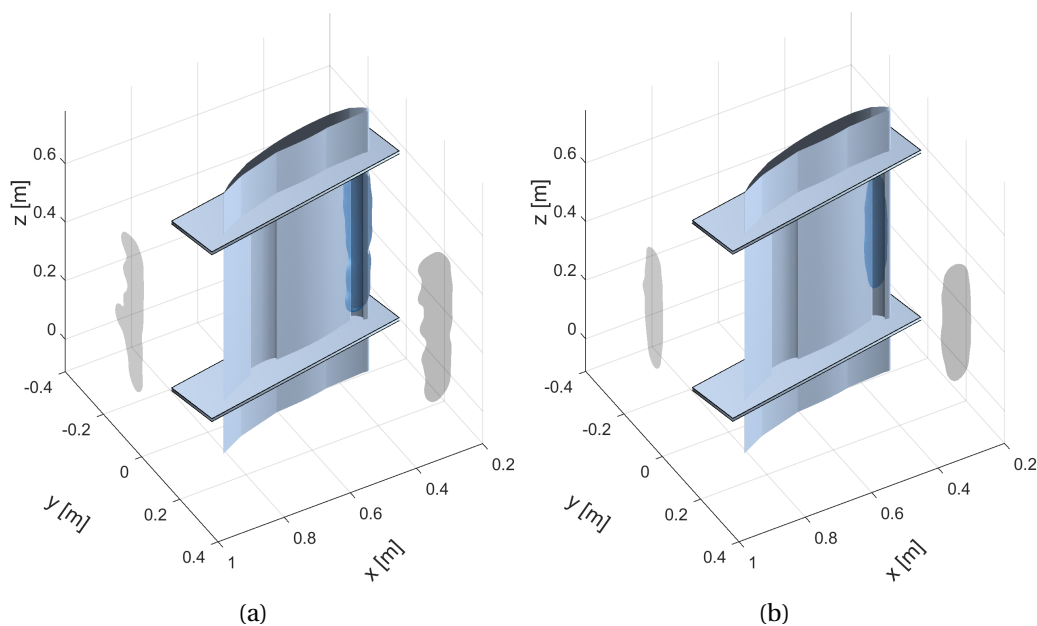


Figure 6.11: Sound maps using CLEAN-SC technique for the high-lift device model at incoming velocity $U_\infty = 30$ m/s and angle of attack $\alpha = 10^\circ$, at two third-octave bands of nominal midband frequency 2.5 kHz (a) and 4 kHz (b) with respectively a maximum value of 48.0 dB and 43.8 dB. The 3D isosurface in each sound map is plotted at 9 dB below the maximum value of the sound map. The shadows and correspond respectively to the projection of the 3D sound source imaging in different directions.

6.4 Summary of the chapter

This chapter is dedicated to the study of the aeroacoustic noise distribution of on a high-lift device model. The far-field acoustic spectra are first given, showing that the noise is of broadband nature at the frequencies under study. The 2D beamforming technique associated with the deconvolution method CLEAN-SC is used for signal processing. The wind-tunnel flow effects are corrected using the Amiet's method in terms of angle correction. Noise sources in the areas of the slat, and the trailing edge of the main element are identified under different testing conditions. The performances of the 3D beamforming technique are evaluated using 256 channels of the acoustic data measured by the 3D array. A dipolar noise source assumption with its orientation being normal to the slat or the flap is used. The identified dominant noise sources for the cases of angle of attack of 0° and 10° confirm the 2D results. However, for the case of angle of attack of 6° , the slat noise is not identified, which may be due to wrong assumption on the sound radiation model.

This page is intentionally left blank.

Part II

Noise source identification based on the time-reversal technique

Chapter 7

2D numerical time-reversal

Contents

- 7.1 2D numerical TR without flow 114**
 - 7.1.1 Validation by a 2D case 114
 - 7.1.2 Identification of an acoustic pulse in a semi-open cavity 116
 - 7.1.3 Identification of an acoustic pulse scattered by an airfoil 120
 - 7.1.4 Feasibility of implementation of an acoustic sink 123
- 7.2 Identification of a dipole scattered by an airfoil in a flow 126**
 - 7.2.1 RANS simulation and validation 126
 - 7.2.2 2D TR results 127
- 7.3 Summary of the chapter 131**

This chapter is dedicated to the applications of the 2D numerical TR technique for the identification of synthetic noise sources (simulated data instead of experimental data). The first part concerns the situations without background mean flow for an acoustic pulse and a monopolar noise source. On the one hand, an acoustic pulse is identified in different situations; on the other hand, the monopolar noise source in a simulation domain without the presence of solid boundaries is identified, and the acoustic sink is applied to the 2D TR process in order to improve the resolution of the TR result. In the second part, the case of a dipolar noise source with background mean flow around a 2D NACA 0012 airfoil is addressed. In this purpose, to obtain a realist background mean flow including the viscous effects, a RANS simulation is carried out for the 2D NACA airfoil.

7.1 2D numerical TR without flow

The TR process is first validated based on the 2D benchmark problem presented in Section 3.3.1. In the context of aeroacoustic applications, the two main advantages of the numerical TR technique are its ability: (i) to deal with heterogeneous media (involving spatial variations of the speed of sound); (ii) to take into account solid boundaries. For this reason, two situations are considered in this section. The identification of an acoustic pulse inside a semi-open cavity using the 2D TR technique is conducted to evaluate its performance. Two situations are distinguished: one is conducted for a medium with a uniform sound speed, the other deals with the case with a medium with non-uniform sound speed. Then the identification of an acoustic pulse scattered by an airfoil is carried out. Several types of TR mirrors are studied in order to compare their performances with the TR cavity. Finally, the identification of a monopolar noise source is conducted. To improve the resolution of 2D TR, the acoustic sink is applied for the 2D TR process.

7.1.1 Validation by a 2D case

The benchmark problem (Section 3.3.1) concerning the scattering of an acoustic pulse in a quiescent medium is revisited for the TR process. To this end, the direct simulation concerning the scattering of the acoustic pulse off the cylinder is conducted with the recording of the acoustic information at the whole boundaries of the simulation domain. Then the TR process is conducted in order to identify the acoustic pulse. The simulation domain has a dimension of $16 \text{ m} \times 16 \text{ m}$. The diameter of the cylinder is 1 m . Three recording points around the cylinder with a distance of 3 m from its center are placed inside the simulation domain. The position of the points are A ($0 \text{ m}, 3 \text{ m}$), B ($-2.1213 \text{ m}, 2.1213 \text{ m}$), and C ($0 \text{ m}, 3 \text{ m}$). Figure 7.1 shows the partitions of the numerical simulation domain, which is more refined for the mesh elements closer to the cylinder. The mesh was decomposed into 190 partitions for the parallel computation, which are shown by different colors. A polynomial order of 3 was used for the nodal DG method. For the direct simulation and 2D TR, the sound speed is 1 m/s , and the density of the medium is 1 kg/m^3 . The direct simulation is firstly conducted. An acoustic pulse with a Gaussian distribution in space was initially placed at the right side of the cylinder with a distance of 4 m from the center of the cylinder. The boundary of the simulation domain uses "free-rec" boundary condition to record the acoustic signals on the nodes of the mesh at the boundary for every time step of the numerical simulation. The physical time of the numerical simulation is 16 s . For simplicity, the results of the direct simulation are not presented. To identify the acoustic pulse, the 2D TR is then conducted: the acoustic signals recorded at the boundary are reversed and re-emitted as monopole sources [49] on the same positions, which is achieved by using "BCfile" boundary condition at the boundary of the simulation domain. Their amplitudes are multiplied by a factor of 2 for the reason that only half of the energy emitted by the monopole sources at the boundary enters the simulation domain. It allows to retrieve the original amplitude of an acoustic pulse using the TR technique (Padois *et al.* [94]).

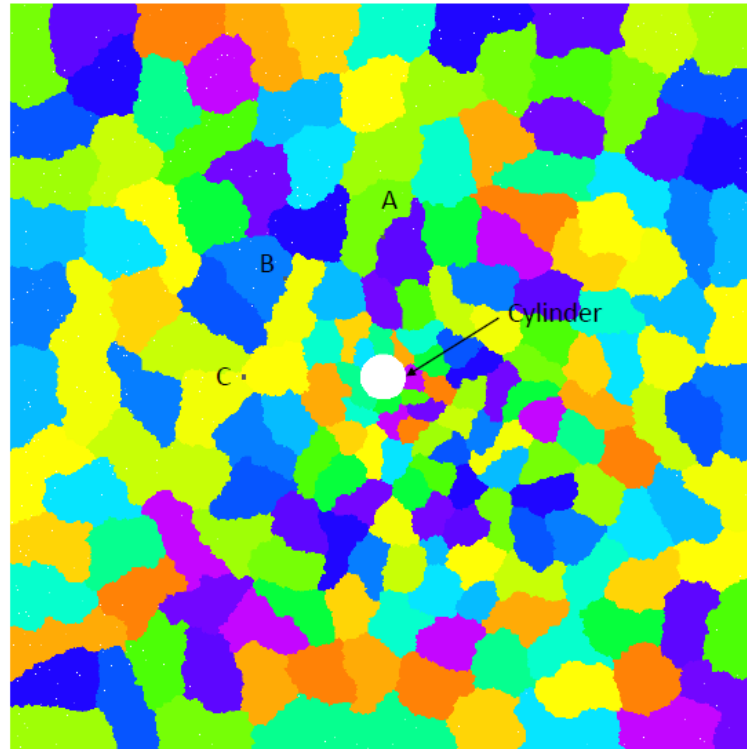


Figure 7.1: Unstructured mesh around a cylinder with 190 partitions shown by different colors.

Figure 7.2(a) shows the pressure field of the 2D TR at an instant when the wavefronts are well established. The wavefront with high strength corresponds to the direct propagation of the acoustic pulse of the direct simulation, whilst the one with lower intensity is related to the reflection by the surface of the cylinder. At the final instant of the 2D TR, the two wavefronts collapse well, and the acoustic pulse is well identified on the position of the source with the same strength of the source (Figure 7.2(b)).

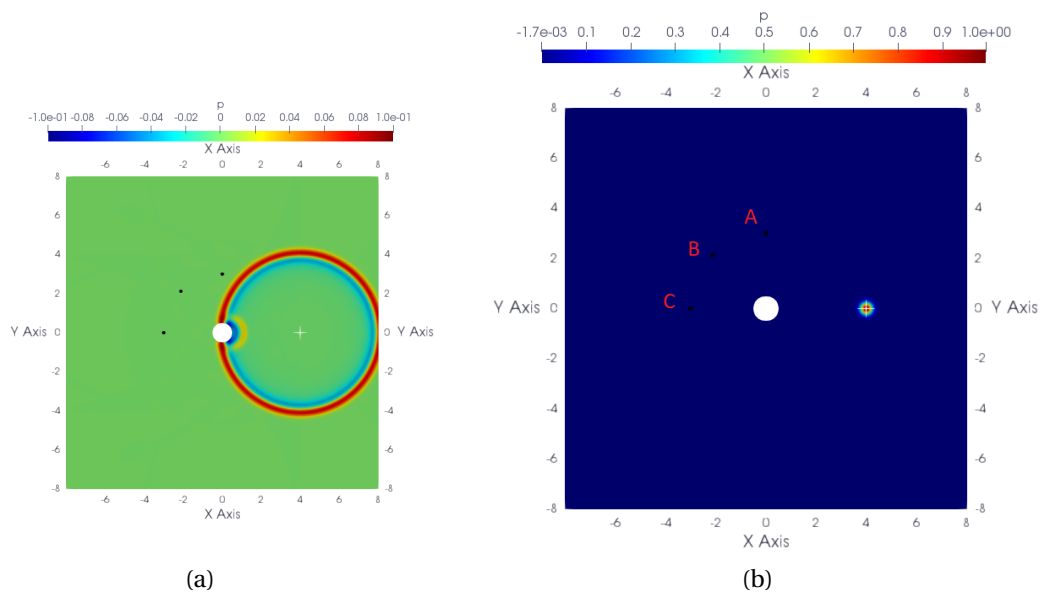


Figure 7.2: Results of 2D TR for an acoustic pulse scattered by a cylinder (a) at the instant $t = 12$ s, (b) at the final instant. The white cross stands for the position of the source.

Additionally, it is possible to check if the wavefronts of 2D TR are well reconstructed inside the simulation domain during the TR process with respect to the direct simulation. Figure 7.3 shows the sound pressure signals recorded at the three points A, B and C of the 2D TR by red lines. They are compared to analytical results (see the benchmark problem of an acoustic pulse in Chapter 2) which are indicated by black points. The numerical and analytical results superimpose well for the signals at the three points. Therefore, the TR process is validated with the presence of solid boundaries in a 2D case.

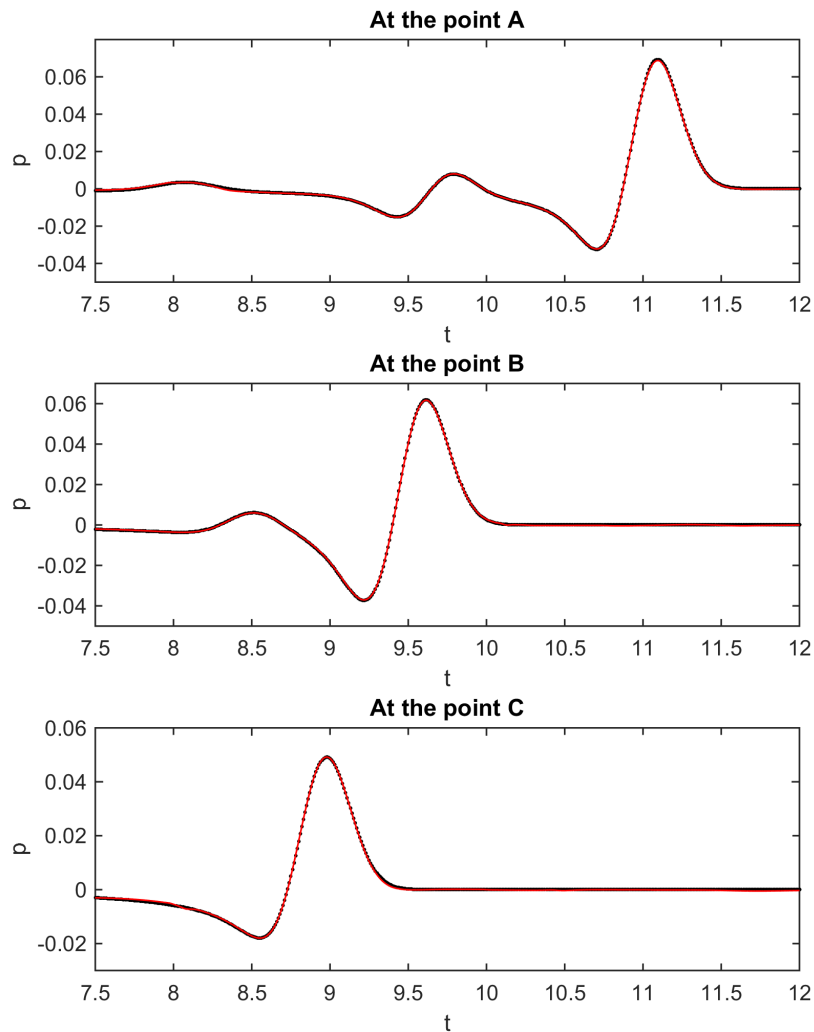


Figure 7.3: Comparison between the analytical and numerical results for the 2D TR. Red lines stand for numerical simulations. Black points stand for analytical solutions.

7.1.2 Identification of an acoustic pulse in a semi-open cavity

An acoustic pulse with a spatial Gaussian distribution of size 0.02 m, which is located at the position (0.3 m, 0.125 m) in a semi-open cavity, is considered. The splits of the semi-open cavity allow the waves to propagate outside the inner space of the cavity. The dimension of the simulation domain is 0.7 m \times 0.6 m. The boundary of the simulation domain uses

“free_rec” boundary conditions to record the signals on the positions of the nodes of the mesh at the boundary of the simulation domain. The boundary of the semi-open cavity uses “wall” boundary condition. The physical time of simulation T is 0.02 s. The polynomial order for the DG method is 3.

7.1.2.1 2D TR in homogeneous medium

The case with a uniform sound speed of 340 m/s is considered. The density of the medium is 1.2 kg/m^3 . The direct simulation is firstly carried out. Figure 7.4(a) shows the pressure field at the initial instant (emission of the acoustic pulse). Figure 7.4(c) shows the waves inside the simulation domain at $t_1 = 7.24 \times 10^{-5}$ s. The wavefront with high strength inside the semi-open cavity corresponds to the direct propagation of the acoustic pulse. The wavefront upside the dominant wavefront originates from the reflection of the wall upside. A part of the wavefront from the direct propagation of the acoustic pulse gets out from the split and is subjected to diffraction. Figure 7.4(e) shows the pressure field at the final instant of the simulation. The pressure field inside the semi-cavity is difficult to interpret due to the complex reflection and interference of the acoustic waves.

To identify the acoustic pulse, the 2D TR process is then conducted. The pressure signals recorded at the boundaries of the simulation domain are firstly reversed and re-emitted as monopolar noise sources from the same positions of the nodes after being multiplied by a factor of 2 for their amplitudes using boundary condition “BCfile”. Figure 7.4(d) shows a snapshot of the pressure field at an instant close to $T - t_1$ where the waves are well established inside the simulation domain as that of the direct simulation. As expected, this pressure field is very close to that at t_1 in the direct simulation. At the final instant of the 2D TR, the waves collapse to a focalization spot centered on the position of source, which identifies the position of the source with a precision of less than 2 cm (Figure 7.4(f)). However, the spot is slightly elongated in the y -direction, and the peak level is 22% lower than that in Figure 7.4(a), which may due to the fact that the final field of the direct simulation (Figure 7.4(a)) is not accounted for for the 2D TR process.

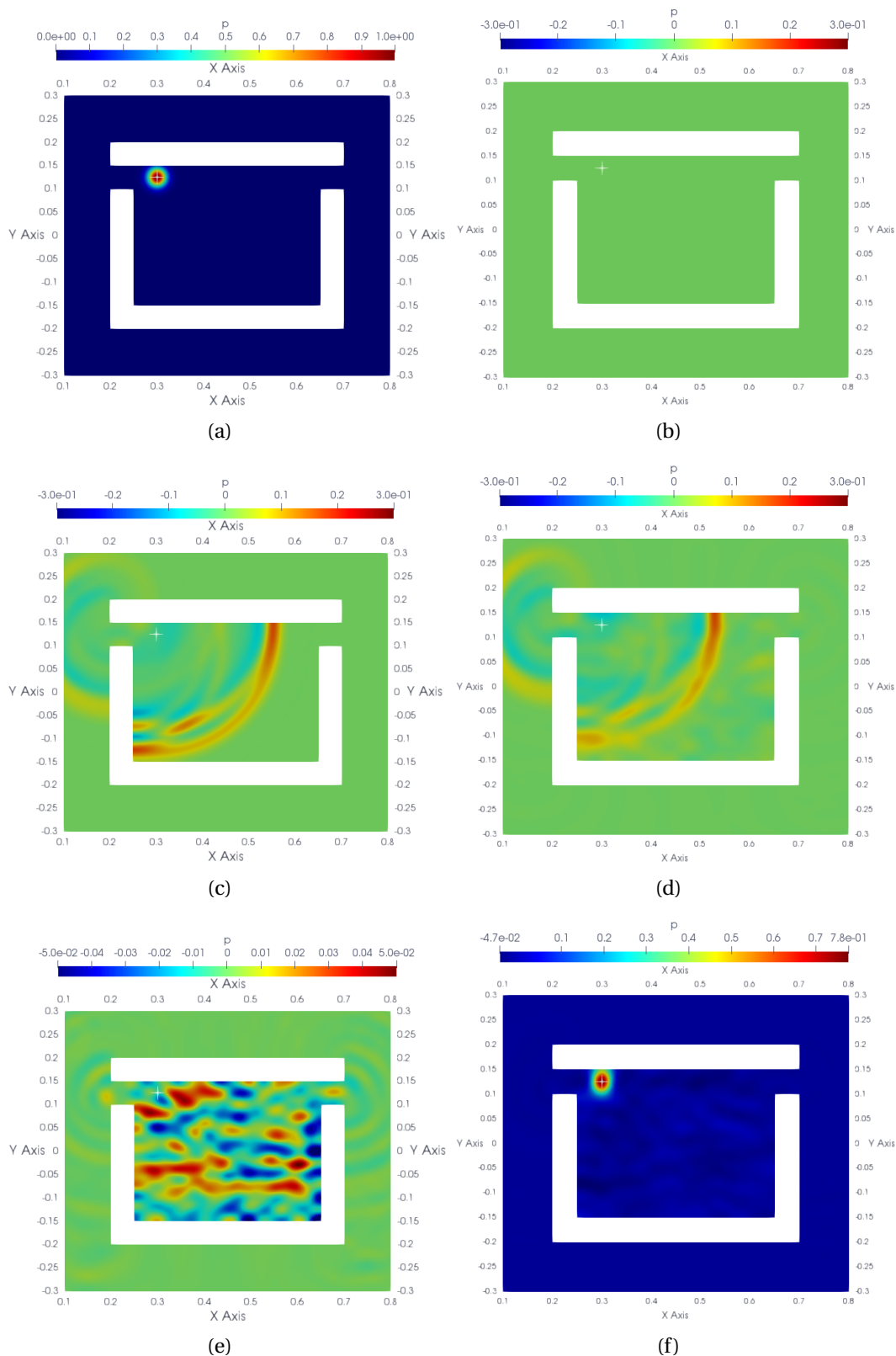


Figure 7.4: Results of 2D direct numerical simulation for an acoustic pulse inside a semi-open cavity (a) at initial instant, (c) at $t_1 = 7.24 \times 10^{-4}$ s, (e) at the final instant. Results of 2D TR for an acoustic pulse inside a semi-open cavity (b) at the initial instant, (d) at an instant close to $T - t_1$, (f) at the final instant.

7.1.2.2 2D TR in a heterogeneous medium

In this part, the situation with a heterogeneous medium is considered, for which the sound speed is non-uniform. More exactly, the sound speed increases from the left part to the right part of the simulation domain. Between the left and the right sides of the simulation domain, the sound speed c_0 is increased linearly by a factor of 2. Figure 7.5 shows the sound speed field for the numerical simulation. The density of the medium is 1.2 kg/m^3 . The same mesh and polynomial order for the DG method are used as for the previous case.

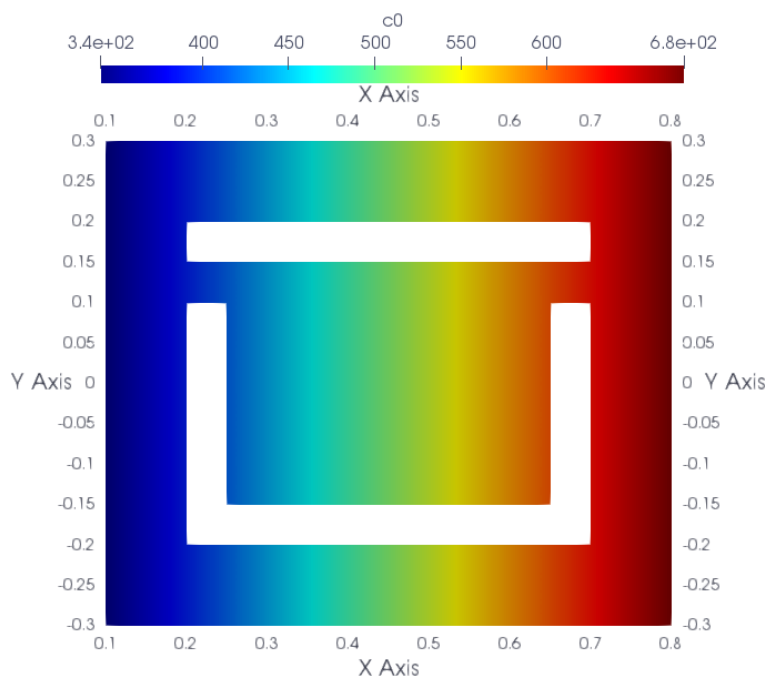


Figure 7.5: Non-uniform sound speed distribution inside the semi-open cavity.

The direct simulation is first conducted. Figure 7.6(a) shows the initial field of the direct simulation (acoustic pulse emission). Figure 7.6(c) shows the pressure field at an instant when the wavefront of the direct propagation of the acoustic pulse reaches the bottom of the semi-open cavity. The wavefront is broadened in the x -direction compared to that shown in Figure 7.4(c) due to the heterogeneity of the propagation domain. A part of the wavefront originating from the direct propagation of the acoustic pulse passed the left split and was then diffracted. That is the reason why a wavefront with lower intensity is observed in the left part of the simulation domain.

To identify the acoustic pulse, the same process is conducted as for the previous case. The initial pressure field of the 2D TR process is zero inside the simulation domain without considering the pressure field at the final instant of the direct simulation. Figure 7.6(b) shows the pressure field of the 2D TR results at an instant $T - t_1$ when the waves are well established and is similar to what is shown in the direct simulation shown in Figure 7.6(c). A focalization spot centering on the position of the source is detected at the final instant. The source position is identified with a precision of less than 2 cm. Therefore, the performance of the 2D TR technique is demonstrated in a case with heterogeneous medium. However, the peak level of the spot is 18% lower than that in Figure 7.6(a) possibly due to the same reason of the previous case.

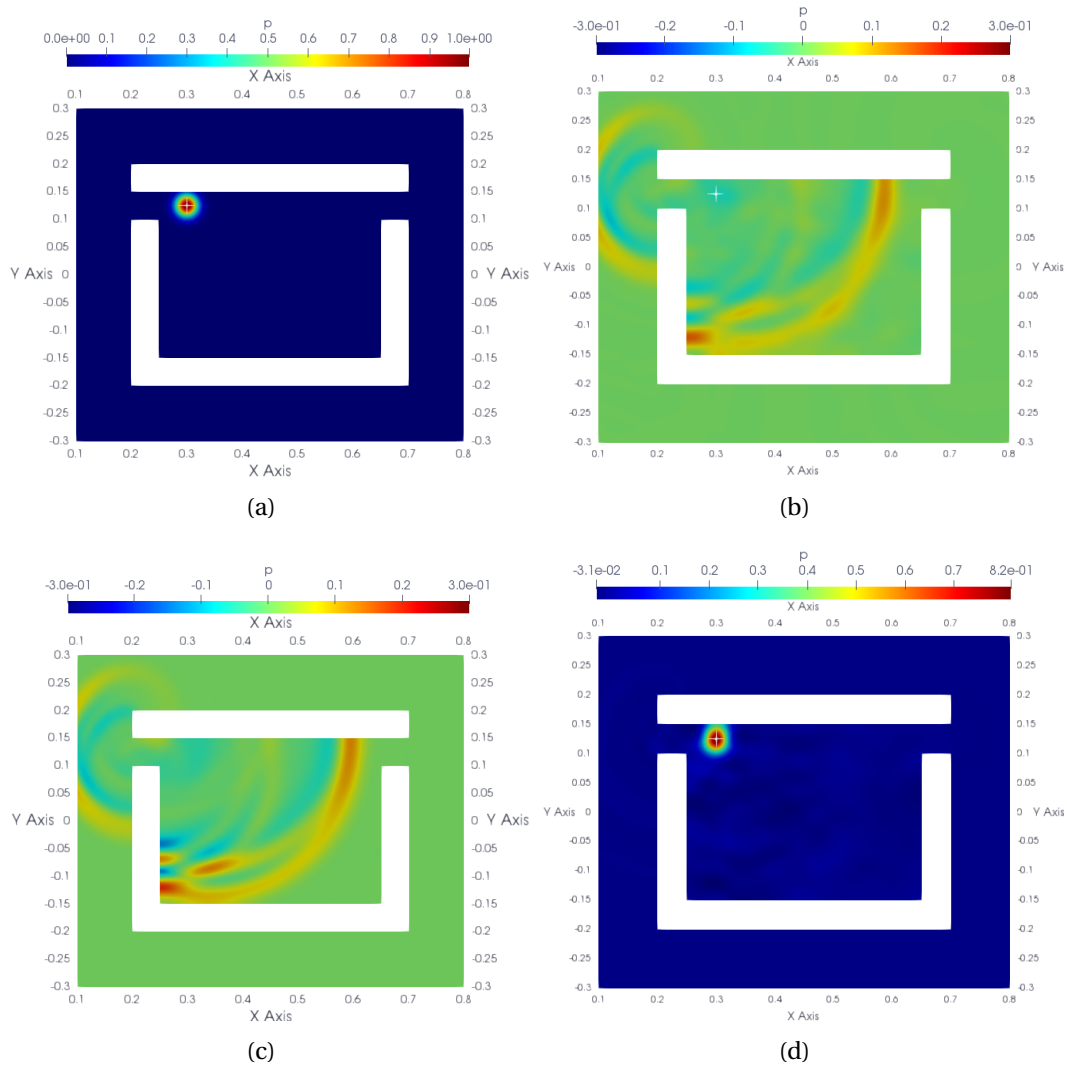


Figure 7.6: Results of 2D direct numerical simulation for an acoustic pulse inside a semi-open cavity with non-uniform sound speed (a) at the initial instant, (c) at $t_1 = 5.69 \times 10^{-4}$ s. Results of 2D TR for an acoustic pulse inside a semi-open cavity (b) at $T - t_1 = 0.0194426$ s, (d) at the final instant.

7.1.3 Identification of an acoustic pulse scattered by an airfoil

Practically, it is not possible to use a TR cavity in a wind-tunnel, but only a mirror partially enclosing the source. This is why in this section the identification of an acoustic pulse by the 2D TR is now conducted to compare its performance for the TR cavity and TR mirror. The acoustic pulse with a spatial Gaussian distribution of size 0.02 m is placed at the position (0.45 m, -0.05 m) below a NACA 0012 airfoil with a chord length of 0.2 m at angle of attack of 0° . The direct simulation is firstly carried out. The dimension of the simulation domain is 0.7 m \times 0.6 m. Figure 7.7(a) shows the mesh for the numerical simulation, for which the mesh elements around the airfoil are refined. The element size at the boundary is 0.01 m. The polynomial order for the DG method is 3. The physical time of the numerical simulation is 0.02 s. The acoustic pressure signals are recorded at all the nodes of the boundary of the simulation domain. To identify the acoustic pulse, the 2D TR process is then conducted. The pressure signals recorded at the boundary are reversed and re-emitted as monopolar noise sources from the same positions of the nodes after being multiplied by a factor of 2

(as previously). Here, the TR cavity and TR mirror are both studied for the 2D TR. The TR cavity is conducted by re-emitting the acoustic pressure information recorded at the whole boundary. As for the TR mirror, only a part of the information is re-emitted as shown in Figure 7.7(b), for which four test cases are considered for the TR mirror.

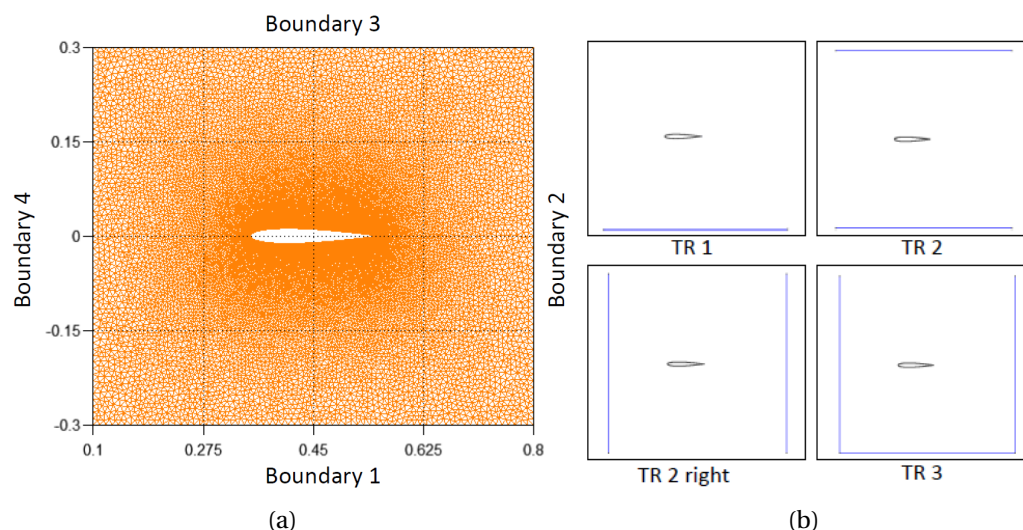


Figure 7.7: (a) 2D mesh for the direct simulation and TR; (b) sketch of the different TR mirrors used for TR.

Figure 7.8(a) shows a snapshot of the pressure field of the direct simulation at an instant when the waves have been reflected and diffracted by the airfoil. The wavefront with high strength shown by a large arc corresponds to the direct propagation of the acoustic pulse. The wavefront inside the cardioid wavefront originates from the reflection from the airfoil surface. Additionally, the waves are diffracted at the leading edge and the trailing edge of the airfoil, which is indicated by the wavefronts with lower strength upside the airfoil.

Figure 7.8(b) shows the pressure field of the 2D TR at the final instant using the information of only the bottom (TR 1). The position of the acoustic pulse is identified by a dominant focalization spot centering on the position of source. The spot is elongated in the x -direction due to the lack of information from the left and right boundaries. A low pressure area near the surface of the airfoil is also detected. Figure 7.8(c) shows the pressure field of the 2D TR at the final instant using the information of two boundaries (top and bottom, TR 2). With the information of an additional boundary upside the airfoil, the elongation of the focalization in the x -direction is slightly reduced with its strength being increased with respect to that in Figure 7.8(b). Figure 7.8(d) shows the pressure field of the 2D TR at the final instant using the information of two boundaries (left and right, TR 2 right). It is found that the focalization spot, centered on the position of the source, is elongated in the y -direction. Figure 7.8(e) shows the pressure field of the 2D TR at the final instant using the information of three boundaries (left, top, and right, TR 3). The performance of the 2D TR is improved by yielding a focalization spot without elongation centered on the position of the source. Additionally, the dynamics of the focalization spot with respect to the residual wavefronts is significantly improved by using three boundaries. By using the information of four boundaries (the whole cavity, TR 4), Figure 7.8(f) shows that the convergent waves collapse very well on the real position of the source at the final instant of the 2D TR, and that a focalization spot is generated without any residual wavefronts inside the simulation domain.

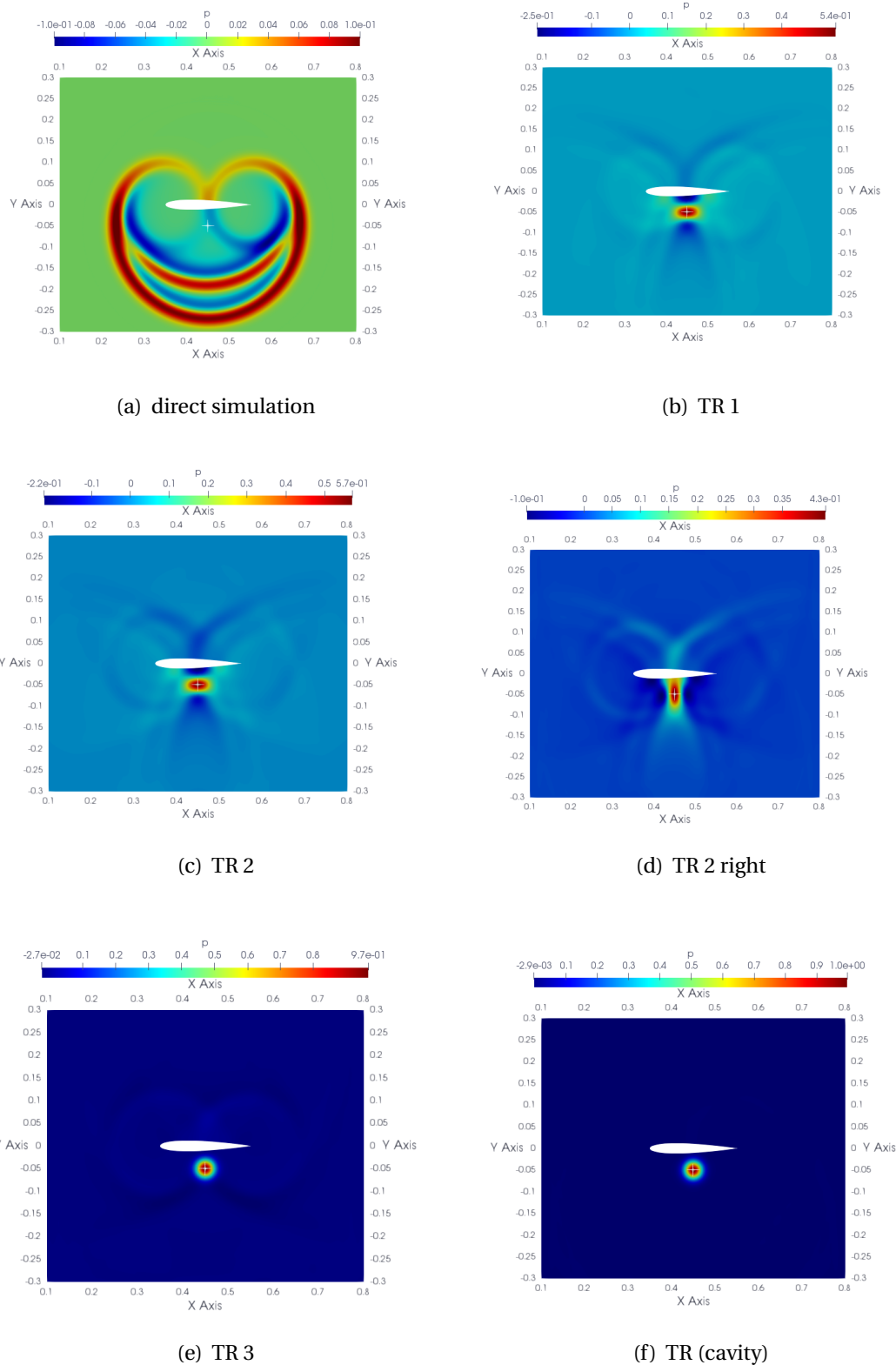


Figure 7.8: (a) Snapshot of the pressure field of 2D direct simulation concerning the scattering of an acoustic pulse by an airfoil. Pressure fields of 2D TR at the final instant using the pressure information recorded (b) at a boundary (bottom, TR 1); (c) at two boundaries (top and bottom, TR 2); (d) at two boundaries (left and right, TR 2 right); (e) at three boundaries (left, bottom, and right, TR 3); (f) at four boundaries (the whole cavity, TR 4)

Figure 7.9(a) shows the pressure profiles over a line in x -direction intersecting the position of the source for the cases of the direct simulation and the 2D TR simulations. It is found that the 2D TR using two boundaries (left and right) presents a maximum error of 58% for the amplitude with respect to that of direct simulation because of the significant loss of acoustic information for the TR process (see Figure 7.9(b)). Nevertheless, the position of the source was identified in this case. In addition, for the 2D TR case using only one boundary (bottom), the maximum error of the amplitude with respect to that of direct simulation is lower than that of the case using two boundaries (left and right) for the reason that the bottom boundary receives more energy and it is well positioned to capture the reflection from the airfoil. As expected, the 2D TR case using four boundaries provides a profile very close to that of the direct simulation.

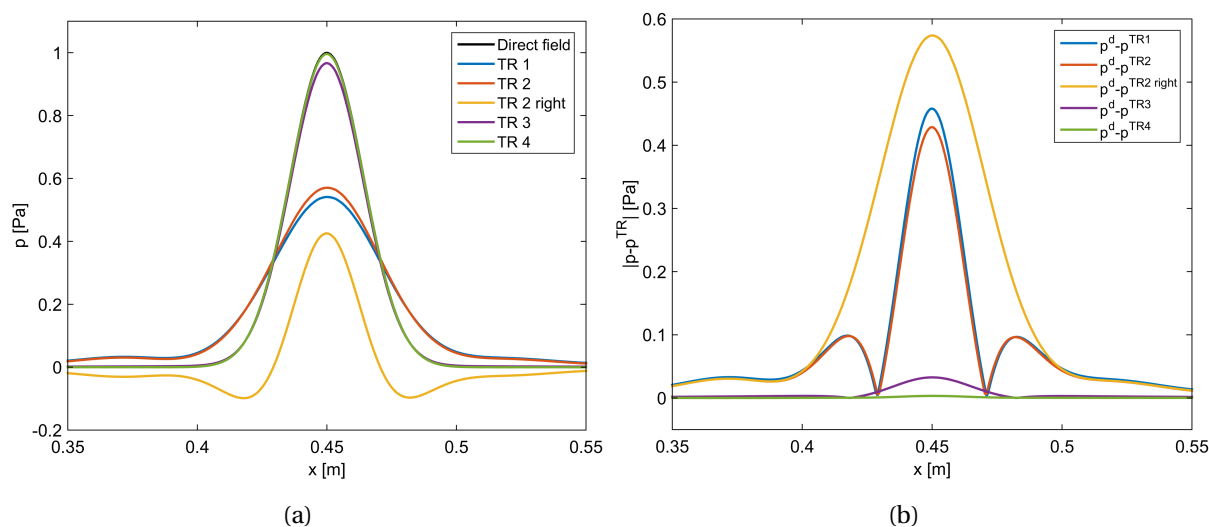


Figure 7.9: (a) The pressure profiles over a line in the x -direction intersecting the position of the source for the direct simulation and for the 2D TR simulations for the different TR mirrors defined in Figure 7.7(b). (b) error between the direct simulation and the 2D TR simulations.

7.1.4 Feasibility of implementation of an acoustic sink

As shown in the literature review of Chapter 1, the resolution of the TR for a pointlike noise source can not be less than half-a-wavelength due to the interference of the convergent waves and divergent waves. To overcome this limit, an acoustic sink can be implemented for the TR process. In Lobréau and Bavu [72], this concept was applied using a double-layer array and an analytical formulation of the sink function. In addition, Rosny and Fink [37] reported that the replacement of the source by its TR image could overcome the limit of TR resolution. The aim of this section is to investigate the feasibility of implementing this concept within the numerical TR technique with a harmonic monopole, knowing *a priori* the position, spatial distribution and driving signal of this acoustic source. Three types of simulation were conducted using the acoustic solver: (i) direct simulation; (ii) TR with acoustic sink; (iii) TR without acoustic sink. The sound speed for the simulation is set as 340 m/s. The density of the medium is 1.2 kg/m^3 . The simulation domain is a square cavity with a dimension of $0.34 \text{ m} \times 0.34 \text{ m}$. The physical time of the numerical simulation is 0.0075 s. A polynomial order of 4 is used for the nodal DG method.

7.1.4.1 Implementation of the acoustic sink

The direct simulation is first conducted. The monopolar noise source with a Gaussian spatial distribution has a frequency of 4 kHz. The source term for the corresponding source in the acoustic solver is given by

$$m(\mathbf{x}, t) = A \cdot \exp(-(x - x_s)^2/\sigma) \cdot \exp(-(y - y_s)^2/\sigma) \cdot \sin(2\pi f t), \quad (7.1)$$

with A the amplitude, (x_s, y_s) the position, σ a factor defining the size and f its frequency. In the test case, it takes place at the origin of coordinates and the size is set to $\sigma = 0.005$.

Two situations are distinguished for the 2D TR, one is conducted without acoustic sink, the other with the acoustic sink, which will be explained in the following. An anti-source should be implemented for TR process to maintain the symmetry. The anti-source (TR image of the monopole source) using as acoustic sink is given by

$$m_{TR}(\mathbf{x}, t) = A \cdot \exp(-(x - x_s)^2/\sigma) \cdot \exp(-(y - y_s)^2/\sigma) \cdot \sin(2\pi f(T - t)) \cdot H(t - T_0) \quad (7.2)$$

with T the physical time of the numerical simulation for the direct simulation and T_0 the instant to active the TR image of the monopole source during the TR process. $H(t)$ is a step function with its value being 0 if $t < 0$, and being 1 if $t \geq 0$. In our case, $T_0 = 0.001$ s.

Figure 7.10 shows the sketch for the implementation of the acoustic sink. The monopole source is simulated for the direct simulation. In our case, the expression for the source term $m(t)$ is *a priori* known, so is the anti-source of the monopole source $m_{TR}(t)$. It is then placed at the position of the source as an acoustic sink for the 2D TR and activated at the instant $t = 0.001$ s.

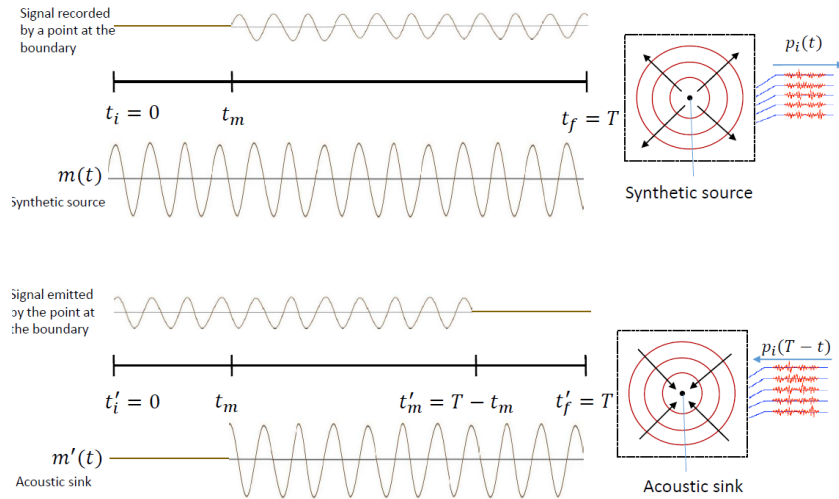


Figure 7.10: Sketch for the implementation of the acoustic sink for the 2D TR, adapted from [49].

7.1.4.2 2D TR result with the acoustic sink

Figures 7.11(a), 7.11(d) and 7.11(g) show the pressure field in the cavity at several instants (t_1 , t_2 , and t_3) for the direct simulation. The pressure field in the cavity at the final instant of the direct simulation is not used as initial field of TR as shown in Figures 7.11(b) and 7.11(c) where the waves propagate towards the position of source at instant $T - t_3$ s for the two

cases of TR. The square wavefront is caused by the geometry of the square boundary of the simulation domain. Figures 7.11(b), 7.11(e) and 7.11(h) show the pressure field in the cavity at several instants ($T - t_3$, $T - t_2$, and $T - t_1$) for the 2D TR without acoustic sink. Interestingly, the strength of the waves inside the domain can be reduced (Figure 7.11(e)) or enhanced (Figure 7.11(h)) due to acoustic interference between the converging and diverging waves at different instants. Figures 7.11(c), 7.11(f) and 7.11(i) show the pressure field in the cavity at the same instants for the 2D TR with acoustic sink. It can be seen that the waves inside the Figures 7.11(f) and 7.11(i) (instants $T - t_2$ and $T - t_1$) are respectively identical to that in Figures 7.11(d) and 7.11(a) (instants t_2 and t_1), because the divergent waves are cancelled by the acoustic sink.

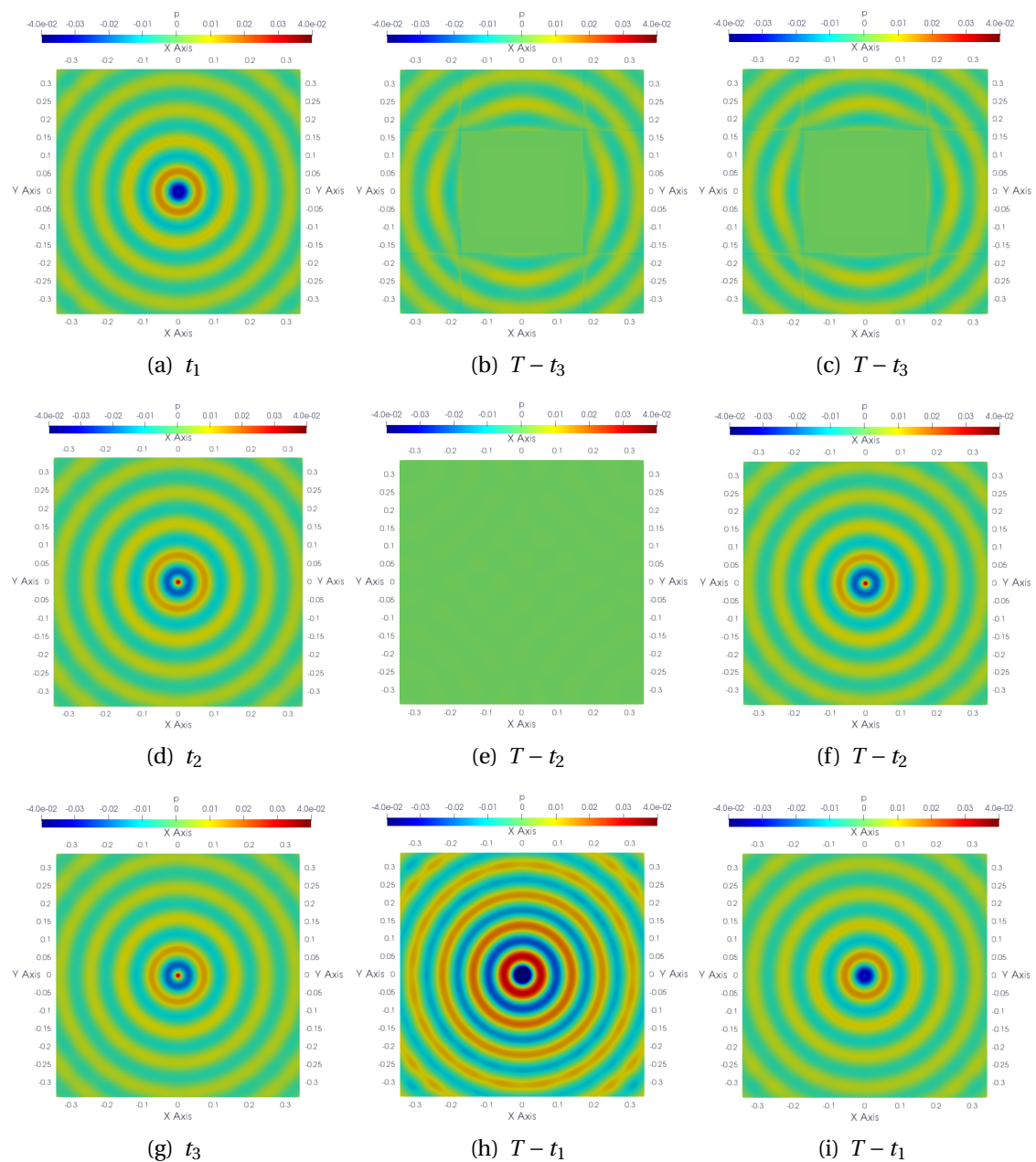


Figure 7.11: Snapshots of the pressure field at: (a) $t_1 = 0.0022$ s, (d) $t_2 = 0.0045$ s, and (g) $t_3 = 0.007$ s; results of 2D TR without acoustic sink (b) $t = T - t_3$, (e) $t = T - t_2$, and (h) $t = T - t_1$; results of 2D TR with acoustic sink (c) $t = T - t_3$, (f) $t = T - t_2$, and (i) $t = T - t_1$. Note that $T = 0.0075$ s.

To identify the monopole noise source, the RMS of the pressure field is computed for the three cases. Figure 7.12(a) shows the RMS of the pressure field of the direct simulation from 0.002 s to 0.0045s. As expected, a dominant spot centers on the position of the source. Figure 7.12(b) presents the RMS of the pressure field of the TR without acoustic sink from 0.003 s to 0.0055s. A focalization spot with larger size than that of the direct simulation takes place on the position of the source, which identifies the acoustic pulse with a precision at wavelength. Additionally, the circles are due to the interference between the convergent waves and divergent waves. Figure 7.12(c) yields the RMS of the pressure field of the TR with acoustic sink from 0.003 s to 0.0055s. It is observed that the circles are removed. Visually, the size of the focalization spot is the same as that of the direct simulation. Therefore, this experiment demonstrated that the acoustic sink can improve of the resolution of 2D TR result. However, this study is only of preliminary nature. Practically, the signal driving the source is not known *a priori* and should be integrated *a posteriori*, following for example the study of Lobréau and Bavu [72].

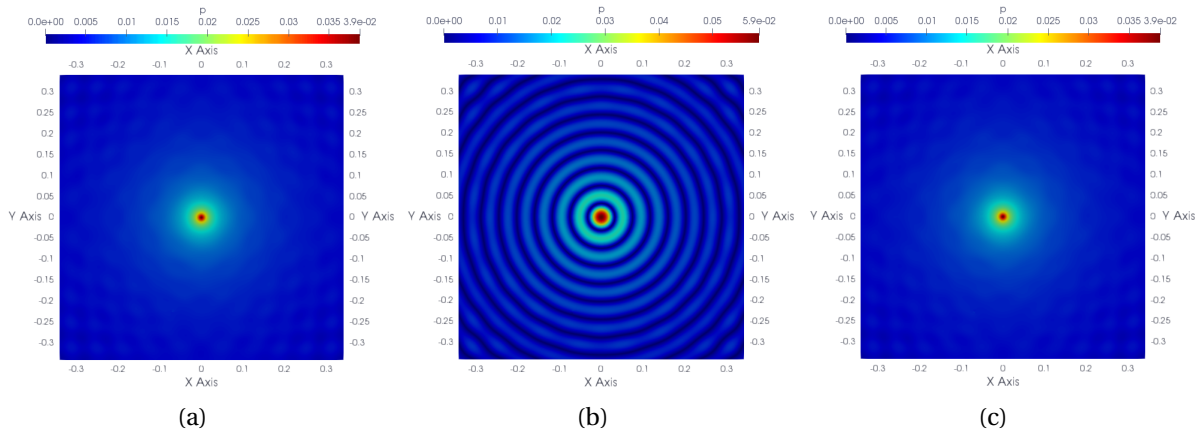


Figure 7.12: RMS of the pressure field of (a) direct simulation from 0.002 s to 0.0045s; (b) TR without acoustic sink from 0.003 s to 0.0055s; (c) TR with acoustic sink from 0.003 s to 0.0055s.

7.2 Identification of a dipole scattered by an airfoil in a flow

The trailing edge noise of an airfoil with sharp trailing edge is of a dipolar nature (see Chapter 1). In this section, the identification of a synthetic dipole scattered by a 2D airfoil in a flow is conducted. The results are taken from [126]. This case is considered to model the diffraction of trailing edge noise by the boundaries of the airfoil. To approach the real applications, the viscous effect of the flow is considered by using a RANS simulation instead of potential flow. The RANS solution is used as the background mean flow for the direct simulation.

7.2.1 RANS simulation and validation

The computation of the mean flow in this work is carried out with the open source software OpenFOAM. The turbulence model used for the simulation is $k - \omega$ SST (see Chapter 3). This work deals with the case of an air flow around a NACA 0012 airfoil with a chord of 0.2 m at an angle of attack of 10° , and an incoming velocity of 39.2 m/s. The chord-based Reynolds number is 5×10^5 . These parameters are similar to those of the experimental applications. Unstructured mesh is used for the simulation (Figure 7.13(a)) with a prism layer

mesh around the airfoil surface to account for the wall-bounded flows. The computation is conducted using 40 processors on a cluster. It should be mentioned that the thickness of the first layer of boundary layer mesh is limited by the maximum of the parameter y^+ , the value of which depends on the wall function and Reynolds number of numerical simulations. The definition of y^+ is given by ¹

$$y^+ = \frac{U^* y}{\nu}, \quad (7.3)$$

with U^* the friction velocity, ν the kinematic viscosity and y the half thickness of the first mesh layer near a wall. The friction velocity is defined as

$$U^* = \frac{\sqrt{\tau_w}}{\rho}, \quad (7.4)$$

with τ_w the wall shear stress and ρ the density of fluid.

The convergence of the simulation and the y^+ values related to the airfoil surface were checked. In order to validate the numerical results, the lift coefficient of the airfoil at these conditions were computed. They were compared with the published experimental results of Critzos *et al.* [36], which are shown in Table 7.1. It is found that the error of the numerical result with respect to the experimental one is less than 5%.

Data source	Lift coefficient
Simulation	0.93
Experiment [36]	0.948±0.049

Table 7.1: Comparison of the lift coefficients of the NACA 0012 airfoil at an angle of attack of 10° and a chord-based Reynolds number of 5×10^5 .

7.2.2 2D TR results

This section deals with the identification of a synthetic dipole source in the mean flow field around the airfoil. Therefore, the solid boundaries of the airfoil were considered by the RANS simulation for the flow and the acoustic solver for wave propagation. In the first step, the direct simulation is conducted. The dimensions of the domain is $1 \text{ m} \times 1 \text{ m}$. The sound speed is 340 m/s. The medium was considered to be air with a density of 1.2 kg/m^3 . Unstructured mesh was prepared for the acoustic solver. A polynomial order of 3 was used for the nodal DG method. It means that there are additional mesh nodes inside the triangle element of the mesh shown in Figure 7.13(b). Therefore the effective size of mesh elements is lower, which allows a higher resolution for the numerical simulations. In our case there are at least 10 mesh nodes within a wavelength. “free_rec” boundary condition were imposed at the boundaries of the domain for the simulation. The simulation time is long enough for the microphones to record non-zero data. Note that the acoustic solver and the software OpenFOAM use different meshes (see Figure 7.13), *i.e.*, the mesh for RANS simulation is refined around the surface of the airfoil whereas the acoustic mesh is uniform. In order to map the mean flow data to the grid of the mesh of the acoustic solver, interpolation of the data between the two meshes was conducted. It is based on a cubic interpolation using a MATLAB function.

¹[https://www.cfd-online.com/Wiki/Dimensionless_all_distance_\(y_plus\)](https://www.cfd-online.com/Wiki/Dimensionless_all_distance_(y_plus))

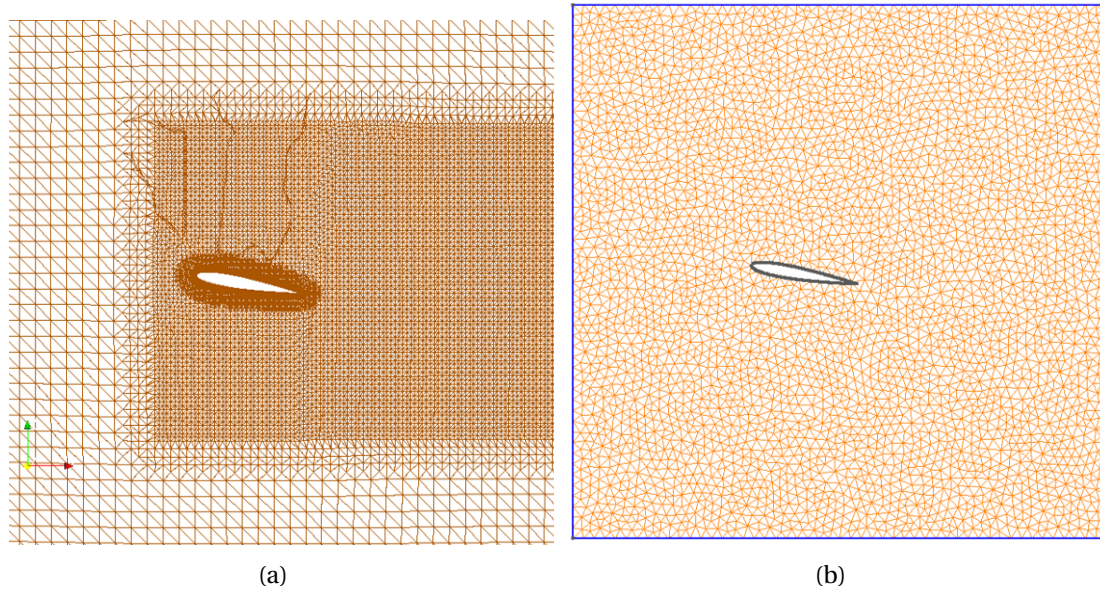


Figure 7.13: Mesh for the numerical simulation by (a) OpenFOAM; (b) Acoustic solver.

Figure 7.14 shows the mean flow around the airfoil with an incoming speed of 39.2 m/s (Mach number of 0.115) on the grid of the acoustic mesh after interpolation. The zone near the leading edge of the airfoil contains the flow with velocities lower than that of the incoming flow. The zone on the suction side and near the leading edge of the airfoil is subjected to velocities higher than that of the incoming flow. The wake of the airfoil is also observed. This corresponds well to the flow characteristics around an airfoil at low Mach number and low angle of attack. The mean flow data can therefore be used for the acoustic solver.

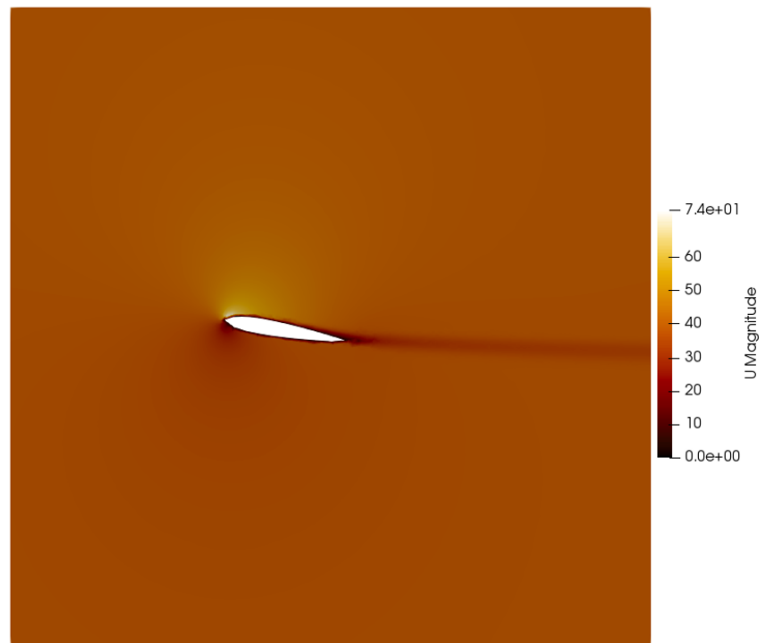


Figure 7.14: Mean flow field around the airfoil NACA 0012 on the grid of the mesh of the acoustic solver.

The synthetic dipole source is simulated near the trailing edge of the airfoil using the

approach: approximation by a Gaussian distribution (see Section 3.2.5.2). Its orientation is perpendicular to the incoming flow direction (see Figure 7.15). The frequency of the dipole source is 3400 Hz with a wavelength of 0.1 m. Figure 7.15 shows a snapshot of the sound pressure field at an instant when the waves inside the simulation domain reach the permanent regime. Two spots with opposite phases are observed. The effect of the background mean flow on the propagation of the acoustic waves is weak due to the low Mach number. The sound radiation is strong in the direction of its orientation, and the amplitude of the waves being attaching on the surface of the airfoil is also amplified. Conversely, the amplitude of the waves propagating downstream perpendicular to the dipole's orientation is weak. It corresponds to the cardioid directivity pattern reported by Roger *et al.* [106] and FfowcsWilliams and Hall [122].

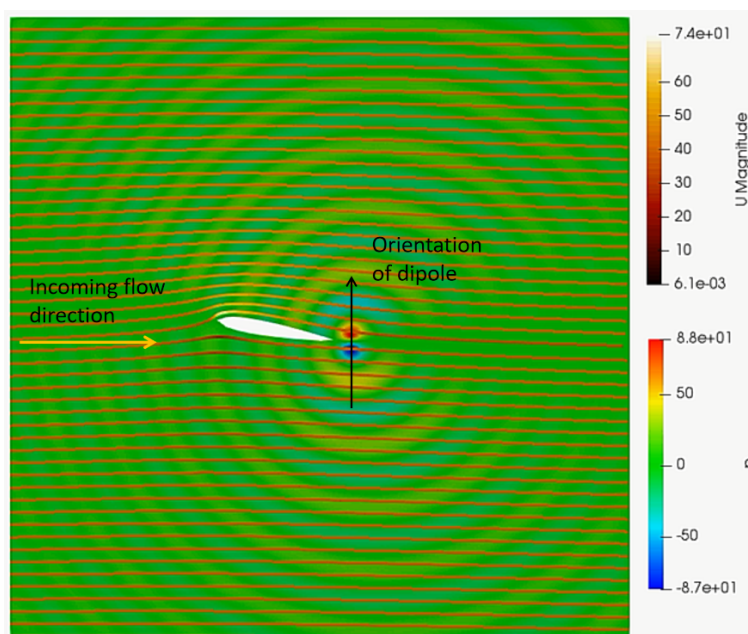


Figure 7.15: Snapshot of the pressure field of the direct simulation of a synthetic dipole source near the trailing edge of the airfoil. The lines inside the domain are streamlines based on the stationary mean flow.

The second step is the TR process, the signals recorded at the boundaries are reversed and re-emitted as monopole sources at the same positions as the nodes of the mesh at the boundary. As previously, the amplitudes of the signals are all multiplied by 2. Meanwhile, the direction of the mean flow around the airfoil must also be reversed to ensure that LEE are invariant with time inversion [38, 94]. The same mesh is used as for the direct simulation. Figure 7.16 shows the pressure field at an instant when the waves collapse on the position of the synthetic dipole source and form two dominant spots with opposite phases, which indicates the existence of a dipole with a precision at wavelength (see Figure 7.16). Note that the convergent wave continues to propagate as a divergent wave after collapsing, and interferes with the convergent waves. Therefore, the two main pressure spots are larger than for the direct simulation (Figure 7.15). This was reported originally in the work of Cassereau and Fink [30] as a focusing limitation of the TR process. To improve the spatial resolution of the TR result, a method such as an acoustic sink [14] could be used.

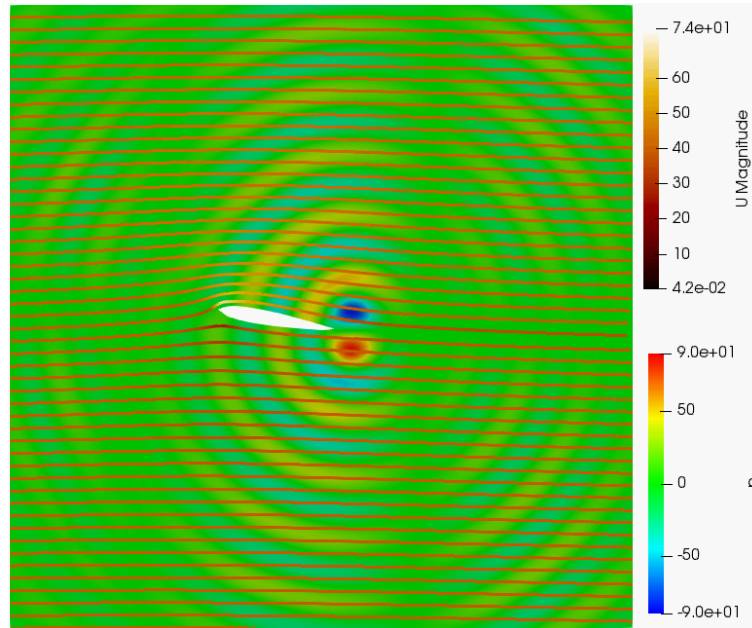


Figure 7.16: Snapshot of the pressure field of the TR of a synthetic dipole source near the trailing edge of the airfoil. All the signals recorded at the boundary are used for the TR. The lines inside the domain are streamlines based on the stationary mean flow.

To be close to the real application of TR, the TR process is now conducted only with a part of the data recorded at the boundary, knowing the number of microphones for array measurement is limited in reality. At each edge of the square domain, 32 isolated sets of nodes, acting as 32 uniformly distributed virtual microphones, recorded the sound pressure signals at the boundaries. Following the same process of 2D TR, Figure 7.17 shows a snapshot of the sound pressure field at an instant when the waves inside the simulation domain reach the permanent regime. Even though not all the energy getting out of the domain are used for the TR process with a loss of information, wavefronts are still established and propagate as convergent waves in the domain. It leads to two focalization spots with opposite phases and larger size with respect to that shown in Figure 7.16. The position of the source is again identified with a precision at wavelength. However, the loss of information for the TR process degrades the performance of the TR because the wavefronts are not as even as that shown in Figure 7.16.

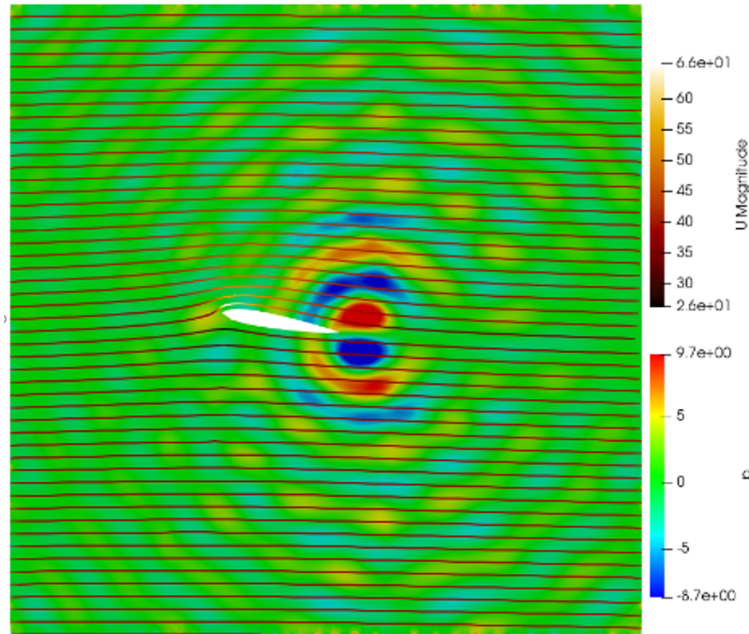


Figure 7.17: Snapshot of the pressure field of the TR of a synthetic dipole source near the trailing edge of the airfoil. A part of the energy recorded at the boundary (128 isolated "microphones") is used for the TR. The lines inside the domain are streamlines based on the stationary mean flow.

7.3 Summary of the chapter

In this chapter, the numerical 2D TR technique was used for the identification of synthetic noise sources. The first part deals with the case with a quiescent medium. The TR process is first validated based on a benchmark problem. The identification of an acoustic pulse inside a semi-open cavity with heterogeneous medium (with special variation of the sound speed) with a localization error inferior to the source size demonstrates the performances of the TR technique. The performances of several types of TR mirrors with respect to the TR cavity are then evaluated through the identification of an acoustic pulse scattered by an airfoil. Finally, the feasibility of implementation of an acoustic sink in order to improve the resolution of the TR results is demonstrated by a preliminary study of the identification of a synthetic monopole.

In the second part, the diffraction of trailing edge noise by the boundaries of the airfoil is modeled by simulating a synthetic dipole near the trailing edge of an airfoil with a background mean flow obtained by a RANS simulation for the direct simulation. Using the 2D TR technique, the dipolar source is identified with a localization error inferior to the wavelength by using all the acoustic information recorded at the boundaries of the direct simulation. With a loss of information for the TR process, using 32 isolated sets of nodes at the boundaries of the simulation domain, the dipolar source is identified with the same localization error, which approaches the real application of the TR technique.

This page is intentionally left blank.

Chapter 8

3D numerical time-reversal

Contents

8.1 Flow simulation by RANS	134
8.1.1 Geometry	134
8.1.2 Velocity fields	135
8.1.3 Validation of the numerical results	136
8.2 3D numerical TR with flow	138
8.2.1 Geometry and acoustic mesh	138
8.2.2 Background mean flow	139
8.2.3 3D TR results	140
8.3 Summary of the chapter	150

In this chapter, the 3D numerical TR technique will be applied to the identification of synthetic noise sources (simulated data instead of experimental data) including a monopolar noise source and a dipolar noise source near a wall-mounted airfoil in a flow. This will allow to evaluate the performance of the 3D numerical TR technique. The mean flow around a wall-mounted airfoil is difficult to obtain by flow measurements. Therefore, the first part concerns the RANS simulation (less computationally expensive than LES) in order to obtain the mean flow information. In the second part, the background mean flow will be considered for the 3D numerical TR technique with the presence of the solid boundaries of the wall-mounted airfoil in flows. The array geometries presented in Chapter 2 will be used for the TR process in order to be close to the real application to measurements in the wind-tunnel.

In preliminary simulations, the performances of the 3D TR for noise source identification in a quiescent medium have been demonstrated. The results of these simulations can be found in Appendix E. The aim of this section is to demonstrate how the 3D TR method can be implemented in a flow for an accurate description of a study case. The chosen case is a synthetic noise source located close to a wall-mounted airfoil, in the presence of an incoming flow. The data are simulated by RANS. In this case the TR method takes into account both the effects of the shear flow on the acoustic propagation, and the diffraction of the waves by the airfoil. The calculation of the mean flow around the NACA airfoil is presented in Section 6.2.1, and the coupling of the flow data with the acoustic solver, together with the TR results, are presented in Section 6.2.2.

8.1 Flow simulation by RANS

Despite the limit of the RANS simulation for resolving the junction flow of wall-mounted airfoils (Gand *et al.* [54]), it is chosen in the study because it is computationally cheap. The numerical simulation was conducted using the cluster of Université de Poitiers with 80 processors for parallel computation. The turbulence model for the numerical simulation is $k - \omega$ SST. It is well adapted for this kind of simulation. The solver *simpleFoam* of the code OpenFOAM was used for the parallel computation. It allows a steady state simulation for the 3D flow around the wall-mounted airfoil and requires less computation time than unsteady ones. The total time for the simulation is 8500 s, which allows to achieve the mean flow in steady state regime. Note that the time step for the solver is pseudo-time: this time step is not the same as that of the real world. Therefore the total simulation time 8500 s means 8500 iterations. It takes almost 20 hours for 8500 time steps using 80 processors. The 3D mesh for the numerical simulation of the flow, the convergence study of the simulation, and some numerical results are presented in Appendix F

8.1.1 Geometry

A wall-mounted airfoil at an angle of attack of 0° was considered for the numerical simulation. Figure 8.1 shows the geometry generated with the help of a website called *Onshape* and the associated coordinate system. The dimensions of the wall-mounted airfoil are the same as that of the test model of the experiment (Section 2.7). What is different is that the boundary layer tripping device was not considered for the geometry. Thus the wall-mounted airfoil is symmetric. The distance between the inlet surface and the leading edge of the airfoil is 0.333 m. The airfoil is centered on the bottom in the y -direction. The dimensions of the cuboid domain (width \times length \times height) is 1 m \times 2 m \times 1 m.

Additionally, the boundary of the simulation domain is divided into 7 patches including the ‘airfoil’, ‘inlet’, ‘outlet’, ‘back’, ‘front’, ‘top’ and ‘bottom’. The boundary condition types of these patches for numerical simulation are respectively “wall”, “fixedValue” with uniform velocity of 39.2 m/s, “zeroGradient”, “symmetry”, “symmetry”, “symmetry” and “wall”. The inlet velocity is set as 39.2 m/s with the chord-based Reynolds number being $Re_c = 5.23 \times 10^5$.

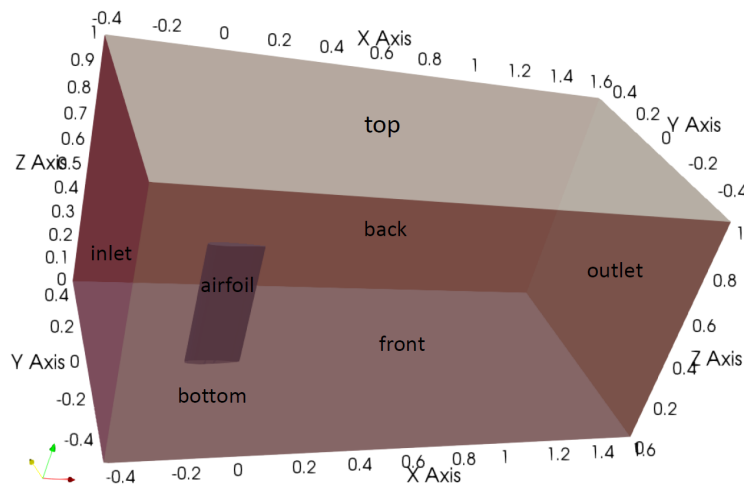


Figure 8.1: Geometry of a wall-mounted airfoil at an angle of attack of 0° and the cuboid domain surrounding the airfoil for the RANS simulation. The different patches of the simulation domain were shown by different colors.

8.1.2 Velocity fields

Figure 8.2(a) shows velocity field (scalar field of the norm of the velocity vector with three components in x , y , and z -directions) in a planar cross section at a height of 253 mm (near the middle span of the wall-mounted airfoil). The low velocities in the zones near the stagnation point and wake of the airfoil are observed. The boundary layer is simulated at the airfoil surfaces and its thickness increases along the flow direction. The free stream flow around the surfaces of airfoil is firstly subjected to an acceleration and then to a deceleration from the leading edge to the trailing edge. Figure 8.2(b) shows the velocity field in a planar cross section at a height 503 mm near the wing tip area of the wall-mounted airfoil. In addition to the diminution of velocity at the zones near the stagnation point and wake of the airfoil, two vortices are generated from the middle chord of the airfoil on both surfaces of the airfoil and move downstream.

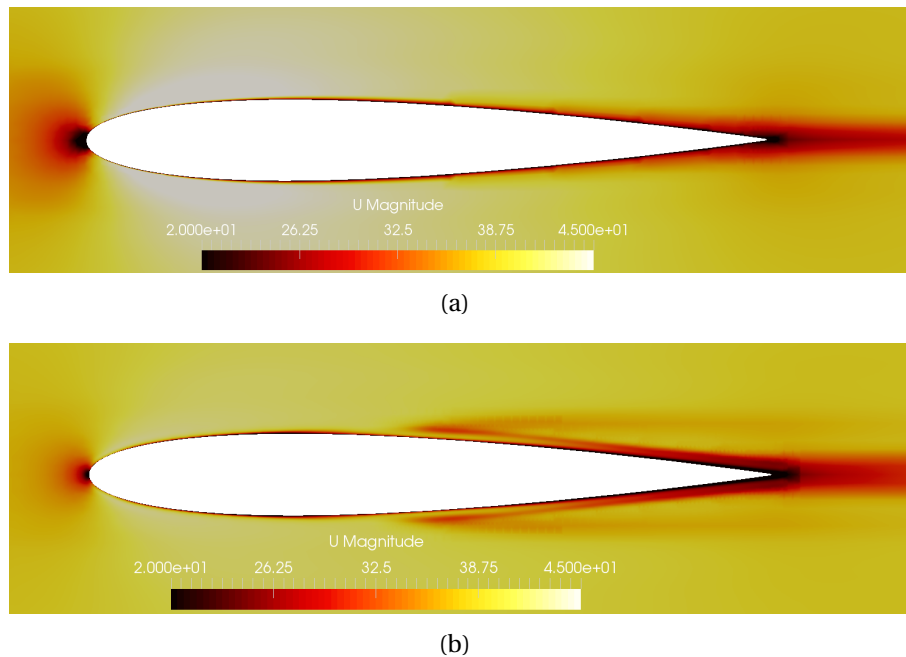
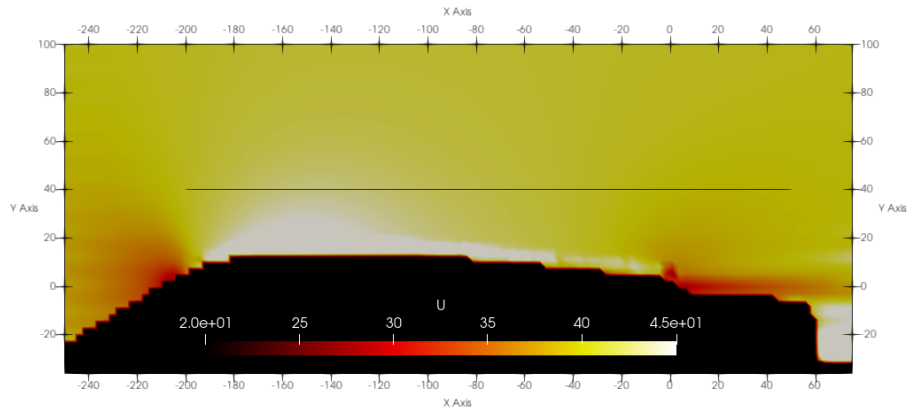


Figure 8.2: Velocity field in a planar cross section for the wall-mounted airfoil (a) at a height of 253 mm; (b) at a height 503 mm.

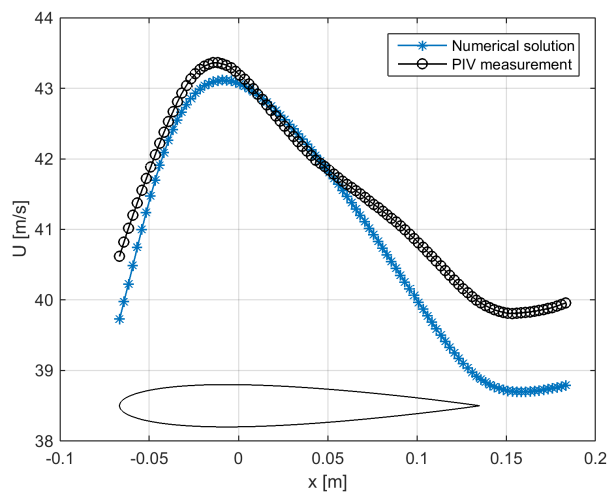
8.1.3 Validation of the numerical results

This section aims at comparing the numerical and experimental velocity profiles near the airfoil. Figure 8.3(a) shows the average velocity field around a NACA 0012 airfoil with a chord length of 0.2 m at angle of attack of 0° at an incoming speed of 40 m/s using a PIV measurement. The trailing edge of the airfoil is located at the position (0 m, 0 m). The black area in the figure is due to the existence of the airfoil and other experimental objects during the PIV measurement. Globally, the experimental velocity field (wake and zones corresponding to acceleration and deceleration) is similar to the numerical one (Figure 8.2(a)). The velocity profile along the black line is shown in Figure 8.3(a). The numerical result was obtained in a planar cross section at a height of $Z = 253$ mm. The difference between the experimental and numerical results is less than 5%.

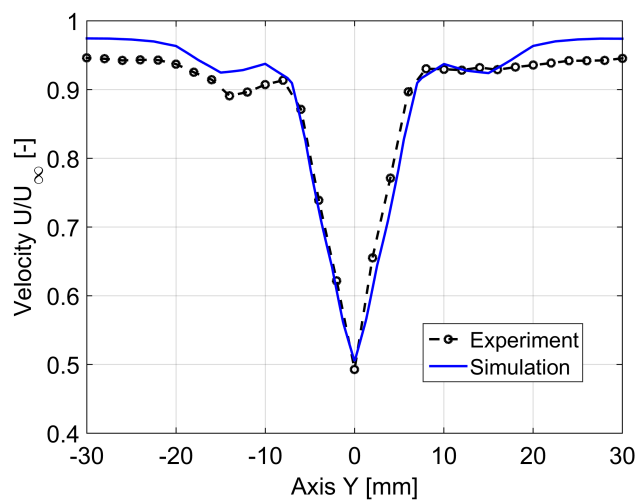
Figure 8.3(c) shows the comparison of the velocity profiles over a line in y -direction at a distance of 5 mm from the trailing edge of the airfoil at a height of 503 mm (near the wing tip). The experimental result was obtained by hot-wire measurements. The experimental velocity profile is not perfectly symmetric because of the boundary layer tripping device on one side of the surface of the wall-mounted airfoil. The numerical and experimental results are consistent on the left side of the figure without boundary layer tripping device for the two cases with a difference less than 5%. The slight diminution of the velocity between $y = -20$ mm and -10 mm are evidenced by both the experimental and numerical results (see Figure 8.3(c)). This diminution is due to the wing tip vortex as seen in Figure 8.2(b).



(a)



(b)



(c)

Figure 8.3: (a) Velocity field around a NACA 0012 airfoil at angle of attack of 0° at an incoming speed of 40 m/s; (b) comparison of the velocity profiles above the surface (along the black line plotted in Figure 8.3(a)) of the wall-mounted airfoil between numerical and experimental results (PIV measurements); (c) comparison of the velocity profiles in the wake of the wall-mounted airfoil between numerical and experimental results (hot wire measurements) at a measurement plane of $Z = 503$ mm (near the wing tip).

8.2 3D numerical TR with flow

In this section, the mean flow information will be used for 3D numerical TR studies. Firstly, the direct simulation of noise radiation by synthetic noise sources (monopole and dipole) located near the wall-mounted airfoil will be conducted. The acoustic information will be recorded on several patches around the dipole noise source and be interpolated to the positions of the 768 virtual microphones for the identification of the synthetic noise sources. Secondly, the 3D TR will be conducted using the interpolated acoustic signal.

8.2.1 Geometry and acoustic mesh

A wall-mounted NACA 0012 airfoil at an angle of attack of 0° was considered for the 3D numerical TR. The chord of the airfoil is 200 mm. The span length of the airfoil is 505 mm. The leading edge of the airfoil is located at a distance of 283 mm from the patch ‘Front’. Figure 8.4(a) shows the geometry displayed in the software GMSH. The patches ‘Left’, ‘Top’ and ‘Right’ use the “free_rec” boundary condition for direct simulations. The 768 microphones of the microphone array, which were presented in Chapter 2, locate on the surfaces of the three patches. The same coordinate system as the one presented in Chapter 2 was used. The patches ‘Front’ and ‘Back’, ‘Left2’, ‘Left3’, ‘Right2’ and ‘Right3’ use the “free” boundary condition. The patches ‘Left1’ and ‘Bottom’, ‘Right1’ and ‘Airfoil’ use the “wall” boundary condition. Figure 8.4(b) shows the 3D mesh generated by GMSH. It is an unstructured mesh with 80 partitions shown by different colors. The size of most of the mesh elements is 2 cm with $N = 1$ (thus it is the effective size of mesh element for the DG method). There are some refinements around the surface of the airfoil in order to model accurately the geometry for the acoustic simulation. The 3D mesh contains 1013363 elements, among which 83870 triangles on all the patches of the boundary of the domain and 929493 tetrahedra inside the domain of the 3D mesh.

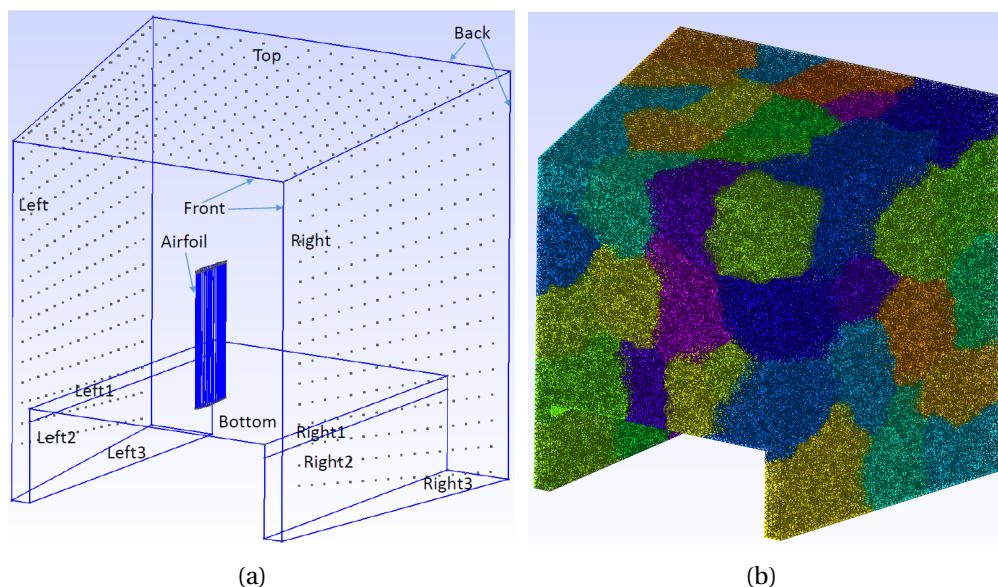


Figure 8.4: Generation of the 3D mesh for the wall-mounted airfoil using GMSH. (a) The domain of the 3D acoustic mesh concerning a wall-mounted airfoil with the positions of the 768 microphones indicated by the black points on the three patches ‘Left’, ‘Top’ and ‘Right’ of the domain; (b) the unstructured 3D acoustic mesh for the wall-mounted airfoil with 80 partitions shown by different colors.

8.2.2 Background mean flow

In this section, the background mean flow will be considered for the 3D TR process. The background mean flow for the 3D acoustic simulations includes three parts: the mean flow field around the wall-mounted airfoil, three shear layers forming a ‘tunnel’ shape around the wall-mounted airfoil and the quiescent flow outside the shear layers. Note that the RANS simulation of the wind-tunnel flow is not available. Therefore, the shear layers use the flow information from the analytical solution (Candel *et al.* [27]) given by Equation (8.1)

$$\frac{U}{U_0} = \frac{1}{2}(1 - \tanh(\eta_{cm})), \quad (8.1)$$

where U_0 is the jet velocity inside the three shear layers forming a ‘tunnel’ shape. The normalized coordinate η_{cm} is given by the following equation

$$\eta_{cm} = \frac{2(y - y_{cm})}{\delta_{cm}}, \quad (8.2)$$

where y_{cm} is the position of the inflection point of the shear layers and δ_{cm} is the half thickness of the shear layer. Its value is set as 3 cm with the thickness of the shear layers being 6 cm based on the typical thickness of the shear layers in the open test section of the wind-tunnel (Tran [117]). The three shear layers are simulated with the same thickness along the x -direction, which simplifies the case of the experiment (shear layers developed from the nozzle of the wind-tunnel BETI with increasing thickness).

The acoustic mesh and the CFD mesh being different, the flow around the airfoil was obtained by conducting interpolations of the mean flow data of the RANS simulation to the grid of the 3D acoustic mesh with a Matlab function ‘scatteredInterpolant’. Figure 8.5(a) shows the acoustic mesh in a planar cross section XY at $z = 0.4$ m. Figure 8.5(b) shows the mean flow information around the airfoil in this section with an incoming velocity of 39.2 m/s. The dark area indicates the quiescent flow. The boundary layer on the surface of the airfoil, the shear layers and the wake of the airfoil are also shown in this figure.

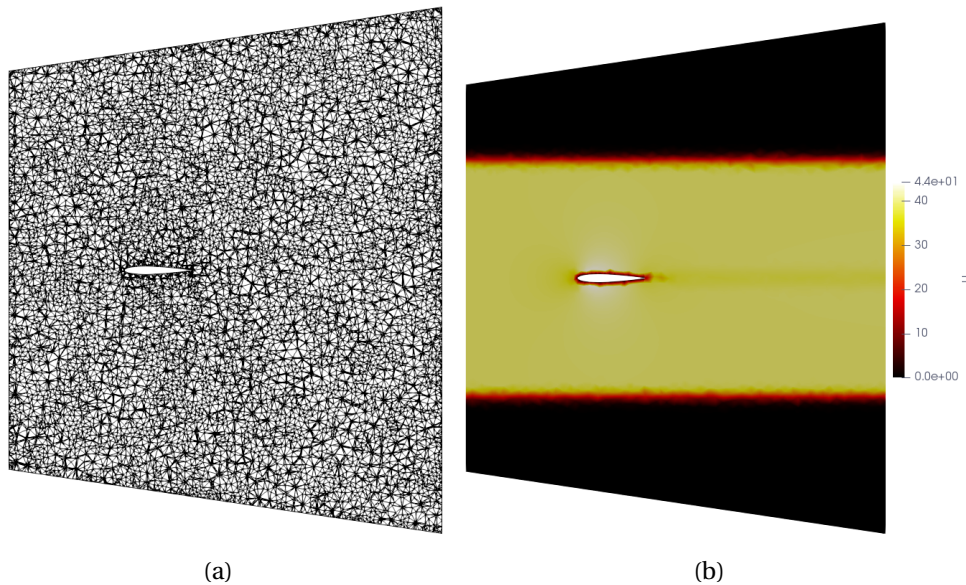


Figure 8.5: Visualisation of the 3D mesh and the mean flow information in a horizontal section. (a) The mesh in a planar cross section XY at $z = 0.4$ m; (b) the velocity field in the same plane.

Figure 8.6(a) shows the mesh in a vertical planar cross section YZ at $x = 0.35$ m. In Figure 8.6(b), the quiescent area, the ‘tunnel’ shaped shear layers, and the boundary layers on the patches ‘Bottom’ and ‘Airfoil’ are well presented with an incoming velocity of 39.2 m/s. The corners of the side shear layers and top shear layer have the shape of an arc.

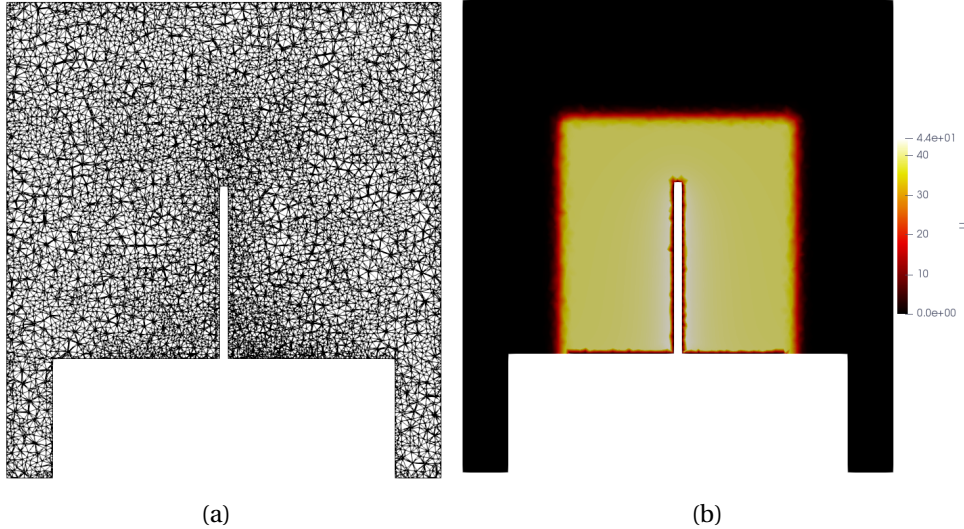


Figure 8.6: Generation of the 3D mesh and the mean flow information in a vertical section. (a) The mesh of in a planar cross section YZ at $x = 0.35$ m; (b) the velocity field in the same plane.

8.2.3 3D TR results

In this section, the 3D mesh and the background mean flow are used for the TR process. Synthetic noise sources near the surface of the wall-mounted airfoil are simulated for the direct simulations using the approach: Dirac distribution with the Lagrangian base function (see Section 3.2.5.2). The TR process will be conducted in order to locate the corresponding noise sources. The physical time of the simulations (direct simulation and TR) is 0.01 s. Note that the background pressure field around the wall-mounted airfoil obtained by the RANS simulation is also non-uniform. Therefore, it is considered for the acoustic simulations by interpolating it to the grid of the 3D acoustic mesh. The sound speed is 340 m/s. The density of the medium is 1.2 kg/m^3 . The heat capacity ratio is $\gamma = 1.4$. The pressure signals are recorded on all the nodes of the patches ‘Left’, ‘Top’ and ‘Right’ of the simulation domain for direct simulations. The numerical simulations using parallel computation were conducted in a cluster with 80 processors. The snapshots of the pressure field in the following sections present the waves reaching the permanent regime inside the simulation domain if not specified. By using the boundary condition “BC_gauss_spot”, the recorded acoustic signals on the three patches ‘Left’, ‘Top’ and ‘Right’ were firstly interpolated to the position of the 768 microphones and then reversed and re-emitted as monopole noise sources with spatial Gaussian distribution during the TR process. The size of the emission spots (see Equation (3.21)) at the positions of the 768 microphones is $\sigma = 3 \text{ cm}$ for the TR simulation. The background mean flow was also reversed for the TR process.

The waves inside the simulation domain, shown by the snapshots of the pressure field in the following sections, reach the permanent regime if not specified. The areas between the parallel lines in the figures stand for the shear layers. The Flow direction is from the left to the right. The white cross indicates the exact position of the noise source.

8.2.3.1 Monopole noise source in the flow

A synthetic monopole noise source of frequency 2 kHz (wavelength $\lambda = 0.17$ m) was placed beside the wall-mounted airfoil at the position (0.4 m, -0.15 m, 0.3 m). The interest of this configuration is to simulate the diffraction / reflection by a neighboring geometrical element (installation effect). Figure 8.7(a) shows a snapshot of the pressure field of the direct simulation in a horizontal section intersecting the position of the source. The waves are reflected and diffracted by the wall-mounted airfoil. That is why the wavefronts on the side of the monopole noise source are not even and the sound pressure fluctuations are reduced on the side of the airfoil opposite to the monopole. The mean flow effect on the propagation of the acoustic waves is weak due to the low Mach number. Figure 8.7(b) shows the distribution of the RMS of the pressure field integrated from 0.05 s to 0.07 s in the same plane. As expected, a dominant spot is well located at the position of the monopole noise source.

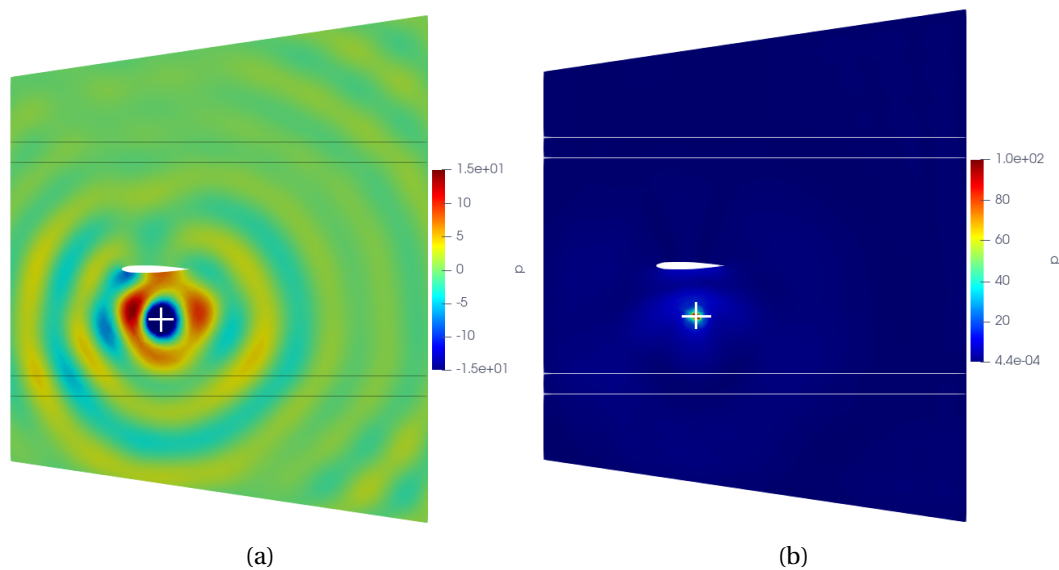


Figure 8.7: Results of the 3D direct simulation for a synthetic monopole noise source of 2 kHz beside the wall-mounted airfoil with an incoming flow speed of 39.2 m/s (left to right) shown in a horizontal section. (a) Snapshot of the pressure field in a planar cross section XY at $z = 0.3$ m; (b) RMS of the pressure field integrated from 0.05 s to 0.07 s in the same plane.

Figure 8.8(a) shows a snapshot of the pressure field of the 3D TR result in a horizontal section intersecting the source position. The wavefronts from the ‘Left’ and ‘Right’ patches are established inside the domain of simulation despite the loss of information for the TR process (only the signals recorded at the patches ‘Left’, ‘Top’ and ‘Right’ are used). A dominant spot is observed at the real position of the monopole noise source with some secondary spots. To identify the position of the noise source, Figure 8.8(b) shows the distribution of the RMS of the pressure field integrated from 0.05 s to 0.07 s in the same plane. The dominant spot indicates the position of the monopole noise source with a precision at wavelength. The elongation of the spot in the x -direction indicates a lower spatial resolution in this direction due to the lack of waves from the ‘Front’ and ‘Back’ patches. The average of the size of the spot at a level of $(1/\sqrt{2})$ times the peak level (-3 dB) is approximately half-a-wavelength (8.5 cm), which is the limit of the spatial resolution without the application of acoustic sink. The dominant spot on the surface of the airfoil may be due to the reflection by the solid bound-

ary. A difficulty of the interpretation of the RMS pressure distribution is encountered for the reason that it can be identified as a source on the surface of the airfoil.

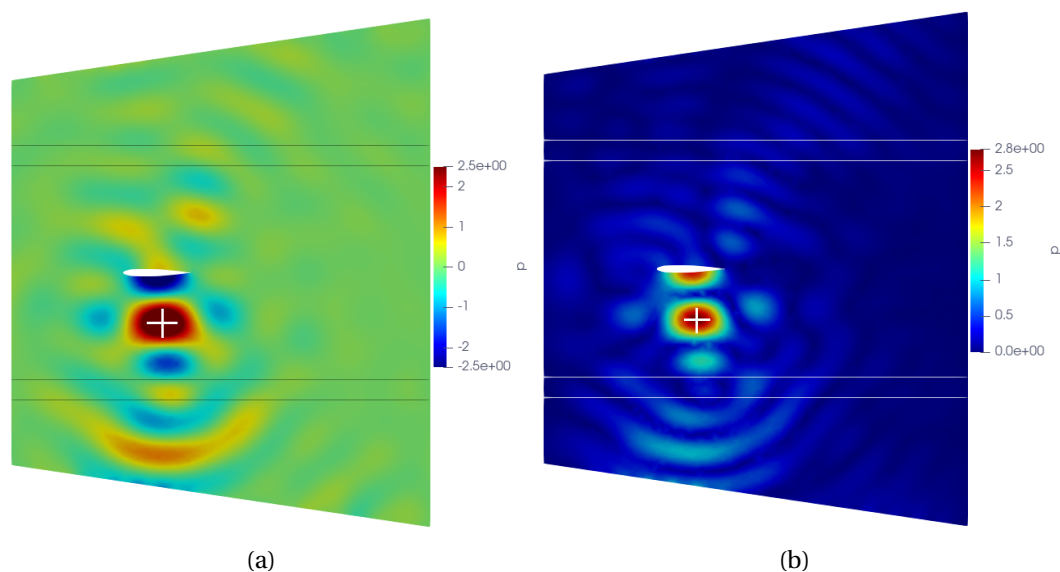


Figure 8.8: Results of the 3D TR for a synthetic monopole noise source of 2 kHz beside the wall-mounted airfoil with an incoming flow speed of 39.2 m/s (left to right) shown in a horizontal section. (a) Snapshot of the pressure field in a planar cross section XY at $z = 0.3$ m; (b) RMS of the pressure field integrated from 0.05 s to 0.07 s in the same plane.

3D TR results for the same source without considering the solid boundaries of the airfoil for the numerical simulation are obtained using the same TR process. Figure 8.9(a) snapshot of the pressure field of the 3D TR result in a horizontal section intersecting the source position. Interestingly, a dominant spot is still observed but not centred on the source position. Figure 8.9(b) shows the distribution of the RMS of the pressure field integrated from 0.05 s to 0.07 s in the same plane. The source is still identified by a dominant spot but with a larger localization error than that of the case shown in Figure 8.8(b). Moreover, the peak level of the RMS of the pressure field is lower than that in Figure 8.8(b). This may be due to the fact that the wavefronts originating from the patch 'Left' are not well established without the boundaries of the airfoil when propagating towards the source position, which degrades the performances of the TR technique.

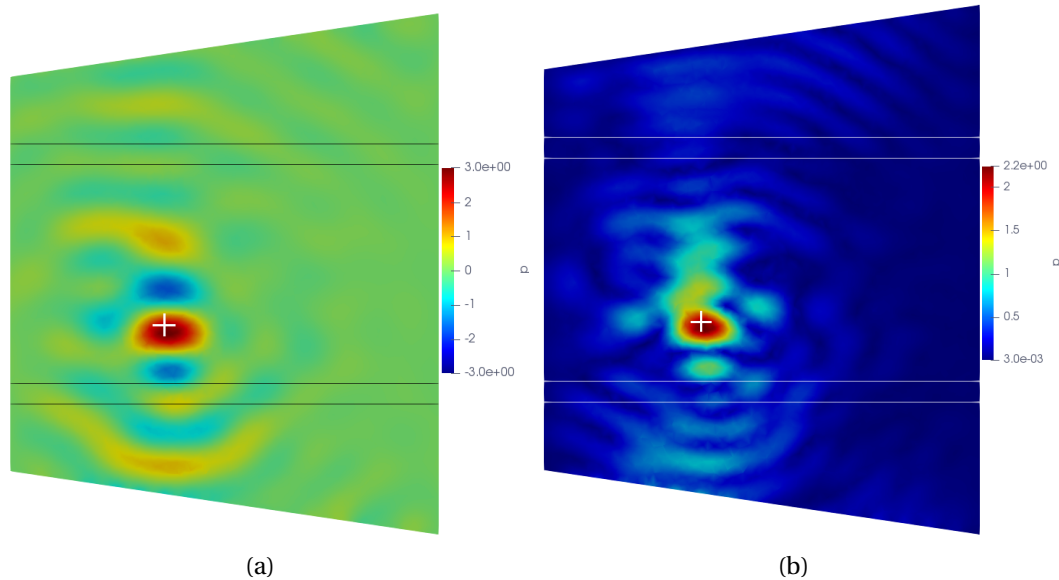


Figure 8.9: Results of the 3D TR for a synthetic monopole noise source of 2 kHz without considering the solid boundaries of the wall-mounted airfoil with an incoming flow speed of 39.2 m/s (left to right) shown in a horizontal section. (a) Snapshot of the pressure field in a planar cross section XY at $z = 0.3$ m; (b) RMS of the pressure field integrated from 0.05 s to 0.07 s in the same plane.

8.2.3.2 Dipole noise source in the flow

3D Direct simulation A synthetic dipole of frequency of 2 kHz (wavelength $\lambda = 0.17$ m) with orientation in the y -direction (perpendicular to the airfoil) is simulated at a distance of 1 cm from the trailing edge of the wall-mounted airfoil at $z = 0.3$ m. The interest of this case is to mimic the self-noise of an airfoil, which origin is located at the trailing edge. This source is known to be a dipole perpendicular to the airfoil (see Chapter 1). With an incoming flow speed of 39.2 m/s, Figure 8.10(a) shows a snapshot of the pressure field in a horizontal section intersecting the source position. As expected, the waves on the two sides of the wall-mounted airfoil are in phase opposition. Contrary to what was observed in Figure E.5(a), the presence of the solid boundaries of the wall-mounted airfoil seems to increase the acoustic intensity of the wavefronts upstream by “attaching” them to the surfaces of the airfoil. Similar to the observation in a 2D case in Chapter 8, it corresponds to a cardioid directivity pattern. The mean flow effect on the propagation of the acoustic waves is weak (due to the low Mach number): the wavelength upstream and downstream of the dipole noise source are almost equal and no evident refraction of the waves is observed when crossing the shear layers. To see more clearly the effects of the flow on the propagation of the acoustic waves and estimate the background mean flow effect on the identification of noise source, the velocities on all the grids of the acoustic mesh were increased by multiplying a factor of 2.55, for which the incoming velocity becomes 100 m/s. The Mach number being equal to 0.29 (less than 0.3), the flow can still be considered as incompressible so that the mean flow simulation remains valid. Figure 8.10(b) shows a snapshot of the pressure field in the same plane as in Figure 8.10(a). As expected, correction effects are stronger: the acoustic waves are “compressed” upstream the noise source, and they are “dilated” downstream. The waves are also clearly refracted when passing the shear layers. Similar to the case with lower intensity, the presence of the wall-mounted airfoil increases the acoustic intensity of the wavefronts in the x -direction.

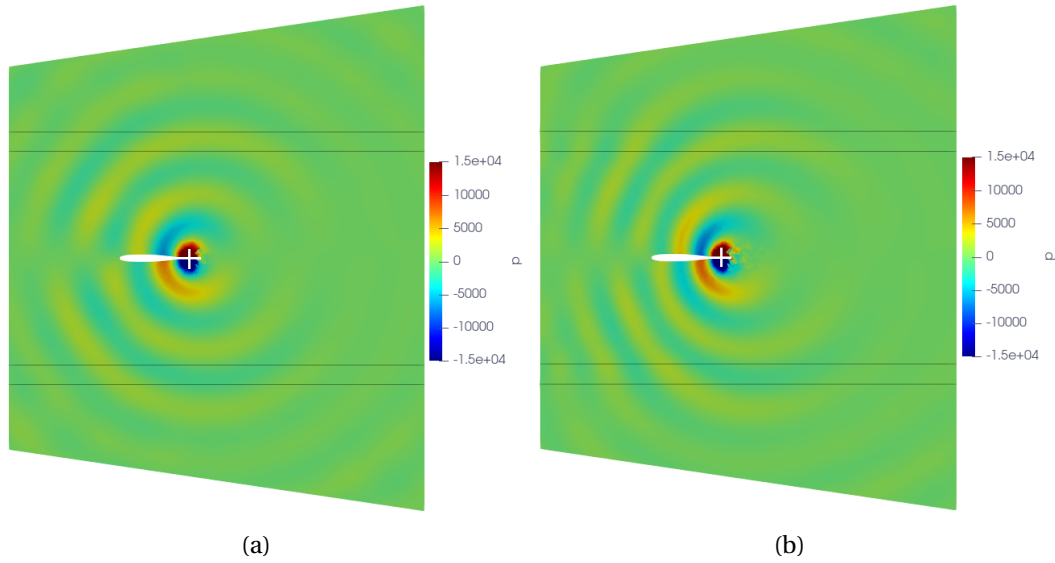


Figure 8.10: Snapshot of the pressure field in a planar cross section XY at $z = 0.3$ m for the 3D direct simulation for a synthetic dipole noise source of frequency 2 kHz near the trailing edge of the wall-mounted airfoil: (a) with an incoming speed of 39.2 m/s; (b) with an incoming speed of 100 m/s.

To identify the position of the noise source, Figure 8.11(a) shows the distribution of the RMS of the pressure field integrated from 0.05 s to 0.07 s in the same plane with an incoming speed of 39.2 m/s. Two close dominant spots well located around the real position of the dipole noise source indicate the exact position. With higher flow speed of 100 m/s (see Figure 8.11(b)), there is no evident difference in comparison with what is shown in Figure 8.11(a).

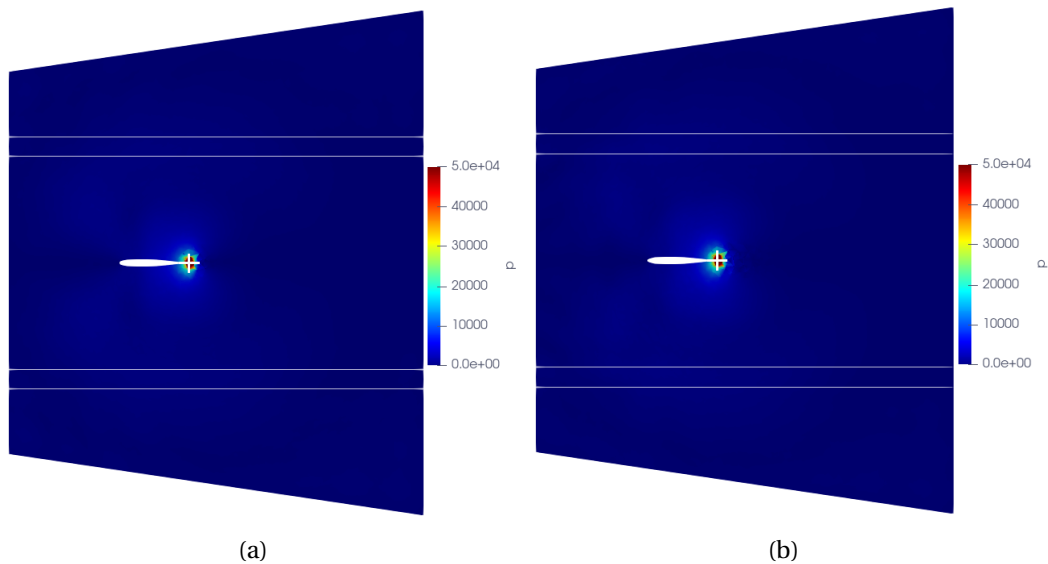


Figure 8.11: RMS of the pressure field integrated from 0.05 s to 0.07 s in a planar cross section XY at $z = 0.3$ m for the 3D direct simulation for a synthetic dipole noise source of frequency 2 kHz near the trailing edge of the wall-mounted airfoil: (a) with an incoming speed of 39.2 m/s; (b) with an incoming speed of 100 m/s.

3D numerical TR With an incoming flow speed of 39.2 m/s, Figure 8.12(a) shows a snapshot of the pressure field in a horizontal section intersecting the source position. The convergent waves established from the 'Left', 'Top' and 'Right' patches collapsed in the area near the trailing edge of the wall-mounted airfoil. Two dominant spots with a peanut shape attaching on the area of the trailing edge and surrounding the position of the dipole noise source are observed. It is found that four dominant spots are created during the TR process with two spots attached to the trailing edge of the wall-mounted airfoil and two others located downstream the source position. Logically, the pressure fluctuation at these two spots are in phase opposition. It can be concluded that the presence of the solid boundary close to the focalization spot of the TR process degrades the spatial resolution. With an incoming flow speed of 100 m/s, Figure 8.12(b) shows a snapshot of the pressure field in the same plane with similar characterization than the one at a lower speed. Similarly to the case with lower background mean flow speed, two dominant spots of peanut shape with inverse phase take place around the real position of the dipole noise source.

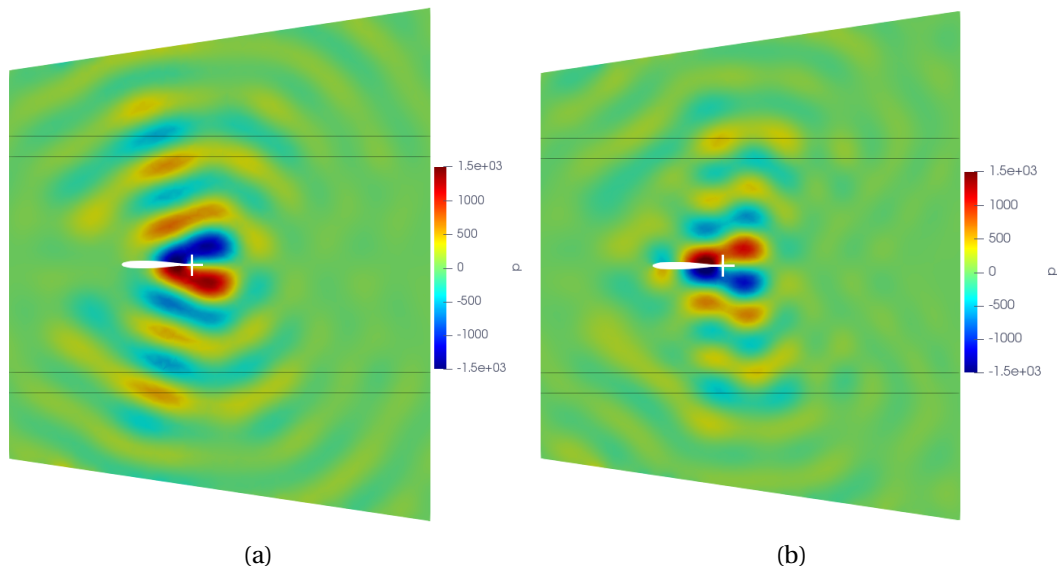


Figure 8.12: Results of the 3D TR for a synthetic dipole noise source of frequency 2 kHz near the trailing edge of the wall-mounted airfoil shown in a horizontal section. Snapshot of the pressure field in a planar cross section XY at $z = 0.3$ m: (a) with an incoming speed of 39.2 m/s; (b) with an incoming speed of 100 m/s.

To identify the position of the noise source, Figure 8.13(a) shows the distribution of the RMS of the pressure field integrated from 0.05 s to 0.07 s in the same plane with an incoming flow speed of 39.2 m/s. Two spots attached on the trailing edge yield a higher level than the two spots downstream. Therefore, the nature and the position of the noise source shown by the 3D TR result are ambiguous. Some oscillating patterns are observed because of the interference between the convergent and divergent waves during the TR process. The reason for the degradation of the performance of the 3D TR process for the identification of the dipole noise source in this case maybe be twofold: (i) there is loss of information from the patches 'Front' and 'Back' during the 3D TR process (no arrays are located on these patches), so the waves inside the domain are not well established; (ii) the solid boundaries degrade the TR process when they are in the close vicinity of the dipolar source of sound. Some studies will be conducted in the following part to understand and to improve the performance the

3D TR process in this case.

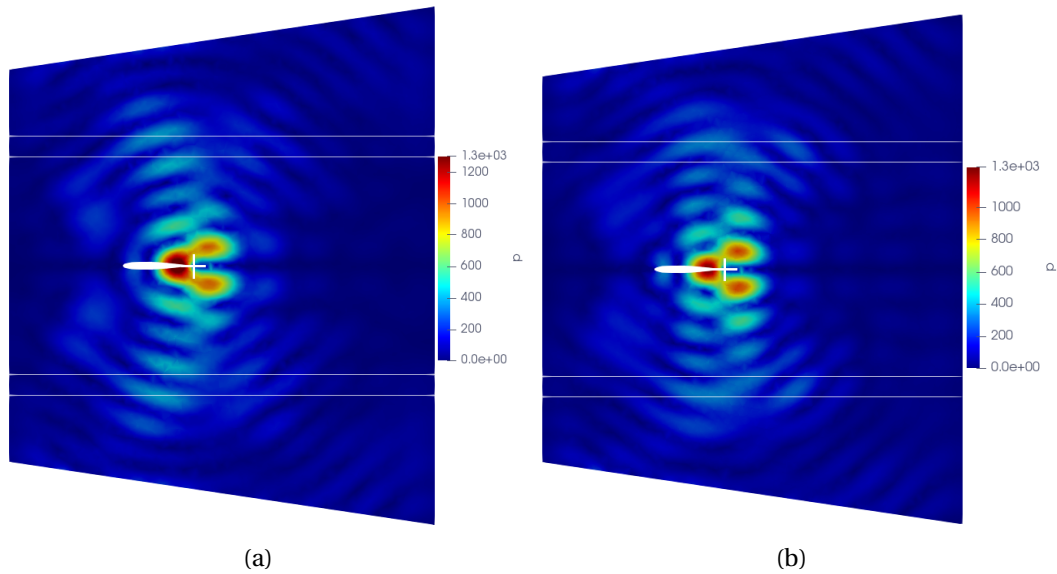


Figure 8.13: Results of the 3D TR for a synthetic dipole noise source of frequency 2 kHz near the trailing edge of the wall-mounted airfoil shown in a horizontal section. RMS of the pressure field integrated from 0.05 s to 0.07 s in a planar cross section XY at $z = 0.3$ m: (a) with an incoming speed of 39.2 m/s; (b) with an incoming speed of 100 m/s.

Two focalization spots near the trailing edge (as what was observed for the TR for a dipole noise source without the presence of solid boundaries) were expected instead of four ones for the RMS of the pressure field of 3D TR result. In order to understand why there are four focalization spots with the wall-mounted airfoil, only one subarray on the 'Left' patch was used during the 3D TR process. Figure 8.14(a) shows a snapshot of the pressure field in a horizontal section intersecting the source position at an instant when the waves reach the area of the trailing edge of the airfoil. It is clearly observed that the wavefronts are not well established like what was shown for the direct simulation because of the lack of convergent waves from the 'Front' and 'Back' patches. There is a strong interaction between the wavefronts and the solid boundaries near the trailing edge. This creates high level pressure area near the trailing edge of the airfoil. So the removal of the interaction between the wavefronts and the surface near the trailing edge may help improving the 3D TR results in terms of the distribution of the focalization spots. Figure 8.14(b) shows the snapshot of the pressure field in the same plane when the waves inside the simulation domain reach the permanent regime. Some wavefronts reflected by the airfoil surface near the trailing edge that interfere with the convergent waves from the 'Left' patch, introducing some discontinuities of the wavefronts on this side. On the other side of the airfoil, the wavefronts are uniform because of the lack of the reflected waves.

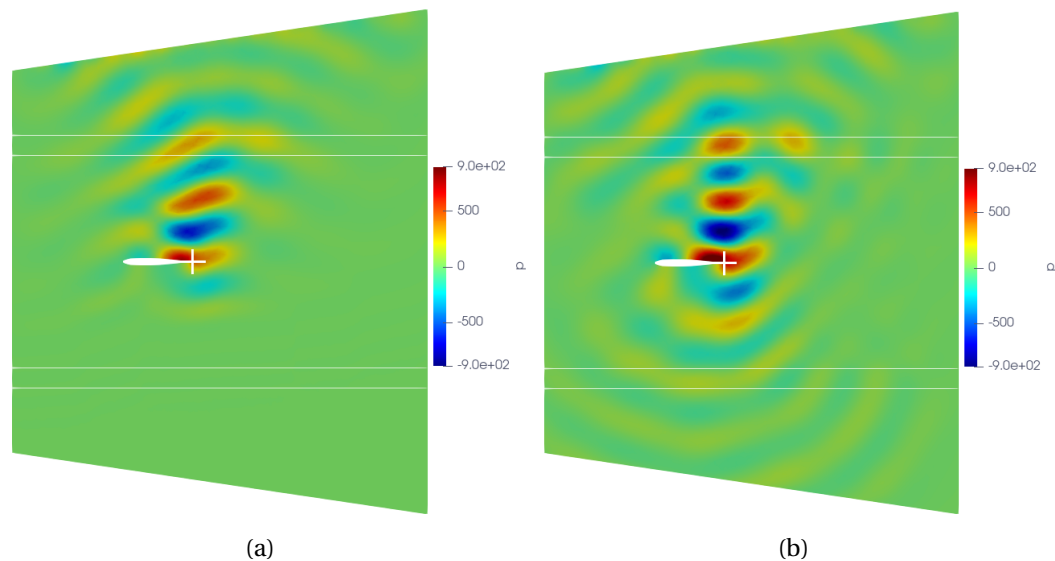


Figure 8.14: Results of the 3D TR for a synthetic dipole noise source of frequency 2 kHz near the trailing edge of the wall-mounted airfoil with an incoming speed of 100 m/s shown in a horizontal section. Only the subarray on the ‘Left’ patch was used for the 3D TR (located at the top of the figure). Snapshot of the pressure field in a planar cross section XY at $z = 0.3$ m (a) at time $t = 2.45 \times 10^{-3}$ s; (b) at time $t = 4.95 \times 10^{-3}$ s.

In order to remove the strong interaction between the acoustic waves and the surface near the trailing edge (see Figure 8.14), two cylinders of almost the same length as the span of the wall-mounted airfoil were added near the trailing edge, for which the surfaces of the cylinders use the “free” boundary condition (allowing outflows without reflection) to act as sinks and to “absorb” the waves during the TR process. Figure 8.15(a) shows the snapshot of the pressure field in a horizontal section intersecting the source position. It is observed that the two dominant spots near the trailing edge of the airfoil are removed and only two dominant spots downstream are observed. Figure 8.15(b) shows the snapshot of the RMS of the pressure field integrated from 0.05 s to 0.07 s in the same plane. The two dominant spots indicate the dipole nature of the identified noise source. However there is a shift downstream between the identified position and the real position indicated by the white cross. So the cylinders acting as acoustic sinks can improve the performance of the 3D TR process but with a shift of the position of the identified noise source. This shift is lower than the wavelength (0.17 m in that case).

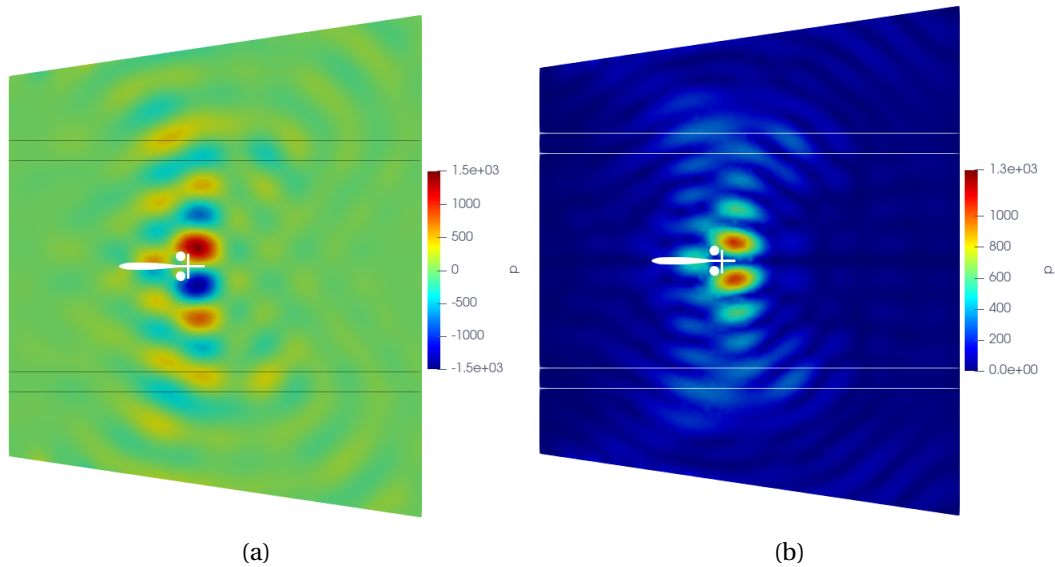


Figure 8.15: Results of the 3D TR for a synthetic dipole noise source of frequency 2 kHz near the trailing edge of the wall-mounted airfoil with an incoming speed of 100 m/s. Two cylinders using “free” boundary conditions near the trailing edge acting as acoustic sinks were placed in the simulation domain. (a) Snapshot of the pressure field in a planar cross section XY at $z = 0.3$ m; (b) RMS of the pressure field integrated from 0.05 s to 0.07 s in the same plane.

Remember that not all the acoustic information passing the boundary of the 3D domain is recorded and used for the 3D TR. The lack of the waves from the patches ‘Front’ (upstream) and ‘Back’ (downstream) may have an influence on the performance of the 3D TR technique. So, an additional simulation was carried out, with two additional subarrays located on the patches ‘Front’ and ‘Back’ of the 3D domain (see Figure 8.16(a)). This is of course not possible in a wind-tunnel, but it can be conducted numerically. The subarrays on the patches ‘Front’ and ‘Back’ contain separately 169 microphones and 196 microphones. The acoustic signals on the five patches ‘Left’, ‘Top’, ‘Right’, ‘Front’ and ‘Back’ were firstly interpolated to the position of the 1133 microphones and then time-reversed and re-emitted as monopole noise sources with a spatial Gaussian distribution during the 3D TR process. Note that the patch ‘Bottom’ uses the “wall” boundary condition which allows to reflect the waves. Figure 8.16(b) shows a snapshot of the pressure field in a horizontal section intersecting the source position. The wavefronts originating from the ‘Front’ and ‘Back’ patches are visible. Using five subarrays allows to establish the wavefronts close to that of the direct simulation (see Figure 8.10(b)). Two focalization spots in phase opposition are attached on the surface near the trailing edge of the airfoil. To identify the position of the noise source, Figure 8.16(c) shows the distribution of the RMS of the pressure field integrated from 0.05 s to 0.07 s in the same plane. It is found that a dominant bent spot, covering the position of the dipole noise source shown by the white cross, is attached on the surface near the trailing edge of the airfoil (shown by high level of the RMS field). The focalization spot still yields some ambiguity for the identification of the noise source.

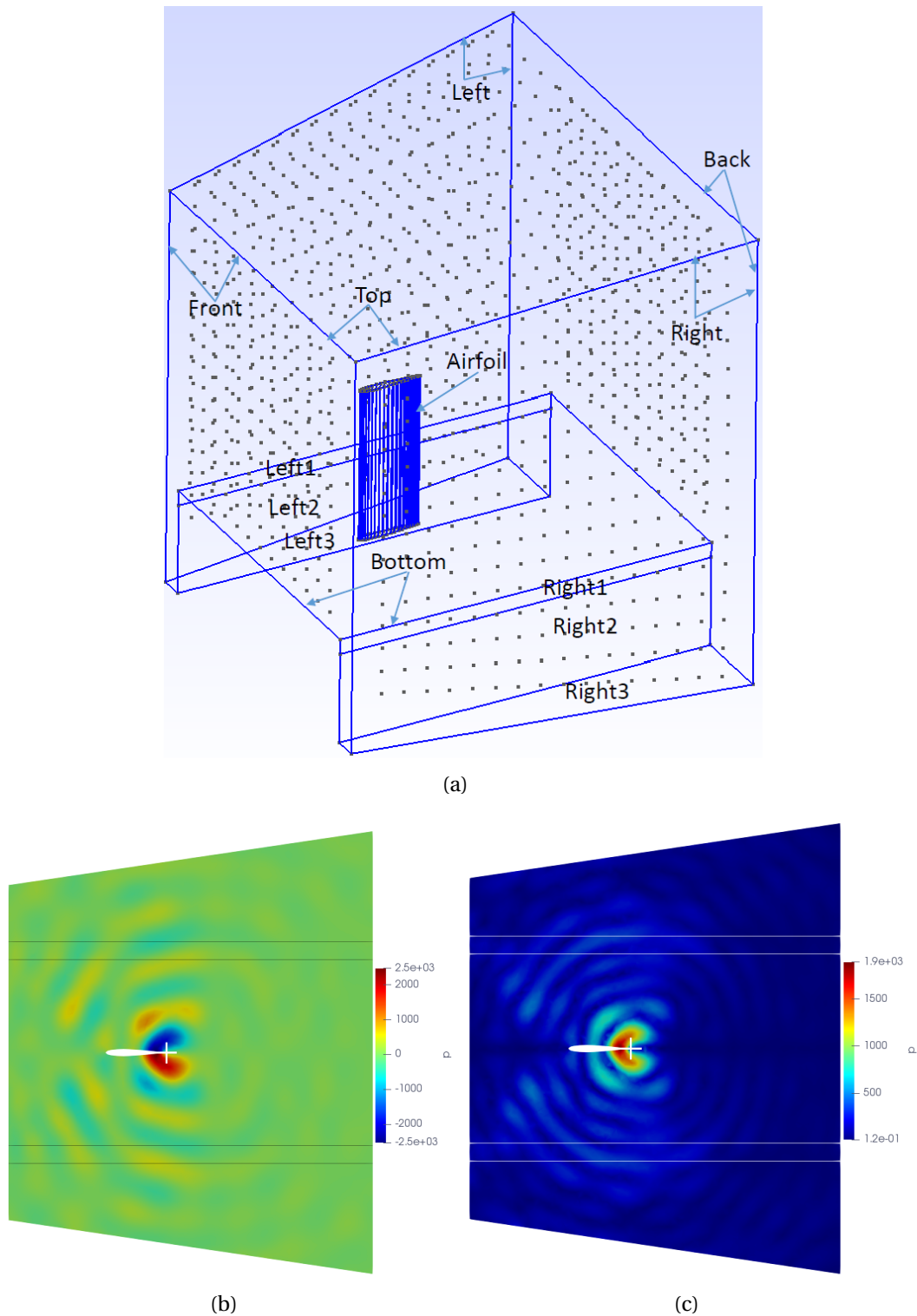


Figure 8.16: Results of the 3D TR for a synthetic dipole noise source of frequency 2 kHz near the trailing edge of the wall-mounted airfoil with an incoming speed of 100 m/s. Five subarrays on the five patches 'Left', 'Top', 'Right', 'Front' and 'Back' were used for the 3D TR process. (a) The domain of the 3D acoustic mesh concerning a wall-mounted airfoil with the positions of the 1133 microphones indicated by the black points on the five patches 'Left', 'Top', 'Right', 'Front' and 'Back'; (b) Snapshot of the pressure field in a planar cross section XY at $z = 0.3$ m; (c) RMS of the pressure field integrated from 0.05 s to 0.07 s in the same plane.

To remove the fake noise sources identified near the trailing edge (see Figure 8.16), the same improvement was conducted as the one demonstrated in Figure 8.15. Figure 8.15(a) shows a snapshot of the pressure field in a horizontal section intersecting the source position. No wavefronts are observed to attach on the surface near the trailing edge and two dominant spots with inverse phase are generated close to the position of the noise source. Figure 8.15(b) shows the snapshot of the RMS of the pressure field integrated from 0.05 s to 0.07 s in the same plane. The fake noise sources are removed. Thanks to the convergent waves downstream the airfoil, two dominant spots are generated, which indicate the dipolar nature of the noise source. The localization error is lower than that of the 3D TR process using three subarrays (compared with Figure 8.15(b)).

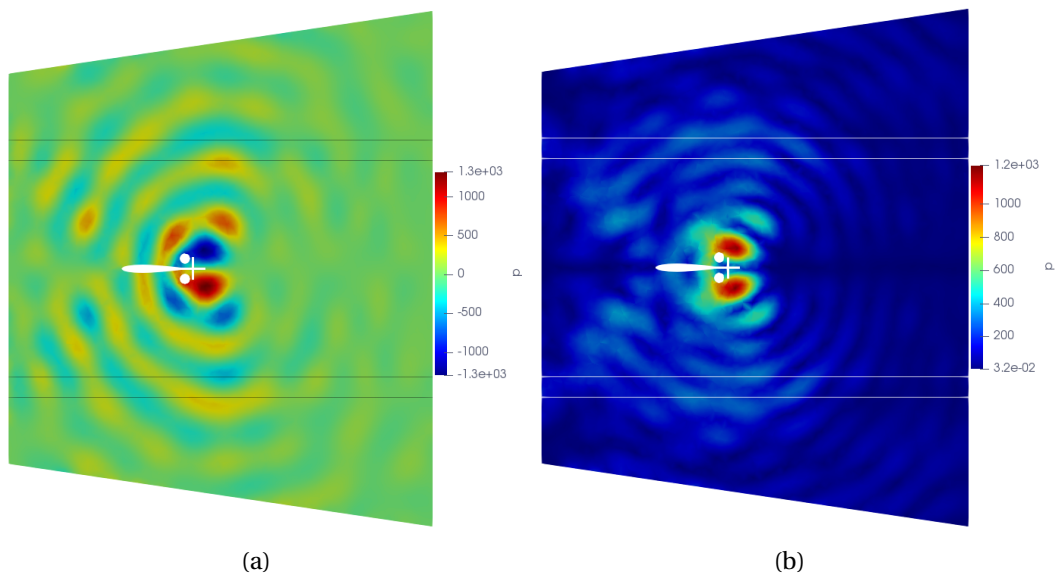


Figure 8.17: Results of the 3D TR for a synthetic dipole noise source of frequency 2 kHz near the trailing edge of the wall-mounted airfoil with an incoming speed of 100 m/s. Five subarrays on the five patches ‘Left’, ‘Top’, ‘Right’, ‘Front’ and ‘Back’ were used for the 3D TR process. Two cylinders using “free” boundary conditions near the trailing edge acting as acoustic sinks were placed in the domain of simulation. (a) Snapshot of the pressure field in a planar cross section XY at $z = 0.3$ m; (b) RMS of the pressure field integrated from 0.05 s to 0.07 s in the same plane.

8.3 Summary of the chapter

In this chapter, the numerical 3D TR technique was used for the identification of synthetic noise sources. Direct simulations concerning different types of noise sources near a wall-mounted airfoil were conducted. The acoustic signals were recorded on several patches of the simulation domain. Then, they were interpolated to the positions of the virtual microphones on the corresponding patches in order to be reversed and re-emitted as monopole noise sources with a spatial Gaussian distribution at the positions of the virtual microphones.

The mean flow around the airfoil was first obtained by a RANS simulation. The numerical result of the mean flow field was validated by comparison with some experimental results. By adding the shear layers given by analytical solutions, the field of the background mean flow similar to the one in the test section of the wind tunnel with a wall-mounted airfoil was obtained. Synthetic noise sources (monopole and dipole) near the airfoil in the background

mean flow were identified using the 3D TR technique by accounting for the solid boundaries of the airfoil and the bottom-boundary, for which the direction of the background mean flow needs to be reversed additionally.

For the monopole noise source beside the airfoil in the flow (a generic installation effect), its position was well identified by the technique with a precision at wavelength. It is also shown that the remove of the solid boundaries of the airfoil for the TR process degrades the performances of the TR technique. For the dipole noise source close to the trailing edge of the wall-mounted airfoil, the performance of the 3D TR was degraded by showing some ambiguities of the focalization spots in the RMS of the pressure field when the waves inside the simulation domain become stationary. After some parametric studies, it is believed that the solid boundaries degrade the TR process when they are in the close vicinity of the dipolar source of sound. So some other post-processing technique of the 3D TR results need to be developed to improve the performance when dealing with the cases of self-noise, when the obstacles in the flow diffract their own aeroacoustic emission (which is the case when they are not acoustically compact).

To sum it up, the TR has an interesting potential to model the installation effects (diffraction or reflection) by neighbouring elements of the noise sources. Conversely, it seems, at the current state of this research, that taking into account the boundaries of an obstacle in a flow will degrade the results if the objective is to identify the self-noise of the obstacle.

This page is intentionally left blank.

Chapter 9

Experimental results using 3D time-reversal

Contents

9.1 Geometry and acoustic mesh	154
9.2 Comparison of the results between beamforming and TR	155
9.2.1 3D beamforming result	159
9.2.2 Comparison	160
9.3 Summary of the chapter	160

In this chapter, the 3D TR technique is applied for the treatment of experimental data obtained from the acoustic measurements using the 3D microphone array in the wind-tunnel. The identification of a noise source diffracted by a NACA airfoil in a quiescent medium will be presented.

The 3D TR and beamforming results of a validation case will be presented. It concerns the acoustic field radiated by the streamlined source and diffracted by the solid boundaries of a NACA 0012 airfoil (see Chapter 2 for the description of the experiment apparatus and the corresponding dimensions). No wind-tunnel flow was generated for this experiment. The noise radiated by the streamlined acoustic source is of broadband nature. In the following results, the third-octave band [2245; 2828] Hz is considered for noise source identification.

9.1 Geometry and acoustic mesh

Figure 9.2(a) shows the geometry of a NACA 0012 airfoil at an angle of attack of 0° and the streamlined acoustic source displayed using the software GMSH. Only the airfoil contains solid boundaries, which is different to the case in Section 9.2.2. The 256 microphones of the microphone array, which are selected from the array with 768 microphones in Chapter 2, are located on the surfaces of the three patches. The same coordinate system as presented in Chapter 2 is used. The emission of the streamlined acoustic source is located at the position (0.402 m, -0.075 m, 0.35 m), which is considered as the real position of the synthetic noise source. The leading edge of the airfoil is located at a distance of 310 mm from the patch 'Front'. The unstructured 3D acoustic mesh with 200 partitions is generated using GMSH. There are some refinements around the surface of the airfoil in order to well describe the geometry for the acoustic simulation. The 3D acoustic mesh contains 1839344 elements, among which 105896 triangles on all the patches of the boundary of the domain and 1733448 tetrahedra inside the domain of 3D acoustic mesh. Figure 9.2(b) shows the triangular mesh elements on the patches of 'Airfoil' and 'StreamlinedSource' using the "wall" boundary condition. Figure 9.1(c) shows the triangular mesh elements on the patches of 'Left', 'Top' and 'Right' using the "BC_gauss_spot" boundary condition. Figure 9.1(d) shows the triangular mesh elements on the patches of 'Front', 'Back', 'Left1', 'Left2', 'Left3', 'Right1', 'Right2', 'Right3' and 'Bottom' using the "free" boundary condition.

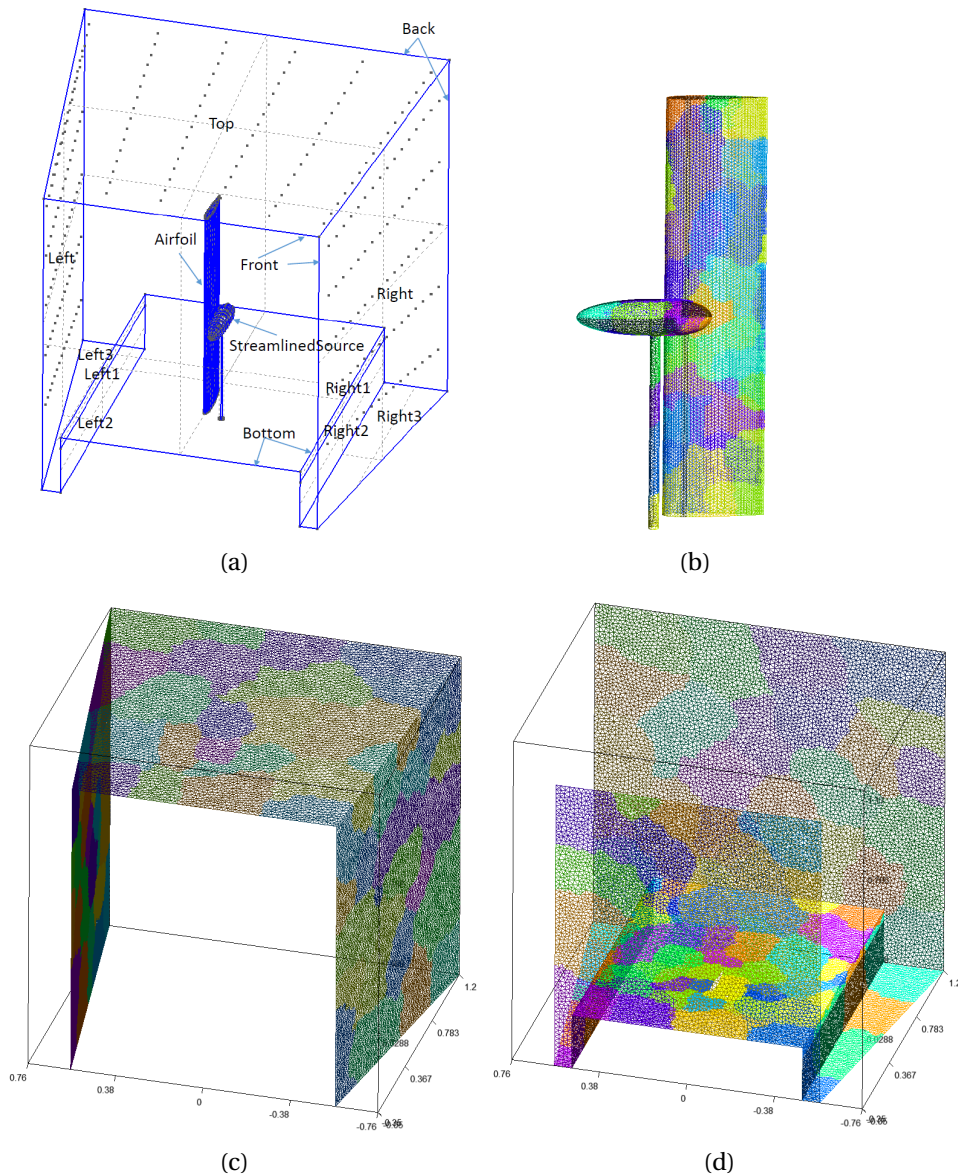


Figure 9.1: Generation of the 3D acoustic mesh of a NACA 0012 airfoil at an angle of attack $\alpha = 0^\circ$ and of the streamlined acoustic source, using GMSH. (a) The domain of the 3D acoustic mesh with the positions of the 256 microphones indicated by the black points on the three patches 'Left', 'Top' and 'Right' of the domain; (b) the triangular mesh elements on the patches of 'Airfoil' and 'Streamlined-Source'; (c) the triangular mesh elements on the patches of 'Left', 'Top' and 'Right'; (d) the triangular mesh elements on the patches of 'Front', 'Back', 'Left1', 'Left2', 'Left3', 'Right1', 'Right2', 'Right3' and 'Bottom'. The mesh elements with different colors in (b), (c) and (d) correspond to different partitions.

9.2 Comparison of the results between beamforming and TR

3D TR result The acoustic signals of the array channels selected from the experimental data were firstly filtered by a band-pass filter of 256th order to study the third-octave band [2245 Hz; 2828 Hz]. First we consider the TR result using only 256 channels of the total data.

The sampling rate for the acoustic measurements by the microphone array is 50 kHz (the sampling period is 2×10^{-5} s). The time step for the numerical simulation, which depends on the CFL number, the mesh element size, and the polynomial order N (see in Appendix C), is 1.77107×10^{-7} s. It is lower than the sampling period, so interpolations should be conducted for the experimental data in order to be applied to the 3D TR process. The physical simulation time for the 3D TR is 0.02 s with the polynomial order $N = 2$. Therefore 1002 data points were used for the interpolation process. Figure 9.2 shows the original signal of the channel 545 and the corresponding signal after interpolations. The numerical simulations using parallel computation were conducted in a cluster with 200 processors. The typical computation time is about two days depending on the number of channels used for the 3D TR.

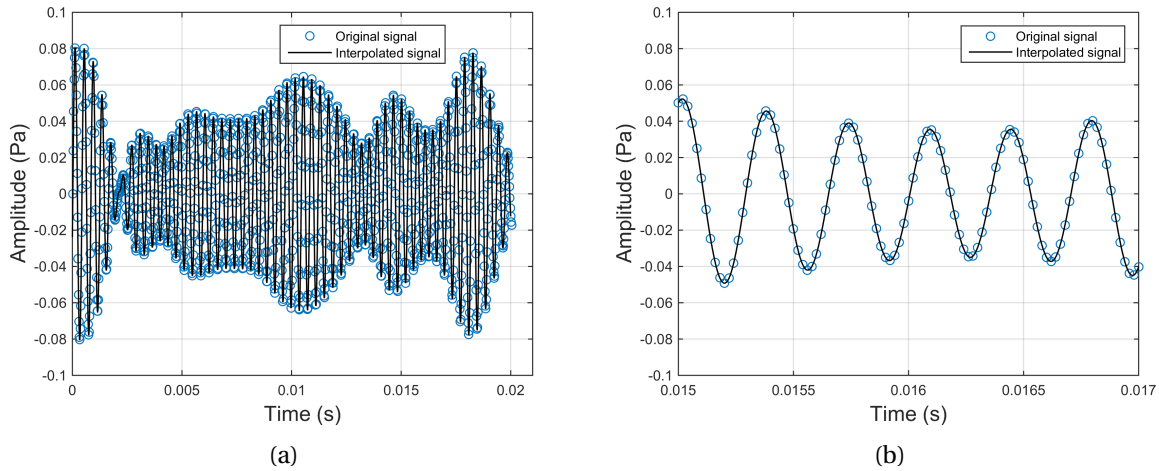


Figure 9.2: (a) Original signal of the channel 545 and the interpolated signal; (b) a zoom of (a).

Figure 9.3(a) shows a snapshot of the pressure field in a planar cross section XY at $z = 0.35$ m when the waves inside the simulation domain reach the permanent regime. The reconstruction of the wavefronts clearly originates from the patch ‘Right’, which is the one which is not shielded by the airfoil. A dominant spot centered on the position of the noise source was observed. The wave reflection on the airfoil boundary is clearly evidenced by the snapshot of Figure 9.3(a). Figure 9.3(b) shows the RMS of the pressure field integrated from 0.005 s to 0.015 s in the same planar cross section XY . The position of the synthetic noise source is well identified by the focalization spot with a precision of wavelength. It can be identified with the same precision in a vertical cross section XZ according to the result shown in Figures 9.3(c) and 9.3(d). The two side lobes in these figures may due to the fact that the waves are not well established using only 256 channels of data. This is shown clearly in Figures 9.3(e) and 9.3(f) in a cross section YZ . The dominant focalization spot reveals the position of the noise source but with some ambiguities caused by other isolated spots (see Figure 9.3(f)). The same results as in Figure 9.3 are now displayed in Figure 9.4, when the 768 channels of the array are used. Considering the snapshots in the different planar cross-section (Figures 9.4(a), 9.4(c), 9.4(e)), it is observed that the wavefronts emanating from the subarrays are better established using 768 channels. The RMS pressure field does not show a clear improvement of the resolution of the energetic spot centered on the source position, but the isolated spots observed in the vertical planes of Figures 9.3(d) and 9.3(f) are not present anymore.

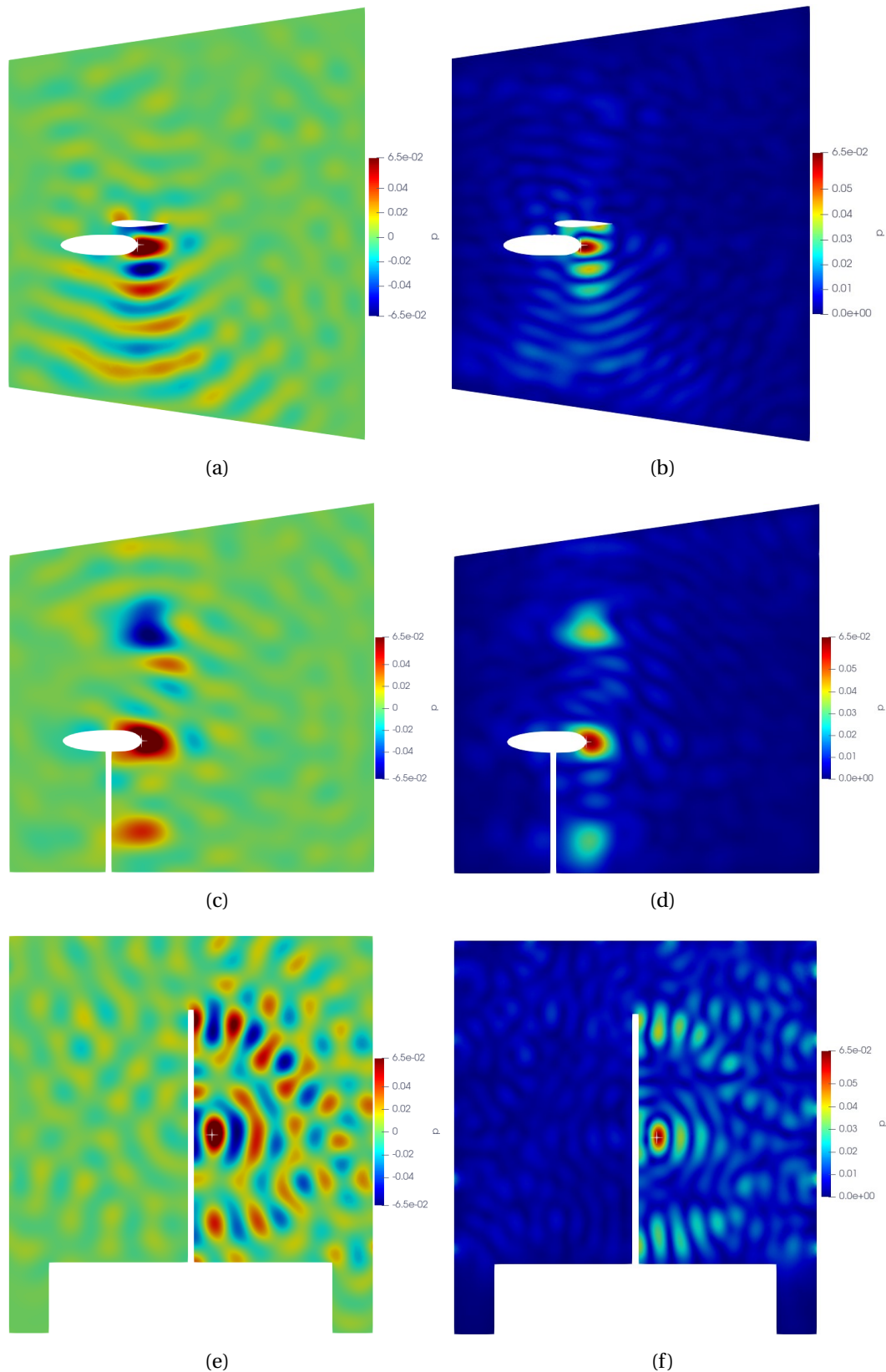


Figure 9.3: Results of the 3D TR concerning the synthetic noise source emitted by the streamlined body shown in different cross sections in the third-octave band [2245; 2828] Hz. 256 channels of acoustic data are used. (a) Snapshot of the pressure field in a planar cross section XY at $z = 0.35$ m; (b) RMS of the pressure field integrated from 0.005 s to 0.015 s in the same plane; (c) snapshot of the pressure field in a planar cross section XZ at $y = -0.075$ m; (d) RMS of the pressure field integrated from 0.005 s to 0.015 s in the same plane; (e) snapshot of the pressure field in a planar cross section YZ at $x = 0.402$ m; (f) RMS of the pressure field integrated from 0.005 s to 0.015 s in the same plane.

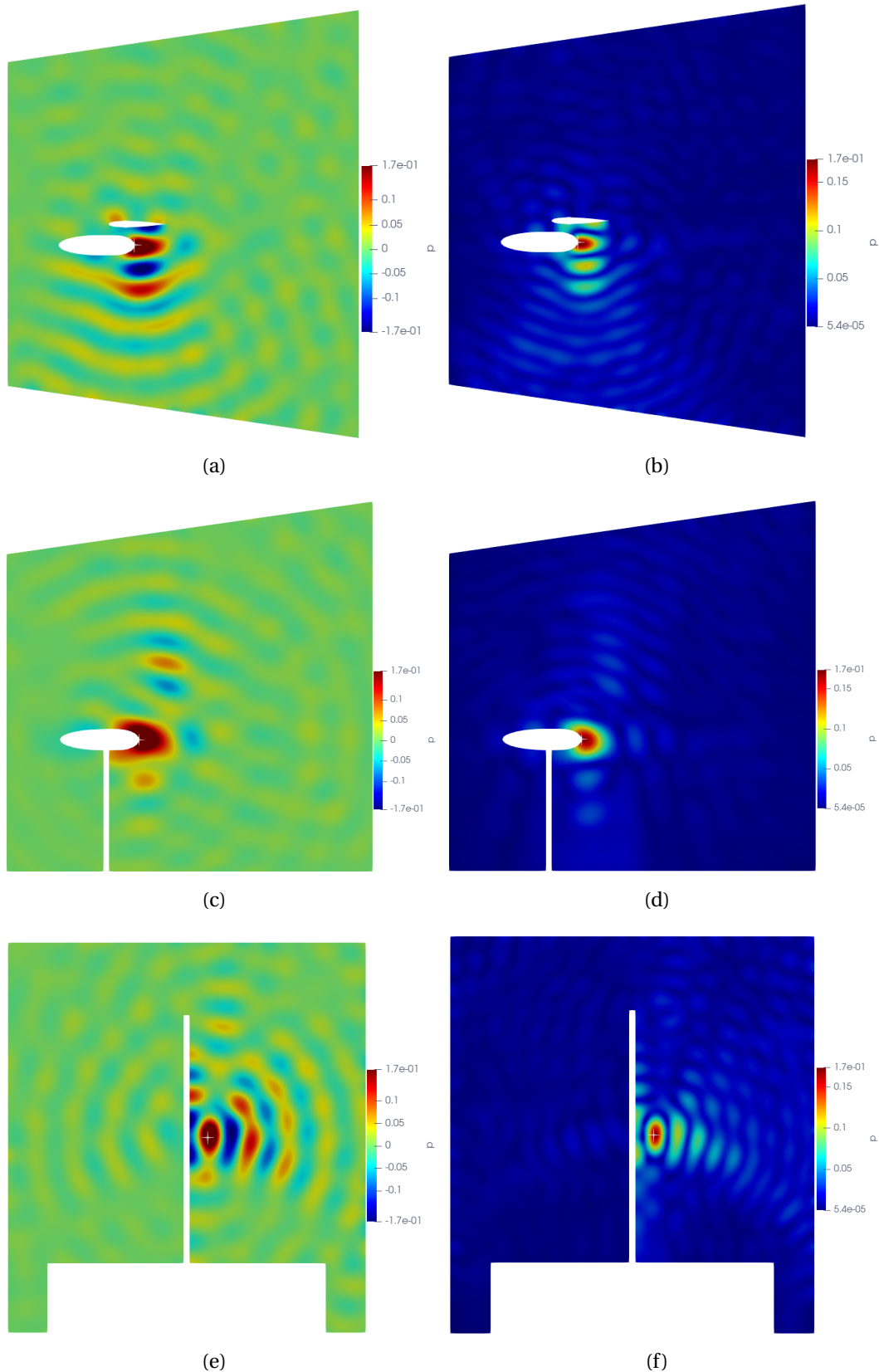


Figure 9.4: Results of the 3D TR concerning the synthetic noise source emitted by the streamlined body shown in different cross sections in the third-octave band [2245; 2828] Hz. 768 channels of acoustic data are used. (a) Snapshot of the pressure field in a planar cross section XY at $z = 0.35$ m; (b) RMS of the pressure field from 0.005 s to 0.015 s in the same plane; (c) snapshot of the pressure field in a planar cross section XZ at $y = -0.075$ m; (d) RMS of the pressure field from 0.005 s to 0.015 s in the same plane; (e) snapshot of the pressure field in a planar cross section YZ at $x = 0.402$ m; (f) RMS of the pressure field from 0.005 s to 0.015 s in the same plane.

9.2.1 3D beamforming result

Figure 9.5(a) presents now the sound map using the 3D beamforming technique for the same case. A 3D scanning grid with a spatial resolution of 5 mm was set for the 3D beamforming. The monopolar steering vector is used for the beamforming algorithm. Note that the propagation model is based on a free-field Green function. For this reason, the airfoil effect is not taken into account in the results. The computation time is about four days using MATLAB on a personal computer with a 3 GHz Intel Xeon processor. The position with maximum level of the 3D beamforming sound map is considered to be the estimated position of the synthetic noise source. The position of the synthetic noise source (0.402 m, -0.075 m, 0.35 m) is indicated by the red cross.

Due to the influence of the solid boundaries of the airfoil, the sound map yields some ambiguities. On the side of the synthetic noise source, a main lobe together with an isolated side lobe and an ambiguous elongated side lobe is centered on the position of the noise source. The peak level of the sound map is located at the position (0.425 m, -0.095 m, 0.35 m). The elongated side lobe is evenly distributed along the y -direction, most of which is on the other side of the noise source. To improve the spatial resolution of the sound map, the CLEAN-SC technique is used. It is observed that the side lobes are successfully removed (Figure 9.5(b)). An isolated noise source, with the peak level on the position (0.425 m, -0.095 m, 0.35 m), is identified. The error of the position of the noise source in the y -direction is 0.02 m, and 0.023 m in the x -direction.

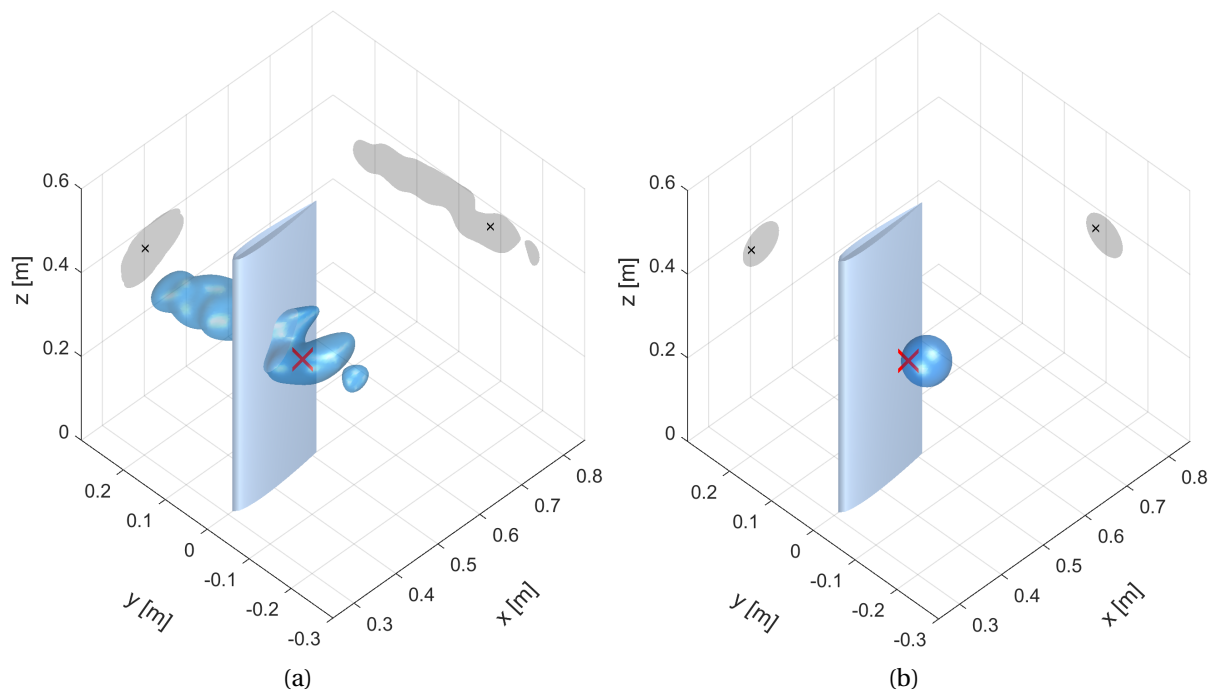


Figure 9.5: Sound maps for the synthetic noise source diffracted by a NACA 0012 airfoil with finite span length at an angle of attack $\alpha = 0^\circ$, at a third-octave bands of nominal midband frequency 2.5 kHz. The shadows and the red symbols 'x' correspond respectively to the projection of the 3D sound source imaging and the noise source position. (a): 3D beamforming with a maximum value of 56.2 dB on the sound map; (b): CLEAN-SC technique with a maximum value of 56.1 dB on the sound map. The 3D isosurface in each sound map is plotted at 9 dB below the maximum value of the sound map.

9.2.2 Comparison

The 3D beamforming result in a third-octave band has been obtained without accounting for the presence of the solid boundaries. The sound map without deconvolution is ambiguous to be interpreted. Using the CLEAN-SC technique, the noise source is identified with a localization error inferior to the wavelength. The CLEAN-SC appears to be quite robust in this situation, probably because the elongated lobe is coherent with the main lobe and can be removed after deconvolution. Conversely, the solid boundaries is considered for 3D TR technique. Without conducting post-processing process similar to deconvolution method, the noise source is also identified with a localization error inferior to the wavelength by 3D TR. But the position error in the y -direction is lower than that of the BF result if we consider the peak level of the RMS of the pressure field as the identified position of the noise source. However, the 3D TR is more complex and computationally expensive compared to the beamforming method.

9.3 Summary of the chapter

This chapter is dedicated to the applications of the 3D TR technique using experimental data obtained from the acoustic measurements in the wind-tunnel. The noise source emitted by a streamlined source diffracted by a NACA airfoil is successfully identified with a localization error inferior to the wavelength. Two cases are considered: one with 256 channels of signals, the other using 768 channels of signals. It is demonstrated that the case with lower number of channels degrades the performance of the 3D TR technique by introducing some unexpected spots for the RMS of the pressure field. The same 256 channels of data are used for the 3D beamforming technique. The 3D beamforming results after deconvolution show that the noise source is identified with a localization error inferior to the wavelength but the precision of the source position in the y -direction is lower than that of the 3D TR results. However, the 3D TR is more complex and computationally expensive.

Conclusions and perspectives

This thesis aims at identifying aeroacoustic sources in a wind-tunnel with open or 3/4 open test section using massive 3D microphone arrays. Two 3D microphone arrays, made of three planar sub-arrays enclosing the test section of the wind-tunnel, are used for the acoustic measurements. One is with 256 channels of MEMS microphones, the other is with 768 channels. The signal processing methods for the acoustic data are the beamforming technique and the TR technique. In the first part of the thesis (Chapters 4 to 6), the beamforming technique is extended to identify noise source in 3D domains (3D beamforming technique) for wall-mounted airfoils and a high-lift device model. In the second part (Chapters 7 to 9), the TR technique is used for noise source identification for both simulated and experimental data. This processing method is based on a numerical propagation solver, and its potential advantages are that it allows to model accurately the influence on wave propagation of: (i) solid boundaries in the flow, due to the obstacles creating sound or geometrical elements creating so-called installation effects; (ii) the mean flow field created by the interaction of the obstacle and the flow (wakes in particular) and the wind-tunnel jet. In this purpose, the numerical tool used in this thesis is an in-house acoustic solver of the linearized Euler equations developed at Institut Jean le Rond d'Alembert, allowing to model the acoustic propagation through arbitrary mean flow fields with diffraction by obstacles. The mean flow around the obstacles in the flow is simulated using an open source software OpenFOAM.

Beamforming results The 3D beamforming results of a synthetic noise source in wind-tunnel flows show that the flow effects (convection and refraction) on sound propagation lead to significant localization errors on sound maps (of the order of the wavelength), and that such effects should be accounted for when using the 3D beamforming technique. Moreover, the Amiet's method for the flow-effect correction is demonstrated to be robust for testing cases with mean flow gradients within the jet core of the wind-tunnel flow, even though such non-uniform effect on sound propagation is not modeled by the method.

The identification of the aeroacoustic sources of a wall-mounted NACA 0012 airfoil was conducted using the 3D microphone array of 256 microphones for angles of attack ranging from 0° to 20° , enclosing the 3/4 open test section. The beamforming technique associated to a deconvolution method (CLEAN-SC) is extended to noise identification in 3D domains. The noise sources of an acoustically compact wall-mounted airfoil is of dipolar nature, so that a dipolar radiation model perpendicular to the airfoil is implemented for the beamforming technique. Simulations based on synthetic noise sources indicate that the 3D beamforming technique allows to identify a linear distribution of non coherent dipoles, similar to that of the broadband trailing edge noise source. 3D beamforming results after deconvolution in the third-octave bands under investigation show that the expected noise source contributions including the trailing edge, the wing tip, the leading edge and the junction are successfully identified, and are in good agreement with experimental results published in

the literature. The 3D beamforming technique is also applied to the identification of two parallel wall-mounted airfoils with different span lengths. The presented results show that the 3D beamforming technique is promising for the investigation of the flow-induced noise of objects in flows with a strong 3D configuration, and that MEMS microphones are good candidates for such studies in spite of their relatively low metrological qualities (compared to measurement microphones).

The performances of the 3D beamforming technique is then assessed through the identification of aeroacoustic sources of on a model of high-lift device with a more complex geometry. The noise source distribution is investigated using the 2D beamforming technique based on a monopolar radiation model. Noise sources in the areas of the slat, and the trailing edge of the main element are identified under different testing conditions. 3D beamforming results are then obtained: the identified dominant noise sources for the cases of angle of attack of 0° and 10° confirm the 2D results. However, for the case of angle of attack of 6° , the slat noise is not identified, which may be due to a wrong assumption on the sound radiation model. It is likely that the beamforming method applied to data obtained with a 3D array is more sensitive to the choice of a valid radiation model than with a 2D array, for the reason that the source radiation is measured over a wide solid angle.

TR results The numerical TR contains two steps: in the first step, an acoustic measurement is conducted with a microphone array. This measurement can be carried out either experimentally or with a numerical simulation (called the direct simulation in this work); in the second step, the TR process is carried out by reversing and re-emitting (totally or partially) the recorded acoustic signals, amplitudes of which are multiplied by a factor 2, as monopoles at the same recording positions in order to identify the noise sources. The TR process is validated by using a 2D benchmark problem concerning the scattering of an acoustic pulse off a cylinder in a quiescent medium.

The performances of the numerical 2D TR technique are demonstrated through some preliminary studies with numerical data, in which the BF technique may fail. First, an acoustic pulse inside a semi-open cavity with a heterogeneous medium is identified with a localization error inferior to the source size. Then, several types of TR mirrors (using partially the recorded acoustic signals) with respect to the TR cavity (using totally the recorded acoustic signals) are studied through the identification of an acoustic pulse scattered by an airfoil. It was found that even with a loss of information for the TR process, the source position was still identified with a localization error inferior to the source size. Finally, the diffraction of trailing edge noise by the boundaries of the airfoil is modeled by simulating a synthetic dipole near the trailing edge with a background mean flow obtained by a RANS simulation for the direct simulation. The dipolar source is identified with a localization error inferior to the wavelength by the 2D TR cavity. Using a TR mirror, the dipolar source is still identified with the same localization error, which approaches the real application of the TR technique. Moreover, the feasibility of implementation of an acoustic sink in order to improve the resolution of the TR results is demonstrated by a preliminary study of the identification of a synthetic monopole.

The 3D numerical TR is used to identify synthetic noise sources near a wall-mounted airfoil in a flow. The first case concerns a harmonic monopole besides the airfoil to approach a generic installation effect. The source is identified with a localization error inferior to the wavelength. If the solid boundaries of the airfoil are not considered, it leads to a larger localization error. The second case deals with a harmonic dipole close to the trailing edge of the

airfoil to approach the self-noise produced by an airfoil. The performance of the 3D TR is degraded by showing some ambiguities of the focalization spots in the RMS of the pressure field. After some parametric studies, it is believed that the solid boundaries corrupt the TR process when they are in the close vicinity of the dipolar noise source.

Finally, 3D TR technique is used to process acoustic signals obtained from array measurements without flow. The broadband noise source emitted by a streamlined body diffracted by a NACA airfoil is successfully identified with a localization error inferior to the wavelength. A parametric study is conducted by using different channels of signals. It is demonstrated that the case with 256 channels of signals degrades the performance of the 3D TR technique by introducing some unexpected spots for the RMS of the pressure field with respect to the case with 768 channels of signals. The same 256 channels of data are used for the 3D beamforming technique. The 3D beamforming results after deconvolution show that the noise source can also be identified with a localization error inferior to the wavelength, but with a larger error in the direction perpendicular to the airfoil surface than that of the 3D TR results. Therefore, on the one hand, the 3D beamforming technique associated the CLEAN-SC method is robust even dealing with the cases with solid boundaries; on the other hand, the 3D TR technique is promising for real applications with installation effects such as reflection and diffraction, but this technique is more complex and computationally expensive.

Perspectives The 3D beamforming technique requires noise source radiation models depending on the nature of the noise sources under investigation. For dipolar noise sources, additional assumptions for their orientations are also needed. This is unpractical when dealing with cases with complex geometries. Therefore, improvements could be conducted for 3D beamforming algorithms in order to estimate the orientations of the dipolar sources, for example, by further developing zonal approaches when different obstacles in the flow follow different orientations (such as in section 5.2). More generally, a technique could be developed to estimate the best radiation model matching the array data; for example, a technique inspired from the generalized beamforming method [114] could be used in this context. Additionally, some post-processing methods could be conducted, using integration methods to remove the influence of spurious noise sources or to focus on some specific geometrical elements. Finally, the 3D beamforming technique could be extended to account for simple installation effects such as reflections [51], and to analyse non-stationary aeroacoustic events such as in [52].

For the TR technique, 3D TR results show that the identification of a dipolar noise source in a quiescent medium leads to two dominant spots around the source position for the RMS distribution of the pressure field. This is similar to what was observed in 3D beamforming results when identifying a dipolar noise source based on a monopolar radiation model. Some improvements could be conducted for the 3D TR technique in order to obtain a peak level at the source position by considering the acoustic velocity instead of the acoustic pressure (as shown in Figure E.4). In addition, some other further post-processing techniques of the 3D TR results need to be developed in order to improve the performances when dealing with the cases of self-noise, in particular when the obstacles in the flow diffract their own aeroacoustic emission (which is the case when they are not acoustically compact). In this thesis, the experimental application of the 3D TR is of preliminary nature, concerning a validation case in a quiescent medium. The technique should now be applied with the wind-tunnel flow, first with the streamlined source and then to identify self-noise of obstacles.

This page is intentionally left blank.

Appendix A

Time-reversed pressure field

According to Cassereau and Fink [30], the Green function corresponding to impulse diverging spherical wave in the time domain is given by

$$G_d(\mathbf{x}, \mathbf{x}_s; t) = \frac{1}{4\pi|\mathbf{x} - \mathbf{x}_s|} \cdot \delta\left(t - \frac{|\mathbf{x} - \mathbf{x}_s|}{c_0}\right). \quad (\text{A.1})$$

The Green function corresponding to impulse converging spherical wave in the time domain is given by

$$G_c(\mathbf{x}, \mathbf{x}_s; t) = \frac{1}{4\pi|\mathbf{x} - \mathbf{x}_s|} \cdot \delta\left(t + \frac{|\mathbf{x} - \mathbf{x}_s|}{c_0}\right). \quad (\text{A.2})$$

By definition of convolution, we have

$$\begin{aligned} G_c(\mathbf{x}, \mathbf{x}_s; t) * \phi(T - t) &= \int_{\mathbb{R}} \frac{1}{4\pi|\mathbf{x} - \mathbf{x}_s|} \cdot \delta\left(\tau + \frac{|\mathbf{x} - \mathbf{x}_s|}{c_0}\right) \cdot \phi(T - (t - \tau)) d\tau \\ &= \frac{1}{4\pi|\mathbf{x} - \mathbf{x}_s|} \cdot \phi\left(T - \left(t - \left(-\frac{|\mathbf{x} - \mathbf{x}_s|}{c_0}\right)\right)\right) \\ &= \frac{1}{4\pi|\mathbf{x} - \mathbf{x}_s|} \cdot \phi\left(T - t - \frac{|\mathbf{x} - \mathbf{x}_s|}{c_0}\right). \end{aligned} \quad (\text{A.3})$$

$$\begin{aligned} G_d(\mathbf{x}, \mathbf{x}_s; t) * \phi(T - t) &= \int_{\mathbb{R}} \frac{1}{4\pi|\mathbf{x} - \mathbf{x}_s|} \cdot \delta\left(\tau - \frac{|\mathbf{x} - \mathbf{x}_s|}{c_0}\right) \cdot \phi(T - (t - \tau)) d\tau \\ &= \frac{1}{4\pi|\mathbf{x} - \mathbf{x}_s|} \cdot \phi\left(T - \left(t - \frac{|\mathbf{x} - \mathbf{x}_s|}{c_0}\right)\right) \\ &= \frac{1}{4\pi|\mathbf{x} - \mathbf{x}_s|} \cdot \phi\left(T - t + \frac{|\mathbf{x} - \mathbf{x}_s|}{c_0}\right). \end{aligned} \quad (\text{A.4})$$

It was demonstrated by Cassereau and Fink [30] and Bavu *et al.* [14] that the time-reversed pressure field is also given by

$$\begin{aligned} p_{TR}(\mathbf{x}, t) &= \frac{1}{4\pi|\mathbf{x} - \mathbf{x}_s|} \cdot \phi\left(T - t - \frac{|\mathbf{x} - \mathbf{x}_s|}{c_0}\right) - \frac{1}{4\pi|\mathbf{x} - \mathbf{x}_s|} \cdot \phi\left(T - t + \frac{|\mathbf{x} - \mathbf{x}_s|}{c_0}\right) \\ &= G_c(\mathbf{x}, \mathbf{x}_s; t) * \phi(T - t) - G_d(\mathbf{x}, \mathbf{x}_s; t) * \phi(T - t) \\ &== G_d(\mathbf{x}, \mathbf{x}_s; -t) * \phi(T - t) - G_d(\mathbf{x}, \mathbf{x}_s; t) * \phi(T - t). \end{aligned} \quad (\text{A.5})$$

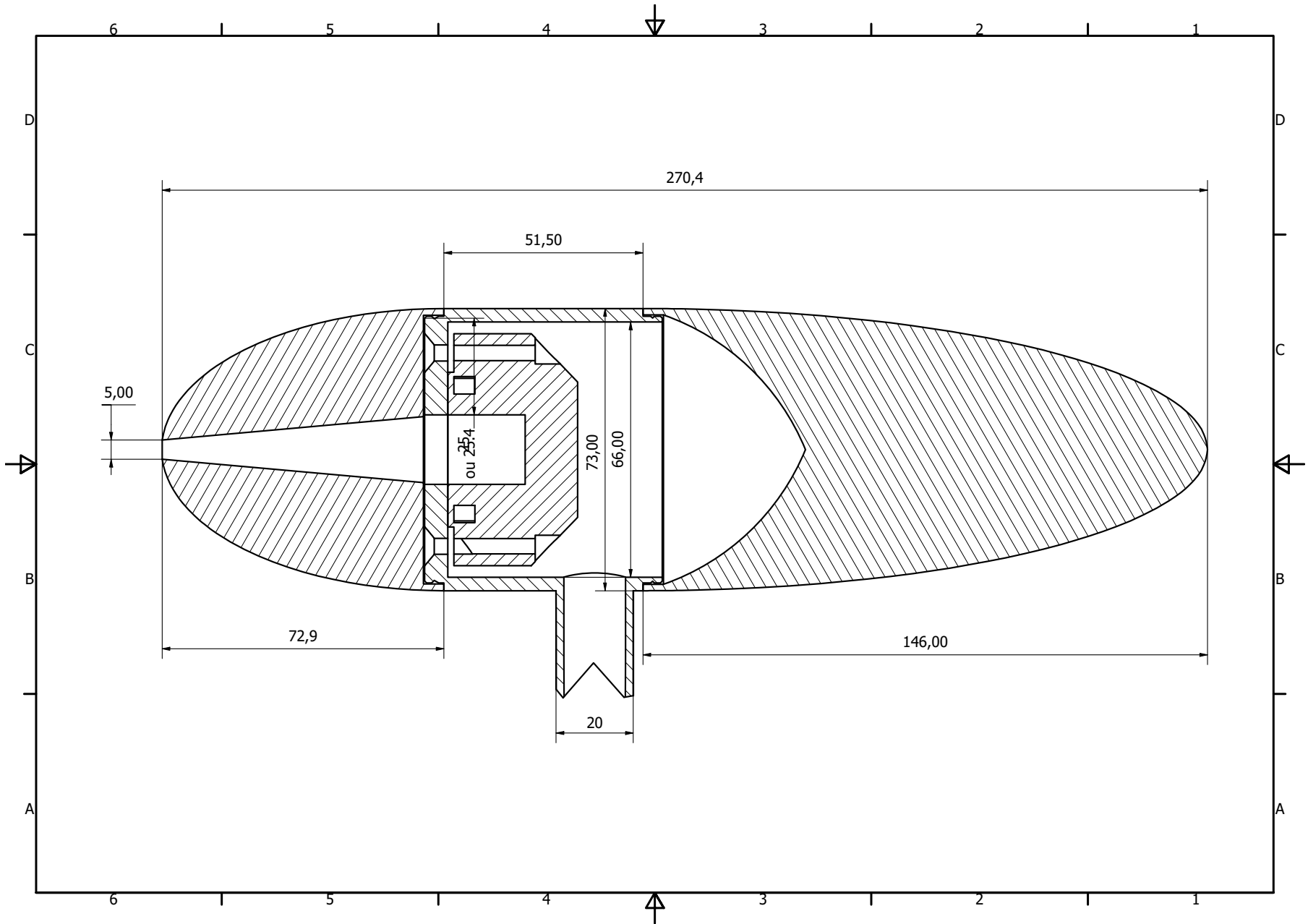
This page is intentionally left blank.

Appendix B

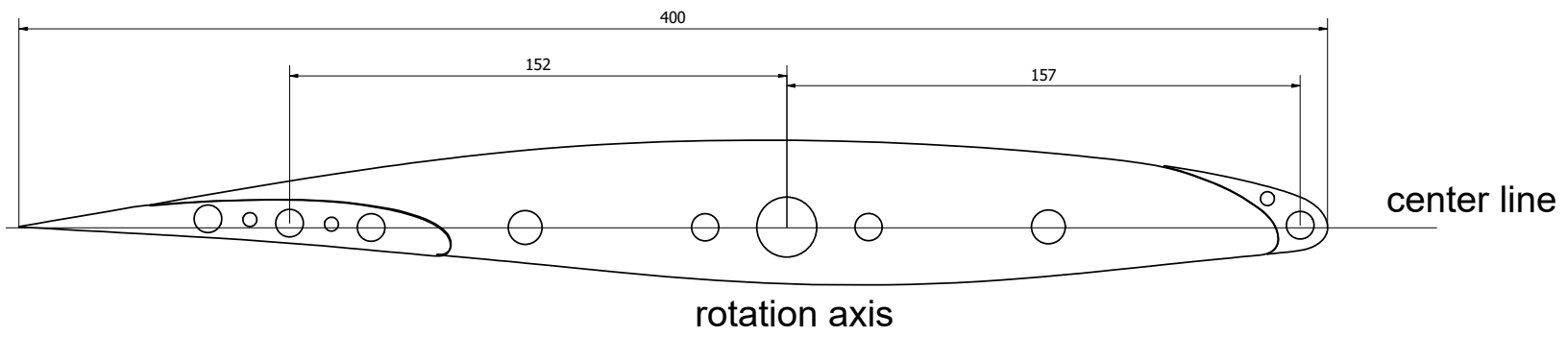
Plans of a streamlined acoustic source and of a high-lift device model

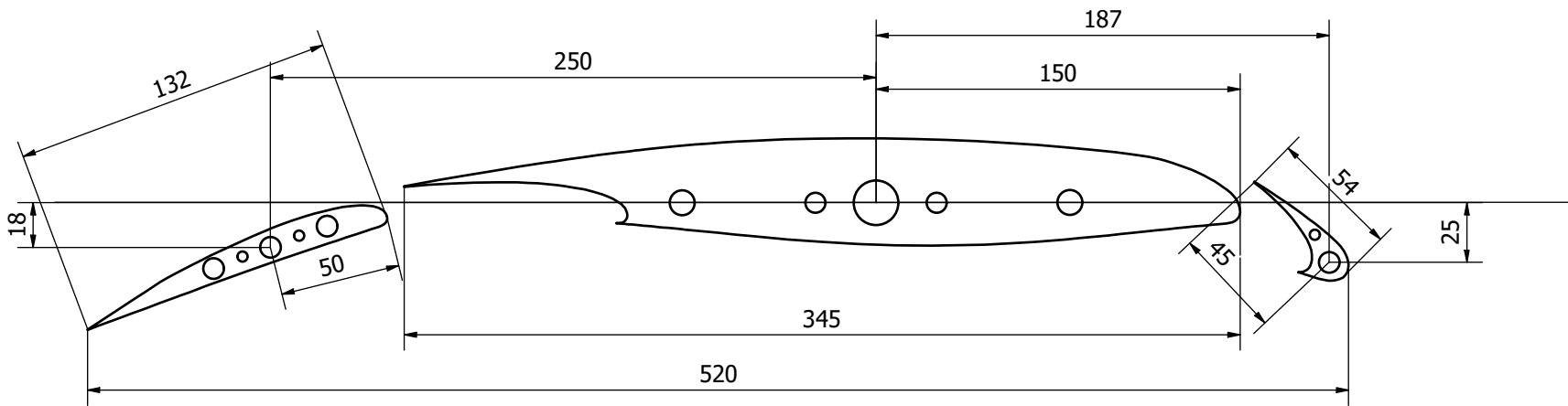
This appendix presents the plans of the streamlined object and of the high-lift device model. The plans are provided by Pascal Biais Sauvetre.

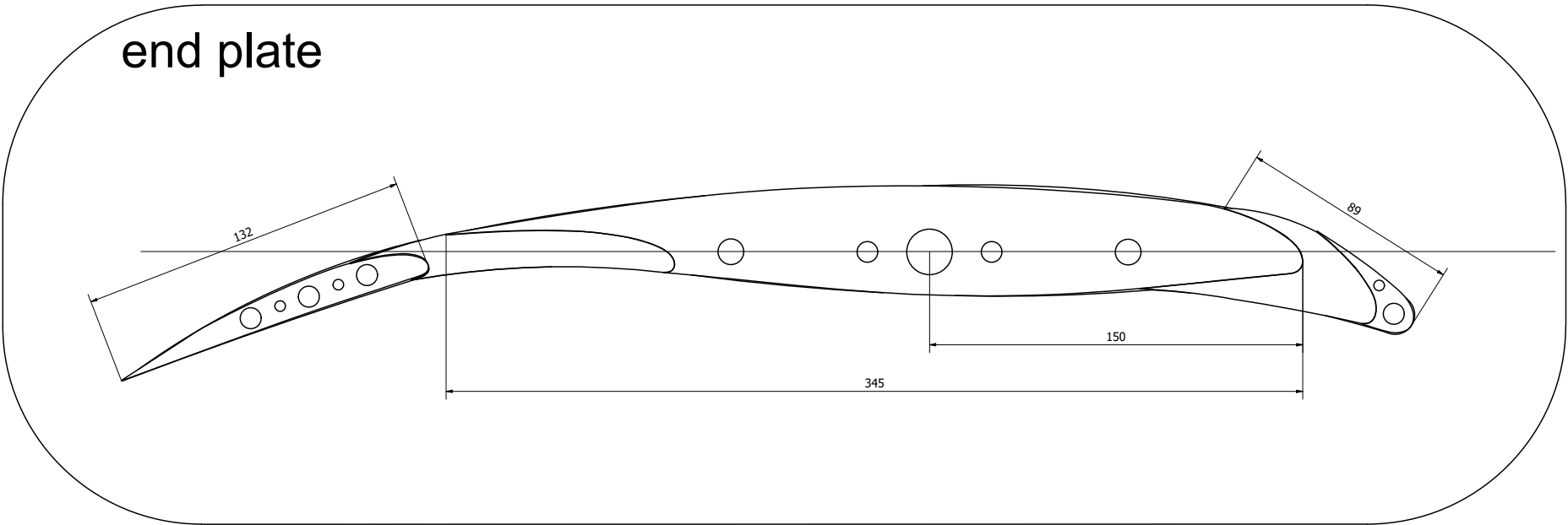
B.1 Plan of the streamlined object

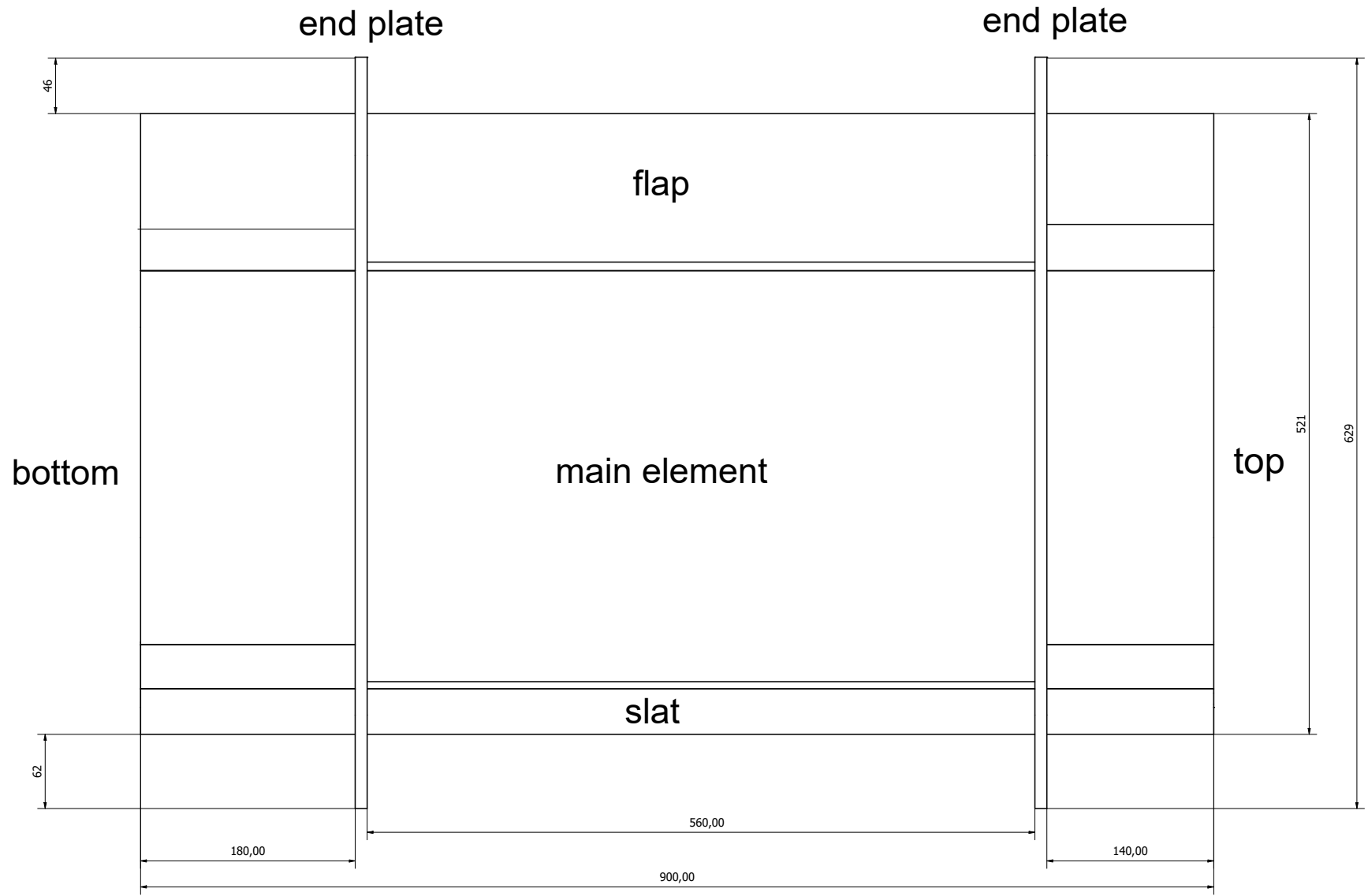


B.2 Plans of the high-lift device model









This page is intentionally left blank.

Appendix C

Numerical methods for the acoustic solver ParadigmS

The in-house acoustic solver ParadigmS¹ is coded in C++ and allows the parallel computation in clusters. Based on a technical report of the acoustic solver provided by Manuel A. DIAZ, the numerical methods for the acoustic solver and their implementation is presented in this Appendix.

The framework ParadigmS is based on message passing interface (MPI) and nodal discontinuous Galerkin (NDG) method [58]. For numerical simulations using the solver, the simulation domain is discretized into a mesh containing tetrahedron elements. The NDG method add additional nodes inside the mesh elements to provide high-order resolution. In order to establish this framework, the NDG weak-formulation corresponding to the LEE system (Equation (3.7)) is required. The process to obtain the NDG weak-formulation is briefly presented in the following subsection.

C.1 Numerical Discretization

Firstly, the domain for numerical simulation Ω is partitioned into K non-overlapping tetrahedral elements as

$$\Omega = \bigcup_{k=1}^K \mathcal{T}^k. \quad (\text{C.1})$$

The weak-formulation for Equation (3.7) is obtained by multiplying it with an arbitrary tests function $\phi(\mathbf{x})$ and integrating over the entire domain Ω , which is given by

$$\int_{\Omega} \frac{\partial \mathbf{q}}{\partial t} \phi \, d\Omega + \int_{\Omega} \nabla \cdot \mathcal{H}(\mathbf{q}) \phi \, d\Omega + \int_{\Omega} \mathbf{H} \phi \, d\Omega = \int_{\Omega} \mathbf{S}(\mathbf{x}, t) \phi \, d\Omega. \quad (\text{C.2})$$

Since the spatial domain has been partitioned into K tetrahedral elements, Equation (C.2) can be written as

$$\sum_{k=1}^K \left[\int_{\mathcal{T}^k} \frac{\partial \mathbf{q}^k}{\partial t} \phi^k \, d\mathbf{x} + \int_{\mathcal{T}^k} \nabla \cdot \mathcal{H}^k(\mathbf{q}^k) \phi^k \, d\mathbf{x} + \int_{\mathcal{T}^k} \mathbf{H}^k \phi^k \, d\mathbf{x} \right] = \sum_{k=1}^K \left[\int_{\mathcal{T}^k} \mathbf{S}^k \phi^k \, d\mathbf{x} \right]. \quad (\text{C.3})$$

¹The Parallel Discontinuous Galerkin Method at Sorbonne universit  (ParadigmS) solver was developed by two researchers (R gis MARCHIANO and Manuel A. DIAZ) at Institut Jean le Rond d'Alembert

Using integration by parts for the second term in Equation (C.3), the weak-form for the k^{th} element reads

$$\int_{\mathcal{T}^k} \frac{\partial \mathbf{q}^k}{\partial t} \phi^k d\mathbf{x} + \int_{\mathcal{T}^k} \mathcal{H}^k \nabla \cdot \phi^k d\mathbf{x} + \int_{\partial \mathcal{T}^k} (\mathbf{n} \cdot \mathcal{H})^k \phi^k d\mathbf{x} + \int_{\mathcal{T}^k} \mathbf{H}^k \phi^k d\mathbf{x} = \int_{\mathcal{T}^k} \mathbf{S}^k \phi^k d\mathbf{x}, \quad (\text{C.4})$$

where $(\mathbf{n} \cdot \mathcal{H})^k = (n_x \mathbf{E} + n_y \mathbf{F} + n_z \mathbf{G})$ is the normal flux across the interfaces between the k^{th} element and its neighboring elements. The flux term $(\mathbf{n} \cdot \mathcal{H})^k$ is replaced by a numerical flux $\{(\mathbf{n} \cdot \mathcal{H})^k\}^*$, which will be presented later in the section.

In the NDG method, the solution is approximated by a finite sum of orthogonal basis functions with a local support. Hence, the local solution \mathbf{q}^k is approximated by \mathbf{Q}^k as follows:

$$\mathbf{q}^k(\mathbf{x}^k, t) \simeq \mathbf{Q}^k(\mathbf{x}^k, t) = \sum_{n=1}^{N_p} \hat{\mathbf{Q}}_n^k(t) \psi_n(\mathbf{x}^k) = \sum_{i=1}^{N_p} \mathbf{Q}^k(\mathbf{x}_i^k, t) l_i^k(\mathbf{x}^k), \quad (\text{C.5})$$

where $\psi(\mathbf{x}^k)$ is a 2-dimensional orthonormal basis defined on the element \mathcal{T}^k , $\hat{\mathbf{Q}}^k(t)$ are the time-dependent modal coefficients, and $l_i^k(\mathbf{x}^k)$ are the two-dimensional Lagrange Polynomials defined on the nodes \mathbf{x}_i^k . N_p is a function of the polynomial order N used for the basis function, which is given by

$$N_p = \frac{(N+1)(N+2)(N+3)}{6}. \quad (\text{C.6})$$

Figure C.1 shows an example of the nodes inside a tetrahedral element for $N = 6$.

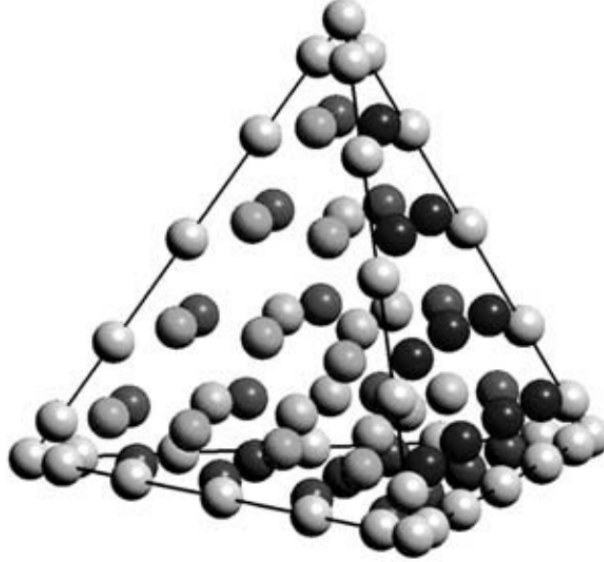


Figure C.1: Node distribution inside a tetrahedral element for $N = 6$, taken from [58].

The choice of the polynomial basis $\psi(\mathbf{x}^k)$ and the nodes \mathbf{x}_i^k is important in the local solution approximation. The nodes ξ_i and their associated basis $l_i(\xi)^k$ proposed in [58] on a reference tetrahedral element \mathcal{T}^R in the coordinate system $\xi = \{\xi, \eta, \zeta\}$.

By inserting the Equation (C.5) in Equation (C.4), and requiring a residual (resulted from the approximation of the local solution) orthogonal to the test function, N_p equations of the

form are obtained

$$\begin{aligned} \int_{\mathcal{T}^k} l_i^k l_j^k d\mathbf{x} \frac{\partial \mathbf{Q}^k}{\partial t} - \int_{\mathcal{T}^k} l_i^k \nabla \cdot l_j^k d\mathbf{x} \mathcal{H}^k - \int_{\partial \mathcal{T}^k} l_i^{\partial k} l_j^{\partial k} d\mathbf{x} \{(\mathbf{n} \cdot \mathcal{H})^k\}^* + \\ \int_{\mathcal{T}^k} l_i^k l_j^k d\mathbf{x} \mathbf{H}^k = \int_{T_k} \mathbf{S}^k l_i^k d\mathbf{x}, \end{aligned} \quad (\text{C.7})$$

where the term $\{(\mathbf{n} \cdot \mathcal{H})^k\}^*$ denotes the numerical flux between elements faces, which is computed using a *local Lax-Friedrichs* approach as

$$\{(\mathbf{n} \cdot \mathcal{H})^k\}_{LLF}^* = \frac{1}{2} [n_x(\mathbf{E}_L - \mathbf{E}_R) + n_y(\mathbf{F}_L - \mathbf{F}_R) + n_z(\mathbf{G}_L - \mathbf{G}_R) + \max(|\mathbf{a}|)(\mathbf{Q}_L - \mathbf{Q}_R)], \quad (\text{C.8})$$

where \mathbf{a} denotes the eigenvalues of the LEE system (Equation (3.7)), which are given by

$$\begin{aligned} a_1 &= n_x u_0 + n_y v_0 + n_z w_0 - c_0, \\ a_2 &= a_3 = a_4 = n_x u_0 + n_y v_0 + n_z w_0, \\ a_5 &= n_x u_0 + n_y v_0 + n_z w_0 + c_0. \end{aligned} \quad (\text{C.9})$$

Equation (C.7) can be written as

$$\mathcal{M}_{ij}^k \frac{\partial \mathbf{Q}^k}{\partial t} - \mathcal{S}_{ij}^{k,x} \mathbf{E}^k - \mathcal{S}_{ij}^{k,y} \mathbf{F}^k - \mathcal{S}_{ij}^{k,z} \mathbf{G}^k + \mathcal{M}_{ij}^{\partial k} \{(\mathbf{n} \cdot \mathcal{H})^k\}^* + \mathcal{M}_{ij}^k \mathbf{H}^k = \mathcal{M}_{ij}^k \mathbf{S}^k, \quad (\text{C.10})$$

where \mathcal{M}_{ij}^k and $\mathcal{M}_{ij}^{\partial k}$ are the volume and faces *mass* matrices, respectively. And similarly, $\mathcal{S}_{ij}^{k,x}$, $\mathcal{S}_{ij}^{k,y}$ and $\mathcal{S}_{ij}^{k,z}$ denotes *stiffness* matrices along the x -, y - and z -directions. Equation (C.10) is written in the coordinate system $\mathbf{x}=\{x, y, z\}$. In NDG method, the tetrahedral element in the coordinate system $\mathbf{x}=\{x, y, z\}$ are transformed to a *reference element*, *i.e.*, a reference tetrahedral element \mathcal{T}^R in the coordinate system $\boldsymbol{\xi}=\{\xi, \eta, \zeta\}$. Therefore, the mass and stiffness matrices can be written as

$$\mathcal{M}_{ij}^k = \int_{\mathcal{T}^k} l_i^k l_j^k d\mathbf{x} = J^k \int_{\mathcal{T}^R} l_i l_j d\boldsymbol{\xi} = J^k \mathcal{M}_{ij}^R, \quad (\text{C.11})$$

$$\mathcal{S}_{ij}^{k,x} = \int_{\mathcal{T}^k} l_i^k \frac{\partial l_j^k}{\partial x} d\mathbf{x} = J^k \int_{\mathcal{T}^R} l_i \left(\frac{\partial \xi}{\partial x} \frac{\partial l_j}{\partial \xi} + \frac{\partial \eta}{\partial x} \frac{\partial l_j}{\partial \eta} + \frac{\partial \zeta}{\partial x} \frac{\partial l_j}{\partial \zeta} \right) d\boldsymbol{\xi} = J^k \left(\frac{\partial \xi}{\partial x} \mathcal{S}_{ij}^{R,\xi} + \frac{\partial \eta}{\partial x} \mathcal{S}_{ij}^{R,\eta} + \frac{\partial \zeta}{\partial x} \mathcal{S}_{ij}^{R,\zeta} \right), \quad (\text{C.12})$$

$$\mathcal{S}_{ij}^{k,y} = \int_{\mathcal{T}^k} l_i^k \frac{\partial l_j^k}{\partial y} d\mathbf{x} = J^k \int_{\mathcal{T}^R} l_i \left(\frac{\partial \xi}{\partial y} \frac{\partial l_j}{\partial \xi} + \frac{\partial \eta}{\partial y} \frac{\partial l_j}{\partial \eta} + \frac{\partial \zeta}{\partial y} \frac{\partial l_j}{\partial \zeta} \right) d\boldsymbol{\xi} = J^k \left(\frac{\partial \xi}{\partial y} \mathcal{S}_{ij}^{R,\xi} + \frac{\partial \eta}{\partial y} \mathcal{S}_{ij}^{R,\eta} + \frac{\partial \zeta}{\partial y} \mathcal{S}_{ij}^{R,\zeta} \right), \quad (\text{C.13})$$

$$\mathcal{S}_{ij}^{k,z} = \int_{\mathcal{T}^k} l_i^k \frac{\partial l_j^k}{\partial z} d\mathbf{x} = J^k \int_{\mathcal{T}^R} l_i \left(\frac{\partial \xi}{\partial z} \frac{\partial l_j}{\partial \xi} + \frac{\partial \eta}{\partial z} \frac{\partial l_j}{\partial \eta} + \frac{\partial \zeta}{\partial z} \frac{\partial l_j}{\partial \zeta} \right) d\boldsymbol{\xi} = J^k \left(\frac{\partial \xi}{\partial z} \mathcal{S}_{ij}^{R,\xi} + \frac{\partial \eta}{\partial z} \mathcal{S}_{ij}^{R,\eta} + \frac{\partial \zeta}{\partial z} \mathcal{S}_{ij}^{R,\zeta} \right), \quad (\text{C.14})$$

$$\mathcal{M}_{ij}^{\partial k} = \int_{\partial \mathcal{T}^k} l_i^{\partial k} l_j^{\partial k} d\mathbf{x} = J^{\partial k} \int_{\partial \mathcal{T}^R} l_i^{\partial} l_j^{\partial} d\boldsymbol{\xi} = J^{\partial k} \mathcal{M}_{ij}^{\partial R}, \quad (\text{C.15})$$

where \mathcal{M}_{ij}^R is the *reference element* mass matrix, $\mathcal{S}_{ij}^{R,\xi}$, $\mathcal{S}_{ij}^{R,\eta}$ and $\mathcal{S}_{ij}^{R,\zeta}$ are the *reference element* stiffness matrices, and $\mathcal{M}_{ij}^{\partial R}$ is the *reference element* mass matrix of all faces in the element. $J^{\partial k}$ and J^k are the Jacobian operators corresponding to the face and volume data for the reference triangle \mathcal{T}^R . Details in the constructions of these matrices and operators can be found in [58]. Introducing Equations (C.11-15) into Equation (C.10) gives the weak-

formulation of the LEE system (Equation (3.7))

$$\begin{aligned}
\frac{\partial \mathbf{q}^k}{\partial t} = & \frac{\partial \xi}{\partial x} (\mathcal{M}_{ij}^R)^{-1} \mathcal{F}_{ij}^{R,\xi} \mathbf{E}^k + \frac{\partial \eta}{\partial x} (\mathcal{M}_{ij}^R)^{-1} \mathcal{F}_{ij}^{R,\eta} \mathbf{E}^k + \frac{\partial \zeta}{\partial x} (\mathcal{M}_{ij}^R)^{-1} \mathcal{F}_{ij}^{R,\zeta} \mathbf{E}^k \\
& + \frac{\partial \xi}{\partial y} (\mathcal{M}_{ij}^R)^{-1} \mathcal{F}_{ij}^{R,\xi} \mathbf{F}^k + \frac{\partial \eta}{\partial y} (\mathcal{M}_{ij}^R)^{-1} \mathcal{F}_{ij}^{R,\eta} \mathbf{F}^k + \frac{\partial \zeta}{\partial y} (\mathcal{M}_{ij}^R)^{-1} \mathcal{F}_{ij}^{R,\zeta} \mathbf{F}^k \\
& + \frac{\partial \xi}{\partial z} (\mathcal{M}_{ij}^R)^{-1} \mathcal{F}_{ij}^{R,\xi} \mathbf{G}^k + \frac{\partial \eta}{\partial z} (\mathcal{M}_{ij}^R)^{-1} \mathcal{F}_{ij}^{R,\eta} \mathbf{G}^k + \frac{\partial \zeta}{\partial z} (\mathcal{M}_{ij}^R)^{-1} \mathcal{F}_{ij}^{R,\zeta} \mathbf{G}^k \\
& - \frac{J^{\partial k} \mathcal{M}_{ij}^{\partial R}}{J^k \mathcal{M}_{ij}^R} \{(\mathbf{n} \cdot \mathcal{H})^k\}^* - \mathbf{H}^k + \mathbf{S}^k.
\end{aligned} \tag{C.16}$$

C.2 Time integration and stability criterion

Associated with Carpenter's 4th-order *low-storage explicit Runge-Kutta* (LSERK) scheme [29], the weak-formulation of the LEE system can be solved numerically to obtain the evolution of the \mathbf{q}^k fields from an initial time t_0 to a final time t_f using a time step Δt , which can be determined by

$$\Delta t = \frac{\text{CFL}}{\max(|\mathbf{a}|)_{k,i}} \min(\Delta x_i^k), \tag{C.17}$$

where $\Delta x_i^k = x_{i+1}^k - x_i^k$ is the distance between inner nodes inside the elements \mathcal{T}^k , \mathbf{a} is the wave speeds (C.9), and the CFL is the dimensionless Courant-Friedrichs-Levy constant that guarantees that the stability of the scheme if $\text{CFL} \leq 1$.

Appendix D

Beamforming results of a high-lift device model

This appendix contains some zoomed versions of the Figures in Section 6.2, and some 3D beamforming results without deconvolution in Section 6.3.

D.1 2D beamforming results

The red sketch on top of the figures indicates the position of the elements of the high-lift device model. The wind-tunnel flow direction is from the right side to the left side.

D.1.1 At incoming velocity $U_\infty = 40$ and angle of attack $\alpha = 0^\circ$

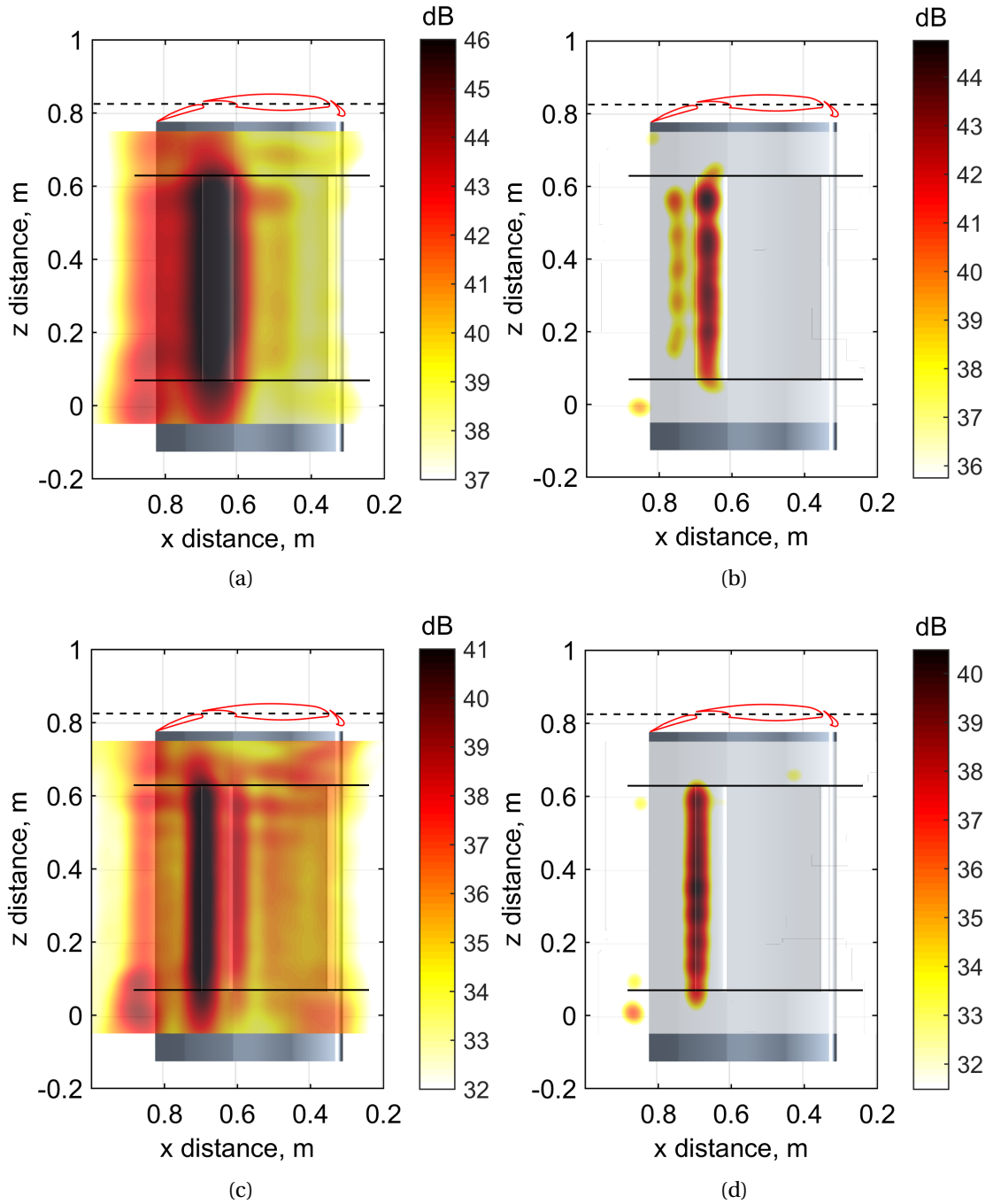


Figure D.1: Sound maps for the high-lift device model at incoming velocity $U_\infty = 40$ m/s and angle of attack $\alpha = 0^\circ$, at two third-octave bands of nominal midband frequency 2.5 kHz (top figures) and 4 kHz (bottom figures). (a) and (c): 2D beamforming using monopole steering vector; (b) and (d): CLEAN-SC technique using monopole steering vector.

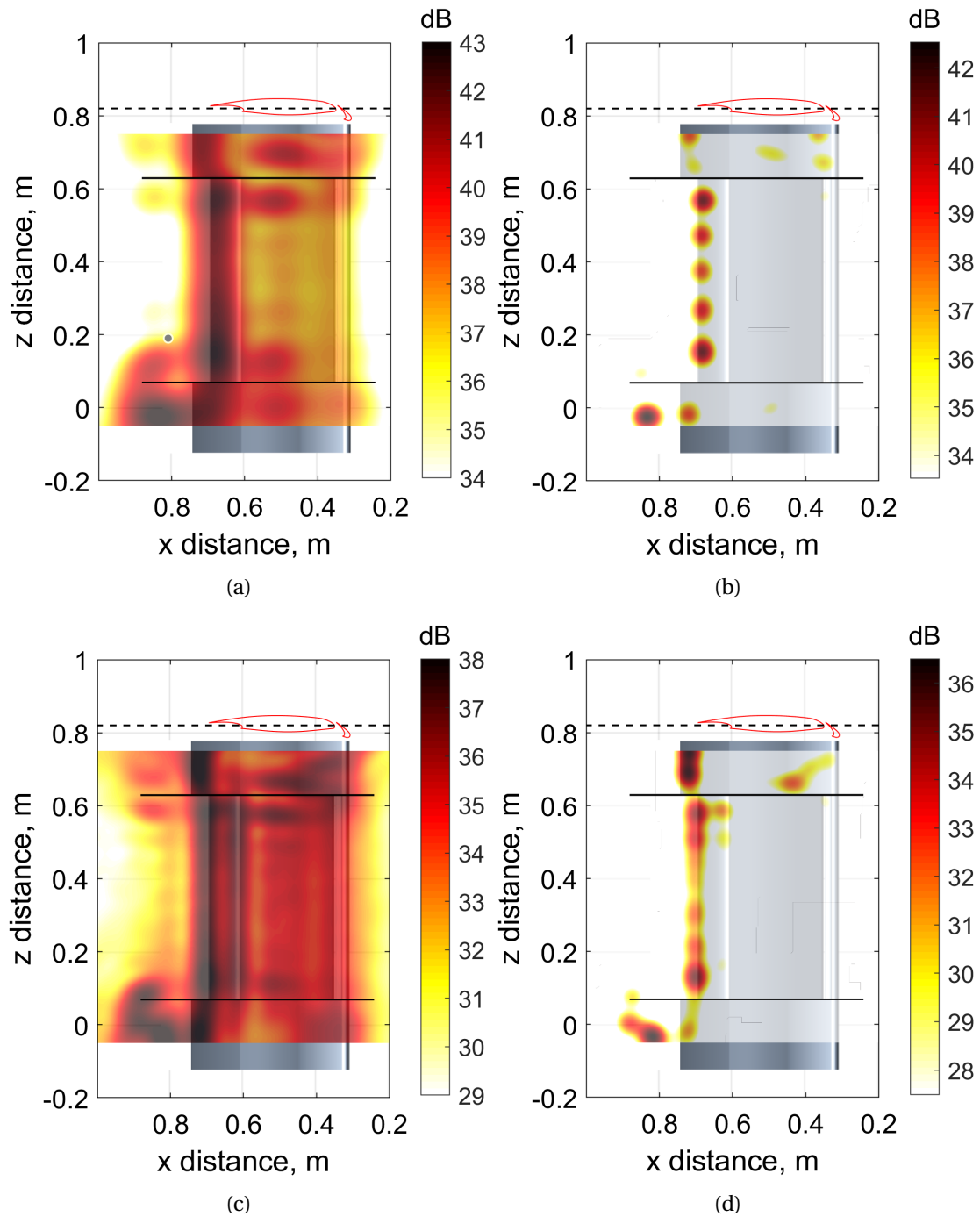


Figure D.2: Sound maps for the high-lift device model without flap at incoming velocity $U_\infty = 40$ m/s and angle of attack $\alpha = 0^\circ$, at two third-octave bands of nominal midband frequency 2.5 kHz (top figures) and 4 kHz (bottom figures). (a) and (c): 2D beamforming using monopole steering vector; (b) and (d): CLEAN-SC technique using monopole steering vector.

D.1.2 At incoming velocity $U_\infty = 40$ and angle of attack $\alpha = 6^\circ$

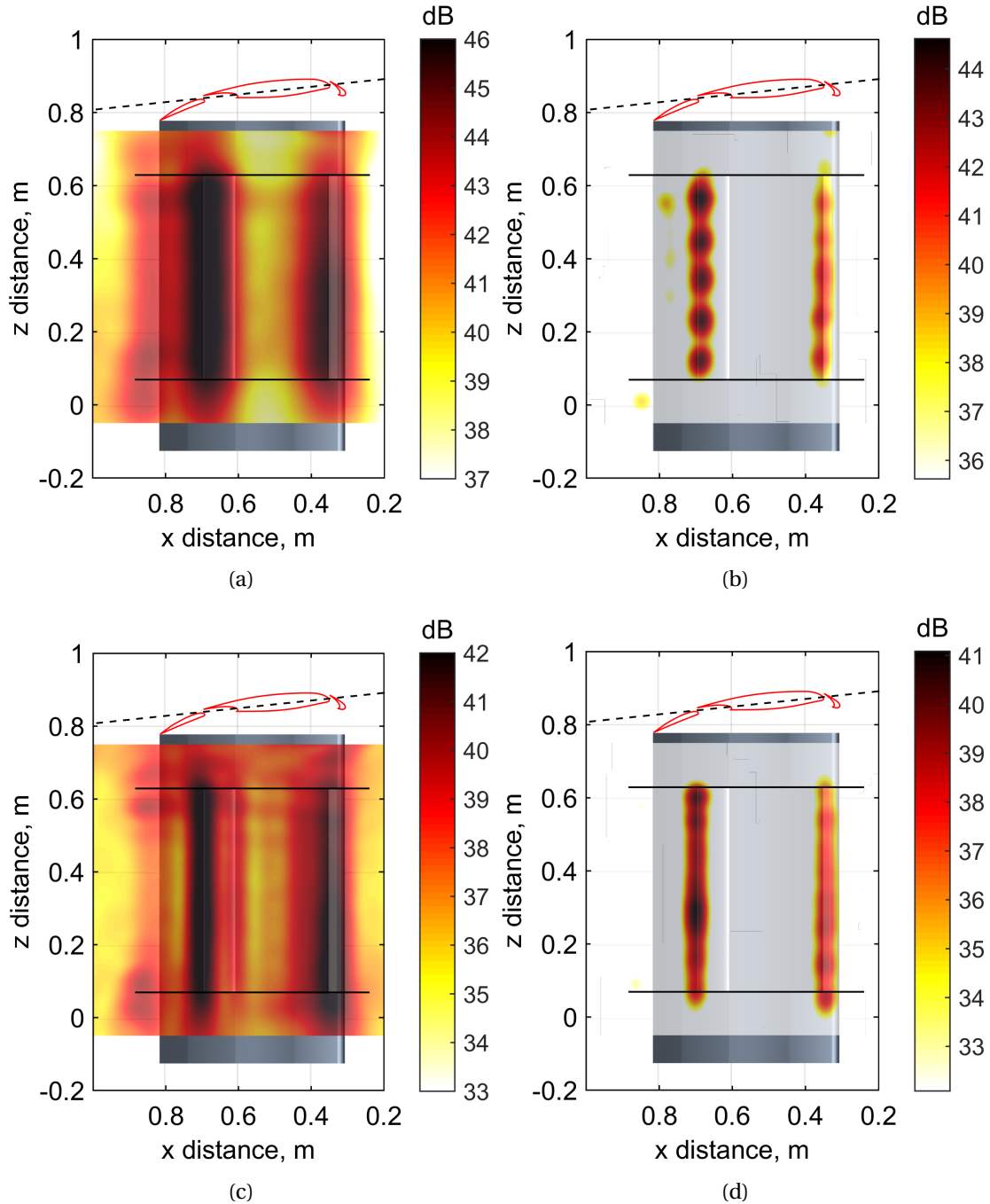


Figure D.3: Sound maps for the high-lift device model at incoming velocity $U_\infty = 40$ m/s and angle of attack $\alpha = 6^\circ$, at two third-octave bands of nominal midband frequency 2.5 kHz (top figures) and 4 kHz (bottom figures). (a) and (c): 2D beamforming using monopole steering vector; (b) and (d): CLEAN-SC technique using monopole steering vector.

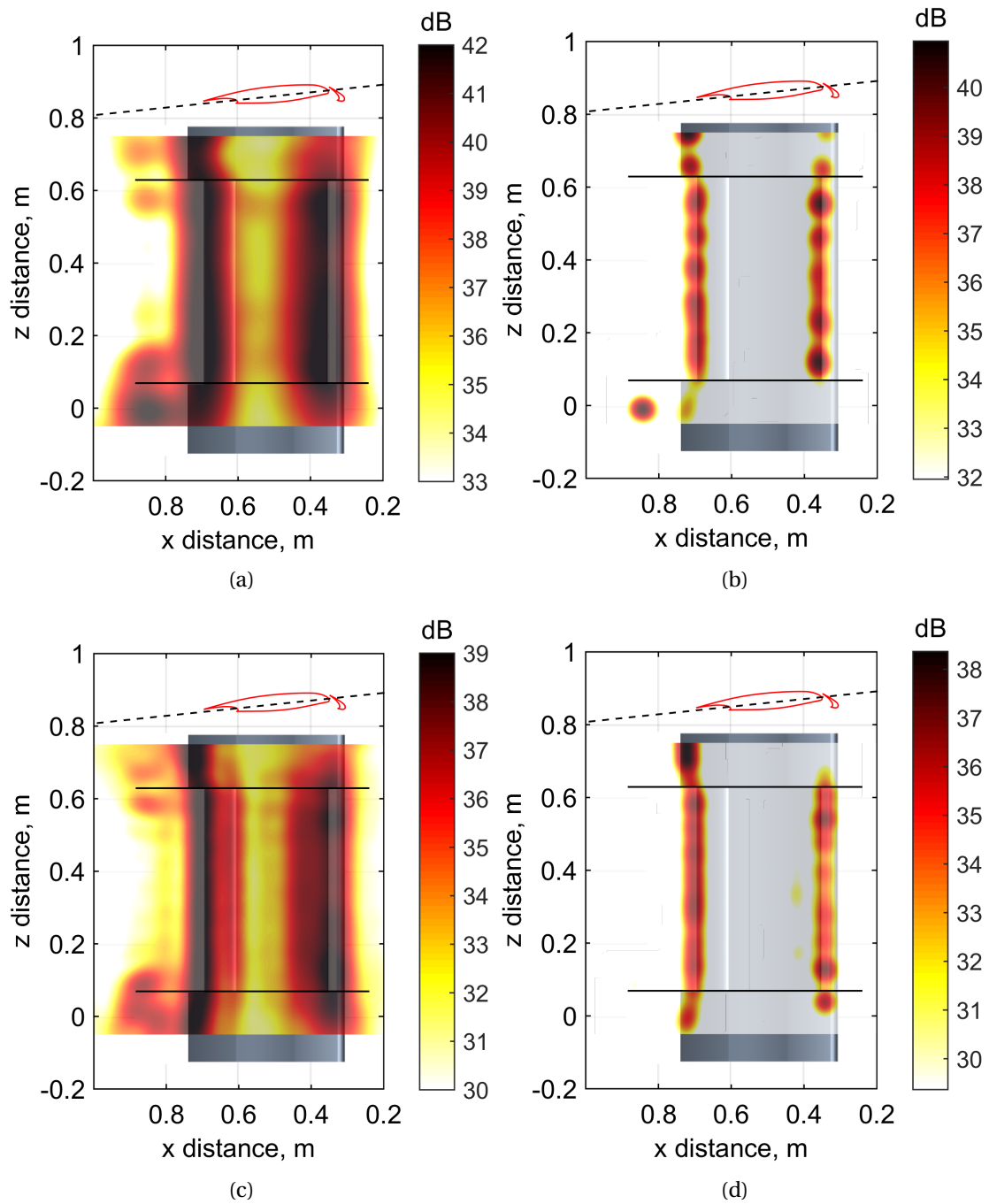


Figure D.4: Sound maps for the high-lift device model without flap at incoming velocity $U_\infty = 40$ m/s and angle of attack $\alpha = 6^\circ$, at two third-octave bands of nominal midband frequency 2.5 kHz (top figures) and 4 kHz (bottom figures). (a) and (c): 2D beamforming using monopole steering vector; (b) and (d): CLEAN-SC technique using monopole steering vector.

D.1.3 At incoming velocity $U_\infty = 30$ and angle of attack $\alpha = 10^\circ$

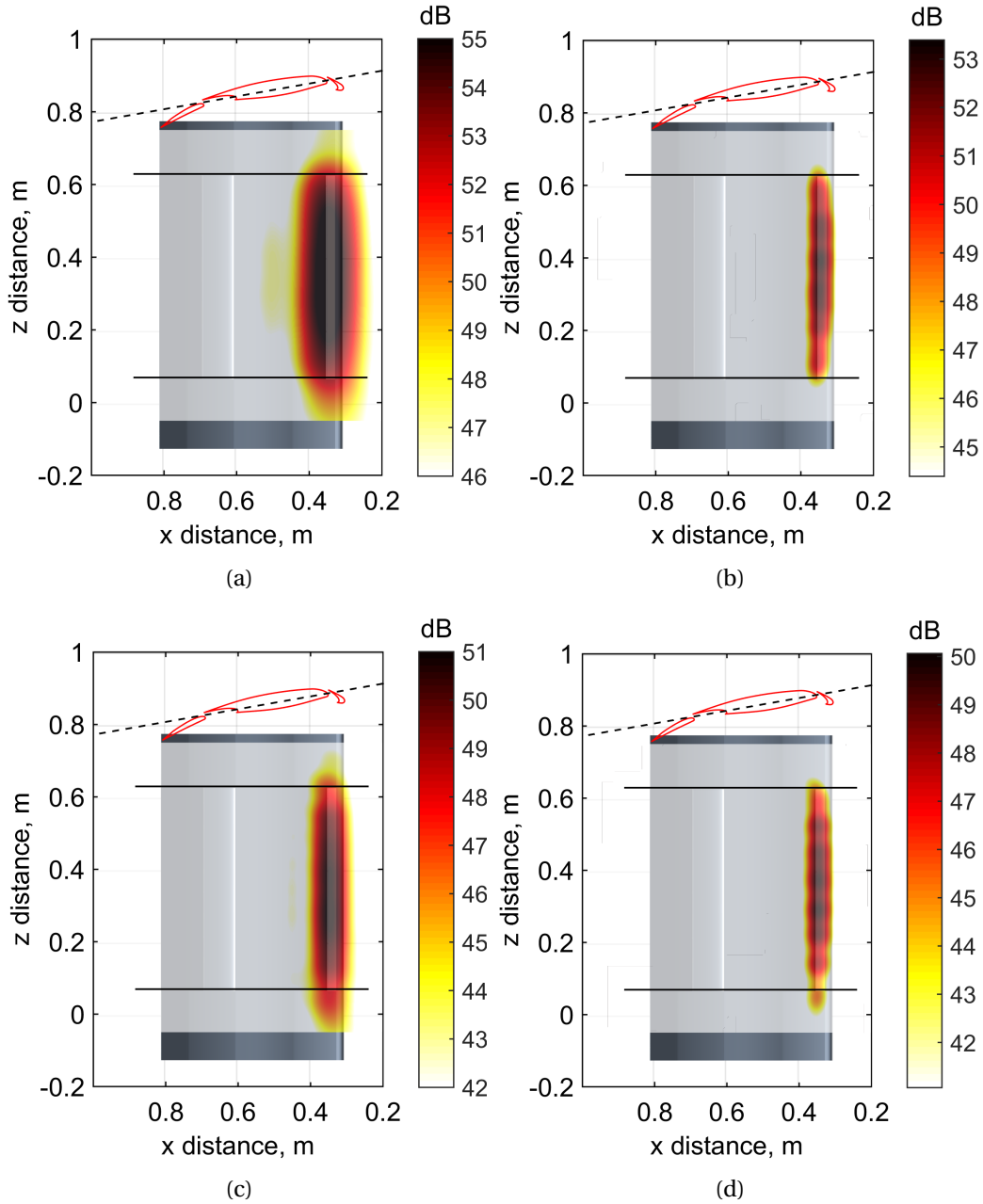


Figure D.5: Sound maps for the high-lift device model at incoming velocity $U_\infty = 30$ m/s and angle of attack $\alpha = 10^\circ$, at two third-octave bands of nominal midband frequency 2.5 kHz (top figures) and 4 kHz (bottom figures). (a) and (c): 2D beamforming using monopole steering vector; (b) and (d): CLEAN-SC technique using monopole steering vector.

D.2 3D beamforming results

The 3D isosurface in each sound map is plotted at 9 dB below the maximum value of the sound map. The shadows correspond to the projection of the 3D sound source imaging in different directions.

D.2.1 At incoming velocity $U_\infty = 40$ and angle of attack $\alpha = 6^\circ$

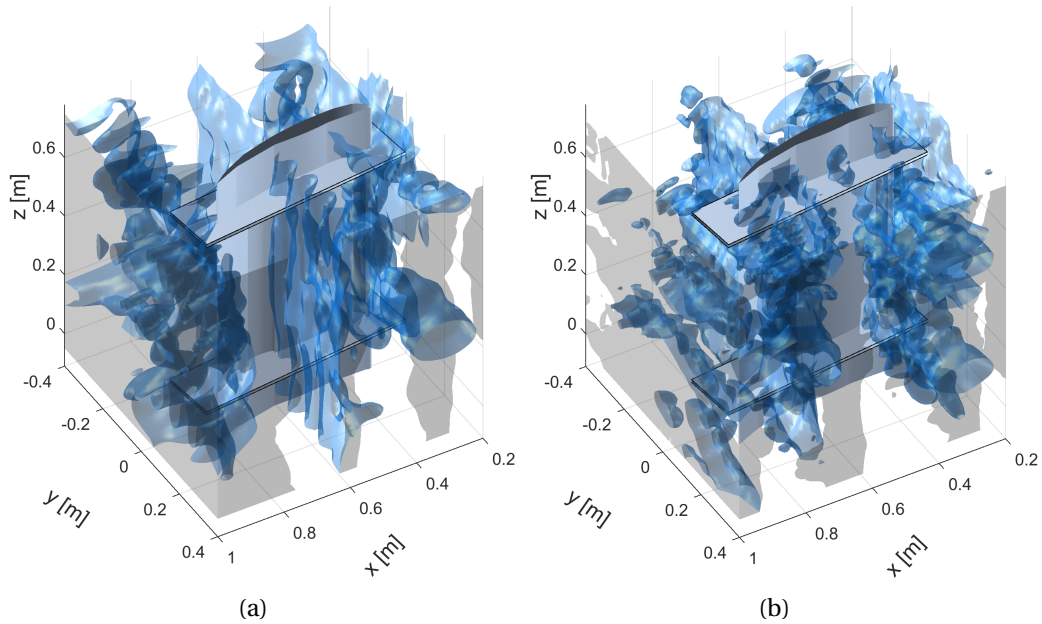


Figure D.6: Sound maps without deconvolution for the high-lift device model at incoming velocity $U_\infty = 40$ m/s and angle of attack $\alpha = 6^\circ$, at two third-octave bands of nominal midband frequency 2.5 kHz (a) and 4 kHz (b) with respectively a maximum value of 41.4 dB and 38.1 dB.

D.2.2 At incoming velocity $U_\infty = 30$ and angle of attack $\alpha = 10^\circ$

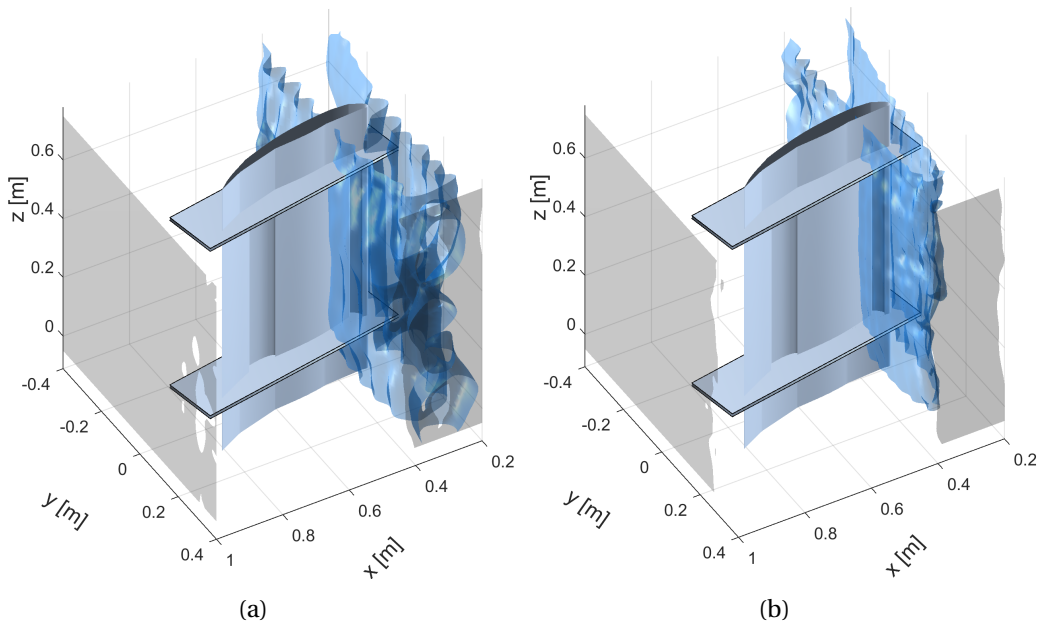


Figure D.7: Sound maps without deconvolution for the high-lift device model at incoming velocity $U_\infty = 30$ m/s and angle of attack $\alpha = 10^\circ$, at two third-octave bands of nominal midband frequency 2.5 kHz (a) and 4 kHz (b) with respectively a maximum value of 48.0 dB and 43.8 dB. The 3D isosurface in each sound map is plotted at 9 dB below the maximum value of the sound map.

This page is intentionally left blank.

Appendix E

Some generic applications of the 3D TR technique

In this section, the ‘tunnel’ shaped microphone arrays presented in Chapter 2 will be used for the 3D TR in order to evaluate their performances in terms of localization error and spatial resolution. Some synthetic noise sources including an acoustic pulse, a monopole, and a dipole will be considered. The monopole and dipole are simulated for the direct simulations using the approach: approximation by a Gaussian distribution (see Section 3.2.5.2). An application for the identification of a dipole noise source in a cavity with splits will also be presented, for which the solid boundaries will be considered for the 3D TR. The medium was considered as water with a sound speed of 1500 m/s and a density of 1000 kg/m³. The advantage of considering a medium with higher sound speed is to reduce the simulation time for the waves inside the simulation domain to reach the permanent regime. Therefore, it is less computationally expensive but still physically meaningful. In addition, the wavelength is longer, which allows to contain more mesh nodes within a wavelength for the acoustic simulation.

E.1 Identification of an acoustic pulse

An acoustic pulse is simulated at the position (0.5 m, 0 m, 0.5 m) in a 3D domain for the direct simulation with its spatial distribution given by Equation (3.13). The dimension and some patches of the 3D domain are presented in Figure E.1. The corresponding mesh for the numerical simulation contains tetrahedral elements inside the domain, with their size being 10 cm. The polynomial order N is 3 for the DG method, for which the effective size of mesh elements is lower (see Chapter 3). It allows a higher resolution for the numerical simulations. The acoustic pulse has a spatial Gaussian distribution with an amplitude of 10 and a size σ of 0.17 m. The acoustic pressure signals were recorded at all the nodes of the patches ‘Left’, ‘Top’ and ‘Right’ of the domain (see Figure E.1(a)) during the direct simulation using the “free_rec” boundary conditions. However, the virtual microphones shown in Figure E.1 are not on the positions of the nodes. The patch ‘Bottom’ uses the “wall” boundary condition. Other patches of the 3D domain use the “free” boundary condition. For simplicity, the result of the direct simulation is not presented.

In order to identify the synthetic monopole noise source, the 3D TR process was conducted. Once the direct simulation was completed, the recorded signals were then interpolated to the position of the 256 microphones on the three patches. They were reversed and

re-emitted as monopole noise sources with a spatial Gaussian distribution of size 3 cm at the position of the 256 microphones for the 3D TR process, using the boundary condition “BC_gauss_spot”. The boundary conditions of other patches remained the same for the 3D TR. Figure E.1(a) shows the pressure field at an early instant of the 3D TR process. The monopole noise sources emitted by the virtual microphones are shown by the blue spots at the ‘Left’, ‘Top’ and ‘Right’ patches. The convergent waves are well established inside the domain shown by the yellow isosurfaces. Figure E.1(b) shows the pressure field at the final instant of the 3D TR simulation. The red focalization spot allows to indicate the spatial resolution of the 3D TR result with a value of $(1/\sqrt{2})$ times the peak level at the final instant (-3 dB). Its shape is an ellipsoid covering the position of the acoustic pulse shown by the white cross. So the position of acoustic pulse is identified, but the spatial resolution is lower in the x -direction to which no sub-array is perpendicular.

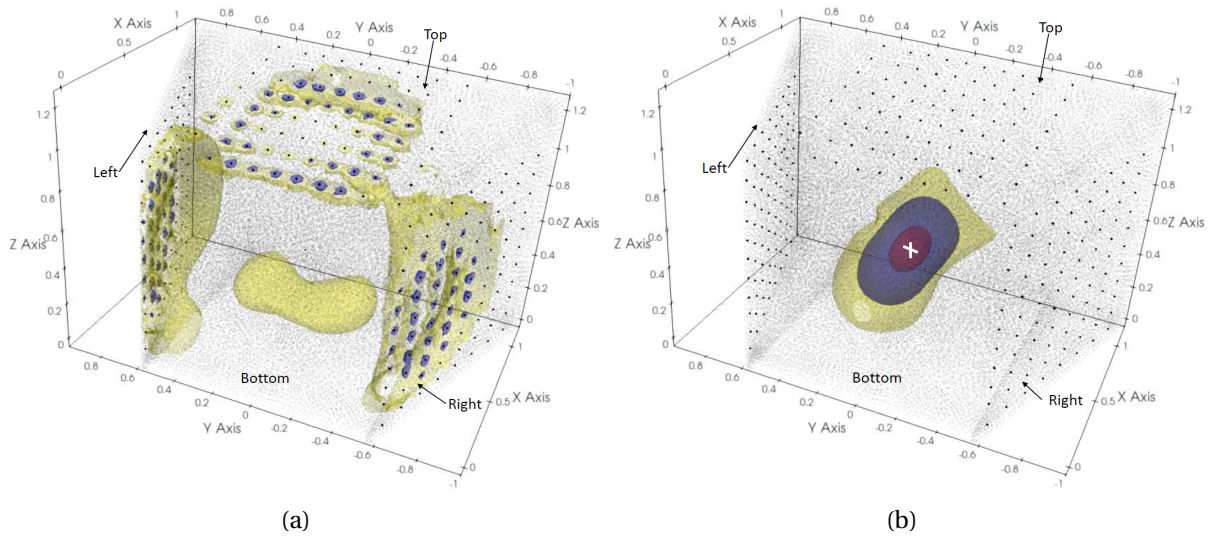


Figure E.1: Results of 3D TR concerning an acoustic pulse at different instants with the pressure field shown by (a) two isosurfaces of 0.025 (yellow isosurface) and 0.08 (blue isosurface) at an early instant; (b) three isosurfaces of 0.025 (yellow isosurface), 0.08 (blue isosurface) and 0.2828 (red isosurface) at the final instant of 3D TR simulation. The grey area represents the nodes of the 3D acoustic mesh with the mesh element size being 10 cm ($N = 3$). The black points on the ‘Left’, ‘Top’ and ‘Right’ patches indicate the positions of the 256 virtual microphones. The white cross in (b) stands for the real position of the acoustic pulse.

E.2 Identification of a monopole using different microphone arrays

A synthetic monopole of frequency 3 kHz (sound speed 1500 m/s, wavelength $\lambda = 0.5$ m) at the position (0.5 m, 0 m, 0.5 m) with a Gaussian distribution in space and a diameter size of 0.17 m (lower than half-a-wavelength) was simulated for the direct simulations in two domains with different dimensions (Figure E.2). The same boundary conditions as the case of an acoustic pulse were used for the patches shown in Figure E.2. For simplicity, the results of the direct simulations are not presented.

In order to identify the synthetic monopole noise source, the 3D TR process was conducted. After the direct simulations, the acoustic signals recorded at the nodes of the patches

‘Left’, ‘Top’ and ‘Right’ of the domains were respectively interpolated to the positions of microphones of different geometries (see black points in Figure E.2). The same TR process is conducted as for the previous case. Figure E.2 shows the maximum pressure fields of the two 3D TR results, which are shown by an isosurface of a value of $(1/\sqrt{2})$ times the peak level (-3 dB). The focalization spot of each case is an ellipsoid centered at the real position of the monopole. Approximately, the average values of the length of the three major principle axis of the ellipsoids are respectively 0.26 m (using 256 microphone in Figure E.2(a)) and 0.25 m (using 672 microphone Figure E.2(b)). Note that the half-a-wavelength corresponding to the monopole noise source is 0.25 m. However, the size of the focalization spot can not be lower than half-a-wavelength because of the limit of the TR process without an acoustic sink (see Chapter 1). In addition, it is found that the case with the array geometry (672 microphones) allows a better spatial resolution in the x -direction, with the length of principal axis in the direction being 0.344 m (see Figure E.2(b)).

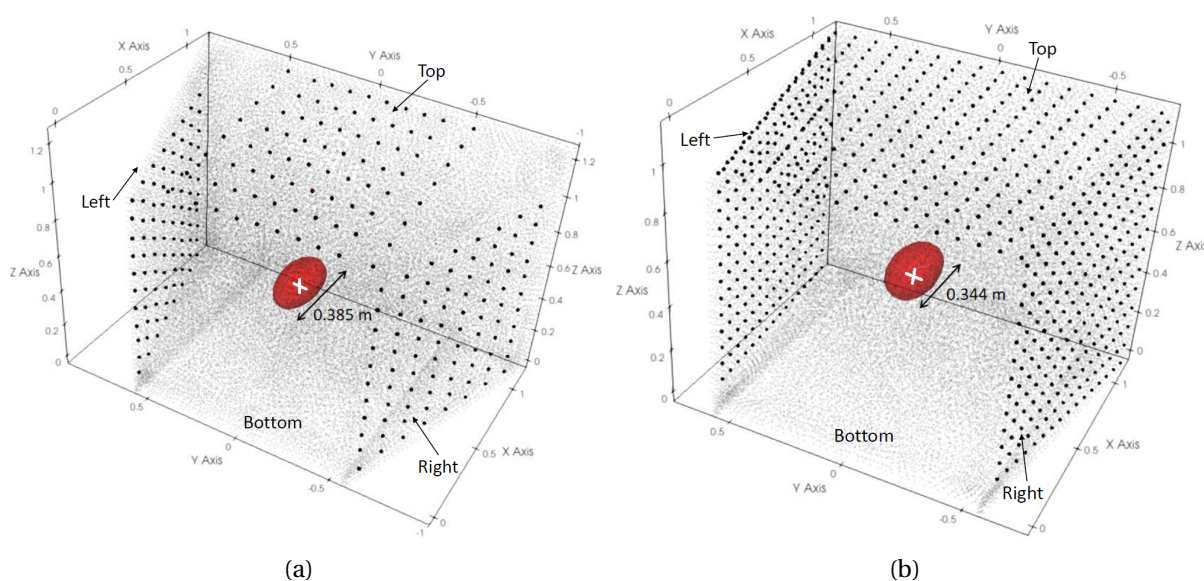


Figure E.2: Maximum pressure fields of 3D TR concerning a monopole noise source of 3 kHz in two simulation domains using (a) 256 virtual microphones; (b) 672 virtual microphones. They are respectively shown by an isosurface of a value of $(1/\sqrt{2})$ times the corresponding peak level at the final instant. The grey area in the two domains represent the nodes of the 3D acoustic mesh with the mesh element size being 10 cm ($N=3$). The black points on the ‘Left’, ‘Top’ and ‘Right’ patches of the two domains indicate the positions of the 256 microphones. The white cross in the two domains stands for the real position of the acoustic pulse.

E.3 Identification of a monopole in a cavity

In order to account for the presence of solid boundaries for the numerical 3D TR, a simulation case with cuboid cavity with 12 rectangular splits enclosing a synthetic monopole noise source was considered. The idea is to generate some significant acoustic reflection and diffraction during the propagation of the acoustic waves inside the simulation domain. The geometry of the microphone array with 768 microphones and the coordinate system presented in Chapter 2 are used. The lengths of the edge of the cavity in the x -direction, y -direction, and z -direction are respectively 0.85 m, 0.8 m, and 0.8 m. The thickness of the

cavity surface is 0.05 m. The center of the cavity is at the position (0.475 m, 0 m, 0.5m). The dimension of each rectangular split is 0.1 m \times 0.6 m. Figure E.3(a) shows this cuboid cavity placed in the simulation domain. The patches ‘Left’, ‘Top’ and ‘Right’ use the “free-rec” boundary condition for direct simulation and the “BC_gauss_spot” boundary condition for TR. The patches of the cuboid cavity use the “wall” boundary condition. The patches ‘Front’, ‘Bottom’ and ‘Back’ use the “free” boundary condition.

Figure E.3(b) shows the 3D acoustic mesh generated by the software GMSH. It is an unstructured 3D mesh with 80 partitions. The size of the mesh elements on the patches ‘Cavity’ is 5 cm. The size of the mesh elements on the patches ‘Left’, ‘Right’, ‘Front’, ‘Back’, ‘Top’ and ‘Bottom’ is 10 cm. Note that the refinements on the patches of the cavity were conducted to well describe the geometry of the cavity for the acoustic simulations. The polynomial order N is 3 for the simulations. The 3D mesh contains 47941 elements, among which 10568 triangles on all the boundary of the domain and 37373 tetrahedra inside the domain of 3D acoustic mesh.

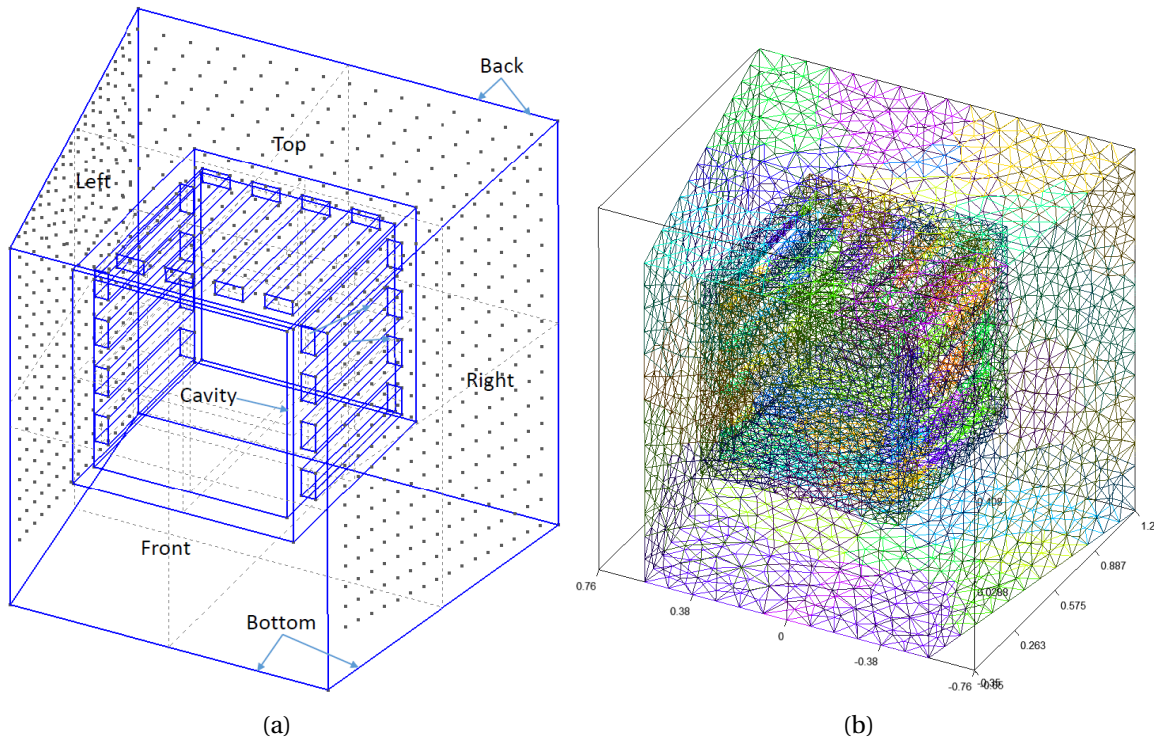


Figure E.3: Generation of the 3D acoustic mesh for a cavity with rectangular splits using GMSH: (a) the positions of the 768 virtual microphones indicated by the black points on the three patches ‘Left’, ‘Top’ and ‘Right’ of the domain; (b) the triangular mesh elements on the patches ‘Left’, ‘Top’, ‘Right’ and ‘Bottom’. The triangular mesh elements with different colors correspond to different mesh partitions.

The direct simulation was firstly carried out. The synthetic monopole noise source of frequency 3.9 kHz (sound speed 1500 m/s, wavelength $\lambda = 0.385$ m) located at the position (0.5 m, 0 m, 0.6 m) has a spatial Gaussian distribution with a size of 5 cm. The physical time of the simulation is 0.005 s (about 20 acoustic periods). The acoustic signals on the positions of the nodes of the patches ‘Left’, ‘Top’ and ‘Right’ were recorded for the whole simulation time. For simplicity, the result of the direct simulation is not presented.

The recorded acoustic signals were firstly interpolated to the positions of the 768 microphones and then the same TR process is conducted as for the previous case. Figure E.4(a)

and E.4(c) show snapshots of the pressure field in planar cross sections when the waves inside the domain reach the permanent regime. A dominant spot centered on the position of the noise source is observed in both figures. Figure E.4(c) shows some wavefronts passing the splits of the cavity. Figure E.4(b) and E.4(d) show the root mean square (RMS) of the pressure field integrated from 0.002 s to 0.004 s in planar cross sections. The position of the noise source is identified by the dominant focalization spot with a precision at wavelength in both figures. Strong interactions between the waves and the solid boundaries at the corners are observed in Figure E.4(b). In Figure E.4(d), the reflection of the acoustic waves by the bottom of the cavity are also evidenced. The interference between the convergent waves and divergent waves seem to be strong inside the cavity, which is shown by the two side lobes in Figure E.4(d). Due to the presence of the solid boundaries of the cavity, additional acoustic reflection and diffraction also occur during the waves propagation of the 3D TR process. Nevertheless, the 3D TR can identify the noise source in terms of nature and position with a precision at wavelength.

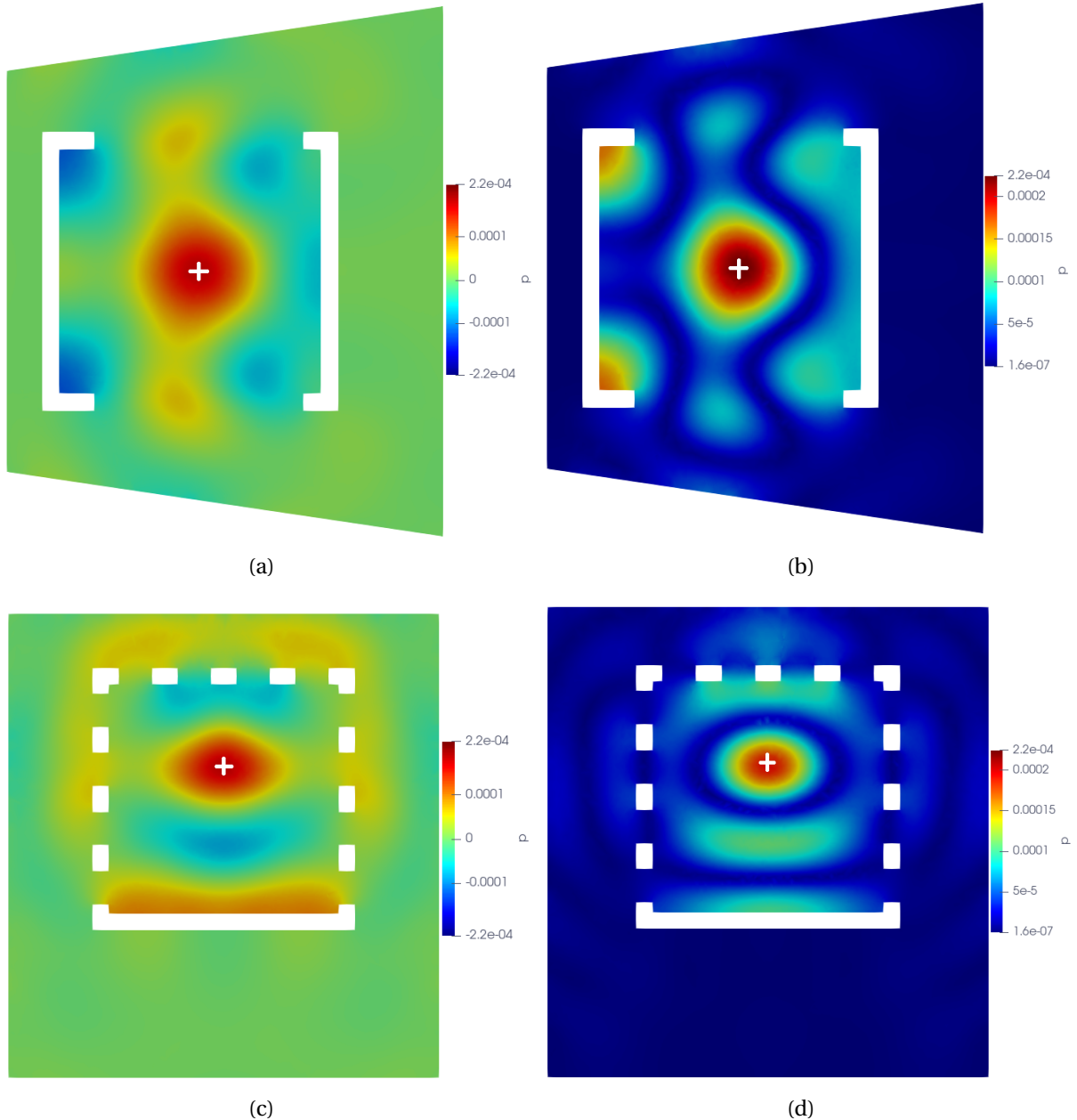


Figure E.4: Results of the 3D TR concerning a synthetic monopole noise source of 3.9 kHz inside a cavity with splits in cross sections of the simulation domain. The white cross indicates the real position of the noise source. (a) Snapshot of the pressure field in a horizontal planar cross section XY at $z = 0.6$ m (X is horizontal, Y is vertical in the figure); (b) RMS of the pressure field integrated from 0.002 s to 0.004 s in the same plane; (c) snapshot of the pressure field in a vertical planar cross section YZ at $x = 0.5$ m (Y is horizontal, Z is vertical in the figure); (d) RMS of the pressure field integrated from 0.002 s to 0.004 s in the same plane.

E.4 Identification of a dipole

This section aims at evaluating the performance of the 3D TR technique for the identification of a dipole noise source. The same simulation domain and 3D acoustic mesh shown in Figure E.2(b) are used. The patches ‘Left’, ‘Top’ and ‘Right’ use the “free_rec” bound-

ary condition for direct simulation and the “BC_gauss_spot” boundary condition for TR. A synthetic dipole of frequency 3 kHz (sound speed 1500 m/s, wavelength $\lambda = 0.5$ m) with the orientation in y -direction was simulated at the position (0.5 m, 0 m, 0.5 m) for the direct simulation. The size of the dipole is 0.1 m. The physical time of the simulation is 0.005 s. Figure E.5(a) shows the snapshot of the pressure field in a planar cross section XY at $z = 0.5$ m when the waves inside the simulation domain reach the permanent regime. As expected, two dominant spots with phase opposition on both sides of the position of the dipole noise source are observed. Figure E.5(b) shows the RMS of the pressure field integrated from 0.002 s to 0.004 s in the same planar cross section. The two dominant spots are located symmetrically around the dipole position. As expected for a dipole, the sound radiation is strong in the direction of the dipole orientation, and weak perpendicularly due to destructive interferences.

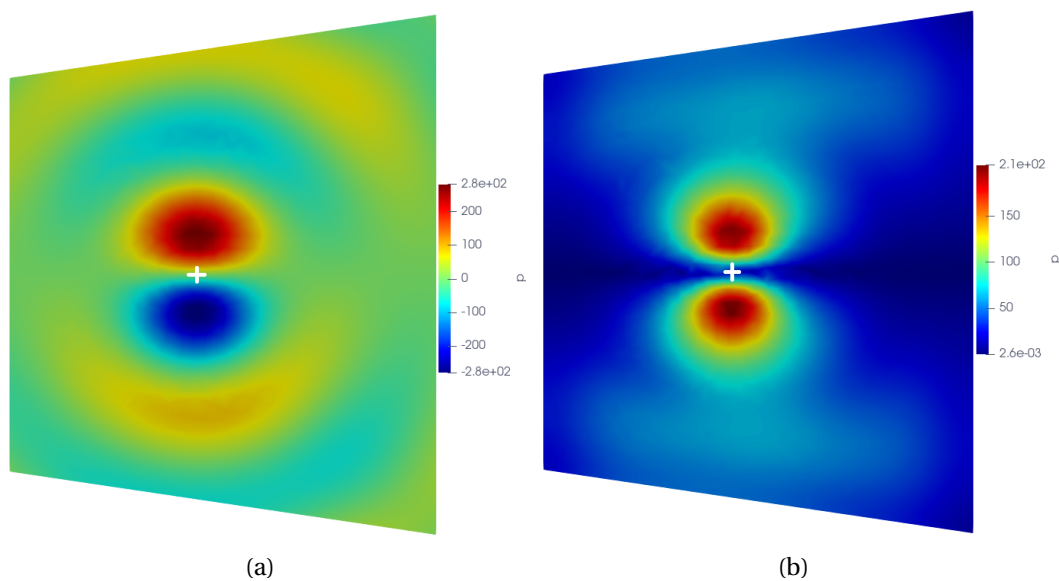


Figure E.5: Results of the 3D direct simulation concerning a dipole noise source of 3 kHz in a horizontal section. The white cross indicates the real position of the noise source. (a) Snapshot of the pressure field in a planar cross section XY at $z = 0.5$ m; (b) RMS of the pressure field integrated from 0.002 s to 0.004 s in the same plane.

The recorded acoustic signals were firstly interpolated to the positions of the 672 microphones and then the same TR process is conducted as for the previous case. Figure E.6(a) shows the snapshot of the pressure field in a planar cross section when the waves inside the domain reach the permanent regime. Despite the interference between the convergent and divergent waves, two dominant spots in phase opposition around the dipole position are generated. Two side lobes are also observed. Figure E.6(b) shows the RMS of the pressure field integrated from 0.002 s to 0.004 s in the same planar cross section. Two dominant spots elongated in the x -direction with two side lobes locate around the real position of the source. This is similar to what was observed for the 3D beamforming of a dipole noise source using the monopole steering vector. To avoid the ambiguity during the identification of noise source using 3D TR technique, some improvement should be conducted in order to generate a dominant focalization spot on the real position of the dipole.

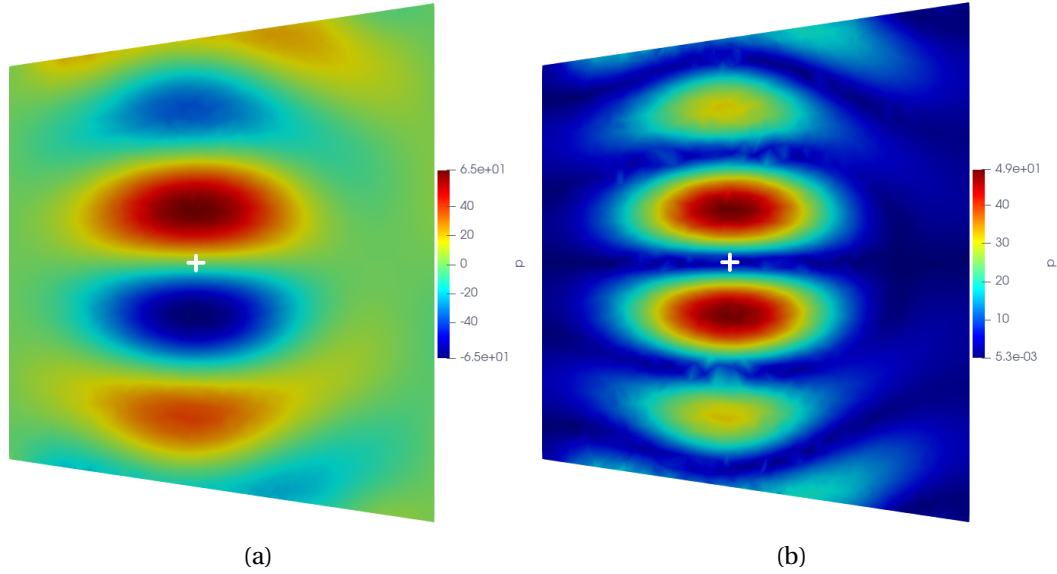


Figure E.6: Results of the 3D TR concerning a dipole noise source of 3 kHz in a horizontal section. The white cross indicates the real position of the noise source. (a) Snapshot of the pressure field in a planar cross section XY at $z = 0.5$ m; (b) RMS of the pressure field integrated from 0.002 s to 0.004 s in the same plane.

Figure E.7(a) shows the maximum pressure field of the 3D TR result from 0.002 s to 0.004 s concerning the dipole noise source with an isosurface of a value of $(1/\sqrt{2})$ times the peak level (-3 dB). Similar to the RMS result shown in Figure E.6(b), two dominant lobes can be observed around the real position of the dipole source. It is different from the result concerning a monopole noise source (see Figure E.2(b)), and very similar to the 3D BF result for a dipolar source (using a monopolar steering vector). It is not surprising as beamforming can be seen as an analytical implementation of a time-reversal process (Rakotoarisoa *et al.* [103]). Following the same strategy for the identification of a synthetic 2D dipole noise source using the data assimilation method (Diaz *et al.* [47]), the maximum amplitude of the acoustic velocity field (the components of the fluctuation velocities are recorded during simulation) from 0.002 s to 0.004 s was computed and shown by an isosurface of a value of $(1/\sqrt{2})$ times the peak level (-3 dB) in Figure E.7(b). A dominant focalization spot with ellipsoidal shape, centered on the position of the dipole noise source, is clearly observed. The stretching of the focalization spot in x -direction is due to the lack of virtual microphone array perpendicular to this direction. Therefore the position of the dipole noise source is identified with a precision at wavelength. The result, with the presence of two additional side lobes, is similar to the 3D beamforming of a dipole noise source using the dipole steering vector. It is concluded that for identifying dipolar sources using TR, the best physical quantity should be the fluctuating acoustic velocity. To remove the side lobes and improve the spatial resolution of the TR result, the acoustic sink could be applied in this case.

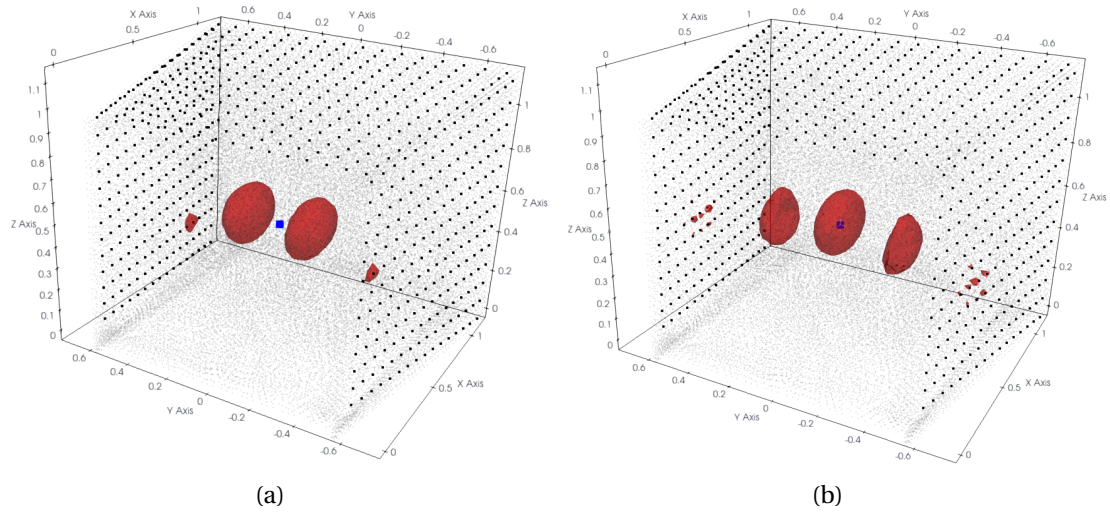


Figure E.7: 3D TR result concerning a dipole noise source of 3 kHz: (a) maximum pressure field; (b) maximum amplitude of the fluctuating velocity field. They are respectively shown by an isosurface of a value of 3dB below the corresponding peak level. The big black points indicate the positions of the 672 microphones. The blue point in the two domains stands for the real position of the dipole noise source.

This page is intentionally left blank.

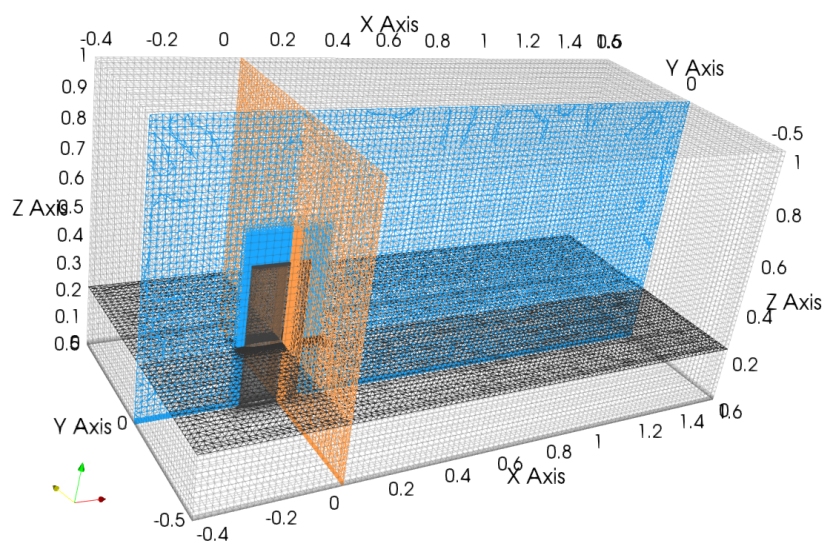
Appendix F

Flow simulation by RANS

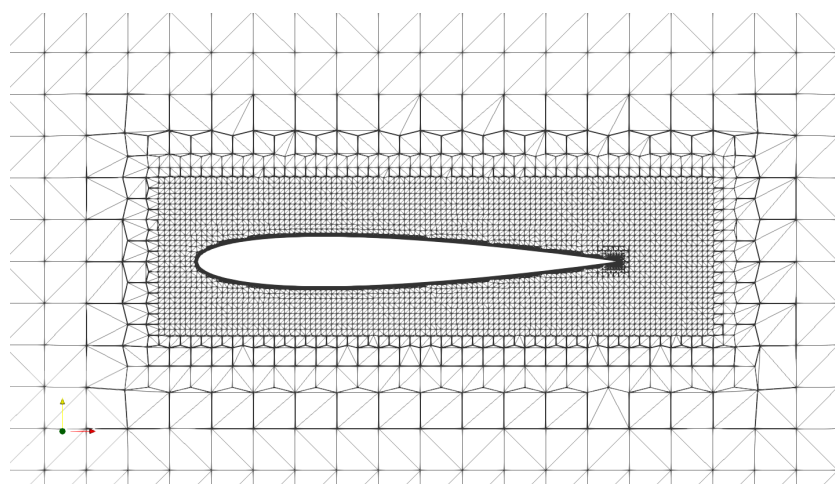
F.1 CFD Mesh

Based on the previous geometry, the mesh generation utility *cfMesh* (a third-part module available for OpenFOAM) was used for the mesh generation. For complex 3D geometries, the *cfMesh* is more robust than the mesh generator of OpenFOAM *snappyHexMesh* in terms of the generation of boundary layer mesh (several prism layers close to the wall). The 3D mesh is shown in Figure F.1(a) with three planar cross sections. It is a hybrid mesh, which contains 5513567 points, 15685582 faces and 5088958 cells. The mesh is dominated by hexahedral elements.

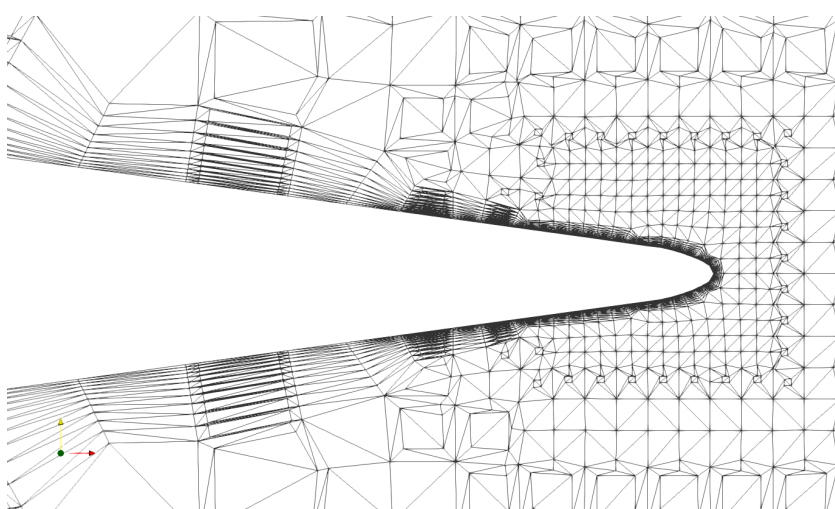
The boundary layers developed on the bottom and the surface of the wall-mounted airfoil should be taken into account for the numerical simulation. To this end, boundary layer mesh was generated for these surfaces. A refinement zone of the mesh was adapted for the vortex around the airfoil (see Figure F.1(b)). Some feature edge refinements were used for the free-end and the junction of the wall-mounted airfoil in order to well present the geometry of the wall-mounted airfoil during the mesh generation. For simplicity, some details of the mesh are not presented. Limited by the quality criteria of good mesh, the sharp trailing edge is not easy to mesh, especially for some open source softwares such as *cfMesh*, *snappyHexMesh* and *Salome*. The strategy for meshing in our case is to make it a little bit round for the airfoil and refine the mesh in the area at the trailing edge (see Figure F.1(c)). In this way, the skewness of the mesh in this area can be significantly reduced and the mesh quality becomes better. Although it exists other methods like structured mesh technique to solve this problem, it can not be conducted using *cfMesh*. The mesh quality in our case is not excellent but good enough to guarantee the convergence of the numerical simulations.



(a)



(b)



(c)

Figure F.1: The hybrid mesh for the RANS simulation concerning a wall-mounted airfoil. (a) 3D mesh for numerical simulation of the wall-mounted airfoil; (b) mesh refinement around the surface of the wall-mounted airfoil; (c) mesh refinement near the trailing edge of the wall-mounted airfoil.

F.2 Numerical results

The laminar solver (without turbulence) of OpenFOAM was firstly used for iterations from 1 to 500. This is used to initialize the fields in the domain. The residuals of these iterations are not presented. Turbulence model $k-\omega$ SST and first-order numerical schemes of divergence term were then used for iterations from 500 to 2500. The first order numerical schemes are stable but not precise for the RANS simulation. Then, second-order numerical schemes of divergence term were used for iterations from 2500 to 8500. Second order schemes are precise and less stable. The large variation of the residuals at iteration 6000 is caused by the change of numerical schemes to improve the stability of simulation which was shown by the less oscillation of the pressure residuals after iteration 7000 (see Figure F.2). The reason for conducting the numerical simulation in this way is to avoid the divergence of numerical simulation. According to the residuals in Figure F.2 and the result of some physical parameters of the simulation like velocity, the simulation was considered to be converged after iteration 7000.

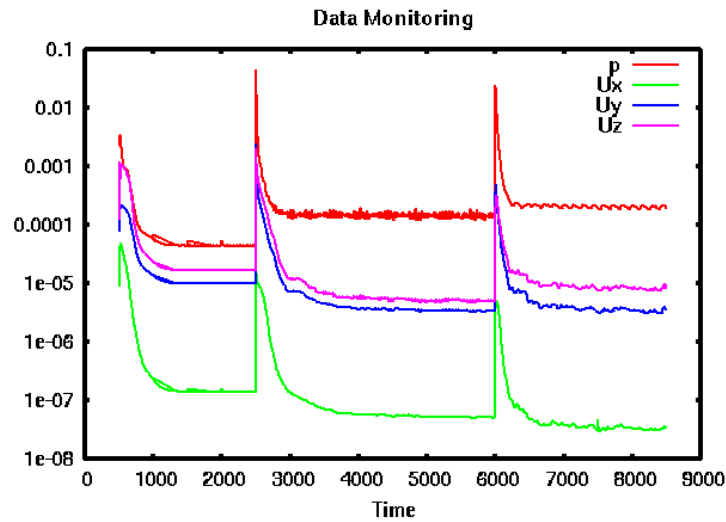


Figure E.2: Residuals of the numerical simulation during the iterations.

The value of y^+ can only be estimated before conducting numerical simulations. The precise distribution of the value of y^+ was computed when the numerical simulation is converged. The wall function used in our numerical simulation requires y^+ to be lower than 300. The statistics of the values of y^+ of the converged numerical result is given in the following Table F.1. The maximum of y^+ in the whole domain is found to be 44.5 which is good enough for the requirement.

Time step	patch	maximum of y^+
7000	bottom	44.6
7000	airfoil	6.7

Table F.1: Statistics of the values of y^+ for the patches of 'airfoil' and 'bottom'.

F.3 Flow structures

To identify the flow structures around the wall-mounted airfoil, the iso-surfaces of Q criterion of vortex were plotted. The Q criterion (Hunt *et al.* [61]) is defined as

$$Q = \frac{1}{2}(\|\boldsymbol{\Omega}\|^2 - \|\mathbf{S}\|^2), \quad (\text{E.1})$$

with $\|\cdot\|^2$ the Frobenius norm, $\boldsymbol{\Omega}$ the vorticity tensor and \mathbf{S} the strain-rate tensor.

The vorticity tensor is defined as

$$\boldsymbol{\Omega} = \frac{1}{2}(\nabla\mathbf{U} - \nabla\mathbf{U}^T), \quad (\text{E.2})$$

with $\mathbf{U} = (u, v, w)$ the velocity vector and the symbol T indicating the transpose operator.

The strain-rate tensor is defined as

$$\mathbf{S} = \frac{1}{2}(\nabla\mathbf{U} + \nabla\mathbf{U}^T). \quad (\text{E.3})$$

Figure E.3 shows the vortex of the mean flow around the wall-mounted airfoil shown by Q criterion iso-surfaces of 100. The vortex on the bottom, airfoil surface and the wing tip area were clearly observed. However, the horseshoe vortex near the junction area were not observed. Similarly, Gand *et al.* [54] performed wind-tunnel measurements, RANS (with turbulence models such as $k-\omega$ SST [78] etc.) and LES computations for a wall-mounted NACA 0012 airfoil with an aspect ratio of 2.5 at a chord-based Reynolds number of 2.8×10^5 for angle of attack of 7° . It was found that the RANS simulations failed to reproduce the flow of experimental results while the LES simulations were consistent with wind-tunnel measurements. The authors concluded that the junction flow simulation is difficult for statistical models of RANS [54]. The break of the development of the wing tip vortex is due to the large mesh cell in the far wake area (see Figure F.1 (b)), for which the precision of the flow structure is not so good.

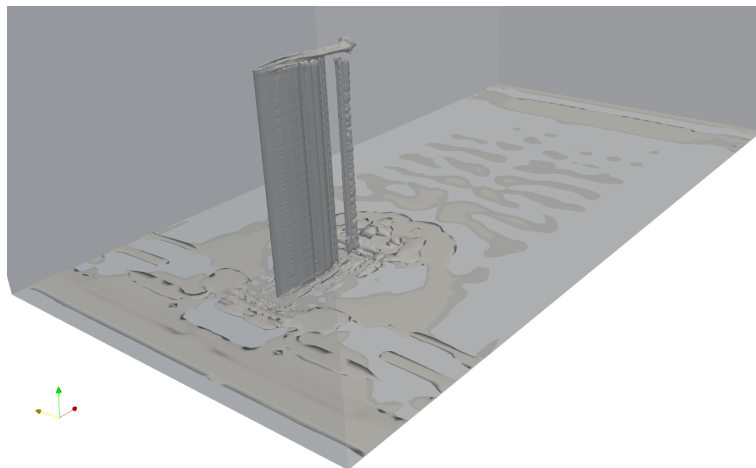


Figure E.3: Iso-surface of Q criterion for the mean flow around the wall-mounted airfoil.

Bibliography

- [1] Getting to grips with aircraft noise. Technical report, Airbus Customer Services: Flight Operations Support Line Assistance, 2003.
- [2] Environmental protection - Annex 16 to the Convention on International Civil Aviation Volume I - Aircraft noise, eighth edition. In *International Standards and Recommended Practices*. INTERNATIONAL CIVIL AVIATION ORGANIZATION, 2017.
- [3] T. Ahlefeldt and J. Quest. Real-flight Reynolds number microphone-array measurements on a scaled model in ETW. In *52nd Aerospace Sciences Meeting, National Harbor, Maryland*, page 1483, 2014.
- [4] C. S. Allen, W. K. Blake, R. P. Dougherty, D. Lynch, P. T. Soderman, J. R. Underbrink, and T. J. Mueller. *Aeroacoustic measurements*. Springer Science & Business Media, 2013.
- [5] R. Amiet. Refraction of sound by a shear layer. *Journal of Sound and Vibration*, 58(4):467–482, 1978.
- [6] B. E. Anderson, J. Douma, T. Ulrich, and R. Snieder. Improving spatio-temporal focusing and source reconstruction through deconvolution. *Wave Motion*, 52:151–159, 2015.
- [7] H. Arbey and J. Bataille. Noise generated by airfoil profiles placed in a uniform laminar flow. *Journal of Fluid Mechanics*, 134:33–47, 1983.
- [8] C. Bahr, N. S. Zawodny, T. Yardibi, F. Liu, D. Wetzel, B. Bertolucci, and L. Cattafesta. Shear layer time-delay correction using a non-intrusive acoustic point source. *International Journal of Aeroacoustics*, 10(5-6):497–530, 2011.
- [9] S. C. Bailey, S. Tavoularis, and B. H. Lee. Effects of free-stream turbulence on wing-tip vortex formation and near field. *Journal of aircraft*, 43(5):1282–1291, 2006.
- [10] C. Bailly and D. Juve. Numerical solution of acoustic propagation problems using linearized Euler equations. *AIAA journal*, 38(1):22–29, 2000.
- [11] G. Battista, P. Chiariotti, M. Martarelli, and P. Castellini. Inverse methods in aeroacoustic three-dimensional volumetric noise source localization and quantification. *Journal of Sound and Vibration*, 473:115208, 2020.
- [12] G. Battista, P. Chiariotti, M. Martarelli, P. Castellini, C. Colangeli, and K. Janssens. 3d acoustic mapping in automotive wind tunnel: Algorithm and problem analysis on simulated data. *Applied Sciences*, 11(7):3241, 2021.

- [13] E. Bavu and A. Berry. High-resolution imaging of sound sources in free field using a numerical time-reversal sink. *Acta Acustica united with Acustica*, 95(4):595–606, 2009.
- [14] E. Bavu, C. Besnainou, V. Gibiat, J. de Rosny, and M. Fink. Subwavelength sound focusing using a time-reversal acoustic sink. *Acta Acustica United with Acustica*, 93(5):706–715, 2007.
- [15] J. Billingsley and R. Kinns. The acoustic telescope. *Journal of Sound and Vibration*, 48(4):485–510, 1976.
- [16] D. Blacodon. Analysis of the airframe noise of an A320/A321 with a parametric method. *Journal of aircraft*, 44(1):26–34, 2007.
- [17] W. K. Blake. *Mechanics of flow-induced sound and vibration V2: complex flow-structure interactions*, volume 2. Elsevier, 2012.
- [18] W. K. Blake and J. L. Gershfeld. The aeroacoustics of trailing edges. In *Frontiers in Experimental Fluid Mechanics*, pages 457–532. Springer, 1989.
- [19] L. B. Bolivar, M. Sanders, L. D. De Santana, C. H. Venner, and F. M. Catalano. Analysis of a semi-empirical leading-edge slat noise prediction model. In *Proceedings of e-Forum Acousticum 2020, Lyon, France*, 2020.
- [20] M. Bordji, F. Gand, S. Deck, and V. Brunet. Investigation of a nonlinear Reynolds-Averaged Navier–Stokes closure for corner flows. *AIAA Journal*, 54(2):386–398, 2015.
- [21] T. Brooks and W. Humphreys, Jr. Effect of directional array size on the measurement of airframe noise components. In *5th AIAA/CEAS Aeroacoustics Conference and Exhibit*, page 1958, 1999.
- [22] T. F. Brooks and T. Hodgson. Trailing edge noise prediction from measured surface pressures. *Journal of sound and vibration*, 78(1):69–117, 1981.
- [23] T. F. Brooks and W. M. Humphreys. A deconvolution approach for the mapping of acoustic sources (DAMAS) determined from phased microphone arrays. *Journal of Sound and Vibration*, 294(4):856–879, 2006.
- [24] T. F. Brooks and M. A. Marcolini. Airfoil tip vortex formation noise. *AIAA journal*, 24(2):246–252, 1986.
- [25] T. F. Brooks, D. S. Pope, and M. A. Marcolini. Airfoil self-noise and prediction. *Tech. Rep. 1218 NASA Reference Publication*, 1989.
- [26] R. Camussi. *Noise sources in turbulent shear flows: fundamentals and applications*, volume 545. Springer Science & Business Media, 2013.
- [27] S. Candel, A. Guedel, and A. Julienne. Resultats preliminaires sur la diffusion d’une onde acoustique par ecoulement turbulent. *Le Journal de Physique Colloques*, 37(C1):C1–153, 1976.
- [28] S. M. Candel. Numerical solution of conservation equations arising in linear wave theory: application to aeroacoustics. *Journal of Fluid Mechanics*, 83(3):465–493, 1977.

- [29] M. H. Carpenter and C. A. Kennedy. Fourth-order 2n-storage Runge-Kutta schemes. 1994.
- [30] D. Cassereau and M. Fink. Time-reversal of ultrasonic fields. III. theory of the closed time-reversal cavity. *IEEE transactions on ultrasonics, ferroelectrics, and frequency control*, 39(5):579–592, 1992.
- [31] M. Choudhari and M. Khorrami. Slat cove unsteadiness: Effect of 3D flow structures. In *44th AIAA Aerospace Sciences Meeting and Exhibit*, page 211, 2006.
- [32] M. M. Choudhari and M. R. Khorrami. Effect of three-dimensional shear-layer structures on slat cove unsteadiness. *AIAA journal*, 45(9):2174–2186, 2007.
- [33] L. Chow, K. Mau, and H. Remy. Landing gears and high lift devices airframe noise research. In *8th AIAA/CEAS Aeroacoustics Conference & Exhibit*, page 2408, 2002.
- [34] L. C. Chow, P. Lempereur, and K. Mau. Aircraft airframe noise and installation effects—research studies. *Air & Space Europe*, 3(1):72–75, 1999.
- [35] V. Clair and G. Gabard. Numerical investigation on the spectral broadening of acoustic waves by a turbulent layer. In *22nd AIAA/CEAS Aeroacoustics Conference*, page 2701, 2016.
- [36] C. C. Critzos, H. H. Heyson, and R. W. Boswinkle Jr. Aerodynamic characteristics of NACA 0012 airfoil section at angles of attack from 0 degrees to 180 degrees. Technical report, National Aeronautics and Space Administration, Washington DC, 1955.
- [37] J. de Rosny and M. Fink. Overcoming the diffraction limit in wave physics using a time-reversal mirror and a novel acoustic sink. *Physical review letters*, 89(12):124301, 2002.
- [38] A. Deneuve, P. Druault, R. Marchiano, and P. Sagaut. A coupled time-reversal/complex differentiation method for aeroacoustic sensitivity analysis: towards a source detection procedure. *Journal of Fluid Mechanics*, 642:181, 2010.
- [39] G. Desquesnes, M. Terracol, and P. Sagaut. Numerical investigation of the tone noise mechanism over laminar airfoils. *Journal of Fluid Mechanics*, 591:155–182, 2007.
- [40] W. J. Devenport, N. K. Agarwal, M. B. Dewitz, R. L. Simpson, and K. Poddar. Effects of a fillet on the flow past a wing-body junction. *AIAA journal*, 28(12):2017–2024, 1990.
- [41] W. J. Devenport, J. K. Staubs, and S. A. Glegg. Sound radiation from real airfoils in turbulence. *Journal of Sound and Vibration*, 329(17):3470–3483, 2010.
- [42] W. Dobrzynski. Almost 40 years of airframe noise research: what did we achieve? *Journal of aircraft*, 47(2):353–367, 2010.
- [43] W. Dobrzynski, R. Ewert, M. Pott-Pollenske, M. Herr, and J. Delfs. Research at DLR towards airframe noise prediction and reduction. *Aerospace Science and Technology*, 12(1):80–90, 2008.

- [44] W. Dobrzynski, K. Nagakura, B. Gehlhar, and A. Buschbaum. Airframe noise studies on wings with deployed high-lift devices. In *4th AIAA/CEAS Aeroacoustics Conference*, page 2337, 1998.
- [45] W. Dobrzynski and M. Pott-Pollenske. Slat noise source studies for farfield noise prediction. In *7th AIAA/CEAS Aeroacoustics Conference and Exhibit*, page 2158, 2001.
- [46] P. Druault, R. Marchiano, and P. Sagaut. Localization of aeroacoustic sound sources in viscous flows by a time reversal method. *Journal of Sound and Vibration*, 332(15):3655–3669, 2013.
- [47] M. D. Escobar, R. Marchiano, and J.-C. Chassaing. Identification of aeroacoustics sources with data assimilation. In *Proceedings of e-Forum Acusticum Conference, Lyon, France*, pages 1535–1535, 2020.
- [48] M. Fink. Time-reversed acoustics. *Scientific American*, 281(5):91–97, 1999.
- [49] M. Fink. Time-reversal acoustics. In *Journal of Physics: Conference Series*, volume 118, page 012001. IOP Publishing, 2008.
- [50] M. Fink and C. Prada. Acoustic time-reversal mirrors. *Inverse problems*, 17(1):R1, 2001.
- [51] J. Fischer and C. Doolan. Beamforming in a reverberant environment using numerical and experimental steering vector formulations. *Mechanical Systems and Signal Processing*, 91:10–22, 2017.
- [52] J. Fischer, V. Valeau, and L.-E. Brizzi. Beamforming of aeroacoustic sources in the time domain: an investigation of the intermittency of the noise radiated by a forward-facing step. *J. Sound Vib.*, 383:464–485, 2016.
- [53] J. Fleming, R. Simpson, J. Cowling, and W. Devenport. An experimental study of a turbulent wing-body junction and wake flow. *Experiments in Fluids*, 14(5):366–378, 1993.
- [54] F. Gand, V. Brunet, and S. Deck. Experimental and numerical investigation of a wing-body junction flow. *AIAA journal*, 50(12):2711–2719, 2012.
- [55] J. Gershfeld. Leading edge noise from thick foils in turbulent flows. *The Journal of the Acoustical Society of America*, 116(3):1416–1426, 2004.
- [56] T. Geyer, E. Sarradj, and J. Giesler. Application of a beamforming technique to the measurement of airfoil leading edge noise. *Advances in Acoustics and Vibration*, 2012, 2012. Article ID: 905461, <http://dx.doi.org/10.1155/2012/905461>.
- [57] Y. Guo and M. Joshi. Noise characteristics of aircraft high lift systems. *AIAA journal*, 41(7):1247–1256, 2003.
- [58] J. S. Hesthaven and T. Warburton. *Nodal discontinuous Galerkin methods: algorithms, analysis, and applications*. Springer Science & Business Media, 2007.
- [59] M. S. Howe. *Acoustics of fluid-structure interactions*. Cambridge university press, 1998.

- [60] W. Humphreys, Jr, T. Brooks, W. Hunter, Jr, and K. Meadows. Design and use of microphone directional arrays for aeroacoustic measurements. In *36th AIAA aerospace sciences meeting and exhibit*, page 471, 1998.
- [61] J. C. Hunt, A. A. Wray, and P. Moin. Eddies, streams, and convergence zones in turbulent flows. 1988.
- [62] T. Imamura, S. Enomoto, H. Kato, Y. Yokokawa, and K. Yamamoto. Numerical simulation of NACA 0012 wingtip flow leading to noise generation. In *11th AIAA/CEAS Aeroacoustics Conference*, page 2864, 2005.
- [63] M. C. JACOB. Introduction to experimental aeroacoustics. In *Design and Operation of Aeroacoustic Wind Tunnels for Ground and Air Vehicles*, pages 1–25. Von Karman Institute, 2017.
- [64] D. H. Johnson and D. E. Dudgeon. *Array signal processing: concepts and techniques*. Simon & Schuster, Inc., 1992.
- [65] W. King Iii and D. Bechert. On the sources of wayside noise generated by high-speed trains. *Journal of Sound and Vibration*, 66(3):311–332, 1979.
- [66] D. König, S. Koh, W. Schröder, and M. Meinke. Slat noise source identification. In *15th AIAA/CEAS Aeroacoustics Conference (30th AIAA Aeroacoustics Conference)*, page 3100, 2009.
- [67] L. Koop. Beamforming methods in microphone array measurements: theory, practice and limitations. *LECTURE SERIES-VON KARMAN INSTITUTE FOR FLUID DYNAMICS*, 1:3, 2007.
- [68] S. Kröber. *Comparability of microphone array measurements in open and closed wind tunnels*. PhD thesis, Technische Universität Berlin, 2014.
- [69] A. Lauterbach, K. Ehrenfried, S. Kröber, T. Ahlefeldt, and S. Loose. Microphone array measurements on high-speed trains in wind tunnels. In *Berlin Beamforming Conference*. Citeseer, 2010.
- [70] Q. Leclere, A. Pereira, C. Bailly, J. Antoni, and C. Picard. A unified formalism for acoustic imaging based on microphone array measurements. *International Journal of Aeroacoustics*, 16(4-5):431–456, 2017.
- [71] M. J. Lighthill. On sound generated aerodynamically. I. general theory. In *Proceedings of the Royal Society of London A: Mathematical, Physical and Engineering Sciences*, volume 211, pages 564–587. The Royal Society, 1952.
- [72] S. Lobréau, É. Bavu, and M. Melon. Hemispherical double-layer time reversal imaging in reverberant and noisy environments at audible frequencies. *The Journal of the Acoustical Society of America*, 137(2):785–796, 2015.
- [73] G. Mahenc. *Localisation par retournement temporel de sources acoustiques supersoniques en milieu réverbérant*. PhD thesis, Conservatoire national des arts et metiers-CNAM, 2016.

- [74] G. Mahenc, E. Bavu, P. Hamery, S. Hengy, and M. Melon. Le retournement temporel en milieu réverbérant pour localiser une source supersonique. In *13ème Congrès de la Société Française d'Acoustique-CFA2016/VISHNO, Le Mans, France*, 2016.
- [75] E. Manoha and M. Pott-Pollenske. LEISA2: an experimental database for the validation of numerical predictions of slat unsteady flow and noise. In *21st AIAA/CEAS Aeroacoustics Conference*, page 3137, 2015.
- [76] K. Meadows, T. Brooks, W. Humphreys, W. Hunter, C. Gerhold, K. Meadows, T. Brooks, W. Humphreys, W. Hunter, and C. Gerhold. Aeroacoustic measurements of a wing-flap configuration. In *3rd AIAA/CEAS aeroacoustics conference*, page 1595, 1997.
- [77] J. Mendoza, T. Brooks, and W. Humphreys. Aeroacoustic measurements of a wing/slat model. In *8th AIAA/CEAS Aeroacoustics Conference & Exhibit*, page 2604, 2002.
- [78] F. R. Menter. Two-equation eddy-viscosity turbulence models for engineering applications. *AIAA journal*, 32(8):1598–1605, 1994.
- [79] R. Merino-Martínez, P. Sijtsma, A. R. Carpio, R. Zamponi, S. Luesutthiviboon, A. M. Malgoezar, M. Snellen, C. Schram, and D. G. Simons. Integration methods for distributed sound sources. *International Journal of Aeroacoustics*, 18(4-5):444–469, 2019.
- [80] P. Migliore and S. Oerlemans. Wind tunnel aeroacoustic tests of six airfoils for use on small wind turbines. *Journal of Solar Energy Engineering*, 126(4):974–985, 2004.
- [81] A. Mimani, C. J. Doolan, and P. R. Medwell. Enhancing the resolution characteristics of aeroacoustic time-reversal using a point-time-reversal-sponge-layer. In *20th AIAA/CEAS Aeroacoustics Conference*, page 2316, 2014.
- [82] A. Mimani, J. Fischer, D. Moreau, and C. Doolan. A comparison of time-reversal and cross-spectral beamforming for localizing experimental rod-airfoil interaction noise sources. *Mechanical Systems and Signal Processing*, 111:456–491, 2018.
- [83] A. Mimani, Z. Prime, D. Moreau, and C. Doolan. An experimental application of aeroacoustic time-reversal to the Aeolian tone. *The Journal of the Acoustical Society of America*, 139(2):740–763, 2016.
- [84] I. Moir. Measurements on a two-dimensional aerofoil with high-lift devices. *A selection of experimental test cases for the validation of CFD codes*, 1, 1994.
- [85] D. J. Moreau and C. J. Doolan. An experimental study of airfoil tip vortex formation noise. In *Proceedings of Acoustics, Brisbane, Australia*, 2016.
- [86] D. J. Moreau and C. J. Doolan. Tonal noise production from a wall-mounted finite airfoil. *Journal of Sound and Vibration*, 363:199–224, 2016.
- [87] D. J. Moreau, Z. Prime, R. Porteous, C. J. Doolan, and V. Valeau. Flow-induced noise of a wall-mounted finite airfoil at low-to-moderate Reynolds number. *Journal of Sound and Vibration*, 333(25):6924–6941, 2014.
- [88] S. Moreau and M. Roger. Back-scattering correction and further extensions of Amiet's trailing-edge noise model. part II: Application. *Journal of Sound and Vibration*, 323(1):397–425, 2009.

- [89] F. Moukalled, L. Mangani, M. Darwish, et al. *The finite volume method in computational fluid dynamics*, volume 113. Springer, 2016.
- [90] C. Norberg. Fluctuating lift on a circular cylinder: review and new measurements. *Journal of Fluids and Structures*, 17(1):57–96, 2003.
- [91] S. Oerlemans. *Detection of aeroacoustic sound sources on aircraft and wind turbines*. PhD thesis, University of Twente, 2009.
- [92] S. Oerlemans, L. Broersma, and P. Sijtsma. Quantification of airframe noise using microphone arrays in open and closed wind tunnels. *International Journal of Aeroacoustics*, 6(4):309–333, 2007.
- [93] T. Padois, C. Prax, and V. Valeau. Numerical validation of shear flow corrections for beamforming acoustic source localisation in open wind-tunnels. *Applied Acoustics*, 74(4):591–601, 2013.
- [94] T. Padois, C. Prax, V. Valeau, and D. Marx. Experimental localization of an acoustic sound source in a wind-tunnel flow by using a numerical time-reversal technique. *The Journal of the Acoustical Society of America*, 132(4):2397–2407, 2012.
- [95] C. C. Pagani Jr, D. S. Souza, and M. A. Medeiros. Slat noise: aeroacoustic beamforming in closed-section wind tunnel with numerical comparison. *AIAA Journal*, 54(7):2100–2115, 2016.
- [96] R. Paterson and R. Amiet. Acoustic radiation and surface pressure characteristics of an airfoil due to incident turbulence. In *3rd Aeroacoustics Conference*, page 571, 1976.
- [97] R. W. Paterson, P. G. Vogt, M. R. Fink, and C. L. Munch. Vortex noise of isolated airfoils. *Journal of Aircraft*, 10(5):296–302, 1973.
- [98] R. Porteous. *The aeroacoustics of finite wall-mounted cylinders*. PhD thesis, University of Adelaide, 2016.
- [99] R. Porteous, Z. Prime, C. J. Doolan, D. J. Moreau, and V. Valeau. Three-dimensional beamforming of dipolar aeroacoustic sources. *Journal of Sound and Vibration*, 355:117–134, 2015.
- [100] M. Pott-Pollenske, W. Dobrzynski, H. Buchholz, S. Guérin, G. Saueressig, and U. Finke. Airframe noise characteristics from flyover measurements and prediction. In *12th AIAA/CEAS Aeroacoustics Conference (27th AIAA Aeroacoustics Conference)*, page 2567, 2006.
- [101] S. Pröbsting, F. Scarano, and S. Morris. Regimes of tonal noise on an airfoil at moderate Reynolds number. *Journal of Fluid Mechanics*, 780:407–438, 2015.
- [102] I. Rakotoarisoa. *Evaluation de technique temporelles pour l’antennerie appliqué à l’imagerie acoustique en écoulement*. PhD thesis, Université de Poitiers, 2015.
- [103] I. Rakotoarisoa, J. Fischer, V. Valeau, D. Marx, C. Prax, and L.-E. Brizzi. Time-domain delay-and-sum beamforming for time-reversal detection of intermittent acoustic sources in flows. *The Journal of the Acoustical Society of America*, 136(5):2675–2686, 2014.

- [104] I. Rakotoarisoa, D. Marx, C. Prax, and V. Valeau. Array processing for the localisation of noise sources in hot flows. *Mechanical Systems and Signal Processing*, 116:160–172, 2019.
- [105] M. Roger, S. Moreau, and A. Guedel. Broadband fan noise prediction using single-airfoil theory. *Noise control engineering journal*, 54(1), 2006.
- [106] M. Roger, S. Moreau, and K. Kucukcoskun. On sound scattering by rigid edges and wedges in a flow, with applications to high-lift device aeroacoustics. *Journal of Sound and Vibration*, 362:252–275, 2016.
- [107] P. Roux and M. Fink. Experimental evidence in acoustics of the violation of time-reversal invariance induced by vorticity. *EPL (Europhysics Letters)*, 32(1):25, 1995.
- [108] R. Sen, A. M. Blackner, P. Yee, and R. Stocker. *Airframe noise generation and radiation*, volume CR NAS1-20090. NASA, 1996.
- [109] P. Sijtsma. Experimental techniques for identification and characterisation of noise sources. *Advances in Aeroacoustics and Applications, VKI Lecture Series*, 5:15–19, 2004.
- [110] P. Sijtsma. Clean based on spatial source coherence. *International journal of aeroacoustics*, 6(4):357–374, 2007.
- [111] H. Siller, M. Drescher, G. Saueressig, and R. Lange. Fly-over source localisation on a Boeing 747-400. In *Berlin Beamforming Conference (BeBeC)*, page 3. sn, 2010.
- [112] M. J. Smith. *Aircraft noise*. Number 3. Cambridge University Press, 2004.
- [113] C. Streett, D. Lockard, B. Singer, M. Khorrami, M. Choudhari, and M. Macaraeg. In search of the physics: The interplay of experiment and computation in airframe noise research, part 1. In *41st Aerospace Sciences Meeting and Exhibit*, page 979, 2003.
- [114] T. Suzuki. L1 generalized inverse beam-forming algorithm resolving coherent/incoherent, distributed and multipole sources. *Journal of Sound and Vibration*, 330(24):5835–5851, 2011.
- [115] C. K. Tam. *Computational aeroacoustics: a wave number approach*, volume 33. Cambridge University Press, 2012.
- [116] C. K. Tam and J. C. Hardin. 2nd computational aeroacoustics (CAA) workshop on benchmark problems. 1997.
- [117] E. Tran. Simulation numérique RANS de l'écoulement d'une soufflerie à veine ouverte sur OpenFOAM. Master's thesis, Sorbonne université, 2019.
- [118] T. Ulrich, B. Anderson, P.-Y. Le Bas, C. Payan, J. Douma, and R. Snieder. Improving time reversal focusing through deconvolution: 20 questions. In *Proceedings of Meetings on Acoustics XVII-ICNEM, Cefalu, Sicily, Italy*, volume 16, page 045015. ASA, 2012.
- [119] A. Uzun and M. Y. Hussaini. Simulations of vortex formation around a blunt wing tip. *AIAA Journal*, 48(6):1221–1234, 2010.

- [120] C. Vanwynsberghe, R. Marchiano, F. Ollivier, P. Challande, H. Moingeon, and J. Marchal. Design and implementation of a multi-octave-band audio camera for realtime diagnosis. *Applied Acoustics*, 89:281–287, 2015.
- [121] D. C. Wilcox et al. *Turbulence modeling for CFD*, volume 2. DCW industries La Canada, CA, 1998.
- [122] J. F. Williams and L. Hall. Aerodynamic sound generation by turbulent flow in the vicinity of a scattering half plane. *Journal of Fluid Mechanics*, 40(04):657–670, 1970.
- [123] P. Yser and C. Bailly. High-order variational multiscale model in finite elements applied to the LEISA-2 configuration. *AIAA Journal*, 56(12):5000–5012, 2018.
- [124] J. Zhang, X. Xiao, D. Wang, Y. Yang, and J. Fan. Source contribution analysis for exterior noise of a high-speed train: Experiments and simulations. *Shock and Vibration*, 2018, 2018.
- [125] Q. Zhang. Analyse de données issues d’une antenne microphonique tridimensionnelle pour l’aéroacoustique expérimentale. Master’s thesis, Sorbonne université, 2020.
- [126] Y. Zhou, M. A. Diaz, R. Marchiano, D. Marx, C. Prax, and V. Valeau. Aeroacoustic source identification with effects of solid boundaries using a numerical time-reversal technique. In *Proceedings of e-Forum Acusticum Conference, Lyon, France*, 2020.
- [127] Y. Zhou, F. Ollivier, P. Challande, R. Marchiano, V. Valeau, D. Marx, and C. Prax. Design and use of a three-dimensional array of MEMS microphones for aeroacoustic measurements in wind-tunnels. In *8th Berlin Beamforming Conference (BeBeC)*, 2020.
- [128] Y. Zhou, V. Valeau, J. Marchal, F. Ollivier, and R. Marchiano. Three-dimensional identification of flow-induced noise sources with a tunnel-shaped array of MEMS microphones. *Journal of Sound and Vibration*, 482:115459, 2020.

Résumé

La réduction de bruit est une préoccupation majeure dans l'aéronautique et les transports terrestres. Elle passe par l'identification des sources de bruit aéroacoustique, laquelle repose sur l'utilisation d'antennes microphoniques. Dans ce contexte, cette thèse concerne des mesures aéroacoustiques avec un prototype d'antenne 3D de microphones MEMS placée dans la section d'essai ouverte d'une soufflerie anéchoïque, ainsi que le développement de stratégies de traitement de signal appropriées. Dans la première partie, la technique de formation de voies (FV), tenant compte du rayonnement dipolaire en espace libre des sources de bruit (type de rayonnement typique pour le bruit d'interaction d'écoulement-obstacle), est étendue à l'identification des sources de bruit dans des domaines 3D. La FV 3D s'est avérée efficace pour identifier les sources aéroacoustiques générées par des profils d'aile encastés. Des tests supplémentaires sur un cas plus complexe - un modèle de dispositif hypersustentateur - suggèrent que l'influence des parois du modèle sur la propagation du son devrait être pris en compte dans la technique d'identification des sources. La deuxième partie introduit ensuite la technique de retournement temporel numérique (RT) pour l'identification des sources de bruit en considérant des frontières solides. Cette technique combine des mesures acoustiques et un outil numérique 3D simulant la propagation du son et un champ d'écoulement moyen. Des cas-test concernant diverses configurations difficiles, dans lesquelles la technique de FV peut échouer, sont conduits. Basée sur des données numériques, la technique RT montre des performances intéressantes pour modéliser l'effet des installations en soufflerie, mais les frontières solides situées à proximité immédiate de la source sonore peuvent dégrader les résultats. Enfin, le RT 3D est appliqué à des données expérimentales de 768 voies concernant une source de bruit synthétique de large bande diffractée par un profil d'aile NACA 0012. On montre que le RT 3D permet une meilleure précision dans la localisation des sources, au détriment du temps de calcul, par rapport à la FV 3D.

Mots clés : aéroacoustique, soufflerie, formation de voies, retournement temporel, source de bruit, profil d'aile

Abstract

Noise reduction is required in engineering domains such as aeronautics and ground transport. This involves the identification of sources of aeroacoustic noise, which is usually done by using microphone arrays. In this context, the present thesis reports aeroacoustic measurements using a prototype 3D MEMS microphone array enclosing the open test section of an anechoic wind-tunnel, and the development of adapted signal processing strategies. In the first part, the beamforming technique, accounting for free-space dipolar radiation of noise sources (a typical radiation pattern for flow-obstacle interaction noise), is extended to noise source identification in 3D domains. It is demonstrated that 3D beamforming is efficient for identifying aeroacoustic sources from wall-mounted airfoils. Further tests on a more complex case - a high-lift device model - suggest that the effect of the model on sound propagation should be introduced in the source identification technique. The second part then introduces the numerical time-reversal (TR) technique for noise source identification with the consideration of solid boundaries. This technique associates acoustic measurements and a 3D numerical tool simulating the sound propagation and mean flow field. Test cases concerning various challenging configurations, in which the beamforming technique may fail, are conducted. Using numerical data, the TR technique shows interesting performances to model installations effect in the wind-tunnel, but the solid boundaries located in the close vicinity of the source of sound may degrade the results. Finally, 3D TR is applied to experimental data of 768 channels concerning a broadband synthetic noise source diffracted by an NACA 0012 airfoil. It is shown that 3D TR allows a better precision of position at the expense of computation time, compared to 3D beamforming.

Keywords: aeroacoustics, wind-tunnel, beamforming, time-reversal, noise source, airfoil